



University of **HUDDERSFIELD**

University of Huddersfield Repository

Oluwajobi, Akinjide O.

Nanomachining Technology Development

Original Citation

Oluwajobi, Akinjide O. (2012) Nanomachining Technology Development. Doctoral thesis, University of Huddersfield.

This version is available at <http://eprints.hud.ac.uk/id/eprint/17813/>

The University Repository is a digital collection of the research output of the University, available on Open Access. Copyright and Moral Rights for the items on this site are retained by the individual author and/or other copyright owners. Users may access full items free of charge; copies of full text items generally can be reproduced, displayed or performed and given to third parties in any format or medium for personal research or study, educational or not-for-profit purposes without prior permission or charge, provided:

- The authors, title and full bibliographic details is credited in any copy;
- A hyperlink and/or URL is included for the original metadata page; and
- The content is not changed in any way.

For more information, including our policy and submission procedure, please contact the Repository Team at: E.mailbox@hud.ac.uk.

<http://eprints.hud.ac.uk/>

NANOMACHINING TECHNOLOGY DEVELOPMENT

Akinjide Olufemi Oluwajobi

A Thesis Submitted to the University of Huddersfield
In Partial Fulfilment of the Requirements for the Degree of
Doctor of Philosophy

October 2012

Abstract

Miniaturization towards the nanoscale is now the trend of technological developments in products and devices for mechanical, optical and electronic applications. Normally, good engineering functional components should have their form and surface tolerances less than one hundredth or even one thousandth of their feature sizes. However the structure fabricated by current nanotechnology can rarely achieve such tolerance ratio in a controllable way. Because of this, the kinematical and dynamical performances of these nano-structured mechanisms are far from ideal. Consequently, this research aims to identify the limit of micro and nano material removal under machining conditions.

There are still many fundamental questions which need to be addressed in nanometric machining. Some of them are the following, namely; what are the fundamental mechanisms underlying nanomachining processes? What is the limit of machining? What is the minimum depth of cut and how does one evaluate atomic surface roughness from nanomachining simulations? This study attempts to find some answers to the above questions or to point the direction towards the answers.

Nanomachining has been modelled using the Molecular Dynamics (MD) method because it has proved to be an effective tool for the prediction and the analysis of these processes at the nanometre scale. Through this investigation, it is identified that the EAM potential is the most appropriate of the 3 potentials commonly used for the modelling of nanomachining of copper with a diamond tool. This is because the EAM potential provides the best description of the metallic bonding in the workpiece, also, the cutting forces variation is smallest; the potential and total energies are most stable for the depth of cut considered. Therefore, the EAM potential should be used, rather than LJ and Morse potentials for the modelling of copper and other fcc metals in MD simulations of nanomachining. For potential pairs; it was observed that the tangential cutting force components are considerably affected by the interatomic potential pair used, but they are not greatly affected by whether the tool is rigid or deformable. The total energy of the system on the other hand is much lower when the tool is non rigid than when it is rigid.

Various MD simulations have been carried out. Results of the investigation of the minimum depth cut (MDC) nanomachining show the nano material removal phenomena of rubbing, ploughing and cutting. In a copper material removal simulation, ploughing starts from 0.2~0.3nm and the formation of chips starts to occur from the depth of cut thickness of 1.5nm. So it can be suggested that the extreme accuracy attainable or MDC for copper atoms workpiece, machined with extremely

sharp diamond tool is around 1.5nm to 3nm. The onset of plasticity for copper atom workpiece machined with extremely sharp diamond tool is around 0.1nm ~ 0.3nm.

In the investigation of the effect of various tool ends on the initiation of the phenomena of rubbing and ploughing; all the tools clearly show the phenomena of rubbing and ploughing in the depth of cut range of 0.05 to 0.5 nm. The tool with the pointed end has the lowest average cutting force and the tool with the flat end has the highest average cutting force. It is important to note that in nanomachining the tool with sharpest end may not necessarily cause the greatest material removal. The different tool ends may be suitable for different machining applications.

On the velocity variation in nanomachining simulations, it can be concluded that the interatomic potentials readily affect the simulation results, whereas the use of rigid and non-rigid tools doesn't show appreciable difference. Also, it was observed that the tangential and the normal cutting force components relatively increase with increase in velocity.

The atomic surface roughness evaluation is affected by the choice of the interatomic potentials used for the simulation.

Acknowledgements

A lot of people contributed to the successful completion of this thesis work and I would like to acknowledge their assistance.

Firstly, I would like to thank my supervisor, Professor Xun Chen for his support, advice and guidance throughout this research.

I would also like to thank the School of Computing and Engineering, University of Huddersfield and the Obafemi Awolowo University for their financial support to undertake this research.

I would like to thank Dr. Violeta Holmes for her assistance with the Linux System. Ibad Kureshi and Shuo Liang assisted a great deal in working on the Huddersfield's High Performance Computing (HPC) clusters.

I would like to thank Steve Plimpton and Axel Kohlmeyer for their helps with LAMMPS Software; and Alexander Stukowski with OVITO software.

I had a lot of discussions with Dr. David Cooke of the School of Applied Sciences on molecular dynamics, for which I am very grateful. The technical help from the following people is highly appreciated, namely; Dennis Town, Allan Kennedy, Dave Andrews, Anver Dadhiwalla, Richard and Phil. The members of the Advanced Machining Technology group, Stanley Obi and Tahsin Opoz have been very helpful.

I thank my parents and siblings for their support and encouragement during the course of this research. Special thanks also go to my wife, Yewande and children, Moyin and Moyo for their support and patience.

Finally, I would like to thank God for the gift of life and sustenance.

Dedication

This thesis is dedicated to the glory of God

	Contents	Page
Abstract	2
Acknowledgements	4
Dedication	5
Contents	6
List of Figures	10
List of Tables	14
List of Symbols	16
1. Introduction	18
1.1 Motivation and Significance of the Study	18
1.2 Short History of Machining	18
1.3 Short History of Nanotechnology	20
1.4 Problems of Conventional Modelling of Micro/Nanoscale Machining Processes	..	21
1.5 Research Aim and Objectives	21
1.6 Structure of the Thesis	21
2. Literature Review	23
2.1 Theory of Nanometric Machining	23
2.1.1 Mechanics of Chip Formation	23
2.1.2 Cutting Forces	24
2.1.3 Cutting Temperature	26
2.1.4 Minimum Depth Cut	27
2.1.5 Atomic Surface Finish	29
2.2 Atomistic Simulation Methods	32
2.2.1 Ab initio Molecular Dynamics Methods	33
2.2.2 Semi-empirical Molecular Dynamics Methods	34
2.2.3 Empirical Molecular Dynamics Methods	34
2.2.4 Monte Carlo Methods	35
2.3 The Molecular Dynamics (MD) Method	36
2.3.1 Thermodynamic Ensembles	37
2.3.1.1 Microcanonical Ensemble (NVE)	38
2.3.1.2 Canonical Ensemble (NVT)	38
2.3.1.3 Isobaric-Isothermal Ensemble (NPT)	38
2.3.1.4 Grand Canonical (μ VT)	38
2.3.2 Steps in MD Simulation	39
2.3.3 Interatomic Potentials for MD	39
2.3.3.1 Lennard-Jones Potential	40
2.3.3.2 Morse Potential	41
2.3.3.3 Born-Mayer Potential	41
2.3.3.4 Tersoff Potential	42

2.3.3.5	Embedded Atom Method (EAM) Potential	43
2.3.3.6	Modified Embedded Atom Method (MEAM) Potential	45
2.3.4	Algorithms for the Integration of the Equations of Motion	47
2.3.4.1	The Basic Verlet Algorithm	48
2.3.4.2	The Verlet Leapfrog Algorithm	49
2.3.4.3	The Velocity Verlet Algorithm	49
2.3.4.4	The Predictor-Corrector Algorithm	49
2.3.4.5	The Beeman's Algorithm	50
2.3.5	Examples of MD Simulation of Nanomachining	51
2.4	Research Gaps and Summary	56
3.	The Methodology for the MD Simulation of Nanomachining	59
3.1	The Simulation Set-up and Procedure	59
3.1.1	Software Consideration	59
3.1.2	Hardware Consideration	61
3.1.2.1	The University of Huddersfield's High Performance Computing (HPC) Clusters	61
3.1.2.1.1	How to Run the Simulation on the Huddersfield HPC	65
3.2	The Simulation Configuration	66
3.2.1	The Workpiece	67
3.2.1.1	The Face-Centred Cubic (FCC) Structure	67
3.2.2	The Tool	67
3.2.2.1	The Diamond Structure	68
3.3	The Selection of the Interatomic Potentials and Parameter Settings	68
3.3.1	Initialization	68
3.3.2	Boundary Conditions	68
3.3.3	Relaxation of the System	69
3.4	Concluding Remarks and Scope of Research	69
4.	Single-Pass Nanometric Machining Simulation Results	70
4.1	The Effect of Interatomic Potentials on Nanomachining	70
4.1.1	Introduction	70
4.1.2	Modelling with LJ Potential	71
4.1.3	Modelling with Morse Potential	71
4.1.4	Modelling with EAM Potential	71
4.1.5	Conclusion	76
4.2	Choosing Appropriate Interatomic Potentials for MD Simulation of Nanomachining	76
4.2.1	Introduction	76
4.2.2	Conclusion	84
4.3	Determination of Minimum Depth Cut in Nanomachining	84
4.3.1	Introduction	84
4.3.2	The Effect of Interatomic Potential on the Evaluation of the Minimum Depth Cut in Nanomachining	84
4.3.3	Prediction of the Onset of Plasticity	92
4.3.4	Conclusion	92
4.4	The Effect of Tool Geometry on Rubbing and Ploughing in Nanomachining	93
4.4.1	Introduction	93

4.4.2	Conclusion	99
4.5	The Effect of the Variation of Velocity in Nanomachining	100
4.5.1	Introduction	100
4.5.2	Modelling with EAM-Morse Potentials and Rigid Tool	102
4.5.3	Modelling with EAM-Morse Potentials and Non-Rigid Tool	106
4.5.4	Modelling with EAM-LJ Potentials and Rigid Tool	109
4.5.5	Modelling with EAM-LJ Potentials and Non-Rigid Tool	112
4.5.6	Conclusion	115
5.	Multiple-Pass Nanometric Machining Simulation Results	116
5.1	Introduction	116
5.2	The Effect of Interatomic Potentials	118
5.2.1	Conclusion	130
5.3	The Effect of Depth of Cut	130
5.3.1	Conclusion	133
5.4	The Effect of Feed Rate	134
5.4.1	Conclusion	136
5.5	The Effect of Rake Angle	137
5.5.1	Conclusion	139
6.	Atomic Surface Roughness Evaluation	140
6.1	Introduction	140
6.2	The Algorithm for the Evaluation of Atomic Surface Roughness	140
6.3	The Implementation and Comparison of Surface Roughness for the Multiple-Pass Simulation Conditions	140
6.3	Discussions and Concluding Remarks	152
7.	Experimental Set-up and Procedure	153
7.1	Introduction	153
7.2	Sample Preparation	153
7.3	Experimental and Measuring Equipment	154
7.3.1	Experimental Set-up	154
7.3.2	Metrology Equipment	155
7.4	Experimental Procedure	155
7.5	Analysis of the AE Signals	156
7.6	Discussion and Concluding Remarks	168
8.	Conclusions and Recommendations	169
8.1	Contributions to Knowledge	169
8.2	Conclusions	169
8.3	Recommendations for Further Work	170
References		172
Appendixes		181
Appendix A:	LAMMPS Input File Structure	181

Appendix B: A PBS Job Script Template182

Appendix C: More Simulation Results183

Appendix D: Publications arising from this Research214

List of Figures	Page
Figure 1.1: Taniguchi Curve	20
Figure 2.1: The Organizational Structure of the Thesis	22
Figure 2.2: Orthogonal Cutting Model	23
Figure 2.3: Diagram of Cutting Forces	24
Figure 2.4a: Schematic of the MD Simulation of Nanometric Cutting (2D)	25
Figure 2.4b: Atomistic Interaction in Nanometric Machining	25
Figure 2.5: Illustration of Interatomic Interaction for a STM	29
Figure 2.6: Illustration of Interatomic Interaction for an AFM	30
Figure 2.7: Simulated Atomic Topography for $\lambda_1 = \lambda_2$	30
Figure 2.8: Simulated Atomic Topography for $\lambda_1 > \lambda_2$	30
Figure 2.9: Scales for Simulation Time and Length	33
Figure 2.10: Schematic of the MD Simulation of Nanometric Cutting (2D)	36
Figure 2.11: Schematic of the MD Simulation of Nanometric Cutting (3D)	36
Figure 2.12: Advanced MD Simulation with Straight Aligned Tool	52
Figure 2.13: Groove Scratching with 2 Grits (top view - 360 000 time steps, 144 ps)	53
Figure 2.14: Snapshots of Atomic Arrays in Vibration-assisted Cutting Process and Travelling Distance from Initial Arrays	54
Figure 2.15: Snapshots of Atomic Arrays and Travelling Distance	55
Figure 3.1: Software Methodology Flowchart	59
Figure 3.2: Network Diagram	61
Figure 3.3: Eridani Cluster Architecture Diagram	64
Figure 3.4: TauCeti Cluster Architecture Diagram	64
Figure 3.5: General Users' Workflow for the Huddersfield HPC	65
Figure 3.6: The MD Simulation Model	66
Figure 3.7: The Face-Centred Cubic Structure	67
Figure 3.8: The Diamond Structure	68
Figure 4.1: The MD Simulation Model for this Investigation	70
Figure 4.2: Simulation with EAM-Morse Potentials	74
Figure 4.3: Cutting Forces for EAM-Morse Potential	75
Figure 4.4: The Comparison of the Potential Energy for the EAM and the EAM-Morse Potentials	75
Figure 4.5: The Variation of Potential Energies for the LJ, Morse and EAM Potentials.. ...	75
Figure 4.6: Comparison of the Total Energy for the Different Potential Pairs (Both Rigid and Non-Rigid Tools)	79
Figure 4.7: Comparison of the Total Energy for the Different Potential Pairs (Rigid Tool)...80	80
Figure 4.8: Comparison of the Total Energy for Potential Pairs EAM-Morse and Morse-Morse (Rigid Tools)	80
Figure 4.9: Comparison of the Total Energy for the Potential Pairs (Non-Rigid Tool)80	80
Figure 4.10: Comparison of the Total Energy for Potential Pairs EAM-LJ and EAM-Morse (Rigid Tools)	81
Figure 4.11: Comparison of the Total Energy for Potential Pairs EAM-LJ and EAM-Morse (Non-Rigid Tools)	81
Figure 4.12: Comparison of the Total Energy for Potential Pair EAM-Morse (Rigid and Non-Rigid Tools)	81
Figure 4.13: Comparison of the Total Energy for Potential Pair Morse-Morse (Rigid and Non-Rigid Tools)	82
Figure 4.14: Comparison of the Total Energy for Potential Pair EAM-LJ (Rigid and Non-Rigid Tools)	82
Figure 4.15: The Tangential Component of the Cutting Forces for the Different	

Pairs of Potentials	82
Figure 4.16: Variation of the Tangential Cutting Force with Depth of Cut for the Potential Pairs	87
Figure 4.17: Variation of the Normal Cutting Force with Depth of Cut for the Potential Pairs	87
Figure 4.18: Variation of the Lateral Cutting Force with Depth of Cut for the Potential Pairs	87
Figure 4.19: Variation of the Potential Energy with Depth of Cut for the Potential Pairs	88
Figure 4.20: Variation of the Potential Energy with Depth of Cut for the EAM-LJ and EAM-Morse Potential Pairs	88
Figure 4.21: Variation of the Total Energy with Depth of Cut for the Potential Pairs	88
Figure 4.22: Variation of the Kinetic Energy with Depth of Cut for the Potential Pairs	89
Figure 4.23: Different Tool Geometries; (a) Tool with Flat End (b) Tool with Pointed End, (c) Tool with Spherical End, (d) Tool with Trapezoidal End	94
Figure 4.24: Tool with Flat End	94
Figure 4.25: Tool with Pointed End	95
Figure 4.26: Tool with Spherical End	95
Figure 4.27: Tool with Trapezoidal End	96
Figure 4.28: Variation of the Tangential Cutting Force with Depth of Cut for the Different Tool Ends	96
Figure 4.29: Variation of the Normal Cutting Force with Depth of Cut for the Different Tool Ends	97
Figure 4.30: Variation of the Lateral Cutting Force with Depth of Cut for the Different Tool Ends	97
Figure 4.31: Variation of the Total Energy with Depth of Cut for the Different Tool Ends	97
Figure 4.32: Velocity Variation with Temperature for EAM-Morse Potentials and Rigid Tool	104
Figure 4.33: Variation of Tangential Cutting Force Component with Velocity for EAM-Morse Potentials and Rigid Tool	105
Figure 4.33b: Variation of Normal Cutting Force Component with Velocity for EAM-Morse Potentials and Rigid Tool	105
Figure 4.34: Variation of Temperature with Velocity for EAM-Morse Potentials and Rigid Tool	105
Figure 4.35: Velocity Variation with Temperature for EAM-Morse Potentials and Non-Rigid Tool	108
Figure 4.36: Comparison of Variation of Tangential Cutting Force Component with Velocity for EAM-Morse Potentials (Rigid Tool and Non-Rigid Tool)	108
Figure 4.37: Comparison of Variation of Temperature with Velocity for EAM-Morse Potentials (Rigid Tool and Non-Rigid Tool)	109
Figure 4.38: Comparison of Variation Tangential Cutting Force Component with Velocity for All Potentials (Rigid Tool and Non-Rigid Tool)	114
Figure 4.39: Comparison of Variation of Velocity with Temperature for All Potentials (Rigid Tool and Non-Rigid Tool)	114
Figure 4.40: Variation of the Cutting Forces with Velocity (1m/s-260m/s)	115
Figure 5.1a: Cross Section of the Machined Grooves with Passes 1-3 (direction of cut is perpendicular to the paper face) 1b: Tool Tip Dimensions	117
Figure 5.2: Comparison of the Total Energy for the Different Potential Pairs (Rigid and Non Rigid Tool)	125
Figure 5.3: Tangential Cutting Force Components for the Different Potentials – Pass 1	125
Figure 5.4: Tangential Cutting Force Components for the Different Potentials – Pass 2	126

Figure 5.5: Tangential Cutting Force Components for the Different Potentials – Pass 3 ..	126
Figure 5.6: Tangential Cutting Force Components for the EAM-LJ Potentials (Rigid Tool) Passes 1-3	126
Figure 5.7: Tangential Cutting Force Components for the EAM-Morse Potentials (Rigid Tool) – Passes 1-3	127
Figure 5.8: Tangential Cutting Force Components for the Morse-Morse Potentials (Rigid Tool) – Passes 1-3	127
Figure 5.9: Tangential Cutting Force Components for the EAM-LJ Potentials (Non Rigid Tool) – Passes 1-3	127
Figure 5.10: Tangential Cutting Force Components for the EAM-Morse Potentials (Non Rigid Tool) – Passes 1-3	128
Figure 5.11: Tangential Cutting Force Components for the Morse-Morse Potentials (Non Rigid Tool) – Passes 1-3	128
Figure 5.12: Variation of F_x with Depth of Cut	131
Figure 5.13: Variation of F_y with Depth of Cut	131
Figure 5.14: Variation of F_z with Depth of Cut	132
Figure 5.15: Variation of F_x , F_y and F_z in Pass 3 with Depth of Cut	132
Figure 5.16: Stress Variation with Depth of Cut for Passes 1-3	132
Figure 5.17: Variation of F_x with Passes 1-3	135
Figure 5.18: Variation of F_y with Passes 1-3	135
Figure 5.19: Variation of F_z with Passes 1-3	136
Figure 5.20: Rake Angle Negative 5 (-ve 5)	137
Figure 5.21: Rake Angle Negative 10 (-ve 10)	137
Figure 5.22: Rake Angle Negative 15 (-ve 15)	137
Figure 5.23: Variation of Cutting Forces with Rake Angles – Pass 1	138
Figure 5.24: Variation of Cutting Forces with Rake Angles – Pass 2	139
Figure 5.25: Variation of Cutting Forces with Rake Angles – Pass 3	139
Figure 6.1: A Near Perfect Surface of the Workpiece	141
Figure 6.2: The Surface Atoms Contributing to the Surface Roughness	141
Figure 6.3: Variation of S_a with Depth of Cut for the EAM-LJ Potentials	150
Figure 6.4: Variation of S_a with Depth of Cut for the EAM-Morse Potentials	150
Figure 6.5: Variation of S_a with Velocity for the EAM-LJ Potentials	151
Figure 6.6: Variation of S_a with Velocity for the EAM-Morse Potentials	151
Figure 7.1: The Nanoform 250 Ultraprecision Machine	154
Figure 7.2: The Experimental Rig	154
Figure 7.3: The CCI Interferometer	155
Figure 7.4: The AFM Machine	155
Figure 7.5: Raw AE Signal for RPM 7000 (Touch)	156
Figure 7.6: Raw AE Signal for RPM 7000 (Touch and Rubbing)	156
Figure 7.7: Raw AE Signal for RPM 5000 (Rubbing and Ploughing)	157
Figure 7.8: Raw AE Signal for RPM 5000 (Ploughing)	157
Figure 7.9: Raw AE Signal for RPM (Cutting)	158
Figure 7.10: Raw AE Signal for RPM 7000 (Touch)	158
Figure 7.11: Raw AE Signal for RPM 7000 (Touch and Rubbing)	159
Figure 7.12: Raw AE Signal for RPM 7000 (Touch and Rubbing)	159
Figure 7.13: Raw AE Signal for RPM 6000 (Touch)	160
Figure 7.14: Raw AE Signal for RPM 6000 (Touch and Rubbing)	160
Figure 7.15: Raw AE Signal for RPM 6000 (Cutting)	161
Figure 7.16: Raw AE Signal for RPM 5000 (Tough and some Rubbing)	161
Figure 7.17: Raw AE Signal for RPM 5000 (Rubbing and Ploughing)	162
Figure 7.18: Raw AE Signal for RPM 5000 (Ploughing)	162

Figure 7.19: Raw AE Signal for RPM 5000 (Cutting)	163
Figure 7.20: Raw AE Signal for RPM 4000 (Touch and Rubbing)	163
Figure 7.21: Raw AE Signal for RPM 4000 (Cutting)	164
Figure 7.22: Raw AE Signal for RPM 3000 (Touch and Rubbing)	164
Figure 7.23: Raw AE Signal for RPM 3000 (Cutting)	165
Figure 7.24: Raw AE Signal for RPM 2000 (Touch and Slight Rubbing)	165
Figure 7.25: Raw AE Signal for RPM 2000	166
Figure 7.26: AFM Image of the Side of the Scratch	166
Figure 7.27: AFM Image of the Side of the Scratch for RPM 3000	167
Figure 7.28: AFM Image of the Scratch for RPM 4000	167
Figure 7.29: AFM Image of the cut (inside) Scratch for RPM 3000	167
Figure 7.30: Comparison of Features in an AFM Image and Simulations	168
Figure 7.31: AFM Scratches on Aluminum	168

List of Tables	Page
Table 2.1: Comparison of Nanometric Cutting and Conventional Cutting Mechanics	32
Table 2.2: Comparison of Some Atomistic Simulation Methods	35
Table 2.3: Comparison of the Thermodynamic Ensembles	38
Table 2.4: Constants for Lennard-Jones Potential	40
Table 2.5: Constants for Morse Potential	41
Table 2.6: Constants for Born-Mayer Potential	42
Table 2.7: Constants for Tersoff Potential	43
Table 2.8: Electron densities and the embedding functions for Nickel	44
Table 2.9: Electron densities and the embedding functions for Gold	45
Table 2.10: Comparison of the Interatomic Potentials	46
Table 2.11: On more Potentials	47
Table 2.12: Comparison of some MD simulations of Nanomachining	57
Table 3.1: Comparison of some MD Software	62
Table 3.2: Hardware Configuration of the Eridani Cluster	65
Table 3.3: Properties of Copper	67
Table 3.4: Properties of Diamond	67
Table 3.5: MD Simulation Parameters	68
Table 4.1: Comparison of the Different Simulations with Different Potentials showing the Cutting Forces	73
Table 4.2: Comparison of the Different Simulations with Different Potentials showing the Energies and the Temperature Variation	74
Table 4.3: Comparison of the Different Simulations with Different Potentials Combinations and Rigid/Non rigid Tool	77
Table 4.4: Comparison of the Different Simulations (Cases 1-6) showing Cutting Forces and the Energies	78
Table 4.5: Forces and Total Energies Comparison for the Different Potential Pairs	83
Table 4.6: Summary on Minimum Depth Cut	89
Table 4.7: Comments on the Minimum Depth Cut Simulation (By Observation of the Chip Formation)	90
Table 4.8: Force Ratio (F_x/F_z) Tangential Force Component/Normal Force Component For the Different Potentials	91
Table 4.9: Summary on Various Tool Geometries (Observed Phenomena)	98
Table 4.10: Force Ratio (F_x/F_z) Tangential Force Component/Normal Force Component for the Different Tool Ends	98
Table 4.11: The Various Timesteps for the Different Velocity for a Distance of 7.2nm	102
Table 4.12: Comparison of the Cutting Forces and the Energies for Velocities (80-260m/s) Case 4.5.1	102
Table 4.13: Comparison of the Cutting Forces and the Energies for Velocities (80-260m/s) Case 4.5.2	106
Table 4.14: Comparison of the Cutting Forces and the Energies for Velocities (80-260m/s) Case 4.5.3	109
Table 4.15: Comparison of the Cutting Forces and the Energies for Velocities (80-260m/s) Case 4.5.4	112
Table 5.1: Comparison of the Material Removal for the Different Interatomic Potentials and the Tool (Rigid and Deformable) Pass 1	118
Table 5.2: Comparison of the Cutting Forces and Energies for the Different Interatomic Potentials and the Tool (Rigid and Deformable) Pass 1	119
Table 5.3: Comparison of the Material Removal for the Different Interatomic Potentials and the Tool (Rigid and Deformable) Pass 2	120

Table 5.4: Comparison of the Cutting Forces and Energies for the Different Interatomic Potentials and the Tool (Rigid and Deformable) <i>Pass 2</i>	121
Table 5.5: Comparison of the Material Removal for the Different Interatomic Potentials and the Tool (Rigid and Deformable) <i>Pass 3</i>	123
Table 5.6: Comparison of the Cutting Forces and Energies for the Different Interatomic Potentials and the Tool (Rigid and Deformable) <i>Pass 3</i>	124
Table 5.7: Comparison for the Different Potential Pairs: Total Energy (eV)	127
Table 5.8: Comparison of the Material Removal for the Three Passes for Depth of Cut (0.5-3nm)	128
Table 5.9: Simulations for Different Feeds (0.5 – 1.5nm)	134
Table 5.10: Simulations for Different Rake Angles (-15, -10, -5, 0, 5, 10, 15)	138
Table 6.1: Surface Roughness Results for the EAM-LJ Potentials for Depth of Cut (0.5-3.0nm)	142
Table 6.2: Surface Roughness Results for the EAM-LJ Potentials for Velocity (40-220m/s) (Depth of Cut 2.0nm)	143
Table 6.3: Surface Roughness Results for the EAM-Morse Potentials for Depth of Cut (0.5-3.0nm)	146
Table 6.4: Surface Roughness Results for the EAM-Morse Potentials for Velocity (40-220m/s) (Depth of Cut 2.0nm).....	147
Table 6.5: Surface Roughness Results for the EAM-LJ and EAM-Morse Potentials for Depth of Cut (0.5-3.0nm)	149
Table 6.6: Surface Roughness Results for the EAM-LJ and EAM-Morse Potentials for Velocity (40-220m/s) (Depth of Cut 2.0nm)	150
Table 7.1: Process Breakdown	153
Table C.1: Simulations with Variations of the Depth of Cut (0.01-4.0nm) for the Three Potential Combinations	183
Table C.2: Comparison of the Cutting Forces for the Simulations with Depth of Cut (0.01-4.0nm)	187
Table C.3: Comparison of the Energies for the Simulations with Depth of Cut (0.01-4.0nm)	191
Table C.4: Comparison of the Variation of Temperature for the Simulations with Depth of Cut (0.01-4.0nm)	194
Table C.5: Comparison of the Simulation for Different Tool Ends with Depth of Cut (0.05-0.5nm)	198
Table C.6: Comparison of the Cutting Forces for the Different Tool Ends (Depth of Cut 0.05-0.5nm)	200
Table C.7: Comparison of the Energies for the Different Tool Ends (Depth of Cut 0.05-0.5nm)	203
Table C.8: Comparison of the Temperature Variation for the Different Tool Ends (Depth of Cut 0.05-0.5nm)	206
Table C.9: Cutting Forces for the Different Cases	209
Table C.10: Temperature Variation for the Different Cases	210
Table C.11: Cutting Forces for Different Depths of Cut (0.5 – 3nm)	211
Table C.12: Cutting Forces Different Feeds (0.5 – 1.5nm)	212
Table C.13: Cutting Forces for Different Rake Angles (-5, -10, -15, 0, 5, 10, 15 degrees) ..	213

List of Symbols

a_i	Acceleration of atom i
A	Material dependent constant
b	Third derivative of position $\frac{d^3 r}{dt^3}$
B_{ij}	A parameter that provides information for the direction and the length of bond
c	Fourth derivative of position $\frac{d^4 r}{dt^4}$
d	Material dependent constant
D	Material dependent constant
e	Material dependent constant
E	Energy of interacting particles
E_{tot}	Total embedding energy
F_i	Force acting on atom i
F_{wtij}	Interatomic forces acting on the i -th workpiece atom from the cutting tool
F_{wwij}	Interatomic forces acting on the i -th workpiece atom from other workpiece material atoms
F_{twij}	Interatomic forces acting on the i -th cutting tool atom from the workpiece material atom
F_{ttij}	Interatomic forces acting on the i -th cutting tool atom from other cutting tool atoms
G_i	Embedding energy for placing atom i into the electron density
G'	First derivative of the embedding energy
G''	Second derivative of the embedding energy
h	Planck constant
m_i	Mass of atom i
N	Number of atoms
N_t	No of cutting tool atoms
N_w	No of workpiece atoms
k_B	Boltzmann constant
r_e	Equilibrium distance between atoms i and j
r_i	Position of atom or particle i
r_{ij}	Instantaneous distance between particles i and j
r_o	Material dependent constant
r_{wtij}	Displacement vector of the i -th workpiece atom and the j -th tool atom
r_{wwij}	Displacement vector of the i -th workpiece atom and the j -th workpiece atom
r_{ttij}	Displacement vector of the i -th tool atom and the j -th tool atom
r_{twij}	Displacement vector of the i -th tool atom and the j -th workpiece atom
t	Time
t_1	Depth of cut
t_2	Chip thickness

$U_{ij}(r)$	<i>Short range pair interaction representing the core-core repulsion</i>
v	<i>Velocity</i>
$V_{ij}, V(r_{ij})$	<i>Interatomic Pair Potential</i>
V_a	<i>Potential due to attractive forces between atoms i and j</i>
V_r	<i>Potential due to repulsive forces between atoms i and j</i>
V_c	<i>Chip velocity</i>
$V_{i,j}$	<i>Short range pair interaction representing the core-core repulsion</i>
α	<i>Material dependent constant</i>
β	<i>Thermodynamic beta ($\frac{1}{k_B T}$)</i>
ε	<i>Material dependent constant</i>
\hbar	$\frac{h}{\pi}$
ϕ	<i>Shear Angle</i>
$\rho(r)$	<i>Electron density</i>
$\rho_j^a(r)$	<i>Atomic electron density of atom j at the distance r_{ij} from the nucleus</i>
$\rho_{h,i}$	<i>Total electron density at atom i due to the rest of the atoms in the system</i>
$\bar{\rho}$	<i>Average electron density</i>
$\Psi(r, t)$	<i>Wave function (The probability of finding any particle at position r, at time t)</i>
Δt	<i>Finite time step</i>
μ	<i>Chemical potential</i>
λ_1, λ_2	<i>Spatial profile along the x and y axes respectively</i>
$z(x, y)$	<i>Atomic topography</i>

Chapter 1. Introduction

1.1 Motivation and Significance of the Study

Humans have been using machine tools for centuries. The usage has evolved from very primitive forms to highly advanced, precise and efficient machines that exist today (Hoffman et al 2011). Machining plays an essential role in modern manufacturing and the demand for miniaturized devices with stringent form and surface requirements is making the process a top choice. The world machine tool industry is worth \$65 billion and global demands for machine tool products will keep growing by 5.2% annually (Freedonia Market Research, 2009).

The need for high accuracy and high efficiency machining of difficult-to-machine materials is making the application of machining technology increasingly important. Also, the use of machining to produce complex three dimensional (3D) nanoscale devices is clearly a distinct advantage over other methods of manufacturing (Jackson, 2008). Many different types of models have been developed to model machining, which range from the macroscopic to the microscopic and they cover analytical, empirical and physical approaches. Some of these are fundamental analytical models, kinematic models, analytic regression models, artificial neural networks models and the finite element analysis approaches (Brinksmeier et al 2006), with special emphasis on grinding. With the trend towards miniaturization and the development of ultra-precision processes which can achieve excellent surface finish at nanometre level, there is a need for simulations at this length scale and many of the above models are not adequate for nanoscale simulations.

1.2 Short History of Machining

In early times, metal removal was achieved by using hand tools made from bones, sticks and stones. Later on, metal cutting machines driven by water, steam and electricity were employed and further innovations advanced the development of machine tools. In 1775, John Wilkinson invented a cannon-boring machine, which was soon after adapted for boring cylinders for steam engines. Eli Whitney in 1815 invented a milling machine and C.H. Norton invented the grinding machines in the late 19th century. According to (El-Hofy 2007), systematic research on machining began in 1850, with the following highlights, namely:

- “1851 – Measurement of the cutting forces and power consumption to remove a given volume of metal
- 1870 – Mechanics of chip formation
- 1893 – Analysis of forces in the cutting zone
- 1907 – Study on tool wear began
- 1950 – Verification of the metal cutting models
- 1960 – Developments of the field of grinding and non traditional machining processes
- 1970 – Developments in the field of non-traditional and hybrid machining processes, including micromachining and nanomachining”
- 1980~2000 – The advancement of technology in Very Large Scale Integrated (VLSI) Circuits (Microprocessors) and Artificial Intelligence have impacted the Ultraprecision machine tools in the controls and dexterity

Now the latest trend of machining development is in nanomachining where atoms (which may be considered as chips) are removed to produce highly precise machined parts in products and devices for mechanical, optical and electronic applications. This supports Taniguchi’s prediction (Taniguchi 1983) of increasing precision as a function of time (Figure 1.1). Many of these nanotechnology applications need to engineer the surface on which the nano-materials can build on. Normally, good engineering functional components should have their form and surface tolerances less than one hundredth or even one thousandth of their feature sizes. However the structure fabricated by current nanotechnology can rarely achieve such tolerance ratio in a controllable way. Because of this, the kinematical and dynamical performances of these nano-structured mechanisms are far from ideal. Improvement of the accuracy of nano-feature shape needs controllable erosion methods which can remove excessive materials as required. At the moment, there is no such controllable method that can be used at the nanoscale. Chemical erosions have poor directional controllability, which are difficult to apply for a good surface finish. (Surface roughness in the micrometre range have been reported – Senthilkumar et al, 2011 and Ruszaj et al, 2003) Electrolytic methods can be used in making micro features, but the electrical poles suffer severe wear and control at the nano scale level is difficult. Conventional abrasive polishing methods can only be applied to large surface features due to large scale flow kinematical requirement, and so the development of a suitable nano surface removal method becomes a critical issue in micro-nano fabrication of nanogrooves – nanochannels.

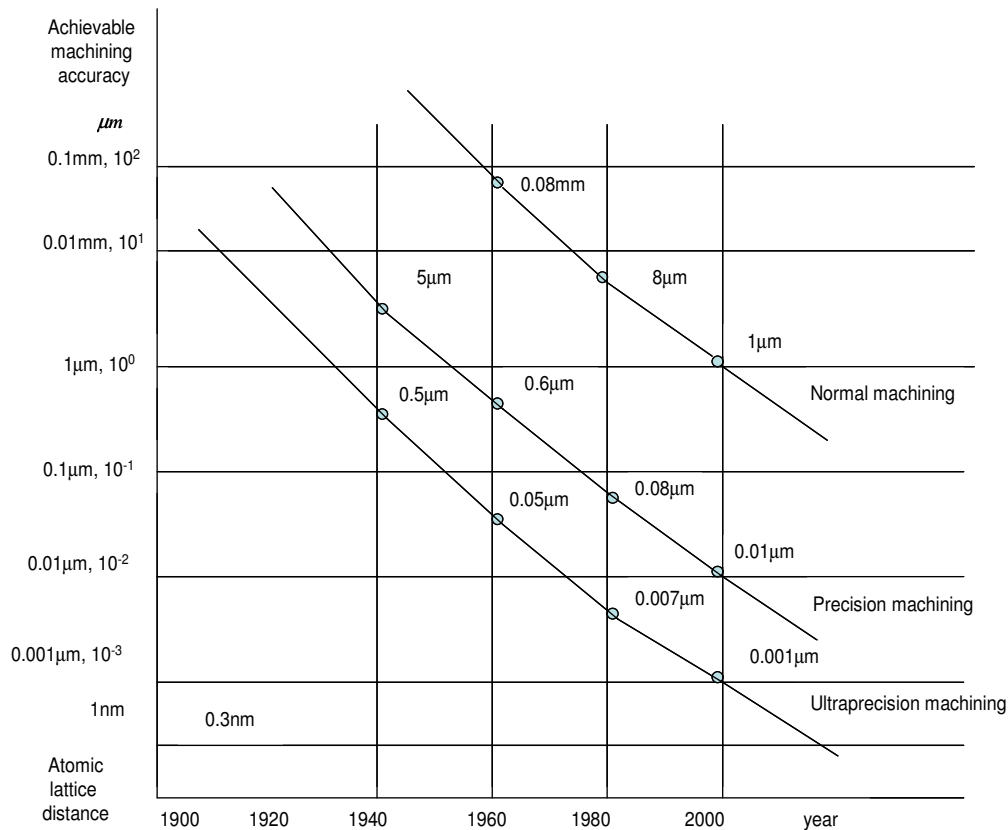


Figure 1.1: Taniguchi Curve (Taniguchi 1983)

1.3 Short History of Nanotechnology

The prefix nano has its origin in Greek, which means dwarf. In modern scientific parlance, a nanometer is one billionth of a metre. Nanotechnology, as we know it now, was first proposed in 1959 by Richard Feynman, in an after-dinner lecture, titled, “There is plenty of room at the bottom” (Feynman, 1959). The following are highlights in the development of nanotechnologies.

- Nario Taniguchi of Tokyo Science University coined the word nanotechnology in 1974 (Taniguchi, 1974)
- In 1981, Gerd Binnig and Heinrich Rohrer invented the Scanning Tunneling Microscope (STM) at the IBM’s Zurich Research Laboratory (Binnig and Rohrer, 1982)
- Invention of the Atomic Force Microscope (AFM) (Binnig et al., 1986)
- In 1990, Don Eigler of IBM and co-workers showed that it is possible to manipulate individual atoms. They positioned 35 xenon atoms on the surface of a nickel crystal, using an AFM, to spell out the letters “IBM” (Eigler and Schweizer, 1990)
- Other landmarks that have high prospects in the development of nanotechnology, are the discovery of buckyball, a molecule consisting of 60 carbon atoms (Curl et al., 1985) and the discovery of carbon nanotube (Iijima, 1991).

1.4 Problems of Conventional Modelling of Micro/Nanoscale Machining Processes

Micro and Nano machining phenomena take place in a small limited region of the tool – workpiece interface, containing few atoms or layers of atoms and it is not continuous as assumed by continuum mechanics. Furthermore, at this range, inherent measurement problems limit the use of analytical and empirical models (Rentsch, 2008). The atomistic simulation methods lend themselves to the solution of this problem, as the dynamics of the material removal process can be modelled in the simulation. Also, the material removal mechanisms on the nanoscale are not fully understood, so more insight is needed to be able to adequately predict nanomachining processes in industry.

1.5 Research Aim and Objectives

The aim of this research work is to understand the fundamental material removal mechanisms in nanomachining and to identify the limit of micro/nano material removal under machining conditions.

The specific objectives are the following, namely:

- To develop an atomistic tool-workpiece model for nanomachining
- To simulate nanomachining process mechanisms using the Molecular Dynamics (MD) method
- To determine the minimum depth cut in nanomachining
- To observe the phenomena of rubbing, ploughing and chip formation in nanomachining
- To evaluate the atomic surface roughness in nanomachining
- To validate the MD models by carrying out experiments on the Nanoform Ultragrind Machine

1.6 Structure of the Thesis

The thesis is sub-divided into 8 chapters and the organizational structure is shown in Figure 2.1.

Chapter 1 explains the motivation, aim and the objectives of the research work.

Chapter 2 provides a review of the theory of nanometric machining and highlights various atomistic simulations methods. It further reviews the molecular dynamics method, with consideration to the various thermodynamic ensembles, the commonly used interatomic potentials, algorithms for the integration of the equations of motion and examples of MD simulation in nanomachining.

Chapter 3 explains the methodology used for the MD simulation of nanometric machining; the MD software used for the simulations and the hardware platform.

Chapter 4 provides the MD simulation results of single-pass nanometric machining. These results include the effect of interatomic potentials on nanomachining, the determination of the minimum

depth cut in nanomachining, the effect of tool geometry on rubbing and ploughing in nanomachining and the effect of the variation of velocity in nanomachining.

Chapter 5 gives an extension to the results in chapter 4, by providing multi-pass nanometric machining simulation results. The effects of the following on nanomachining were observed, namely; the interatomic potentials, depth of cut, feed rate, rake angle and velocity.

Chapter 6 provides the evaluation of the atomic surface roughness, S_a from MD simulation of nanometric machining.

Chapter 7 explains the experimental set-up and the procedure for the validation of the MD simulation results. The features which can be compared with the simulations results are presented.

Chapter 8 is a summary of the contribution of this research work and proposes directions for future work.

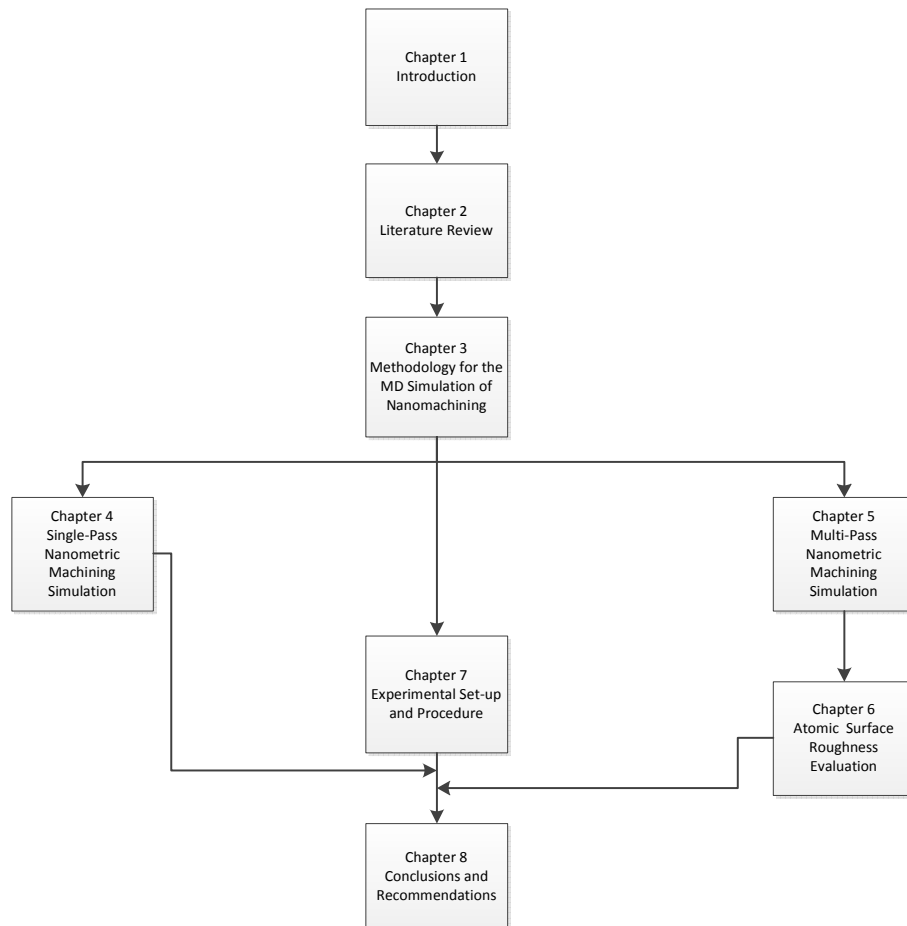


Figure 2.1: The Organizational Structure of the Thesis

Chapter 2. Literature Review

2.1 Theory of Nanometric Machining

Nanometric machining can be defined as a material removal process in which the dimension of the chip removed from the workpiece and the dimensional accuracy of the final product are in the order of 100nm or less. This can be categorized under the following headings, namely; (Jackson, 2007) Mechanical Nanometric Machining, Loose Abrasive Nanometric Machining, Non Mechanical Nanometric Machining and Lithographic Material Removal Methods.

2.1.1 Mechanics of Chip Formation

The Merchant's model is one of the most popular models of orthogonal cutting, where the cutting edge is perpendicular to the relative cutting velocity between the tool and the workpiece. (See Figures 2.2 and 2.3). The model is suitable for macro level cutting and the materials are considered as continuous media.

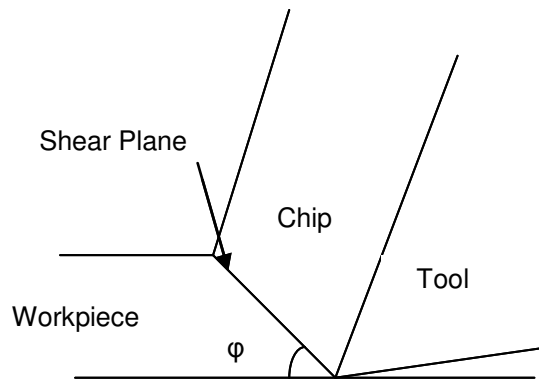


Figure 2.2: Orthogonal Cutting Model (Merchant 1945a, 1945b) (Luo, 2004)

A metal chip with a width of cut and uncut chip thickness is sheared away from the workpiece. The cutting forces are exerted only in the direction of velocity and uncut chip thickness namely tangential force and feed force.

Merchant Assumptions

- The tool tip is a perfectly sharp edge
- Deformation is 2 –D
- Stresses on the shear plane are uniformly distributed
- The resultant force on the chip applied at the shear plane is equal, opposite and collinear to the force applied to the chip at the tool-chip interface.

2.1.2 Cutting Forces

In nanometric machining, the cutting forces are the interatomic forces (Luo et al, 2003). These forces are the superposition of the interaction forces between the cutting tool and the workpiece atoms. A low cutting force is a result of fine cutting conditions, which will in turn decrease the vibration of the cutting system and then result in better surface roughness (Jackson, 2005).

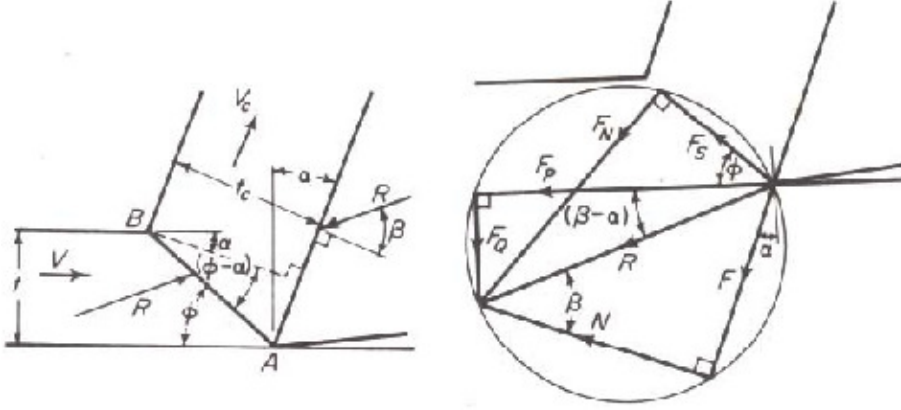


Figure 2.3: Diagram of Cutting Forces (Merchant 1945a, 1945b) (Luo, 2004)

From Figure 2.3 the resultant cutting force (at the macroscale) can be obtained as follows;

$$F_R = \frac{F_s}{\cos(\phi_c + \beta_\alpha - \alpha_r)} = \tau_s bt \frac{1}{\sin \phi_c \cos(\phi_c + \beta_\alpha - \alpha_r)} \quad (2.1)$$

Where τ_s - shear yield stress on the plane assumed uniform over the plane

ϕ_c - shear angle

α_r - tool rake angle

β_β - friction angle

Also, the tangential and feed cutting forces can be expressed in terms of the resultant cutting force at macro level, as,

$$F_t = \tau_s bt \left[\frac{\cos(\beta_\alpha - \alpha_r)}{\sin \phi_c \cos(\phi_c + \beta_\alpha - \alpha_r)} \right]$$

$$F_f = \tau_s bt \left[\frac{\sin(\beta_\alpha - \alpha_r)}{\sin \phi_c \cos(\phi_c + \beta_\alpha - \alpha_r)} \right] \quad (2.2)$$

Many different types of models have been developed to study the machining processes. These range from the macroscopic to the microscopic methods. Conventionally, the Finite Element Methods (FEM) have been used to model machining processes (Strenkwoski and Carroll 1985, 1988, Shih, 1995) and a lot of studies have been conducted. FEM has been capable of obtaining useful

information on chip formation, temperature distribution, cutting forces and stress distribution. The FEM is able to handle macroscale and microscale models, but as the length scale reduces to the nanoscale, it becomes unreliable. This is because at the nanoscale, the material can no longer be considered to be a continuum, but rather discrete in nature. The current product miniaturisation and the development of ultra-precision processes which can achieve excellent form and surface finish, call for nanoscale models which the above mentioned methods cannot handle. Discrete atomistic models are suitable for modelling nanometric machining processes and will be discussed further in section 2.2.

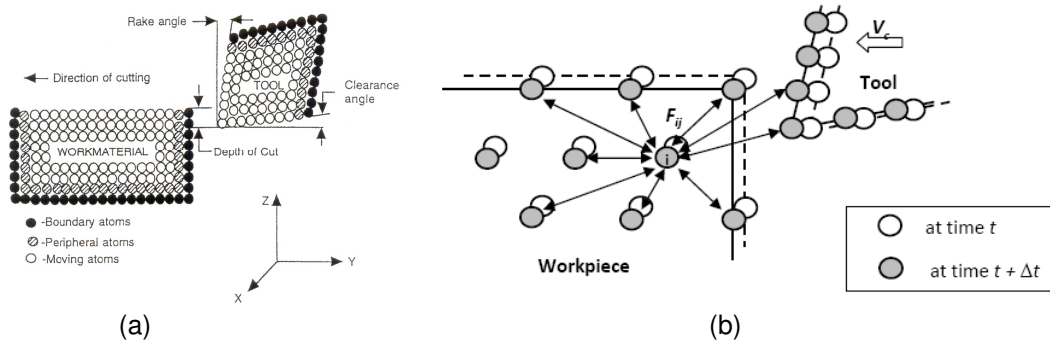


Figure 2.4a: Schematic of the MD Simulation of Nanometric Cutting (2D) (Komanduri and Raff 2001); 2.4b: Atomistic Interaction in Nanometric Machining (Ikawa et al 1991, Promyoo et al. 2008)

Figure 2.4a shows the initialization of the MD simulation and Figure 2.4b shows the time increment (Δt), in which every atom changes its position and interacts with its surrounding neighbour atoms in a manner that is determined from the interatomic potential function.

E.g. for atoms described by Lennard Jones potential, V_{ij} , the interatomic force between atoms i and j is

$$F(r_{ij}) = -\frac{dV_{ij}}{dr_{ij}} \quad (2.3)$$

The force acting on the i -th workpiece atom is thus a summation of the interaction with the surrounding atoms (Luo et al 2003);

$$F_{wi} = \sum_{j \neq i}^{N_t} F_{wtij} + \sum_{j \neq i}^{N_w} F_{wwij} = \sum_{j \neq i}^{N_t} -\frac{dV(r_{wtij})}{dr_{wtij}} + \sum_{j \neq i}^{N_w} -\frac{dV(r_{wwij})}{dr_{wwij}} \quad (2.4)$$

Similarly, the force on each tool atom is

$$F_{ti} = \sum_{j \neq i}^{N_t} F_{ttij} + \sum_{j \neq i}^{N_w} F_{twij} = \sum_{j \neq i}^{N_t} -\frac{dV(r_{ttij})}{dr_{ttij}} + \sum_{j \neq i}^{N_w} -\frac{dV(r_{twij})}{dr_{twij}} \quad (2.5)$$

The above approach is logical as the cutting forces are based on the interatomic forces between the interacting atoms, which in turn are based on the interatomic potentials modelling them. The cutting forces have contributions from the interaction of atoms within the workpiece, within the tool and between the tool and the workpiece (the tool-workpiece interface).

For the model in this study, the cutting force is usually negative at the beginning of the process, as the tool is maintained at a distance from the workpiece. At this stage, there would be an attractive force between the tool atoms and the copper atoms. Later, when the tool starts to cut through the workpiece, there would be a repulsive force between the tool and the workpiece atoms, which would eventually result in the positive values of the force (Lin et al, 2007).

2.1.3 Cutting Temperature

In MD simulations, it is assumed that the cutting energy is totally transferred into cutting heat and this results in an increase of the cutting temperature and kinetic energy of the system (Jackson, 2007). The thermal motion of the atoms actually originates from the lattice vibrations and the average kinetic energy of the system can be given as

$$E_{KE} = \sum_i \frac{1}{2} m_i v_i^2 = \frac{3}{2} N k_B T \quad (2.6)$$

and consequently the cutting temperature,

$$T = \frac{2E_{KE}}{3Nk_B} \quad (2.7)$$

Where m_i is the mass of the i th atom, v_i is the resultant velocity of the i th atom, N is the number of the thermostat atoms, T_i is the temperature of the i th atom and k_B is the Boltzmann constant ($1.3806504 \times 10^{-23} \text{ JK}^{-1}$).

Whenever the temperature of the thermostat atoms exceeds the preset bulk temperature of 293K, their velocities are scaled by using equation (2.8),

$$v_{i,new} = v_i \sqrt{\frac{T_{desired}}{T_{current}}} \quad (2.8)$$

Where $T_{current}$ is the current temperature that is calculated from the KE and the $T_{desired}$ is the desired temperature.

2.1.4 Minimum Depth Cut

The Minimum Depth of Cut (MDC) is defined as the minimum undeformed chip thickness that can be removed stably from a work surface at a cutting edge under perfect performance of a machine tool (Ikawa et al, 1992). The concept of MDC is that the depth of cut must be over a certain critical thickness before any chip is formed. This phenomenon of MDC leads to a rising of slipping forces, burr formation and surface roughness (Ducobu et al, 2009). Conventionally, the tool- workpiece material interface has been considered to be homogeneous and continuum mechanics are used in the analysis of the MDC. In nanomachining, analysis is based on discrete atoms whose interactions are governed by appropriate interatomic potentials. The understanding and the accurate prediction of the MDC is very crucial in improving the ultra-precision metal removal technologies, as this would assist in the selection of appropriate machining parameters and optimal geometry design

The significance of MDC has been a topic of research in metal cutting mechanics since the last century (Sokolowski, 1955 and Brammertz, 1961). Subsequently, there has been a lot of focus on the estimation of the MDC in micromachining. The relationship between the cutting edge sharpness and the MDC was analyzed for an aluminium alloy, by Yuan et al 1996. They obtained MDC in the range of $0.05\mu\text{m} - 0.2\mu\text{m}$ for diamond tool cutting edge radii of $0.2\mu\text{m} - 0.6\mu\text{m}$, using the equation (Yuan et al 1996) (2.9);

$$\lambda_{\min} = r \left(1 - \frac{F_y + \mu F_x}{\sqrt{(F_x^2 + F_y^2)(1 + \mu^2)}} \right) \quad (2.9)$$

Where λ_{\min} is the MDC, r is the tool edge radius, F_x is the horizontal force, F_y is the vertical force and μ is the coefficient of friction.

Weule et al 2001 observed the MDC effect in micromilling process. The cutting experiments were carried out with tungsten carbide tools edge radii of around $5\mu\text{m}$, on SAE 1045 steel. The minimum chip thickness to edge radius ratio of 0.293 was obtained for micromachining.

A Finite Element (FE) model has been used to determine the MDC for the single-phase ferrite and pearlite phases at micromilling length scales (Vogler et al, 2004a). The edge radii of $2\mu\text{m}$ and $7\mu\text{m}$ with a range of chip thickness of $0.1\mu\text{m} - 3\mu\text{m}$ were used. Results showed that the MDC value for ferrite is greater than for pearlite. Similarly, the effect of MDC on the cutting forces in micromilling was studied by (Vogler et al, 2004b). It was concluded that the MDC requires two separate force models to be able to handle the situations of chip and non-chip formations. The slip-line plasticity model for chip formation and the force model for non-chip formation. Also, it was found that the

frequency spectra of the forces contain a component that is a subharmonic of the tooth-passing frequency at feed rates less than the MDC and appears as a stepping behaviour of the forces in the time domain.

Son et al 2005 proposed an ultra precision cutting model in which the tool edges radius and the friction coefficient are the major factors for the determination of the MDC with a continuous chip. The model was based on equation (2.10).

$$\lambda_{\min} = r \left(1 - \cos \left(\frac{\pi}{4} - \frac{\beta}{2} \right) \right) \quad (2.10)$$

Where λ_{\min} is the MDC, r is the tool edge radius and β is the friction angle between a tool and an uncut workpiece passed under the tool.

From the model, MDC obtained for aluminium, brass and Oxygen Free High Conductive (OFHC) copper were in the range 0.09 μ m -0.12 μ m. It was noted that surface quality was best and continuous chip was generated when cutting was at the minimum thickness. Liu et al 2006 developed an analytical model, based on the molecular-mechanical theory of friction, for the prediction of the normalized chip thickness (λ_n) for 1030 steel and Al6082-T6. The λ_n was defined as the ratio of the minimum chip thickness to the tool edge radius. The model was based on the Kragelsky-Drujanov equation (Kragelsky et al, 1982) (see equation 2.11).

$$\lambda_n = \frac{h_{\min}}{r_n} = \frac{tc_{\min}}{r_e} = 0.5 - \frac{\tau_a}{\sigma} \quad (2.11)$$

Where h_{\min} is the limiting depth of penetration of an indenter and it is equivalent to the minimum chip thickness tc_{\min} in micromachining, r_n is the radius of indenter and it is equivalent to the rounded cutting edge radius r_e , σ is the effective flow stress of strain-hardened bulk material, τ_a is the shear strength of the adhesive junction of chip/tool interface.

It was found that λ_n increases as the cutting velocity and tool edge radius increases when machining carbon steels. On the other hand, the λ_n remains constant over a range of cutting velocities and tool radii, when machining Al6082-T6.

On nanomachining, the Ikawa group in Osaka did a lot of work on the MDC, with the aim of achieving machining nanometric accuracy (Ikawa et al 1991, Ikawa et al 1992 and Shimada et al 1993). A 2-D simulation of copper atoms machined by a diamond tool, with edge radius of 5 to 10nm was used for the MD studies. Using the Morse potential and a cutting speed of 200m/s, initial

stage of chip removal was observed for depth of cut larger than 0.3nm and the MDC increased to 0.6nm with a larger edge radius of 10nm. From their studies, they proposed that the MDC in nanocutting would be about 0.5nm to 1nm, (which is 0.05 to 0.1 of the edge radius).

The different approaches for the determination of the MDC include the Molecular Dynamics approach (Shimada et al, 1993), experimentation (Yuan et al, 1996), FEM approach (Vogler et al, 2004) and analytical approach (Liu et al, 2006). The experimental method for the estimation of the MDC would be very tedious and expensive (it is not feasible presently for nanometric cutting) and the accuracy will be strongly affected by experimental uncertainties (Liu et al, 2006). The Finite Element Method (FEM) approach is not suitable either. Also, the analytical approach to nanomachining would be very difficult, as the basis of analysis would be in quantum mechanics. The Molecular Dynamics (MD) lends itself to the solution of this problem, as the dynamics of the material removal process can be modelled in the simulation.

2.1.5 Atomic Surface Finish

The atomic surface finish or roughness can be defined as the roughness limit of a surface. Its value has been demonstrated both in theory and in experiments to be non-zero (Yu and Namba 1998 and Namba et al 2000). This parameter is very important in assessing the quality of high performance nano surfaces and so its understanding is very crucial. Namba et al 2000 presented equations for the evaluation of 2-D and 3-D atomic surface roughness on atomic topography, where λ is the interatomic spacing and r is the radius of the surface atom.

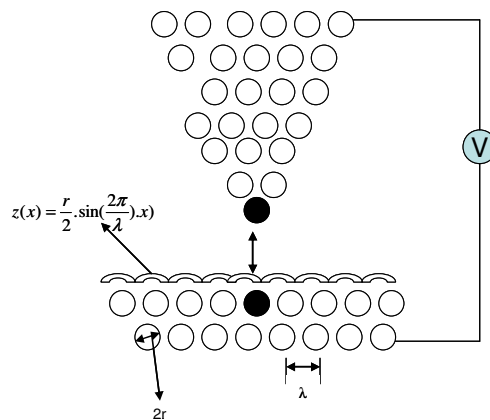


Figure 2.5: Illustration of Interatomic Interaction for a STM (Adapted from Yu and Namba, 1998 and Namba et al, 2000)

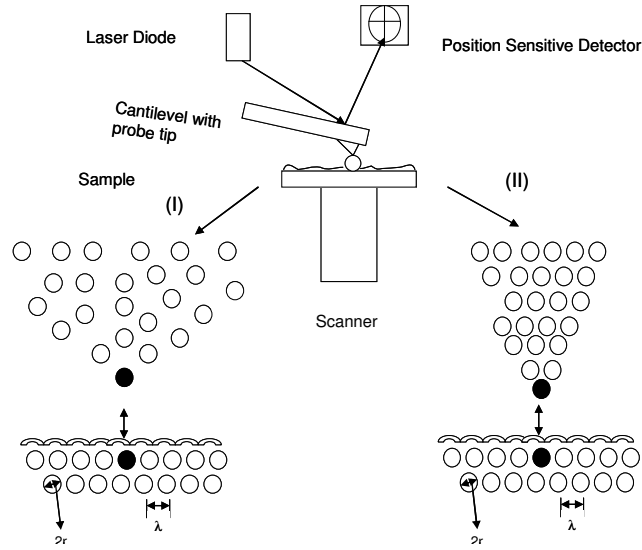


Figure 2.6: Illustration of Interatomic Interaction for an AFM (Adapted from Yu et al, 1999)

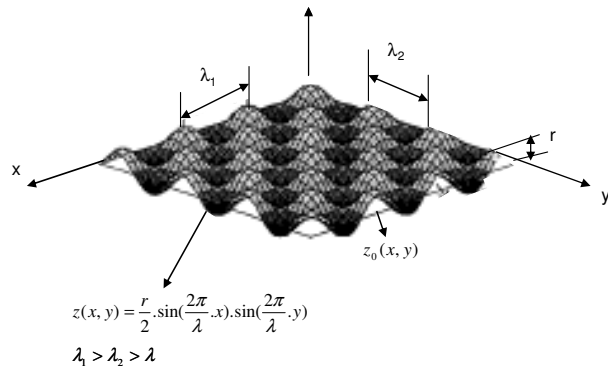


Figure 2.7: Simulated Atomic Topography for $\lambda_1 = \lambda_2$ (Yu and Namba, 1998 and Namba et al, 2000)

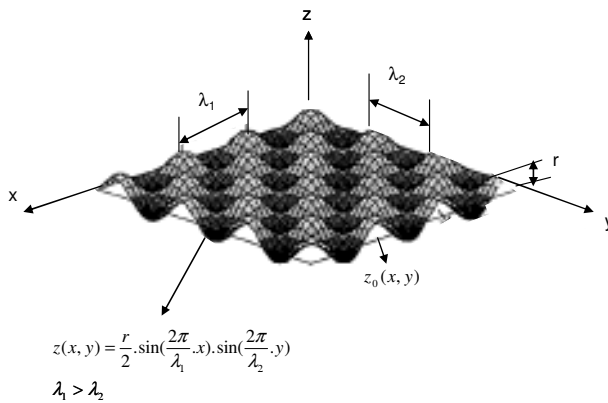


Figure 2.8: Simulated Atomic Topography for $\lambda_1 > \lambda_2$ (Yu and Namba, 1998 and Namba et al, 2000)

For two dimension (2-D),

$$\begin{aligned}
 R_a &= \frac{1}{n\lambda} \int_0^{n\lambda} \left| \frac{r}{2} \sin\left(\frac{2\pi}{\lambda} x\right) \right| dx \\
 &= \frac{1}{\pi} r
 \end{aligned} \tag{2.12}$$

$$\begin{aligned}
 \sigma &= \left\{ \frac{1}{n\lambda} \int_0^{n\lambda} \left[\frac{r}{2} \sin\left(\frac{2\pi}{\lambda} x\right) \right]^2 dx \right\}^{\frac{1}{2}} \\
 &= \frac{1}{2\sqrt{2}} r
 \end{aligned} \tag{2.13}$$

For three dimension (3-D),

$$\begin{aligned}
 S_a &= \frac{1}{n\lambda_1 n\lambda_2} \iint_s \left| \frac{r}{2} \sin\left(\frac{2\pi}{\lambda_1} x\right) \sin\left(\frac{2\pi}{\lambda_2} y\right) \right| dx dy \\
 &= \frac{1}{n\lambda_1 n\lambda_2} \frac{r}{2} \int_0^{n\lambda_1} \left| \sin\left(\frac{2\pi}{\lambda_1} x\right) \right| dx \int_0^{n\lambda_2} \left| \sin\left(\frac{2\pi}{\lambda_2} y\right) \right| dy \\
 &= \frac{2}{\pi^2} r
 \end{aligned} \tag{2.14}$$

$$\begin{aligned}
 \sigma &= \left\{ \frac{1}{n\lambda_1 n\lambda_2} \iint_s \left[\frac{r}{2} \sin\left(\frac{2\pi}{\lambda_1} x\right) \sin\left(\frac{2\pi}{\lambda_2} y\right) \right]^2 dx dy \right\}^{\frac{1}{2}} \\
 &= \left[\frac{1}{n\lambda_1 n\lambda_2} \left(\frac{r}{2}\right)^2 \int_0^{n\lambda_1} \sin^2\left(\frac{2\pi}{\lambda_1} x\right) dx \int_0^{n\lambda_2} \sin^2\left(\frac{2\pi}{\lambda_2} y\right) dy \right]^{\frac{1}{2}} \\
 &= \frac{1}{4} r
 \end{aligned} \tag{2.15}$$

The evaluation of the roughness limit of a surface is of great importance for ultra-precision machining and silicon fabrication.

Table 2.1 shows the comparison of nanometric cutting and conventional cutting mechanics and it can be observed that the cutting mechanism on the nanoscale is quite different from that on the macro/conventional scale. Nanometric cutting is based on a very small region of the tool-workpiece interface, which contains few atoms and so discrete mechanics apply. On the other hand,

conventional cutting is based on continuum mechanics. The cutting forces are based on the interatomic potentials in classical MD studies, but are dependent on the plastic deformation in conventional cutting. It is worth stating that the basic physics of material removal on the nanoscale is not fully understood yet and much study is still needed for further insight.

Table 2.1: Comparison of Nanometric Cutting and Conventional Cutting Mechanics
(Adapted from Luo et al 2003)

	Nanometric Cutting	Conventional Cutting
Fundamental Cutting Principles	Discrete Molecular Mechanics	Continuum Mechanics
Workpiece Material	Heterogeneous	Homogeneous
Cutting Physics	Atomic Cluster Model	Shear Plane Model
Energy Consideration	Interatomic Potential Functional	Shear/Friction Power
Cutting Force	Interatomic Forces	Plastic Deformation
Chip Formation	Inner Crystal Deformation (Point Defects or Dislocation)	Inter Crystal Deformation (Grain Boundary Void)
Deformation and Stress	Discontinuous	Continuous
Cutting Tool Edge Radius	Significant	Ignored
Cutting Tool Wear	Cutting Face and Cutting Edge	Rake Face

2.2 Atomistic Simulation Methods

These are simulation methods that take into account the discrete nature of the system under study. It is not assumed that the system is a continuum, but that it consists of a set of interacting atoms or molecules. The interacting atoms are bound by chemical reactions, and these reactions are interactions between electrons and nuclei. The exact prediction of the correlation between the micro/nano-structure and properties of materials requires a solution of the time dependent Schrödinger wave equation (equation 2.16) for nuclei and electrons, with a Hamiltonian, H describing the entire particle interactions involved in the problem (Li et al., 2008, Marx and Hutter, 2000).

$$i\hbar \frac{\partial}{\partial t} \Psi(\{r_i\}, \{R_I\}; t) = H \Psi(\{r_i\}, \{R_I\}; t) \quad (2.16)$$

$$\text{where } H = -\sum_I \frac{\hbar^2}{2M_I} \nabla_I^2 - \sum_i \frac{\hbar^2}{2m_e} \nabla_i^2 + \sum_{i<j} \frac{e^2}{|r_i - r_j|} - \sum_{I,i} \frac{e^2 Z_I}{|R_I - r_i|} + \sum_{I<J} \frac{e^2 Z_I Z_J}{|R_I - R_J|}$$

where Ψ is the wave function, \hbar is the reduced Planck constant and H is the Hamiltonian operator.

This is extremely computationally demanding and to overcome this limitation, many atomistic simulations have been developed with various approximations, for different applications, namely; Monte Carlo (MC), Molecular Mechanics (MM), Molecular Dynamics (MD), et cetera. The MC and MD are among the most popular of these methods. The MC methods have different variants, but are more suitable for applications at exact thermodynamic states. On the other hand, the MD can readily handle dynamic states and can be categorized into the following, namely;

- Ab initio Molecular Dynamics Method
- Semi-empirical Molecular Dynamics Method
- Empirical Molecular Dynamics Method

2.2.1 Ab initio Molecular Dynamics Method

Ab initio Molecular Dynamics Method is a first principle MD approach, in which the forces acting on the nuclei are obtained from electronic structure calculations that are performed ‘on the fly’ as the MD trajectory is generated. These include viz; Ehrenfest (E), Born-Oppenheimer (BO), Car-Parrinello (CP) et cetera. These methods use different approaches for the electronic structure calculations like the Density Functional Theory (DFT), Hartree-Fock (HF) and post HF theories which include Generalized Valence Bond (GVB) et cetera (Marx and Hutter, 2000). The BO approximation employs classical equation to describe the nuclei and adds the electronic structure by solving the time independent Schrödinger equation for each MD step. The CP method on the other hand, calculates the valence electrons from first principles, describes the inner electrons by pseudo potentials and then treats the motion of the nuclei classically (Marques et al., 2005). Figure 2.9 shows various simulation methods with time and length. It shows increase in the time scale along the vertical axis and increase in the length scale on the horizontal axis. The various simulation techniques are also shown in relation to each other.

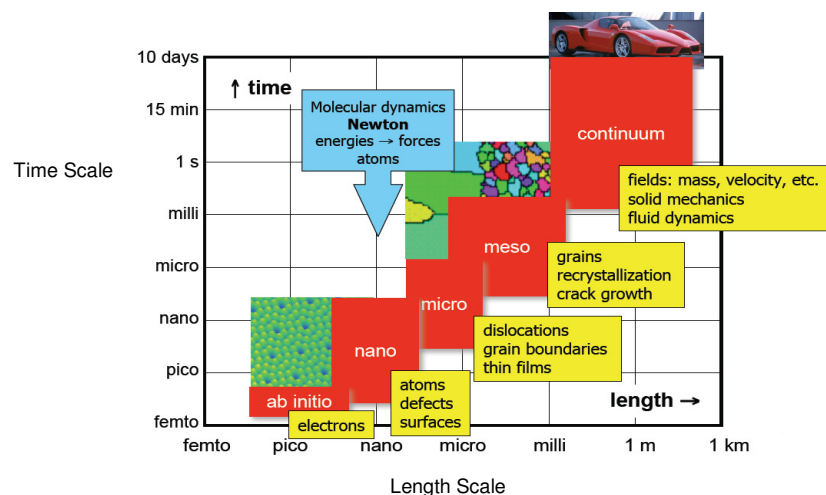


Figure 2.9: Scales for Simulation Time and Length (Thijsse, 2007)

The problem of calculating the total energy and the corresponding interatomic potentials in the ground state of matter is quite complex. For example, what DFT (which is one of the most popular electronic structure calculation methods) does is to map the problem onto the problem of calculating the wave function and energy of a single electron with no approximations (Hohenberg & Kohn, 1964). The central idea of the DFT is that, for a system of N_e electrons, a functional $E[\rho]$ exists such that when E is minimized with respect to the variation in the electron density ρ , its value is the ground state energy of the system. The minimization of E must be carried out subject to the constraint,

$$\oint \rho(r)dr = N_e \quad (2.17)$$

Where N_e is the number of electrons and ρ is the electron density as a function of position, r . It is assumed that the functional is semi local, i.e. it depends on the local electron density and its derivatives, and that the contribution to the electron density, at an atom due to the remaining atoms of the system, is slowly varying.

2.2.2 Semi-empirical Molecular Dynamics Method

The semi-empirical MD method is a trade-off between ab initio and the classical MD methods. It allows the establishment between the first principles interactions obtained from electronic structure methods and empirical potentials. The method is set up with structure similar to a Hartree-Fock (HF) calculation, with certain information like electron integrals approximated or completely removed. An example of the semi-empirical MD is tight binding. The tight binding MD includes quantum mechanical effects in the MD simulation through explicit evaluation of the electronic structure of the system at each time step (Kopidakis et al., 1997, Wang & Ho, 1996).

2.2.3 Empirical Molecular Dynamics Method

This is also known as the classical molecular dynamics method that uses empirical potentials for the determination of the forces on the interacting atoms or molecules. This is the approach that has been used for the simulations in this study and is detailed in section 2.3. The classical MD method is a very powerful and an easy to use computational technique for atomistic studies, when compared to more complex quantum mechanical approaches. Some of its drawbacks are the following, namely; the use of classical forces, pre-defined potentials and the limitations of the system's size and the simulation times.

2.2.4 Monte Carlo Methods

Most of Monte Carlo methods are based on the generation of statistically uniform independent values in the interval (0 and 1). Atomistic MC methods are based on exploring the energy surface of the system by randomly probing the geometry or configuration space, they make use of interatomic potentials for the calculation of the atomic forces, but differ in the way the atomic positions are evaluated and unlike the MD are stochastic or non-deterministic.

Steps in Using Monte Carlo Method for atomistic simulations (Medyanik, 2007)

- Compute the total potential energy, V from the atomic positions
- Randomly choose one atom and move it from its original position for random distance in a random direction. Then compute the total potential energy, V^*
- Accept or decline the move:
 - If $V^* < V$: Accept
 - If $V^* > V$: Accept with a probability proportional to $\exp[-\beta(V^* - V)]$, where $\beta = 1/kT$

Table 2.2: Comparison of Some Atomistic Simulation Methods

Method	Applications and Advantages	Disadvantages
Ab initio Molecular Dynamics Methods	More accurate solution	Computationally expensive – suitable for hundreds of atoms
Semi Empirical Molecular Dynamics Methods	A trade off between ab initio and classical MD methods. Can handle up to thousands of atoms	Less accurate solution than in ab initio methods
Empirical/Classical Molecular Dynamics Methods	Less computationally expensive than ab initio MD	Simulations are for shorter times than in MC
Monte Carlo Methods	More efficient /time saving, can be used for larger time frames, time is controllable	Don't allow the time evolution of the system in a suitable form for viewing

Table 2.2 shows a comparison of some commonly used atomistic simulation methods. The classical MD uses a reasonable approximation, and with appropriate potentials, it can handle systems up to millions of atoms, which is not possible for other MD methods. For classical MD, it is assumed that quantum effects are negligible on the dynamics of the atoms and the only limitation is that the assumption is not valid for light nuclei like hydrogen, helium, et cetera (Turkerman & Martyna, 2000, Ercolessi, 1997). The use of the classical MD method has proved to be an effective tool for the investigation of machining processes at the nanometre scale. (Subsequently, the use of the term MD would mean the empirical/classical MD). The method also gives higher resolution of the

cutting process than is possible by continuum mechanics on that length scale (Komanduri & Raff, 2001). The MD method is considered in more detail in the next section.

2.3 The Molecular Dynamics (MD) Method

Molecular dynamics (MD) is a computer simulation technique used in the study of the motions of a set of particles – molecules (for metals it can be atoms) (Allen and Tildesley 1988, Haile 1997, Field 1999, Frenkel and Smit 2001, Leach 2001, Schlick 2002, Rapaport 2004). The technique works by following the time evolution of a set of interacting atoms while integrating the equations of their motion. The MD is deterministic, once the positions, velocities and accelerations of the particles are known, the state of the system can be predicted. The method is also based on statistical mechanics – a way to obtain a set of configurations distributed according to some statistical distribution functions (Ercolessi 1997, Hernandez, 2008).

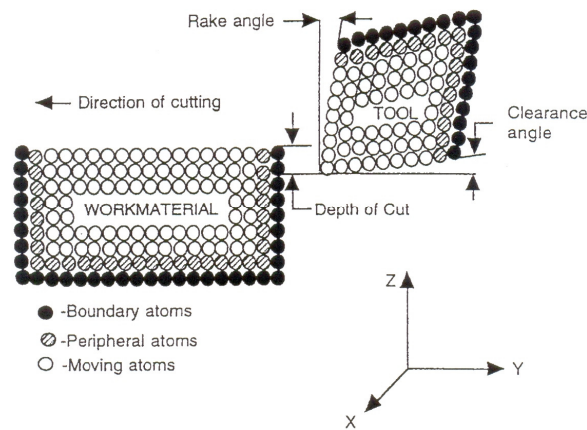


Figure 2.10: Schematic of the MD Simulation of Nanometric Cutting (2D) (Komanduri and Raff, 2001)

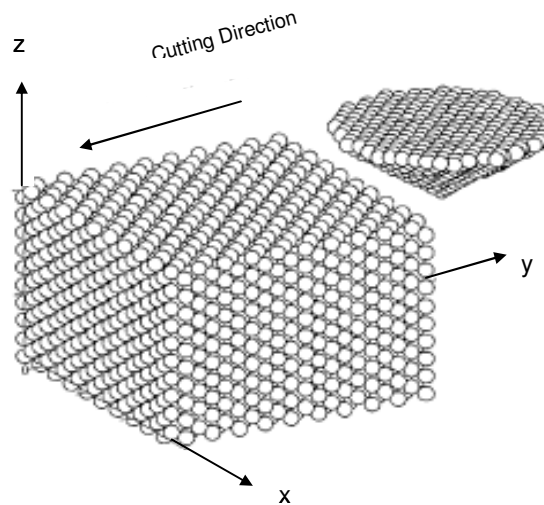


Figure 2.11: Schematic of the MD Simulation of Nanometric Cutting (3D) (Fang and Weng ,2000)

The MD method was initiated in the late 1950s at Lawrence Radiation Laboratory in the US by Alder and Wainwright in the study of statistical mechanics (Alder and Wainwright, 1959). Since then, the use of the simulation method has spread from Physics to Materials Science and now to Mechanical Engineering. In the field of nanometric cutting, Belak pioneered work on the study of cutting copper with a diamond tool (Belak and Stowers, 1990). Initially, the method was used extensively to model indentation and cutting (see Figures 2.10 and 2.11). In 1991, Belak and Stowers first applied the MD to abrasive processes (Belak and Stowers, 1991) and Rentsch and Inasaki's study later presented the first results of simulations targeted on the pile-up phenomenon in abrasive machining (Rentsch and Inasaki, 1994). Relatively, not many studies have been carried out on abrasive machining, and this may likely be due to difficulties in developing suitable models in terms of the micro topography and in terms of the required potential functions for the material and interactions of interest. Also, MD studies have been restricted to single or few grits interfering with a workpiece (Brinksmeier et al, 2006). The MD simulation is based on Newton's second law of motion. It consists of the numerical step-by-step solution of the classical equations of motion. For a set of N atoms,

$$F_i = m_i a_i \quad (2.18)$$

Where m_i is the mass of atom i , $a_i = \frac{d^2 r_i}{dt^2}$ is the acceleration of the atom i and F_i is the resultant force acting on atom i . These forces should be balanced by the potential energy between atoms, which are usually presented as the gradient of a potential energy function.

2.3.1 Thermodynamic Ensembles

An ensemble is a large group of atoms or systems which are in different microscopic states, but have the same macroscopic or thermodynamic states. If a system of N atoms in a given macrostate is defined in terms of thermodynamic quantities no of atoms, N ; pressure, P ; temperature, T ; entropy, S ; volume, V etc, there are many configurations at the atomic scale, which will lead to the same macrostate. The microstate of a system, defined by the atomistic positions and momenta cannot be known in a deterministic manner, because of the uncertainty principle of quantum mechanics. To avoid this problem, a statistical mechanics approach is used for the atomic description. Some common thermodynamic ensembles are considered below and a comparison is given in Table 2.3.

2.3.1.1 Microcanonical Ensemble (NVE)

This is an isolated system, with N atoms, which occupies a constant volume and the overall energy, E of the system is constant. The ensemble can have copies of an isolated system, with each of the system having constant energy. Its thermodynamic potential is entropy, S and the partition function is $\sum 1$.

2.3.1.2 Canonical Ensemble (NVT)

This is a system in a temperature bath, with N atoms and the volume, V and the temperature, T of the system are kept constant. It models a system in thermal interaction with a heat reservoir and having constant temperature. Each system in canonical ensemble generally has a different energy. Its thermodynamic potential is Helmholtz, A and the partition function is $\sum e^{-\beta E_i}$.

2.3.1.3 Isobaric Isothermal Ensemble (NPT)

This is a system in a temperature and pressure bath, with N atoms and the pressure, P and the temperature, T of the system are kept constant. Its thermodynamic potential is Gibbs, G and the partition function is $\sum e^{-\beta(E_i + PV_i)}$.

2.3.1.4 Grand Canonical Ensemble (μVT)

This is a system in contact with a reservoir with which it is possible to exchange energy and particles. It is characterized by a constant chemical potential and temperature T . Its thermodynamic potential is Hill, $(-PV)$ and the partition function is $\sum e^{-\beta(E_i + \mu N_i)}$.

Table 2.3: Comparison of the Thermodynamic Ensembles (Adapted from Cross, 2012)

Ensemble	Partition Function	Probability Distribution	Bridge Equation
Microcanonical	$\Omega = \sum 1$	$\pi_i = \frac{1}{\Omega}$	$\frac{S}{k} = \ln \Omega(N, V, E)$
Canonical	$Q = \sum e^{-\beta E_i}$	$\pi(E_i) = \frac{1}{Q} e^{-\beta E_i}$	$-\beta A = \ln Q(N, V, T)$
Isothermal-isobaric	$\Delta = \sum e^{-\beta(E_i + PV_i)}$	$\pi(E_i, V_i) = \frac{1}{\Delta} e^{-\beta(E_i + PV_i)}$	$-\beta G = \ln \Delta(N, P, T)$
Grand-canonical	$\Xi = \sum e^{-\beta(E_i + \mu N_i)}$	$\pi(E_i, N_i) = \frac{1}{\Xi} e^{-\beta(E_i + \mu N_i)}$	$\beta PV = \ln \Xi(\mu, V, T)$

2.3.2 Steps in MD Simulation

The outline of the MD simulation is as follows:

- Select the model, choose an appropriate interatomic potential and the algorithms for calculating the equations of motion;
- Initialize the model;
- Relax the model from its initial state to its dynamically equilibrium condition;
- Run the simulation and analyse the results.

Select the Model and Choose an Appropriate Interatomic Potential and the Algorithms for Calculating the Equations of Motion

The model should be selected correctly to reproduce what is expected (whether 2D/3D). Then, the next thing is a major task in MD simulation, which is the selection of the potential function. This is a function, $V(r_i, \dots, r_N)$ of the position of the nuclei which represents the potential energy of the system. Where (r_i, \dots, r_N) represents the complete co-ordinate position of the atoms. Then forces are derived from it as,

$$F_i = -\frac{\partial}{\partial r_i} V(r_i, \dots, r_N) \quad (2.19)$$

Strictly speaking, the problem of modelling a material is that of finding a potential function for that material. If the potential function could not model atom behaviour correctly, the results produced from the simulation could be wrong.

2.3.3 Interatomic Potentials for MD

Consider the energy of N interacting particles, which can be written as (Tersoff, 1988)

$$E = \sum_i V_1(r_i) + \sum_{i < j} V_2(r_i, r_j) + \sum_{i < j < k} V_3(r_i, r_j, r_k) + \dots + \sum_{i < j < k \dots < N} V_N(r_i, r_j, r_k, \dots, r_N) \quad (2.20)$$

Where r_i, r_j, r_k are the positions of the particles and the functions $V_1, V_2, V_3, \dots, V_N$ are the m-body potentials.

For simplicity, pair potentials models are normally used for atomic interactions, and it follows from equation (2.20), that the second term, $\sum_{i < j} V_2(r_i, r_j)$ is the two-body or pair potential, (which also can be re-written as in equation 2.21), and the third term is the three-body potential and so on.

$$V = \sum_i \sum_{j > i} V(r_{ij}) \quad (2.21)$$

Where r_{ij} is the distance between particles i and j.

The pair potentials are the simplest interatomic potentials used for the interaction of a set of particles. The crucial task in a MD simulation is the selection of the potential function, and if the potential doesn't model the behaviour of the atoms correctly, the results produced from the simulation would be useless. Most times, it can be observed that the basis of the choice of the interatomic potentials for MD simulation is often shrouded in mystery. The lack of clear understanding about the scope and the limitations of a given model may lead to its innocent misuse and sometimes, to the dissemination of nonsensical results (Finnis, 2003). The most popularly used is the Lennard-Jones potential; others are Morse potential, Born-Mayer potential et cetera. Apart from the pair potentials, there are multi-body potentials, like Tersoff and Embedded-Atom Method potentials, et cetera.

2.3.3.1 Lennard-Jones Potential

Lennard-Jones started with the general form equation (Lennard-Jones, 1924 and Brush, 1970).

$$V(r) = \frac{f}{r^m} - \frac{g}{r^n} \quad (2.22)$$

(The inverse nth power attractive force dominates at large distances and the inverse mth power repulsive force dominates at short distance.) He later arrived at $n = 6$, $m = 12$; $n = 7$ and $m = 13$, as the special cases of the equation. He didn't derive the equation as it were from first principles, but arrived at it by fitting experimental data. The values $n = 6$, $m = 12$ are widely used nowadays.

$$V_{ij} = 4\epsilon \left[\left(\frac{\sigma}{r} \right)^{12} - \left(\frac{\sigma}{r} \right)^6 \right] \quad (2.23)$$

Where ϵ and σ are constants which are dependent on the interacting particles. Some values of ϵ and σ for rare gases are given in Table 1. The LJ potential is ideal for rare gases, where the interactions between the non-bonded and uncharged atoms are due to weak Van der Waal forces

Table 2.4: Constants for Lennard-Jones Potential (Hansen and McDonald, 1976)

Gas	$\epsilon/k_B (K)$	$\sigma(10^{-9})$
Helium	10.2	0.256
Neon	35.8	0.275
Argon	119.8	0.341
Krypton	116.7	0.368
Xenon	225.3	0.407

2.3.3.2 Morse Potential: (Morse, 1929)

Morse started with the wave equation for the nuclear motion of the diatomic molecule of nuclear masses M_1 and M_2 ; and charges Z_1 and Z_2 respectively as in equation 2.24.

$$\nabla^2 \Psi + \frac{8\pi^2 \mu}{h^2} \left[W - \left(\frac{e^2 Z_1 Z_2}{r} \right) + V_e(r) \right] \Psi = 0 \quad (2.24)$$

Where $\mu = \frac{M_1 M_2}{(M_1 + M_2)}$, r is the distance between the nuclei, W is allowed energy levels, $V_e(r)$ is the electronic energy calculated by considering the two nuclei as fixed in space with a distance r apart.

In order to obtain the exact solution of equation 2.24, Morse chose a potential V_{ij} , expressed as equation 2.15, which is equal to $\left(\frac{e^2 Z_1 Z_2}{r} - V_e(r) \right)$. The choice of V_{ij} was based on the following criteria, viz;

- should come asymptotically to a finite value as $r \rightarrow \infty$
- should have its only minimum point at $r = r_0$
- should become infinity at $r = 0$
- should exactly give the allowed energy levels as a finite polynomial

$$V_{ij} = D \{ \exp[-2\alpha(r_{ij} - r_e)] - 2 \exp[-\alpha(r_{ij} - r_e)] \} \quad (2.25)$$

Where, r_{ij} and r_e are instantaneous and equilibrium distances between atoms i and j respectively; α and D are constants determined on the basis of the physical properties of the material. The examples are given in Table 2.5, for interaction up to first neighbours. The Morse potential is suitable for cubic metals and they can be used to model the interactions between an atom and a surface.

Table 2.5: Constants for Morse Potential (Das et al, 1977)

Metals	$D (\times 10^{-20} J)$	$\alpha (\times 10^{10} m)$	$r_e (\times 10^{-10})$
Gold	10.1374	1.6506	2.8709
Copper	9.4332	1.4311	2.5421
Nickel	11.9572	1.4415	2.4817
Silver	7.9609	1.4509	2.8749
Lithium	6.7414	0.7899	3.0000

2.3.3.3 Born-Mayer Potential

Born and Mayer suggested that the repulsion between the atoms would have a roughly exponential dependence on distance (Born and Mayer, 1932).

$$V_{ij} = A \left\{ \exp \left[-\frac{r}{a_{BM}} \right] \right\} \quad (2.26)$$

Where A and a_{BM} are constants dependent on the material. This potential is used for metals, Group III-V semiconductors and ceramics.

Table 2.6: Constants for Born-Mayer Potential (Smith and Carter 1969, Khukhryansky et al. 2004)

Interactions	A(keV)	$a_{BM} (10^{-10} m)$
Argon-Argon	8.89	0.24
Gold-Gold	200±60	0.20±0.4
Argon-Gold	42380	0.219
Gallium-Gallium	15.365	0.2813
Gallium-Phosphorus	9.27	0.2716
Phosphorus-Phosphorus	5.5963	0.2712

2.3.3.4 Tersoff Potential

Tersoff modelled the total energy of the system as a sum of pair like interactions and as a function of the atomic coordinates, given as equation (2.27). The potential is based on the concept that the strength of a bond between two atoms is not a constant, but depends on the local environment (Tersoff 1988a and Tersoff 1988b).

$$E = \sum_i E_i = \frac{1}{2} \sum_i \sum_{j \neq i} V_{ij} \quad (2.27)$$

and

$$V_{ij} = f_C(r_{ij})[a_{ij}f_R(r_{ij}) + b_{ij}f_A(r_{ij})] \quad (2.28)$$

where

$$f_R(r) = A \exp(-\lambda_1 r),$$

$$f_A(r) = -B \exp(-\lambda_2 r),$$

$$f_C(r) = \begin{cases} 1, & r < R - D \\ \frac{1}{2} - \frac{1}{2} \sin \left[\frac{\pi}{2} (r - R) / D \right], & R - D < r < R + D \\ 0, & r > R + D \end{cases}$$

$$b_{ij} = (1 + \beta^n \zeta_{ij}^n)^{-1/2n},$$

$$\zeta_{ij} = \sum_{k(\neq i, j)} f_C(r_{ik}) g(\theta_{ijk}) \exp[\lambda_3^3 (r_{ij} - r_{ik})^3],$$

$$g(\theta) = 1 + \frac{p^2}{q^2} - \frac{p^2}{[q^2 + (h - \cos \theta)^2]},$$

$$a_{ij} = (1 + \alpha^n \eta_{ij}^n)^{-1/2n},$$

$$\eta_{ij} = \sum_{k(\neq i, j)} f_C(r_{ik}) \exp[\lambda_3^3 (r_{ij} - r_{ik})^3]$$

The Tersoff potential is used for covalently bonded materials like silicon atoms and the values of the parameters for Silicon and Carbon are given in Table 2.7.

Table 2.7: Constants for Tersoff potential (Tersoff, 1988b),(Rafii-Tabar and Mansoori, 2003), (Saito et al, 2001)

Parameters	Silicon	Carbon
A(eV)	1.8308×10^3	1.3936×10^3
B(eV)	4.7118×10^2	3.467×10^2
$\lambda_1 (nm^{-1})$	24.799	34.879
$\lambda_2 (nm^{-1})$	17.322	22.119
α	0.0	0.0
β	1.0999×10^{-6}	1.5724×10^{-7}
N	7.8734×10^{-1}	7.2751×10^{-1}
P	1.0039×10^5	3.8049×10^4
Q	16.218	4.384
H	-5.9826×10^{-1}	-5.7058×10^{-1}
$\lambda_3 (nm^{-1})$	17.322	22.119
R (nm)	0.285	0.18
D(nm)	0.015	0.02

Where R and D are cut-off parameters; $A, B, \lambda_1, \lambda_2, \lambda_3, \alpha, \beta, n, p, q, h$ are fitting parameters of the Tersoff potential.

2.3.3.5 Embedded-Atom Method Potential

In deriving the embedded-atom method potential, it can be stated that the major contribution to the energetics is the energy to embed the atom into the electron density of the neighbouring atoms.

The total energy of the system can be written as (Foiles 1985), (Foiles et al, 1986).

$$E_{tot} = \sum_i G_i(\rho_{h,i}) + \frac{1}{2} \sum_{i,j} V_{ij}(r_{ij}) \quad (2.29)$$

$\rho_{h,i}$ is the total electron density at atom i due to the rest of the atoms in the system.

G_i is the embedding energy for placing an atom into the electron density

$V_{i,j}$ is the short range pair interaction representing the core-core repulsion

r_{ij} is the separation of atoms i and j

Using a model needed for the host electron density

$$\rho_{h,i} = \sum_{j \neq i} \rho_j^a(r_{ij}) \quad (2.30)$$

$\rho_j^a(r)$ is the atomic electron density of atom j at the distance r_{ij} from the nucleus.

Replace $G(\rho)$ with a Taylor-series expansion about the average host electron density $\bar{\rho}$. The electron density at site i will be written as

$$\rho_{h,i} = \bar{\rho} + \sum_{j \neq i} [\rho_j^a(r_{ij}) - \delta] \quad (2.31)$$

Where $\delta = \frac{\bar{\rho}}{(N-1)}$ and N is the number atoms in the system. Keeping the terms in the Taylor expansion through the second order,

The expression for the embedding energy is

$$\begin{aligned} \sum_i G(\rho_{h,i}) = & NF(\bar{\rho}) + \sum_{i,j(j \neq i)} G'_i(\bar{\rho}) [\rho_j^a(r_{ij}) - \delta] + \frac{1}{2} \sum_{i,j(j \neq i)} G''_i(\bar{\rho}) [\rho_j^a(r_{ij}) - \delta]^2 \\ & + \frac{1}{2} \sum_{i,j,k(k \neq j \neq i \neq k)} G''_i(\bar{\rho}) [\rho_k^a(r_{ik}) - \delta] [\rho_j^a(r_{ij}) - \delta] \end{aligned} \quad (2.32)$$

Where G' and G'' are the first and the second derivatives of the embedding energy of the atom i with respect to the electron density, evaluated at $\bar{\rho}$ respectively. The first term on the right of equation is the simplest approximation to the total embedding energy, the third term is a pair-potential-like contribution to the embedding energy in that they involve a double sum over the pairs of atoms and the last term is the three-body contribution.

Neglecting the three-body term, and in the thermodynamic limit $N \rightarrow \infty$, the terms involving δ can be dropped, then the embedded atom energy can be approximated by

$$E_{tot} \approx N[G(\bar{\rho}) - \bar{\rho}G'] + \frac{1}{2} \sum_{i,j(j \neq i)} V(r_{ij}) \quad (2.33)$$

Where the pair potential $V(r_{ij})$,

$$V(r_{ij}) = U_{ij}(r_{ij}) + 2G'_i(\bar{\rho})\rho_j^a(r_{ij}) + G''_i(\bar{\rho})(\rho_j^a(r_{ij}))^2 \quad (2.34)$$

The values of electron densities and the embedding functions for Nickel and Gold are listed in Tables 2.8 and 2.9 (Foiles, 1985).

Table 2.8: Electron densities and the embedding functions for Nickel

ρ (Angstrom) ⁻³	$F(\rho)$ eV
0.0	0.0
0.01446	-3.5847
0.02891	-5.1449
0.05783	-3.4041
0.06650	0.0

Table 2.9: Electron densities and the embedding functions for gold

ρ (Angstrom) ⁻³	$F(\rho)$ eV
0.0	0.0
0.00728	-3.2170
0.01455	-4.6278
0.02910	-2.7699
0.03347	0.0

The embedded-atom potential was developed for a wider range of metals. It incorporates an approximation for the many-atom interactions neglected by the pair-potential scheme.

2.3.2.6 Modified Embedded-Atom Method (MEAM) Potential

The MEAM is theoretically an extension of the EAM potential (Baskes, 1992) with modifications to include the directionality of the bonding. The bond-angle was explicitly handled so as to accommodate covalent systems. The total energy is given by (Equation 2.29). The MEAM is suitable for modelling metals and alloys with fcc, bcc, hcp and cubic structures, and also for covalent materials such as silicon and carbon.

The list of the potentials is not exhaustive; and there are other potentials which are modified forms of the ones already discussed. Generally, the most commonly used interaction model is the Lennard-Jones (LJ) pair potential. It is the standard potential to use for all the investigations where the focus is on the fundamental issues, and not studying the properties of a specific material. To obtain physically meaningful results from atomistic simulations, it is essential that reliable interatomic potentials are used. A reliable potential would reproduce various physical properties of the relevant elements or alloys, including the elastic, structural, defect, surface and thermal properties etc (Lee et al 2005). For example, Tersoff potential was designed for the description of covalent materials like silicon, germanium, carbon, silicon carbide etc. and it cannot adequately model metals. Also, the EAM potential was designed for metals, as it describes the bonding in metals more satisfactorily, but the MEAM potential can be used for the modelling of both metallic systems and covalently bonded materials. Table 2.11 shows some more interatomic potentials and their suitability.

Table 2.10: Comparison of the Interatomic Potentials

Name	Model	Application
<i>Lennard-Jones Potential</i>	$V_{ij} = 4\epsilon \left[\left(\frac{\sigma}{r} \right)^{12} - \left(\frac{\sigma}{r} \right)^6 \right]$ σ and ϵ are constants which are dependent on the physical property of the materials. (Lennard-Jones, 1924)	Mostly suitable for rare gases
<i>Morse Potential</i>	$V_{ij} = D \{ \exp[-2\alpha(r_{ij} - r_e)] - 2 \exp[-\alpha(r_{ij} - r_e)] \}$ r_{ij} and r_e are instantaneous and equilibrium distances between atoms i and j respectively α and D are constants determined on the basis of the physical properties of the material (Morse, 1929)	Mostly suitable for cubic metals
<i>Born-Mayer Potential</i>	$V_{ij} = A \{ \exp[-2\alpha(r_{ij} - r_0)] \}$ A and r_0 are constants dependent on the material (Born and Mayer, 1932)	Mostly suitable for ceramics
<i>Tersoff Potential</i>	$V_{ij} = V_r(r_{ij}) - B_{ij} V_a(r_{ij})$ V_r and V_a are the potentials due to repulsive and attractive forces between atoms i and j and B_{ij} is a parameter that provides the information for the direction and the length of the bond. (Tersoff, 1988a and Tersoff, 1988b)	Mostly suitable for covalently bonded materials
<i>Embedded-Atom Potential (EAM)</i>	$E_{tot} = \sum_i G_i(\rho_{h,i}) + \frac{1}{2} \sum_{i,j} V_{ij}(r_{ij})$ $\rho_{h,i}$ is the total electron density at atom i due to the rest of the atoms in the system. G_i is the embedding energy for placing an atom into the electron density $V_{i,j}$ is the short range pair interaction representing the core-core repulsion r_{ij} is the separation of atoms i and j (Foiles 1985, Foiles et al 1986)	Mostly suitable for a wide range of metals

Table 2.11: On more Potentials

Potential	Suitability	References
Finnis-Sinclair	For body-centred cubic elemental metals, noble metals	Finnis and Sinclair 1984
Stillinger-Weber	For Silicon	Stillinger and Weber 1985
The Glue Model	For Gold, Lead, Aluminium, Magnesium	Ercolessi et al.1986
Sutton-Chen	For face-centred cubic elemental metals	Sutton and Chen 1990
Rafii-Tabar-Sutton	For face-centred cubic random binary alloys	Rafii-Tabar and Sutton 1991
Force Matching Method	For Aluminium, Magnesium	Ercolessi and Adams 1994
Effective Medium Theory	For face-centred cubic metals	Wang et al. 1995
Murrell-Mottram Cluster	For Aluminium, Copper, Silver, Lead	Cox et al. 1999, Murrell et al 1990
Second-Moment Approximation of Tight Binding	For Iron and its alloys	Chamati et al. 2006

For molecular dynamic analysis, an interatomic potential should have the following properties (Rafii-Tabar and Mansoori, 2003),

- Flexibility – it must be flexible enough to accommodate a wide range of fitting data
- Accuracy – it should be able to accurately reproduce an appropriate database
- Transferability – it should be able to describe structures not included in the fitting database
- Computational Efficiency – the evaluation of the potential should be relatively efficient

In summary: for metals; the EAM and the MEAM potentials should be used, for covalent materials; Tersoff and MEAM should be employed, and for the interface of materials where suitable potentials have not yet been developed, appropriate available LJ and Morse potentials can be used with caution.

2.3.4 Algorithms for the Integration of the Equations of Motion

After the choice of the potential, the next step is to select an appropriate algorithm for the integration of the equations of motions. This is the main kernel of the simulation program. The time integration algorithms for the solution of these equations are based on finite difference methods. It is important to note that this is so because the collisions between atoms are not instantaneous, but they are strong repulsive and attractive interactions that occur over a finite duration. MD simulations use time steps from a few femto seconds (10^{-15} s) (Shimada et al, 1993).

There are several numerical schemes that have been developed for the integration of the equations of motions. Some of these are the Verlet algorithm (Verlet, 1967), the predictor-corrector algorithm (Rahman 1964, Gear and Tu 1975, Gear and Watanabe 1974) and the Beeman's algorithm (Beeman 1976). The Verlet algorithm is of three types, namely; the basic (position) Verlet, the Verlet Leapfrog and the velocity Verlet algorithms. The basic Verlet algorithm uses the second and the third order Taylor expansions, and calculates the positions at the next time step from the positions at the previous and current time steps (Van Gunsteren and Berendsen, 1990). The predictor-corrector algorithm, on the other hand consists of three steps. The first step is to predict (by Taylor expansion) positions and their time derivatives at time, $t + \Delta t$, from values known at a time t . The second step is to compute the force by taking the potential at the predicted positions, and comparing the resulting acceleration, with the predicted acceleration. The last step is to correct the positions and their derivatives by using the difference between the computed and the predicted acceleration (known as the error signal). The Beeman's algorithm is similar to the velocity Verlet algorithm, but it is more complex, and it requires more memory. The merit of the algorithm is that, it provides more accurate expressions for the velocities and better conservation. The predictor-corrector algorithm gives very accurate results, it is computationally expensive and requires large storage.

All the above integration schemes make the assumption, that the positions, velocities and accelerations can be approximated using a Taylor series expansion:

$$\begin{aligned} r(t + \Delta t) &= r(t) + v(t)\Delta t + \frac{1}{2}a(t)\Delta t^2 + \dots \\ v(t + \Delta t) &= v(t) + a(t)\Delta t + \frac{1}{2}b(t)\Delta t^2 + \dots \\ a(t + \Delta t) &= a(t) + b(t)\Delta t + \frac{1}{2}c(t)\Delta t^2 + \dots \end{aligned} \quad (2.35)$$

Where Δt is a finite time step, r is the position, v is the velocity, a is the acceleration; b and c are the third and the fourth derivative of position with time.

2.3.4.1 The Basic Verlet Algorithm (Verlet, 1967)

Using this method, the next step of position can be predicted as follows;

$$r(t + \Delta t) = r(t) + v(t)\Delta t + \frac{1}{2}a(t)\Delta t^2 + \dots \quad (2.36)$$

In the same way, the previous step;

$$r(t - \Delta t) = r(t) - v(t)\Delta t + \frac{1}{2}a(t)\Delta t^2 - \dots \quad (2.37)$$

Summing equations (2.36) and (2.37), we have

$$r(t + \Delta t) = 2r(t) - r(t - \Delta t) + a(t)\Delta t^2 \quad (2.38)$$

It can be observed that the Verlet algorithm uses no explicit velocities. The method is straightforward, easy to implement and its storage requirements are modest.

2.3.4.2 The Verlet Leapfrog Algorithm

In this algorithm, the velocities are calculated by taking the average value halfway between position steps. The equations are as follows;

$$r(t + \Delta t) = r(t) + v(t + \frac{1}{2}\Delta t)\Delta t \quad (2.39)$$

$$v(t + \frac{1}{2}\Delta t) = v(t - \frac{1}{2}\Delta t) + a(t)\Delta t \quad (2.40)$$

In this method, the velocities leap over the positions and then, the positions leap over the velocities. Consequently, the positions and the velocities are not known simultaneously, but the velocities are calculated explicitly.

2.3.4.3 The Velocity Verlet Algorithm

This algorithm calculates new positions, velocities and accelerations using their values at time t based on the following equations deduced from equations (2.35) and (2.38) ignoring infinitesimals.

$$r(t + \Delta t) = r(t) + v(t)\Delta t + \frac{1}{2}a(t)\Delta t^2 \quad (2.41)$$

$$v(t + \Delta t) = v(t) + \frac{1}{2}[a(t) + a(t + \Delta t)]\Delta t \quad (2.42)$$

This algorithm requires low memory.

2.3.4.4 The Predictor-Corrector Algorithm (Rahman 1964, Gear and Tu 1975, Gear and Watanabe 1974)

Velocities at time $t + \Delta t$ are predicted and the forces calculated, and then the corrected forms of the velocities are later calculated. Combining the $r(t + \Delta t)$ and $a(t + \Delta t)$ in equation 2.35, the position can be expressed as:

$$r(t + \Delta t) = r(t) + v(t)\Delta t + \frac{2}{3}a(t)\Delta t^2 - \frac{1}{6}a(t - \Delta t)\Delta t^2 + O(\Delta t^4) \quad (2.43)$$

The velocities at time $t = t + \Delta t$ are then calculated from the positions. Combining the $r(t + \Delta t)$ and $a(t + \Delta t)$ in equation (2.33), the position can be expressed as:

$$\text{(Predicted)} \quad v(t + \Delta t) = v(t) + \frac{3}{2} a(t) \Delta t - \frac{1}{2} a(t - \Delta t) \Delta t \quad (2.44)$$

The acceleration at $t = t + \Delta t$ are calculated from the positions and the predicted velocities.

$$\text{(Corrected)} \quad v(t + \Delta t) = v(t) + \frac{1}{3} a(t + \Delta t) \Delta t + \frac{5}{6} a(t) \Delta t - \frac{1}{6} a(t - \Delta t) \Delta t \quad (2.45)$$

This algorithm has the advantage that, by comparing the predicted and the corrected values of parameters, it is possible to perform a self-check on the algorithm for accuracy.

2.3.4.5 The Beeman's Algorithm

The Beeman's algorithm (Beeman, 1976) is based on equations (2.46) and (2.47), which can be deduced from the equations (2.43) and (2.45). The algorithm is more complicated and requires more memory than the velocity Verlet, but it provides more accurate expression for the velocities and better energy conservation.

$$r(t + \Delta t) = r(t) + v(t) \Delta t + \frac{2}{3} a(t) \Delta t^2 - \frac{1}{6} a(t - \Delta t) \Delta t^2 \quad (2.46)$$

$$v(t + \Delta t) = v(t) + v(t) \Delta t + \frac{7}{6} a(t) \Delta t - \frac{1}{6} a(t - \Delta t) \Delta t \quad (2.47)$$

When choosing an integration algorithm following factors need to be considered:

- Accuracy – it should produce an approximate result close to the exact solution
- Memory requirement – it should require little memory
- Efficiency – it should be fast and computationally efficient
- Time Step – it should permit long time step Δt for the integration

Initialize the Model

To initialize the simulation, the MD 'box' (the control volume) must be defined; then initial positions and velocities of the atoms must be assigned – this is a kind of initial randomization. Positions of the atoms can be defined, by assuming certain crystal structure and the initial velocities can be randomly assigned.

Relax the Model from its Initial State to its Dynamically Equilibrium Condition

The model of having atoms positioned and assigned velocities as above implies that additional potential energy between atoms has been artificially applied to the system. This is not the case in real solids, where atoms are actually vibrating around their equilibrium positions. So, it is necessary to relax this initial model from its artificially assigned initial conditions to its natural, dynamically equilibrium condition. This would involve running the MD program under constant temperature for a specified number of time steps, so that the velocities of atoms that are initially assigned randomly or based on a normal distribution, will gradually reach equilibrium at the specified temperature of the simulation (Cheong et al 2001). This relaxation may take 50 time steps or more depending on the time needed for the model to reach its natural, dynamically equilibrium state, that is consistent with the environmental temperature.

Run the Simulation and Analyze the Results

The simulation is then run and the results analyzed. Using the MD, the effect of such variables as edge effect, cut depth et cetera can be defined and the simulations conducted accordingly. It is also easy to vary the properties of the work materials and the cutting tools in MD simulations (Komanduri and Raff, 2001)

2.3.5 Examples of MD Simulation of Nanomachining

The fundamental part of the abrasive process is the interaction of two bodies, where one is carrying out work upon the other one and it is a massive deformation process. By exerting work on each other, energy is added to the bodies and thereby to the system, therefore the temperature would rise. The implementation of thermostat areas along the boundaries allows the temperature of the systems to be controlled by releasing energy to the not modelled environment (Marinescu et al, 2004).

(Rentsch and Inasaki, 1994) modelled a copper work material and a diamond tool for their study. They used the Lennard-Jones potential function for the copper atom interactions, but kept the boundaries and the tool stiff. A total of 11476 atoms in 13 horizontal (1,1,1) – layers of fcc-lattice were used for the copper, and the tool was shaped from a diamond lattice block by clearing on the four (1,1,1) –planes. Using a cutting speed of 100m/s, they observed a pronounced build-up phenomenon after 25000 time steps (see Figure 2.12).

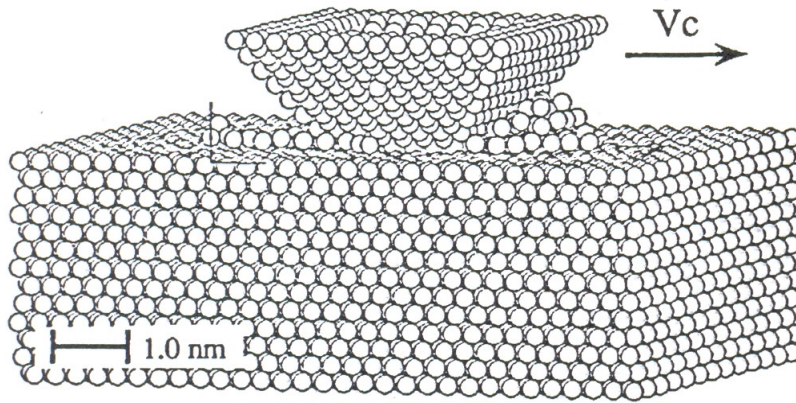


Figure 2.12: Advanced MD Simulation with Straight Aligned Tool (Rentsch and Inasaki,1994)

The MD simulation of nanometric cutting was carried out by Komanduri team with a range of negative-rake tools to simulate the Ultra-Precision Grinding (UPG) process (Komanduri et al 1999). A copper work material and an infinitely hard tool (tungsten) were used in the simulations. A pairwise sum of Morse potential was used for the study, in which they concluded that simulation tests can facilitate a better understanding of the process without the need for expensive and time consuming machining or grinding experimental work.

The investigation of the fundamental atomistic processes in chemical mechanical polishing of copper was carried out by Ye et al (2002). They simulated the nanoscale polishing of a copper surface by a single abrasive particle, using the embedded-atom potential. The temperature was controlled by maintaining 1.2nm of the substrate at 300K and the rescaling of atom velocities was performed whenever the temperature deviated more than 10K from the specified value. This allowed the transfer of heat from the machined region to the bulk of the work-material. They focused on the mechanical abrasion aspect of material removal and found that dislocations and atomically rough planarized surface were formed. They also studied the nature of the material removal, chip formation, materials defects and frictional forces as function of the cutting speed, depth of cut and abrasive geometry. They established that the material removal rate scales linearly with the depth of planarization and is directly proportional to the velocity of cut.

Lin et al (2003) used the MD method to survey the features of grinding energy dissipation, grinding stress, strain state and grinding temperature in the atomic space. The workpiece and the tool materials were assumed to be monocrystalline silicon and diamond respectively. A Tersoff potential function, suited to a multibody system was employed for the simulation. They found out that as the abrasive grain cut into the workpiece continuously, the value of the grinding force increased

gradually in a repeated fluctuating manner. Also, it was observed that atoms of the crystal lattice were reconstituted and parts of the non-crystal atoms were piled up on the front of the abrasive grain.

To be more realistic, (Rentsch and Inasaki, 2006) extended the MD material modelling to consider fluids like coolants. They considered the impact of such fluids on the surface generation and the tribological contact conditions. The fluid-fluid interactions were calculated on the basis of the Lennard-Jones potential function and the embedded-atom potential function was used for the inner workpiece reactions (the internal tool dynamics were ignored). They observed an intensive self-diffusion of the fluid atoms, and these filled the whole free space above the workpiece. No impact on the stress distribution was observed, but the whole fluid-tool/workpiece contact was heated up in a narrow range.

Rentsch and Brinksmeier obtained a 3-D MD simulation of the grinding process (Brinksmeier et al 2006). Using the embedded atom method potential and 100000 atoms, they modelled two abrasives that cut through a workpiece over its whole length at 100m/s (see Figure 2.13). They reported that the periodic borders in the horizontal plane led to complete groove formation in the cutting direction.

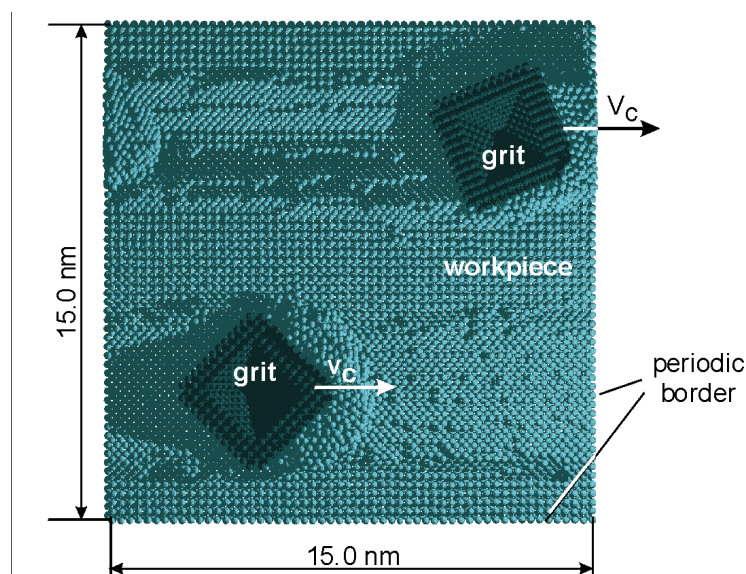


Figure 2.13: - Groove Scratching with 2 Grits (top view - 360 000 time steps, 144 ps) (Brinksmeier et al, 2006)

Shimizu et al (2006) reported on molecular dynamics simulations of the effect of vibration, acceleration and velocity on the reduction of both the plastic flow and cutting forces in the vibration assisted cutting. The workpiece material used was aluminium with rigid diamond as the tool. The Morse potential was used for the atomic interactions. They observed that the effect of the vibration on the plastic flow and cutting forces is more than the effect due to acceleration. Figure 2.14 shows

some snapshots of the simulation, where the material removal process can be clearly seen. In Figure 2.14a, it can be seen that the tool is not in full contact with the chip due to the tool oscillation cycle progresses (Figure 2.14b), strain is visible in the workpiece and the observed shear plane phenomena is similar to what is seen in macro scale.

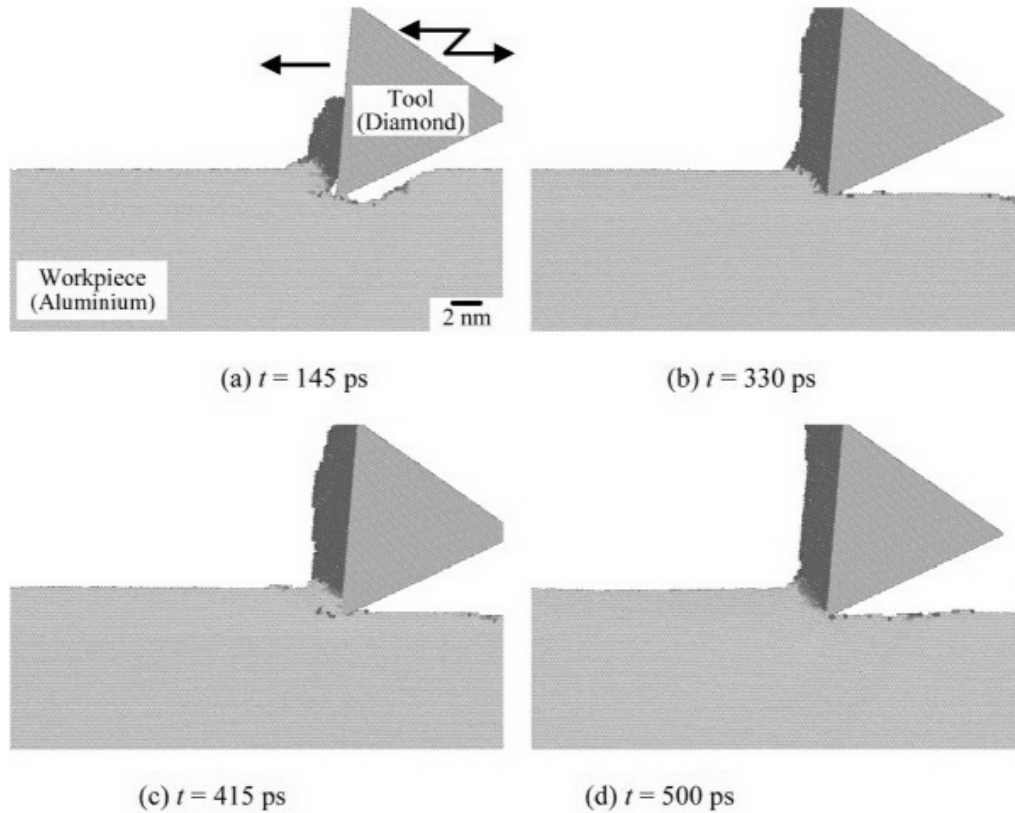


Figure 2.14: - Snapshots of atomic arrays in vibration-assisted cutting process and travelling distance from initial arrays. Cutting speed, $V_c = 50 \text{ m/s}$, Amplitude, $A = 4 \text{ nm}$ and Frequency, $f = 4 \text{ GHz}$ (Shimizu et al, 2006)

The MD simulations of nanoindentation followed by scratching at constant depth on the Si-terminated (0 0 1) surface of 3CSiC was carried out by (Noreyan and Amar, 2008). They investigated the dependence of the friction coefficient, scratch hardness, and wear on scratching depth, velocity, direction, and indenter size and shape. The workpiece was assumed to have the 3C SiC cubic crystal structure, and a diamond tip was used. Both were modelled using the Tersoff potential. They found that the friction coefficient and the scratch hardness increased with indentation depth but decreased with increasing scratching velocity. They also noted that the direction dependence of the friction coefficient is weaker at high scratching velocity. These findings are certainly providing good insight to nanometric machining processes.

(Shimizu et al, 2008) furthered their research, by using the molecular dynamics method to study the material deformation and removal mechanism of a face centred cubic (fcc) metal by a diamond abrasive grain. They assumed the workpiece and the abrasive grain to consist of mono-crystalline copper and rigid diamond respectively, and the influence of the polishing pad was taken into consideration. They employed Morse potential for the simulation. It was concluded that the growth of cutting chip and the stick-slip behaviour of tangential force are deeply related. It was also noted that the MD simulation has an advantage for the estimation of the proper stiffness of the grinding wheel and the actual depth of cut in nanoabrasive machining processes, where the tool stiffness is considered. See Figure 2.15 for a snapshot of part of the simulation.

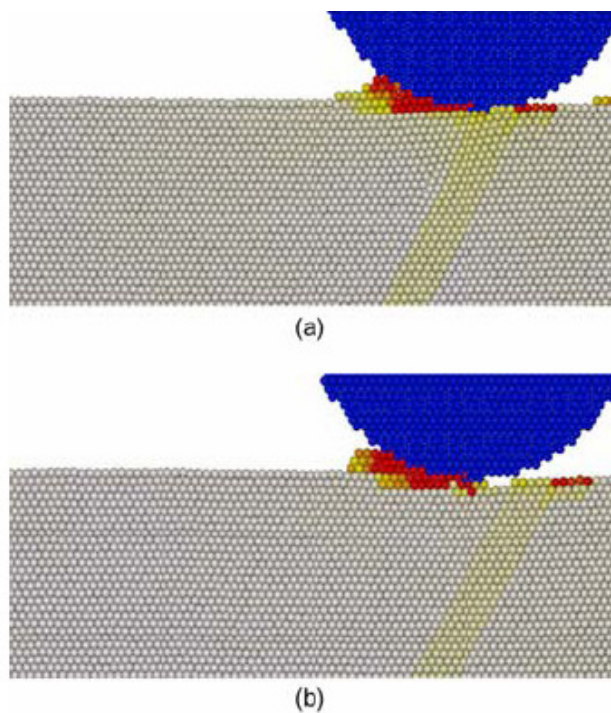


Figure 2.15: - Snapshots of atomic arrays and travelling distance (Shimizu et al, 2008)

Table 2.12 lists a comparison of MD simulations of nanomachining. The potentials used for MD simulations of metals include LJ, Morse, EAM and MEAM. In many cases, the rationale or justification for their use are not given except for reference to the use in earlier studies. Ideally, multi-body potentials (EAM and MEAM) should be used for metals, rather than pairwise potentials (LJ and Morse); because they could more correctly model the metallic bonding. The range of velocity considered are from 5m/s to 360m/s which covers representatively what occurs in practical processes. Most of the studies use diamond as the abrasive/cutting tool and this suggests that other abrasives and cutting tools like cubic born nitride, aluminium oxide, silicon carbide et cetera should be further investigated. Also, most of the MD simulations were not validated by experiments even though many researchers are beginning to consider this issue. Besides excellent exploration of MD

application in machining research, some fundamental questions remain. For example, the limits of nanomachining process in terms of the best surface finish and the minimum depth of cut for minimum material removal are still unclear. Many investigations only give some simulation observations of nanometric machining phenomena without detailed quantitative measures. Some physical parameters that were used for macro world were directly applied to nanometric world, which do not provide good explanation of causal relationships. Many results from MD simulations have not been verified by physical experiments, though they match with common intuitive sense. All of these indicate that there is still a long way to go in order to fully take the advantages of molecular dynamics for nanomachining researches.

Although many questions remain in the application of MD in nanomachining, the MD has demonstrated its advantages in the explanation of material behaviour at the nanometre scale, which is difficult and expensive to observe in experiments. Molecular dynamics is a useful tool to investigate effects of material property and material defects on surface creation in nanomachining and tool wear mechanism.

2.4 Research Gaps and Summary

From available literature, it can be inferred that the simulation of atomic and molecular behaviour using the Schrödinger wave equation for real machining is still not feasible due to the complexity of obtaining a solution. The common methods to enable so-called MD simulation of machining are based on using interatomic potentials. Many potential functions have been proposed for MD analyses, and some of them have been applied in nanomachining simulations. It is important to stress that appropriate potentials should be used for MD simulations. Previous works suggest that the EAM potential should be used for the modelling of fcc metals (Pei et al 2006, Promyoo et al 2008). The Tersoff potential should be used for covalent materials and the MEAM should be used for both metallic and covalent materials. Recent studies have demonstrated that using EAM potential will result in lower cutting forces than LJ and Morse potentials (Pei et al, 2006). The MD simulation is a powerful tool for the understanding of the machining processes on the nanometre scale. It can be used to obtain information on material behaviour, such as the changes in cutting forces, observation of rubbing, ploughing and the chip formation phenomena, and it can also be used to predict minimum depth cut and material deformation conditions which cannot be easily duplicated experimentally (Belak and Stowers 1990, Ikawa et al 1991 and Komanduri et al 1998, 1999).

Table 2.12: Comparison of some MD simulations of Nanomachining

Reference	Model	Potential/s Used	Workpiece Material	Tool	Cutting Speed	Experimental Validation
Shimada et al (1992)	2D	Morse for Cu-Cu	Copper	Diamond	20-200m/s	Yes
Rentsch and Inasaki (1994)	2D and 3D	Lennard-Jones for Cu-Cu and Cu-C	Copper	Diamond	20m/s	No
Komanduri et al (1999)	3D	Morse for Cu-Cu and Cu-tungsten	Copper	Infinitely Hard Tungsten	500m/s	No (Just comparisons with published experimental results)
Shimada et al (1999)	2D	Tersoff for the Si-Si, C-C and Si-C	Silicon	Diamond	200m/s	No
Han et al (2002)	2D	Tersoff for Si-Si	Silicon	Diamond	Not known	No
Ye et al (2002)	2D/3D	EAM for Cu-Cu	Copper	A Single Abrasive Particle	8-180m/s	No
Lin et al (2003)	Quasi 3D	Tersoff for Si-Si and C-C	Silicon	Diamond	Not Known	No
Cheng et al (2003)	2D	MEAM for Si-Si	Silicon	Diamond	20m/s	Yes
Fang et al (2005)	Quasi 3D	Tersoff for Si-Si	Silicon	Diamond	24.5m/s	Yes
Rentsch and Inasaki (2006)	2D/3D	EAM for Cu-Cu, LJ for Cu-C and LJ for Fluid-Fluid	Copper	Diamond With the effect of fluid	(Workpiece velocity at 100m/s)	No
Shimizu et al (2006)	2D	Morse for Al-Al and Al-Cu	Aluminium	Diamond	50-360m/s	No
Pei et al (2006)	2D	EAM for Cu-Cu and Morse for Cu-C	Copper	Diamond	100m/s	No
Cai et al (2007)	2D/3D	Tersoff for Si-Si and Morse for Si-C	Silicon	Diamond	20m/s	No
Shimizu et al (2008)	2D	Morse for Cu-Cu and Cu-C	Copper	Diamond	5m/s	No
Noreyan and Amar (2008)	3D	Tersoff for Si-C	SiC	Diamond	214m/s	No

Such information could open up a huge potential to improve machining performance at the nanometre scale. In this study, the MD method would be used for the simulation and the study of nanometric machining of monocrystalline diamond tool on a monocrystalline copper workpiece. The MD is favoured over the Monte Carlo (MC) method as the MC is often the most appropriate method for the investigation of systems at exact temperatures and pressures, but may not be suitable for the calculations of time-dependent quantities (Leach, 2001). The major problem with the application of the conventional MC to machining applications is that there is no time variable in an MC calculation and this is an issue for systems that are neither canonical nor microcanonical (Narulkar et al, 2004). The MD method is accurate when compared to experiments, (if accurate interatomic potentials are used) and it can be used to study phenomena that are not available to experimentation (Allen, 2004).

When compared with the FEM, the MD should be used in machining when the depth of cut is less than $1\mu\text{m}$. This is because, for these small regions (below $1\mu\text{m}$), quantum mechanics are applicable and not the continuum elastic theory (Rudd and Broughton, 1998). FEM machining simulations performed using Abaqus/Explicit and Deform3D encountered difficulties for depth of cuts below $3\text{--}4\mu\text{m}$. For example, a 3D FEM simulation with depth of cut of $2\mu\text{m}$, will require 1000 days for a tool advancement of 1mm (Opoz, 2012).

In summary it should be stated that there are still many fundamental questions which need to be addressed in nanometric machining. Some of them are the following, namely what are the fundamental mechanisms underlying nanomachining processes? What is the limit of machining? What is the minimum depth of cut and how can the atomic surface roughness be evaluated from the MD simulation of nanomachining? How to predict the onset of plasticity in nanomachining? This study attempts to find some answers or to point the direction towards the answers to the above questions.

Chapter 3. The Methodology for the MD Simulation of Nanomachining

3.1 The Simulation Set-up and Procedure

3.1.1 Software Consideration

There are many open MD software that are available. Many are free programs, some require licences for use and others are commercial software. A comparison of some of these software is shown in Table 3.1. As can be observed from the table, many of the software were developed for different applications and benchmarking would be quite difficult. The choice of the software will depend on the intended application and the available operating system platform and the hardware. DL_PLOY and LAMMPS MD software would be suitable for this research, but LAMMPS was used because of initial personal preference and the available good users' forum support. Also, it allows the portability of many pre- and post processing software.

The MD simulation in this study was carried out by using the following software namely;

- Metadise – Minimum Energy Techniques to Dislocation, Interface and Surface Energies
- XenoView
- LAMMPS – Large-Scale Atomic/Molecular Massively Parallel Simulator (Plimpton, 1995)
- VMD – Visual Molecular Dynamics and OVITO – The Open Visualization Tool (Stukowski, 2010)

The Metadise and the XenoView were used for pre-processing and VMD and OVITO were used for post-processing (visualization and analysis). The LAMMPS was used for the actual MD simulation.

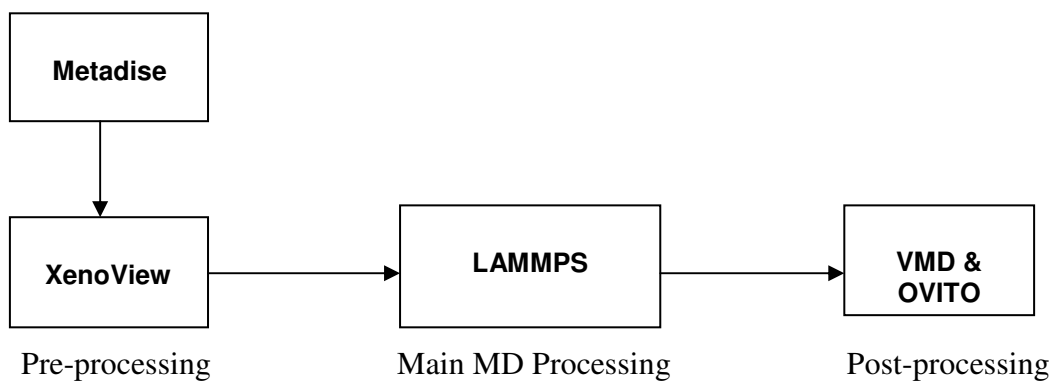


Figure 3.1: Software Methodology Flowchart

Pre-processing

The Metadise

The three-dimensional (3D) structures of the materials used for the MD simulation (Copper and Diamond – Carbon) were generated by using the Metadise. To obtain these, the following information are required by the software, which are;

- The unit cells
- Fractional co-ordinates and the type of atoms
- Space group symmetry

The XenoView

The XenoView is a windows-based software for MD simulation. Its interactive graphical user interface was explored for the preparation of the geometry configuration for the simulation.

The Metadise's output was imported to XenoView, and consequently the output of XenoView was exported to LAMMPS.

LAMMPS

This is a classical MD software that models an ensemble of atoms using a variety of empirical potentials and boundary conditions. It runs on single and parallel processor computer. It is an open-source code and it is distributed under the terms of the GNU public licence. The LAMMPS computes the Newton's equation of motion for a system of interacting atoms. It requires as its input; the types of atoms and the list of their initial co-ordinates, molecular topology information and the empirical potentials assigned to all the atoms.

Post-processing

VMD

The VMD is a molecular visualization software for displaying and analyzing atomic systems by using 3-D graphics technology. The VMD was employed for the visual display of the LAMMPS MD simulation results (Chapters 4 and 5).

OVITO

The OVITO is a very powerful visualization and analysis software for atomistic simulation data. OVITO was used for some analysis and the visualization of simulation results in Chapter 6.

3.1.2 Hardware Consideration

The simulations were carried out initially on a single processor computer and later on the newly installed University of Huddersfield's High Performance Computer (HPC) clusters. Specifically, the simulations were run on the Eridani Hybrid cluster (See Figure 3.2 below).

3.1.2.1 The University of Huddersfield's High Performance Computing (HPC) Clusters

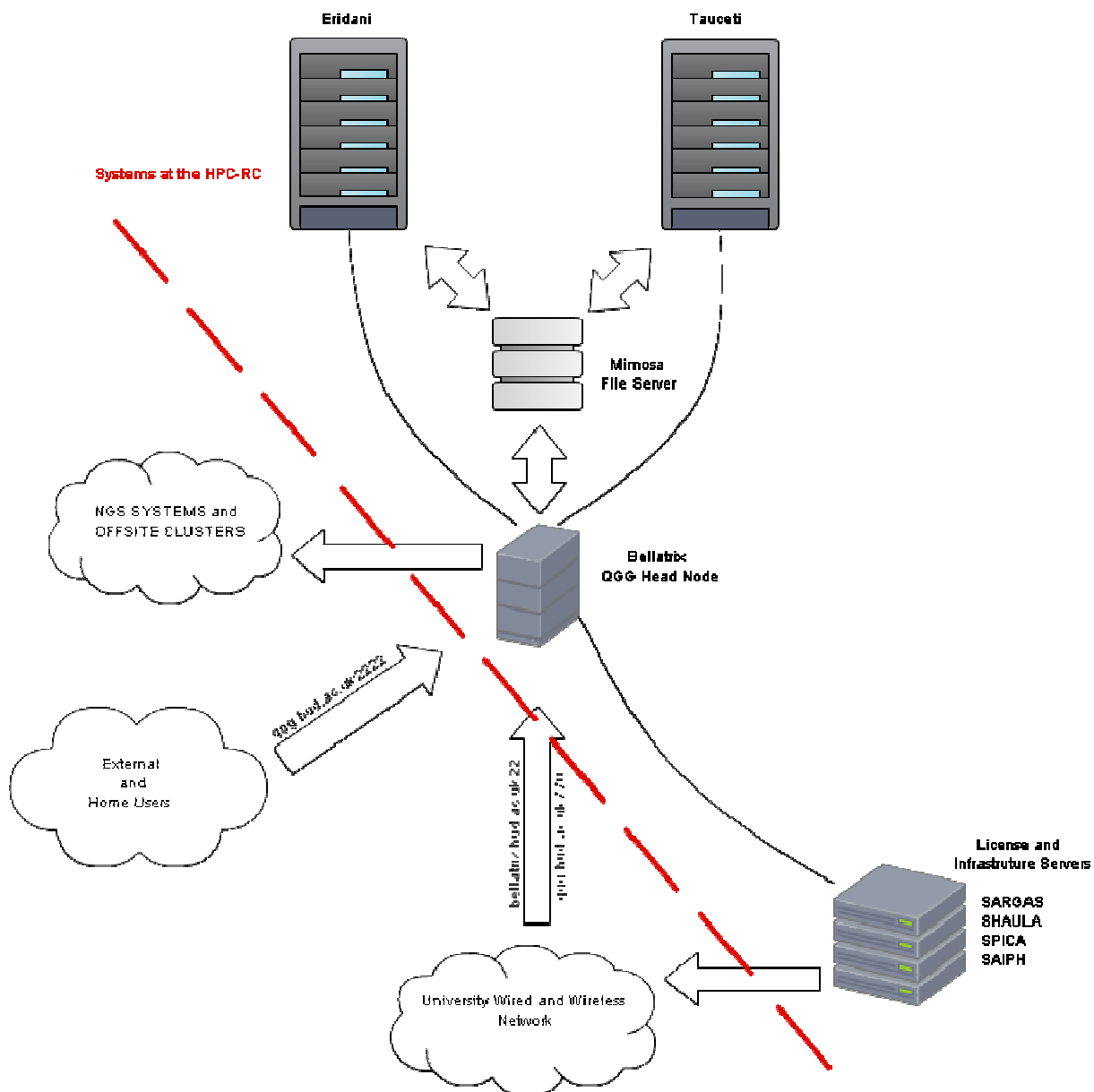


Figure 3.2: Network Diagram

Table 3.1: Comparison of some MD Software

Software	Capabilities	Platform/s Supported	Developer/Country	Free/Commercial
CHARMM (Chemistry at HARvard Macromolecular Mechanics)	A general MM and MD software. Most suitable for biological molecules	Unix. Supports both serial and parallel architectures	Martin Karplus, Harvard University/USA	Free (but it has a commercial version – CHARM as part of the Quanta Package) Latest release: Version c3661 August 2011
DL_POLY	A general purpose MD software for the simulation of a wide range atomic and molecular systems. It also accommodates many boundary conditions, namely; cubic periodic, slab, orthorhombic periodic, parallelepiped periodic etc.	Unix Supports both serial and parallel architectures.	Originally by W. Smith, T.R. Forrester and later with I.T. Todorov, Daresbury Laboratory/UK	Free (Licence would have to be obtained from Daresbury Laboratory) Latest release: Version 4.02 July 2011
GROMACS (GRONingen Machine for Chemical Simulation)	A MD software primarily designed for biochemical molecules such as proteins, lipids etc, but can also be used for polymers	Unix Supports both serial and parallel architectures.	Originally by researchers at the University of Groningen/Netherlands	Free Latest release: Version 4.5.5 September 2011
LAMMPS (Large-scale Atomic/Molecular Massively Parallel Simulator)	This is classical MD software that models an ensemble of atoms using a variety of empirical potentials and boundary conditions.	Unix Supports both serial and parallel architectures.	Originally by Steve Plimpton and later with Aidan Thompson and Paul Crozier, Sandia National Laboratories/USA	Free Latest release: December 2011
MDynaMix (Molecular Dynamics of Mixtures)	This is MD software for the simulation of mixtures of rigid and flexible molecules	Unix	A. Laakonen and A. Lyubartsev, University of Stockholm/Sweden	Free Latest release: Version 5.2.4 June 2011
Moldy	A general purpose MD software for atomic, ionic	Unix and Windows 95.NT	Keith Refson formerly at Oxford, then at Rutherford	Free

	and molecular systems		Appleton Laboratory/UK	
NAMD	This is a parallel MD software for high-performance simulation of large biomolecular systems	Unix	Theoretical and Computational Biophysics Group, University of Illinois/USA	Free Latest release: Version 2.8 May 2011
PMD (Parallel Molecular Dynamics)	This is a parallel MD software	Unix	University of Columbia/USA	Free
TINKER	A MD software for molecules (biomacromolecules, biopolymers etc)	Unix	Jay Ponder and Co Researchers, Washington University/USA	Free Latest release: Version 6.0 December 2011
Tremolo-X	This is a parallel MD software with user-friendly graphical user interface (GUI) end. It allows the design of new innovative materials	Unix	Michael Griebel, University of Bonn/Germany	Free (Licence needed)
XMD	A MD software designed for metals and ceramics	Unix	Jon Rifkin, University of Connecticut/USA	Free
XenoVIEW	A MD software with built-in graphical user interface (GUI) for the simulations of inorganics, polymers and proteins	Windows	Sergei Shenogin and Rahmi Ozisik, Rensselaer Polytechnic Institute (RPI)/USA	Free for non-commercial users

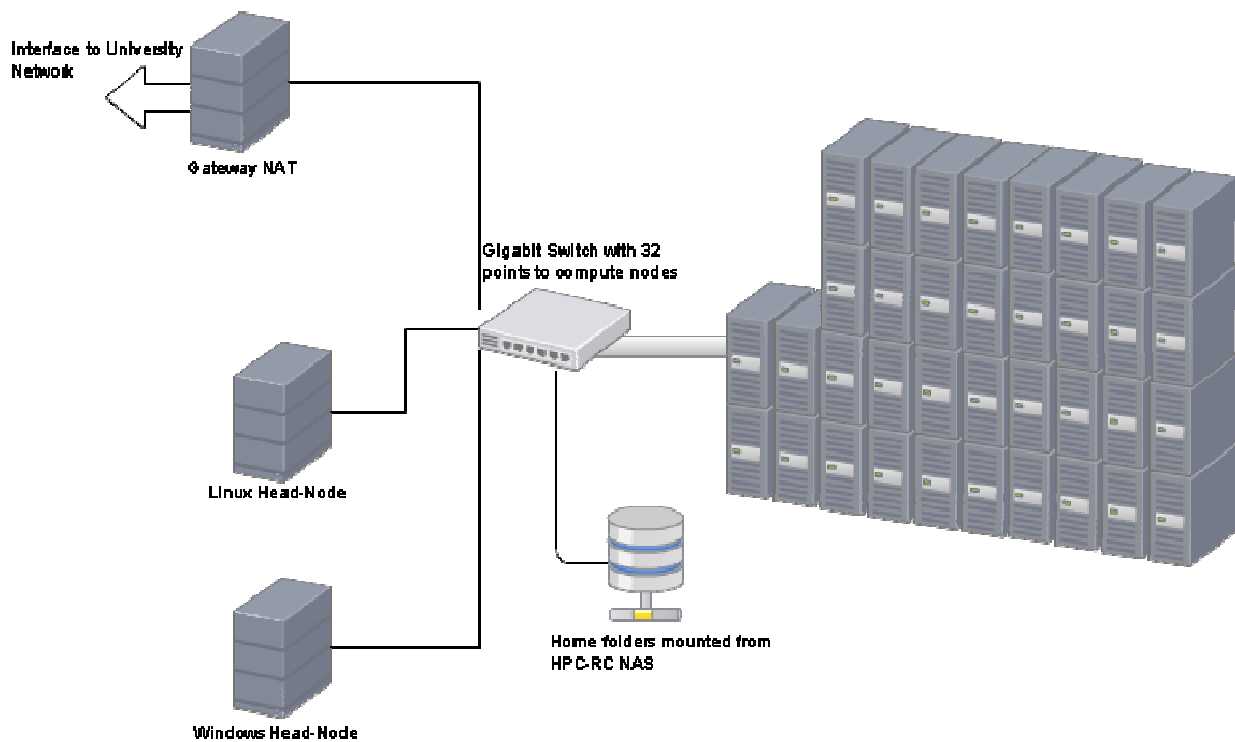


Figure 3.3: Eridani Cluster Architecture Diagram (Kureshi, 2010)

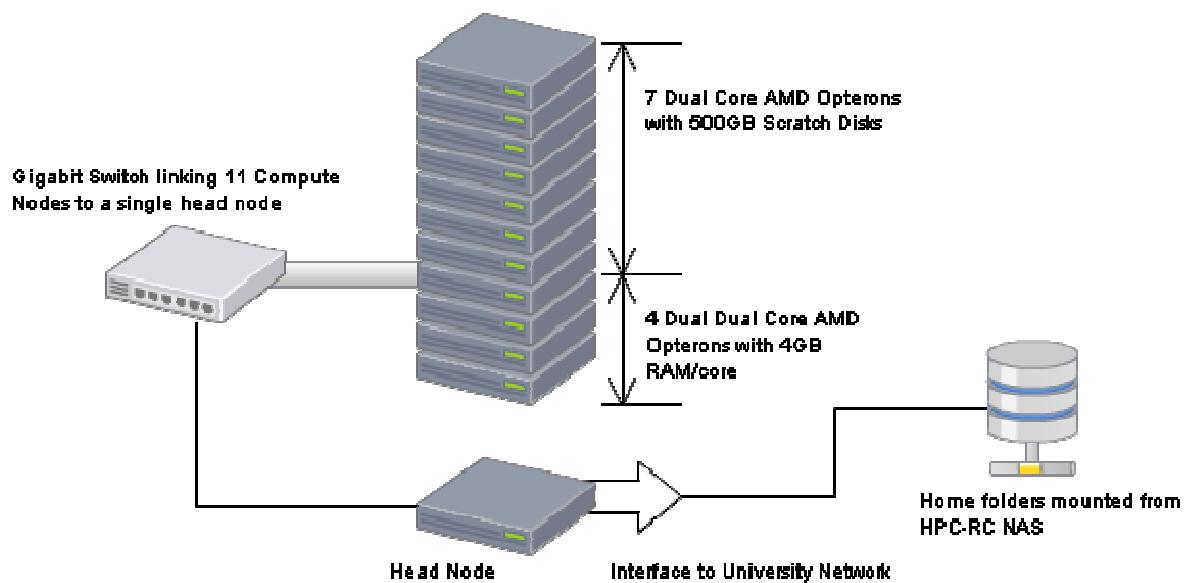


Figure 3.4: TauCeti Cluster Architecture Diagram (Kureshi, 2010)

The Eridani cluster has two head nodes which comprise the Windows Server/HPC 2008 and the Linux CentOS/OSCAR. The configuration of the clusters are shown below;

Table 3.2: Hardware Configuration of the Eridani Cluster (Kureshi, 2010)

Resource	Description
Total Systems	37
Total Cores	148
Processing Cores	128
Service Cores	16
Processor	Inter Core 2 Quad Q8200 4M Cache 2.33GHz 13333FBS & Inter Core 2 Quad Q8300 4M Cache 2.50GHz 13333FBS
RAM	4 x Kingston Value 2 GB 800Mhz
HDD	Seagate Barracuda 250 GB 7200RPM SATA-II

3.1.2.1.1 How to run the Simulation on the Huddersfield HPC

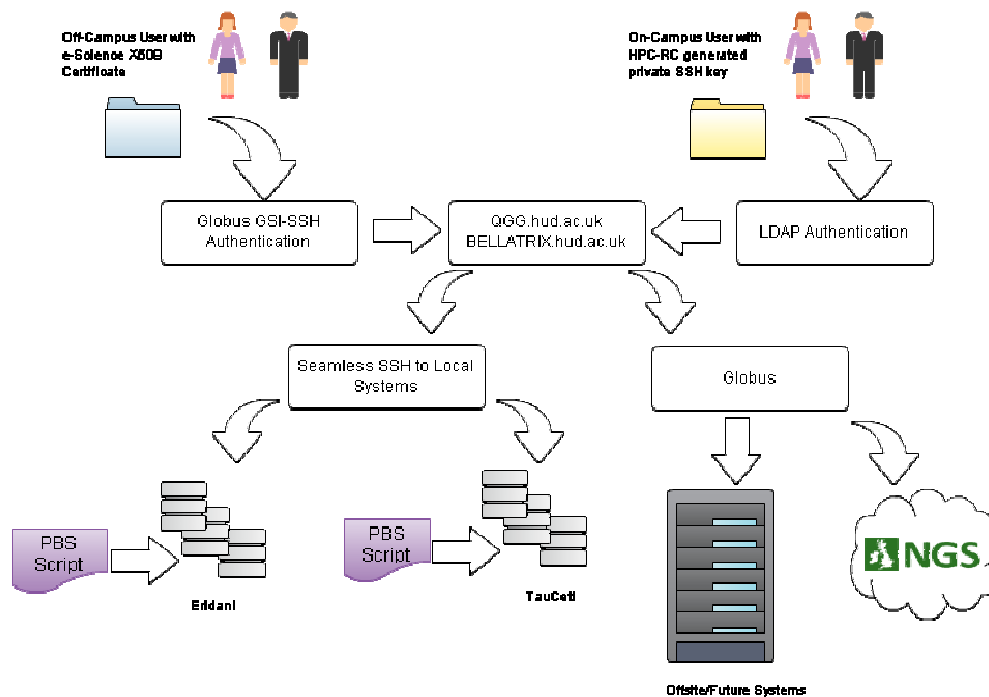


Figure 3.5: General Users' Workflow for the Huddersfield HPC

The user can either log on to the system on the campus or from an-off campus site. The system requires an initial authentication to access the HPC. The workflow for the system is shown in Figure 3.5. The on-campus users need a SSH key, while the off-campus users need a GSI-SSH key. Once the verification is successful, the user would get a prompt on the clusters. (The user also has the option of getting access to other NGS cluster sites). The user can then submit a PBS job script to

the clusters. The LAMMPS simulation was run on the eridani cluster and an example of the PBS job script template is shown in Appendix B. The sections 1 and 2.2 of the template are only to be specified by the user, the other sections are defaults for the cluster. Once the script is prepared, it can be submitted to the cluster via the PBS using the PBS commands on the Linux console. The job is then accepted and assigned a job number. The output of the simulation is obtained from the directory, from which the PBS command was run.

The major advantage of the HPC is in time savings. Several hundreds of simulations were run and the HPC affords the opportunity to run simulations concurrently on multiple processors to save time.

3.2 The Simulation Configuration

Various configurations were used for the simulations to optimize computational resources. All the configuration share the same features in that they consist of the workpiece and the tool and the workpiece is divided into boundary, Newtonian and thermostat atoms.

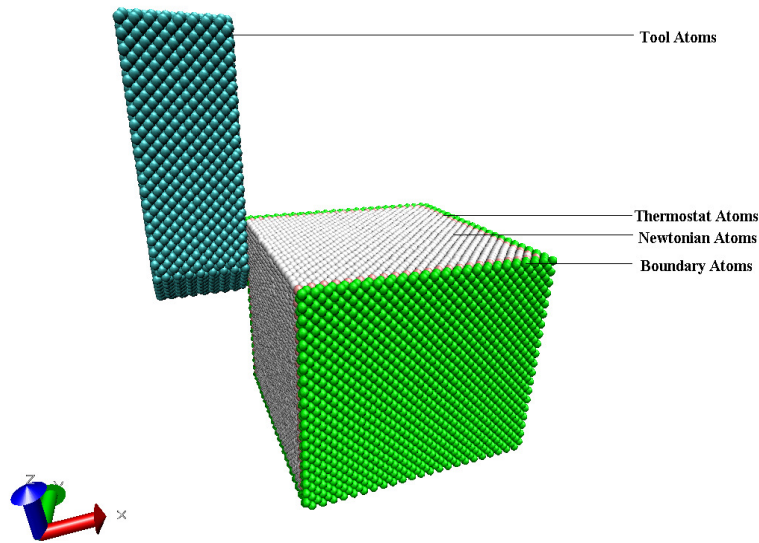


Figure 3.6: The MD Simulation Model

The Newtonian atoms obey the Newton's equation of motion. The thermostat atoms conduct the heat generated during the cutting process out of the cutting region. This is achieved by the velocity scaling of the thermostat atoms, (with the conversion between the kinetic energy (KE) and temperature via Equation 2.6).

3.2.1 The Workpiece

The workpiece is monocrystalline copper, which is ductile and has good machinability properties.

Table 3.3: Properties of Copper

Chemical Symbol	Cu
Atomic Number	29
Atomic Weight	63.54
Density	8960kg/m ³
Melting Point	1356K
Thermal Conductivity	394W/mK
Crystal Structure	Face-Centred Cubic
Hardness	0.369GPa

3.2.1.1 The Face-Centred Cubic (FCC) Structure

The Face-Centred Cubic structure has atoms arranged at the corners and at the centre of each cube face. It has co-ordination number of 12 and each cell has a net total of 4 atoms.

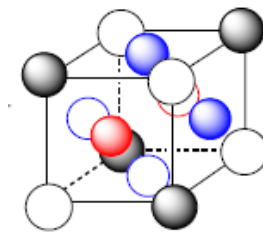


Figure 3.7: The Face-Centred Cubic Structure

3.2.2 The Tool

The tool is crystalline diamond and it's the hardest known natural material, which makes it suitable as a tool for machining.

Table 3.4: Properties of Diamond

Chemical Symbol	C
Density	3500kg/m ³
Melting Point	3820K
Young Modulus	1050GPa
Thermal Conductivity	400W/mK
Crystal Structure	Diamond
Hardness	45GPa

3.2.2.1 The Diamond Structure

The diamond structure is made up of repeating units of four carbon atoms which are joined to four other carbon atoms by strong covalent bonds.

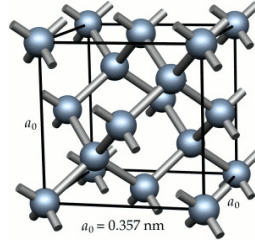


Figure 3.8: The Diamond Structure

3.3 The Selection of the Interatomic Potentials and Parameters Setting

The three potentials used in the simulation are Lennard-Jones, Morse and Embedded-Atom Method (EAM) potentials. The cutting depth and the cutting speed were varied depending on the actual simulation.

Table 3.5: MD Simulation Parameters

Parameters	Values
<i>Bulk Temperature</i>	<i>293 K</i>
<i>Cutting Direction</i>	<i>[100]- Along the x-axis</i>
<i>Cutting Speed</i>	<i>150m/s (Varies)</i>
<i>Time Step</i>	<i>0.3fs</i>
<i>Simulation Run</i>	<i>100000steps (Varies)</i>

3.3.1 Initialization

The model was initialized by assuming the FCC crystal structure for the workpiece and the diamond structure for the tool. The positions are then extracted from these configurations for the modelling.

3.3.2 Boundary Conditions

The boundary for the global simulation box in each dimension is set. For the x and y axes, the box is set to be non-periodic. This means that the atoms do not interact across the boundary and they do not move from one side of the box to the other. For the z axis, the position of the face is set so as to accommodate the atoms in that dimension, no matter how far they move.

3.3.3 Relaxation of the System

The model atomic configuration was run at NVT for 50000 time steps to relax the system and so that the velocities of atoms that are initially assigned randomly will gradually reach their natural, dynamically equilibrium states.

3.3.4 Concluding Remarks and Scope of Research

In this research study, the MD method is used for the study of nanometric machining of monocrystalline diamond tool on monocrystalline copper workpiece. The effect of wear is not considered on the tool and the materials are assumed to be without defects.

Chapter 4. Single-Pass Nanometric Machining Simulation Results

4.1 The Effect of Interatomic Potentials on the MD Simulation of Nanomachining

4.1.1 Introduction

The major task in a MD simulation is the selection of the potential function, and if the potential doesn't model the behaviour of the atoms correctly, the results produced from the simulation would be useless. Three popular potentials namely; EAM, Morse and the Lennard-Jones, were employed to model nanometric machining.

The three potentials used in the simulation are given below;

- *Lennard-Jones (LJ) Potential*
- *Morse Potential*
- *Embedded-Atom Potential (EAM)*

The simulation parameters of Table 3.5 were used with a depth of cut of 1nm.

Table 4.1 shows the simulation conditions applied in this study. The workpiece consists of 16000 copper atoms with perfect FCC lattice. It includes 3 kinds of atoms namely; boundary atoms, thermostat atoms and Newtonian atoms. The boundary atoms are kept fixed to reduce edge effects. The thermostat atoms conduct the heat generated during the cutting process out of the cutting region (See Figure 4.1). This is achieved by the velocity scaling of the thermostat atoms, (with the conversion between the kinetic energy (KE) and temperature via equation (2.7).

The Newtonian atoms obey the Newton's equation of motion. The cutting tool consists of 912 carbon atoms with diamond lattice structure. The cutting tool is pointed shaped and it is modelled as a rigid body.

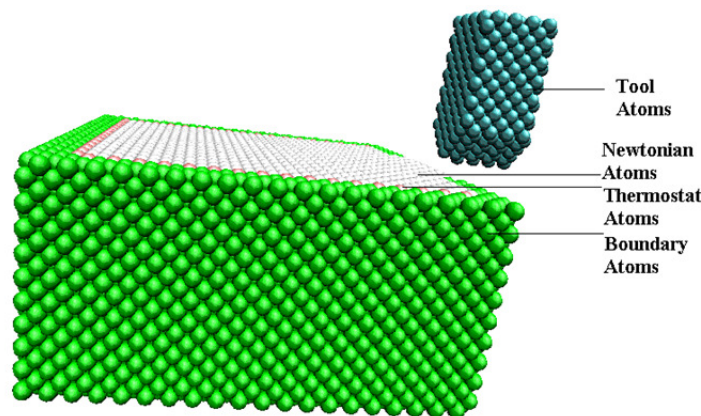


Figure 4.1: The MD Simulation Model for this Investigation

The atomic interactions in the simulation are the following, namely;

Cu-Cu : interactions between copper atoms

Cu-C : interactions between copper atoms and diamond atoms

C-C : interactions between the diamond atoms (treated as rigid in this paper)

4.1.2 Modelling with LJ Potential

Equation (2.25) was employed, and the LJ parameters used for the atom interactions are $\sigma = 2.2277$ Angstroms and $\varepsilon = 0.415\text{eV}$ (Hwang et al, 2004), which apply to both the Cu-Cu and the Cu-C interactions.

The simulation and the cutting forces are shown in Table 4.2. The potential energy and the total energy for the LJ modelling and the temperature variation are shown in Table 4.3.

4.1.3 Modelling with Morse Potential

Equation (2.26) was used, and the parameters are given below;

For Cu-Cu interactions: (Girifalco and Weizer1959, Pei et al 2006)

$$D = 0.3429\text{eV}, \alpha = 0.13588(\text{nm})^{-1}, r_e = 0.2866\text{nm}$$

For Cu-C interactions: (Hwang et al 2004)

$$D = 0.087\text{eV}, \alpha = 0.17(\text{nm})^{-1}, r_e = 0.22\text{nm}$$

The cut-off distance chosen was 6.4 Angstroms (that is, the interactions between atoms separated by more than this distance are neglected).

The simulation and the cutting forces are shown in Table 4.2. The potential energy and the total energy for the Morse modelling and the temperature variation are shown in Table 4.3.

4.1.4 Modelling with EAM Potential

Equation (2.30) was used, where the potential parameters used for the Cu-Cu interactions were read from the file - Cu_u3.eam in LAMMPS). The file contains the following, namely; the lattice constant of copper (3.615 Angstroms), the spacing in density (5.01E-4) and the spacing in distance (1.00E-2). Also, it contains three arrays of tabulated values of the embedding function, $G_i(\rho_{h,i})$ - 500 values; effective charge function, Z_{ij} , - 500 values, from which the pair potential interaction is calculated (the relationship between the effective charge and the pair potential is given by equation (4.1) and the density function, $\rho_{h,i}$ - 500 values (A total of 1500 tabulated values). The cut-off distance was 4.95 Angstroms (Hwang et al, 2004). (There are no available EAM potential parameters between Cu and C atoms).

$$V_{ij}(r_{ij}) = \frac{Z^2(r_{ij})}{r_{ij}} \quad (4.1)$$

The simulation and the cutting forces are shown in Table 4.2. The potential energy and the total energy for the EAM modelling and the temperature variation are shown in Table 4.3.

For a more realistic situation, another simulation (Figure 4.2) was also carried out with EAM potentials for the Cu-Cu interactions (with parameters same as above) and Morse potential parameters for the Cu-C interactions. The Morse parameters used are below,

$$D = 0.087\text{eV}, \alpha = 0.17(\text{nm})^{-1}, r_e = 0.22\text{nm}$$

The comparison of potential energy in the two simulations (EAM and the EAM-Morse) shows that the error or difference is very minimal (Figure 4.3). Since, the forces are derived from the potential energy, the difference in the cutting forces will also be small.

Results and Discussion

For the LJ model, the potential energy and total energy were initially unstable, but stabilized after 60000steps, also, the potential energy was initially high but reduced considerably to around -5200eV, towards the end of the simulation at 100000steps (Table 4.2 – LJ and Figure 4.5); the tangential component of cutting forces varied in the range from around -354E-9N to 346E-9N with an average of -1.33E-9N (eV/Angs = 1.602×10^{-9} N); the phenomenon of ploughing was not observed. As observed in (Table 4.2 – LJ), the copper atoms behave more like gases rather than solids, as they do not show the cohesiveness in solids – they loosely move around. The temperature variation shows a slight average decrease with the increase in the number of simulation steps. For the Morse model, the potential energy and total energy fluctuate initially and stabilize after 80000steps, also, the potential is higher than for the EAM potential (Figure 4.5); the tangential component of cutting forces are in the range from around -5.62E-9N to 70.51E-9N with an average of 37.34E-9N; the phenomenon of ploughing was observed with pile-up of 4 layers of atoms. The temperature variation shows a slight average increase with the increase in the number of simulation steps. The atoms behave as in solids – bonded together. For the EAM model, the potential energy and total energy were relatively stable, also, the potential energy is lower compared with the Morse potential; the tangential component of cutting forces are in the range from around -6.74E-9N to 58.2E-9N with an average of 24.99E-9N; the phenomenon of ploughing was observed, with pile-up of 5 layers of atoms. The temperature variation shows a slight average increase with the increase in

the number of simulation steps. The atoms behave as in solids – bonded together, similar to what was observed for the Morse potential. The ratio between the tangential, lateral and the normal components of the cutting forces is similar to that found in conventional machining for the Morse and the EAM potentials. The results of the EAM model are comparable with reported results (Pei et al 2006, Promyoo et al, 2008), that the EAM potential best describes the metallic bonding in the copper atoms. In contrast, the pair potentials (both LJ and Morse potentials), do not incorporate the many-body effects; they have no environmental dependence and they do not account for the directional nature of bonding in metals (Li et al, 2008).

Table 4.1: Comparison of the Different Simulations with Different Potentials showing the Cutting Forces

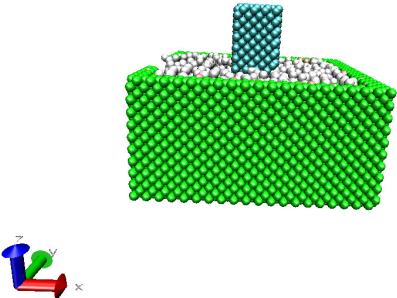
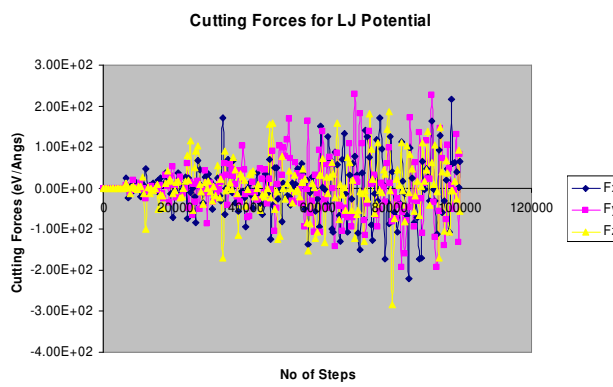
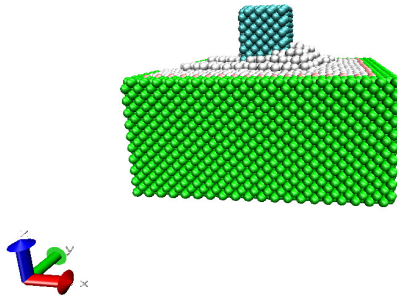
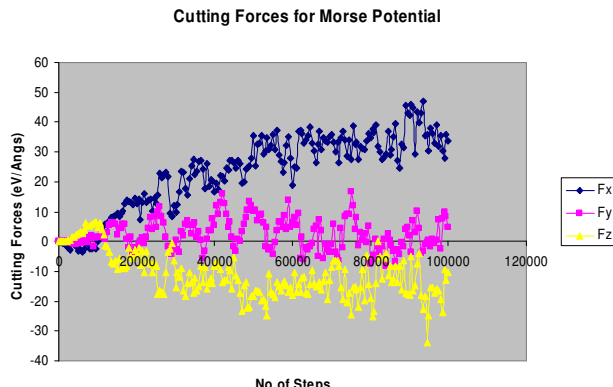
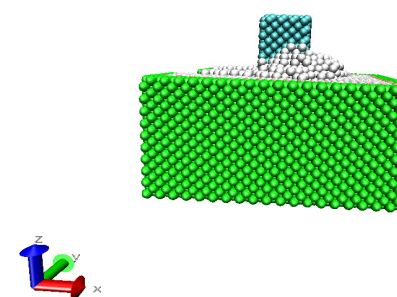
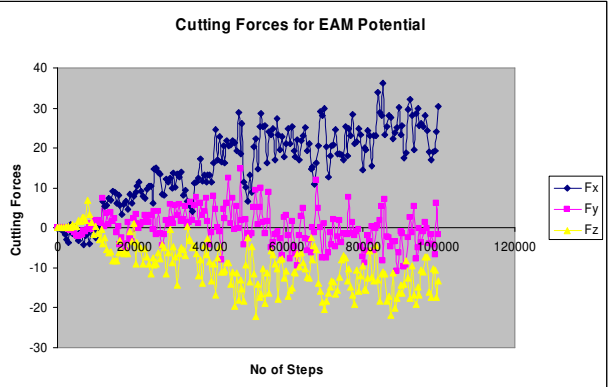
Potential	Simulation	Cutting Forces
LJ		
Morse		
EAM		

Table 4.2: Comparison of the Different Simulations with Different Potentials showing the Energies and the Temperature Variation

Potential	Potential and Total Energies	Temperature Variation
LJ	<div> <div> <div>Potential and Total Energies for LJ Potential</div> </div> <div> <div>Temperature Variation for LJ Potential</div> </div> </div>	
Morse	<div> <div>Potential and Total Energies for Morse Potential</div> </div> <div> <div>Variation of Temperature for Morse Potential</div> </div>	
EAM	<div> <div>Potential and Total Energies for EAM Potential</div> </div> <div> <div>Variation of Temperature for EAM Potential</div> </div>	

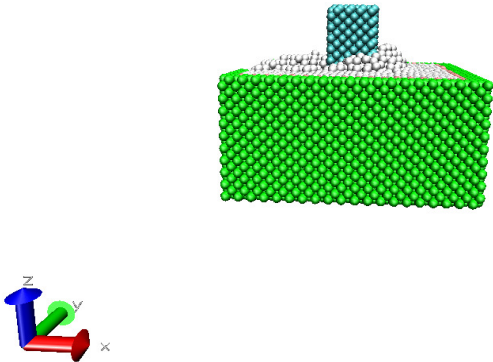


Figure 4.2: Simulation with EAM-Morse Potentials

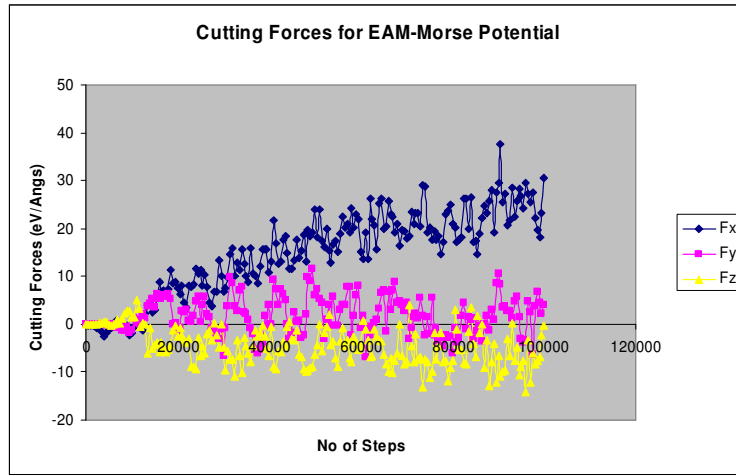


Figure 4.3: Cutting Forces for EAM-Morse Potential

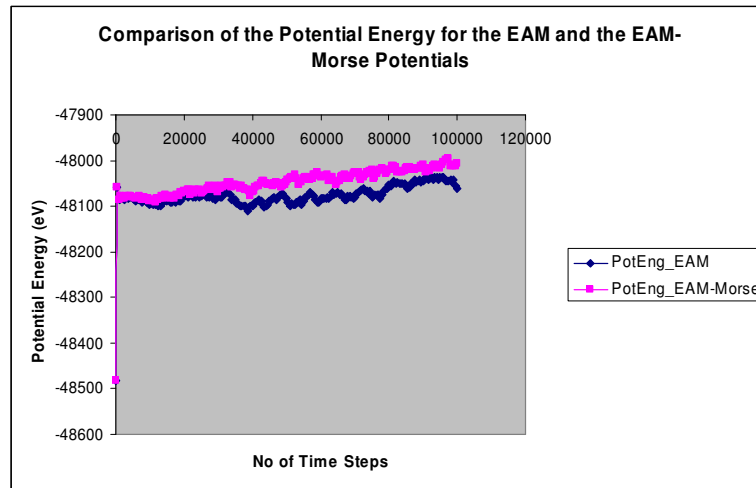


Figure 4.4: The Comparison of the Potential Energy for the EAM and the EAM-Morse Potentials

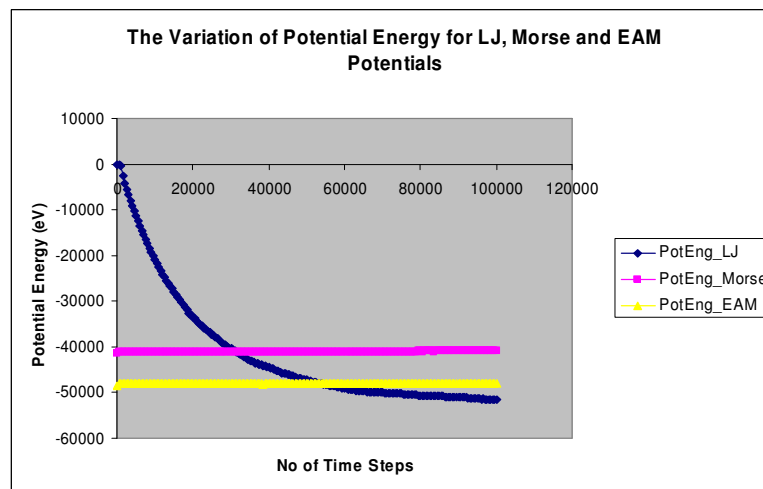


Figure 4.5: The Variation of Potential Energies for the LJ, Morse and EAM Potentials

4.1.5 Conclusion

Through this investigation, it is identified that the EAM potential is the most appropriate of the 3 potentials commonly used for the modelling of nanomachining of copper with diamond tool. The choice of the best potential is based on the cutting forces and the potential energy. The EAM potential provides the best description of the metallic bonding in the workpiece, also, the cutting forces variation is smallest; the potential and total energies fluctuations are least for the depth of cut considered. Therefore, the EAM potential should be used, rather than LJ and Morse potentials for the modelling of copper and other fcc metals in MD simulations of nanomachining.

For more realistic simulation, the interface between copper and carbon atoms should be modelled by a suitable potential; and the Morse potential more suitable than the EAM potential. So, technically the EAM-Morse is better than the singly EAM potential for the overall modelling.

4.2. Choosing Appropriate Interatomic Potentials for Nanomachining MD Simulations

4.2.1 Introduction

To extend the previous study in 4.1, different potentials were considered for different interfaces and comparisons were made between assuming the tool to be rigid and deformable. For the MD simulation results to be useful in the prediction of experimental data, the interactions between atoms are to be modelled with suitable empirical potentials. In many MD simulations, the tool has been modelled as a block/body of stiff atoms, undeformable. The dynamics of the tool is not considered, but only its impact on the workpiece atoms. Other reported studies usually use the Morse potential to model the interatomic forces between metal atoms. For more realistic modelling, each material requires its own material-specific interatomic potential and the each material interface (atomic interactions) requires suitable interatomic potentials.

For the simulations in this study, 6 different cases were considered, which are shown below;

Case 4.2.1: The Cu-Cu interactions were modelled by Morse, the Cu-C interactions were modelled by Morse potential and the tool was assumed to be rigid.

Case 4.2.2: The Cu-Cu interactions were modelled by Morse, the Cu-C interactions were modelled by Morse potential and the tool was assumed to be non-rigid.

Case 4.2.3: The Cu-Cu interactions were modelled by EAM, the Cu-C interactions were modelled by Morse potential and the tool was assumed to be rigid.

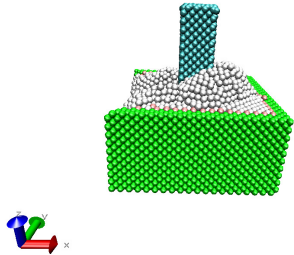
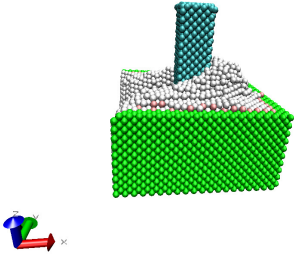
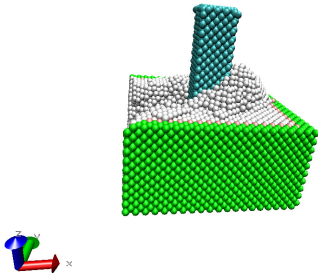
Case 4.2.4: The Cu-Cu interactions were modelled by EAM, the Cu-C interactions were modelled by Morse potential and the tool was assumed to be non-rigid.

Case 4.2.5: The Cu-Cu interactions were modelled by EAM, the Cu-C interactions were modelled by LJ potential and the tool was assumed to be rigid.

Case 4.2.6: The Cu-Cu interactions were modelled by EAM, the Cu-C interactions were modelled by LJ potential and the tool was assumed to be non-rigid.

The simulation parameters of Table 3.5 were used for the simulations with a depth of cut of 2nm. The non-rigid tool was model with Tersoff potential as given in Table 3.6.

Table 4.3: Comparison of the Different Simulations with Different Potentials Combinations and Rigid/Non rigid Tool

Interatomic Potentials	Tool (Rigid or Deformable)	Simulation (Material Removal)
Cu-Cu Interaction: Morse Cu-C Interaction: Morse (Case 4.2.1)	Rigid	
Cu-Cu Interaction: Morse Cu-C Interaction: Morse (Case 4.2.2)	Deformable	
Cu-Cu Interaction: EAM Cu-C Interaction: Morse (Case 4.2.3)	Rigid	

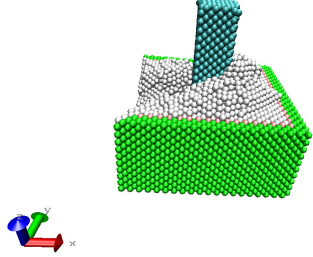
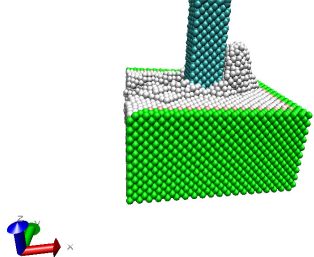
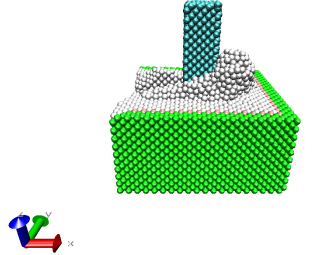
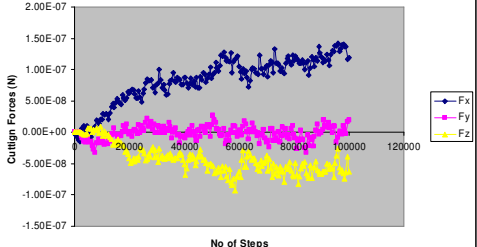
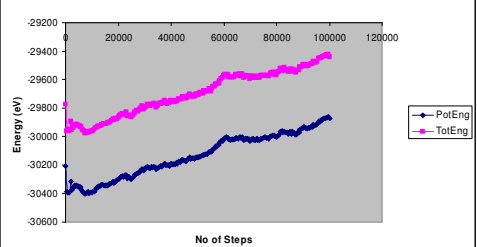
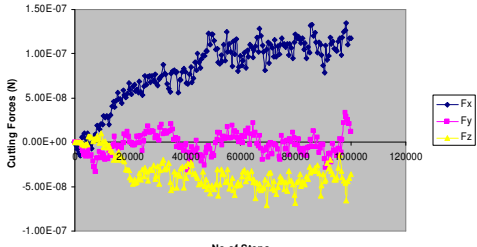
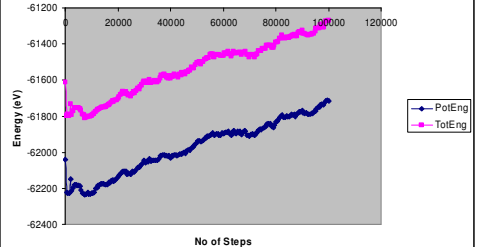
Cu-Cu Interaction: EAM Cu-C Interaction: Morse (Case 4.2.4)	Deformable	
Cu-Cu Interaction: EAM Cu-C Interaction: LJ (Case 4.2.5)	Rigid	
Cu-Cu Interaction: EAM Cu-C Interaction: LJ (Case 4.2.6)	Deformable	

Table 4.4: Comparison of the Different Simulations (6 Cases) showing Cutting Forces and the Energies

Simulation Cases	Cutting Forces	Potential and Total Energies
Case 4.2.1	<p>Cutting Forces for Morse-Morse Potentials (Rigid Tool)</p> 	<p>Potential and Total Energies for Morse-Morse Potentials (Rigid Tool)</p> 
Case 4.2.2	<p>Cutting Forces for Morse-Morse Potentials (Non Rigid Tool)</p> 	<p>Potential and total Energies for Morse-Morse (Non-Rigid Tool)</p> 

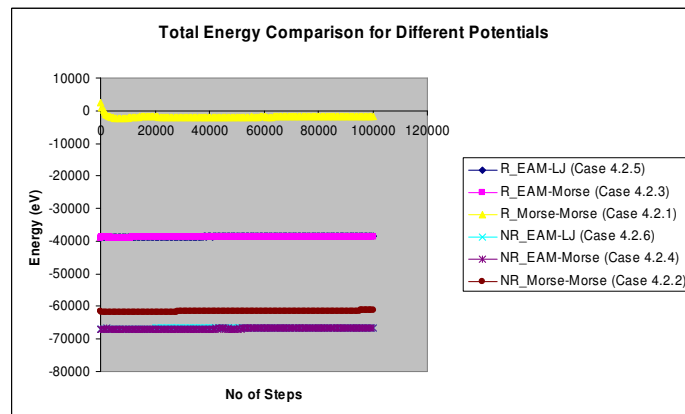
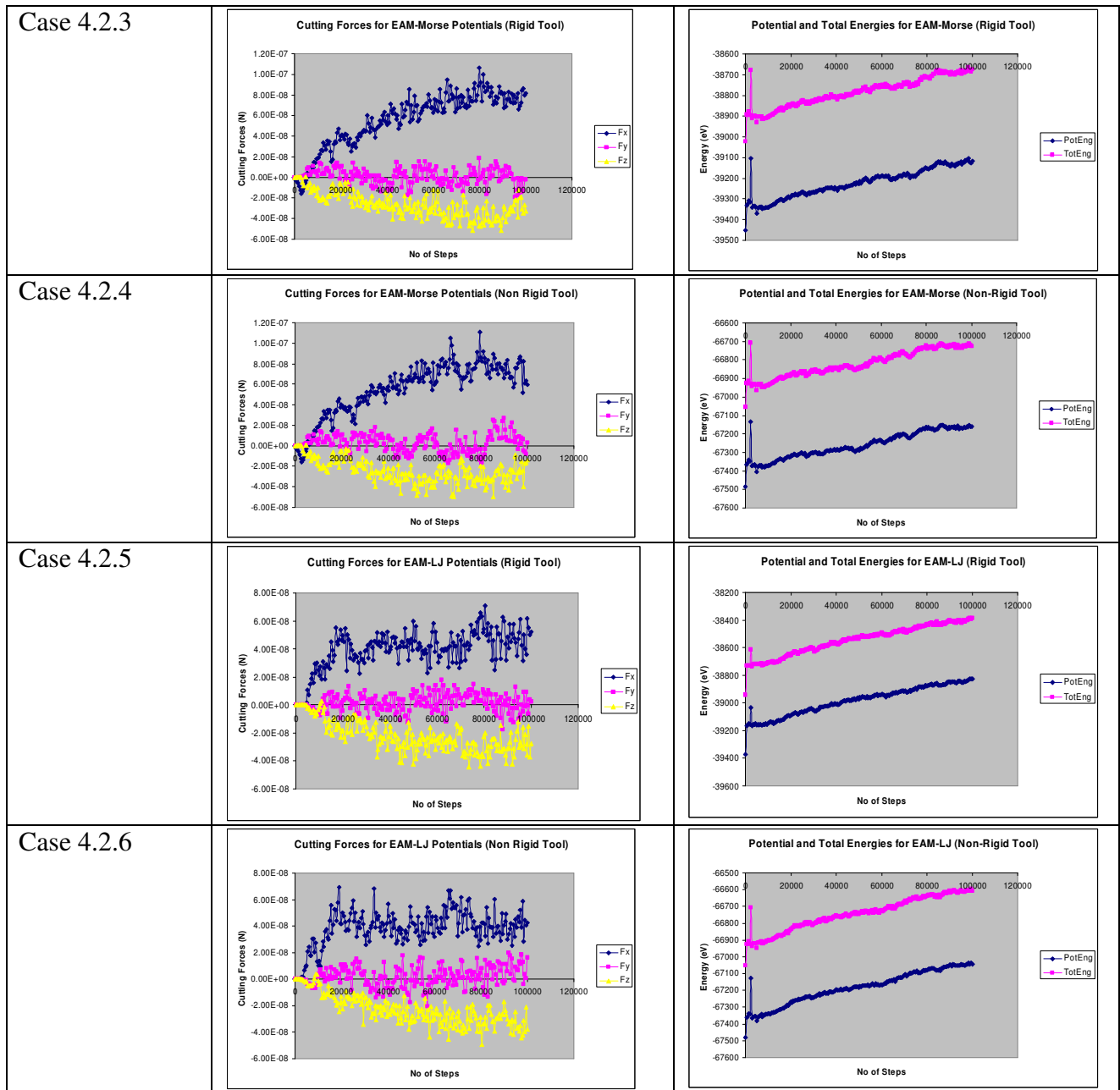


Figure 4.6: Comparison of the Total Energy for the Different Potential Pairs (both Rigid and Non-Rigid Tools)

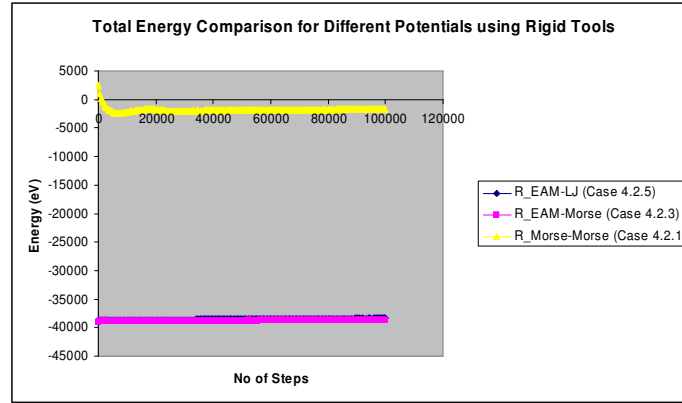


Figure 4.7: Comparison of the Total Energy for the Different Potential Pairs (Rigid Tool)

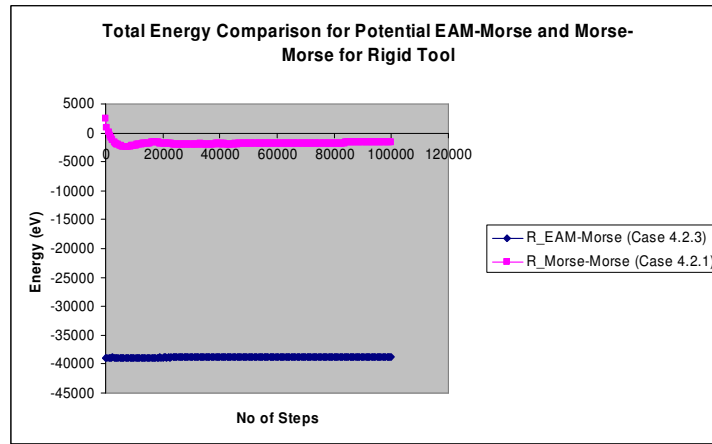


Figure 4.8: Comparison of the Total Energy for Potential Pairs EAM-Morse and Morse-Morse (Rigid Tools)

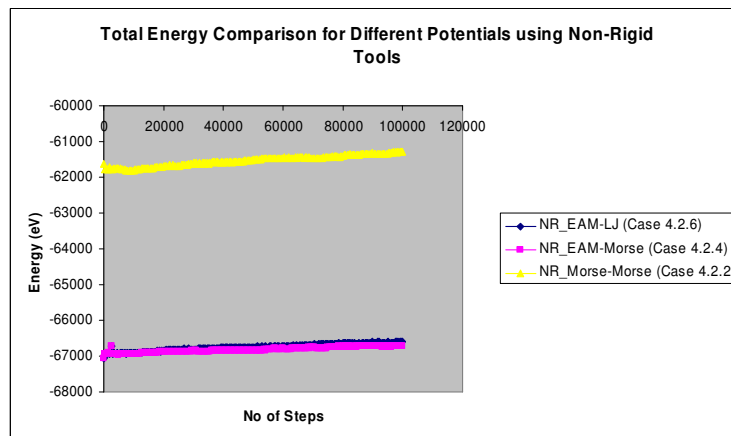


Figure 4.9: Comparison of the Total Energy for the Potential Pairs (Non-Rigid Tool)

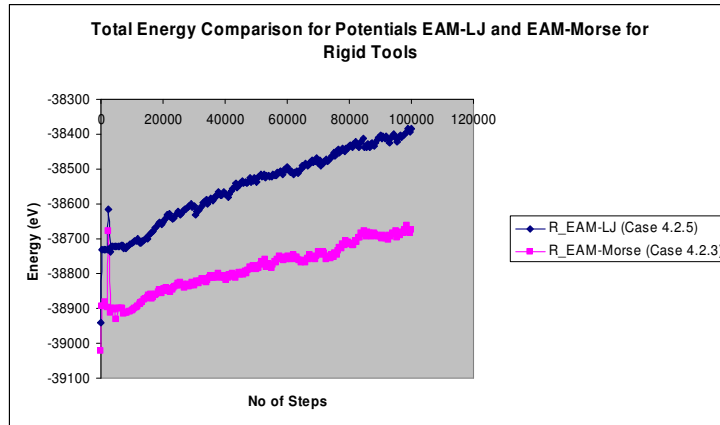


Figure 4.10: Comparison of the Total Energy for Potential Pairs EAM-LJ and EAM-Morse (Rigid Tools)

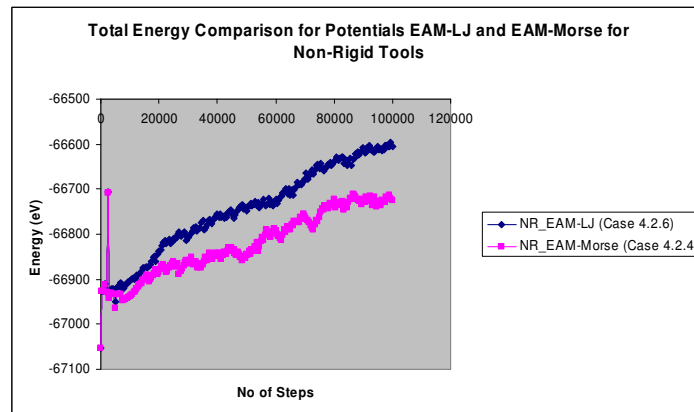


Figure 4.11: Comparison of the Total Energy for Potential Pairs EAM-LJ and EAM-Morse (Non-Rigid Tools)

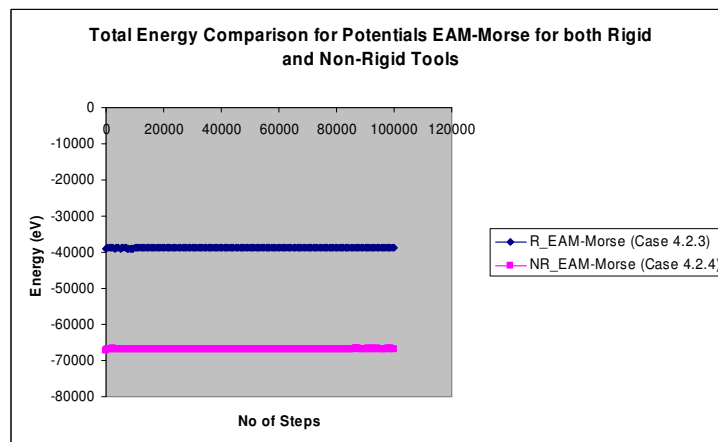


Figure 4.12: Comparison of the Total Energy for Potential Pair EAM-Morse (Rigid and Non-Rigid Tools)

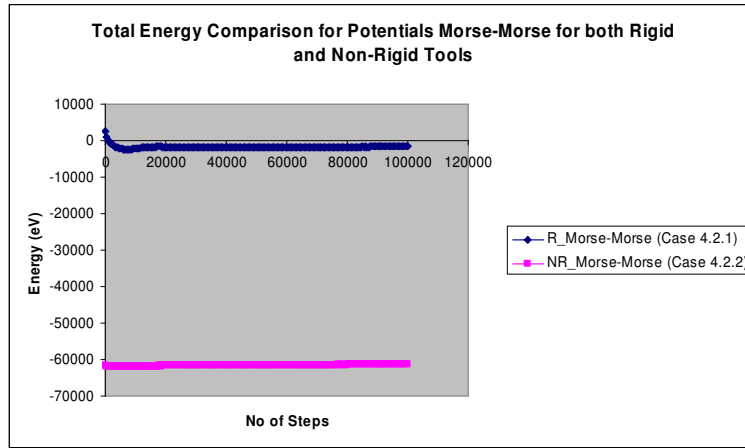


Figure 4.13: Comparison of the Total Energy for Potential Pair Morse-Morse (Rigid and Non-Rigid Tools)

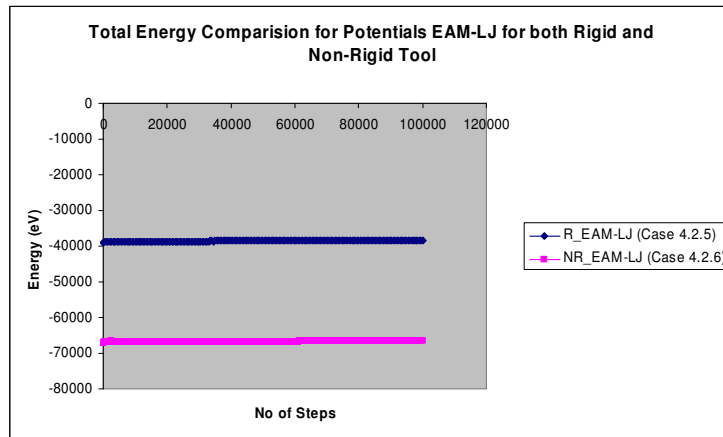


Figure 4.14: Comparison of the Total Energy for Potential Pair EAM-LJ (Rigid and Non-Rigid Tools)

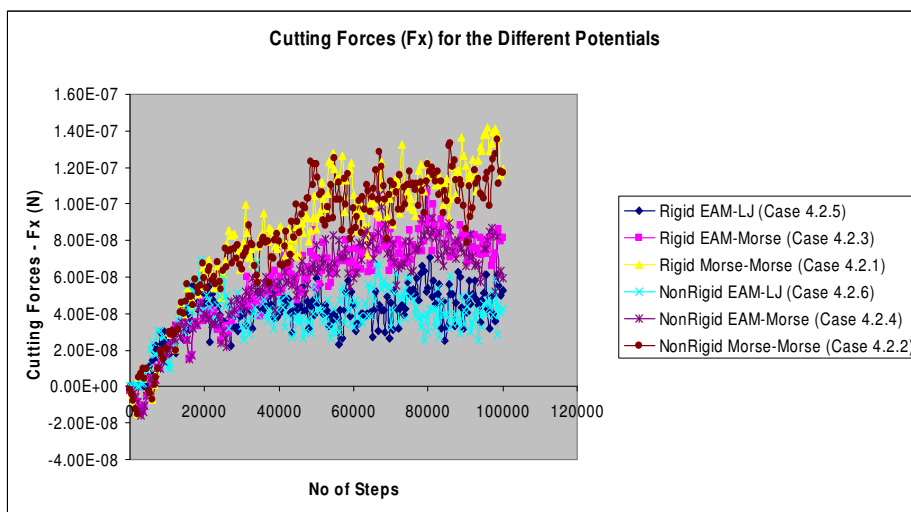


Figure 4.15: The Tangential Component of the Cutting Forces for the Different Pairs of Potentials

Table 4.5: Forces and Total Energies Comparison for the Different Potential Pairs

Potentials	Case Number	Average Cutting Forces (N)	F_x/F_z	Total Energy (eV)
Morse-Morse (Rigid Tool)	Case 4.2.1	8.33878E-08	1.945	-29698.95682
Morse-Morse (Non-Rigid Tool)	Case 4.2.2	8.10952E-08	2.383	-61538.24872
EAM-Morse (Rigid Tool)	Case 4.2.3	5.58455E-08	2.113	-38786.89569
EAM-Morse (Non-Rigid Tool)	Case 4.2.4	5.51902E-08	2.258	-66822.78799
EAM-LJ (Rigid Tool)	Case 4.2.5	3.94834E-08	1.800	-38548.82619
EAM-LJ (Non-Rigid Tool)	Case 4.2.6	3.84535E-08	1.681	-66747.00457

Discussions

Table 4.3 shows the chip formation after the simulation for the six cases. It can be observed that build-ups of atoms are more pronounced for the cases with EAM-LJ and EAM-Morse (for both rigid and non-rigid tools). However, atoms appear more loosely bonded together for the Morse-Morse pair cases. This shows that the EAM potential better models the Cu-Cu interactions than the Morse potential. Table 4.4 shows the cutting forces and the potential and total energies for the six cases. The total energy greatly reduced for the simulations with non-rigid tool. The total energy for the different potentials are compared in Figure 4.6. and with reference to Table 4.5 shows the EAM-Morse potential pair with non-rigid tool has the lowest energy.

A comparison of the cutting forces for all the cases are shown in Figure 4.14. The cutting forces and the ratio of the tangential force component to the normal force component, F_x/F_z are lowest for the EAM-LJ potential pair (for the rigid and non-rigid tool); see also Table 4.5. The cutting forces appear more stable after the initial 20000 steps. Figures 4.7 and 4.8 show the comparison of the total energy for the different potentials, with the rigid tool and the non-rigid tool respectively. Figures 4.9 and 4.10 show the total energy for the potential pairs EAM-LJ and EAM-Morse for rigid tool and non rigid tool respectively. Figures 4.11-4.13 show the comparison of each of the potential pairs for both rigid and non-rigid tools. Comparing the potential pairs based on the cutting forces, the EAM-LJ with the non-rigid tool is the best and comparing based on the potential energy, the EAM-Morse with the non-rigid tool is the best.

4.2.2 Conclusion

From the above observations, the EAM-LJ potential pair has the lowest average tangential cutting force component and the lowest force ratio. The EAM-Morse pair on the other hand has the lowest energy value of all the cases. The EAM-Morse pair may be the most appropriate for the modelling, as verified in Chapters 6 and 7.

4.3. Determination of Minimum Depth Cut in Nanomachining

4.3.1 Introduction

MD simulation was conducted to evaluate the MDC in nanomachining of copper workpiece with a diamond tool. The workpiece consists of 43240 atoms with FCC copper lattice. It includes 3 kinds of atoms namely; boundary atoms, thermostat atoms and Newtonian atoms. The boundary atoms are kept fixed to reduce edge effects. The thermostat atoms conduct the heat generated during the cutting process out of the workpiece and the Newtonian atoms obey the Newton's equation of motion and so are free to move. The tool consists of 10992 atoms with diamond lattice structure, and it is modelled as a deformable, non-rigid body.

The atomic interactions in the simulation are the following, namely;

Cu-Cu : interactions between copper atoms

Cu-C : interactions between copper atoms and diamond atoms

C-C : interactions between the diamond atoms

Three potential pairs were used for the Cu-Cu and the Cu-C interactions namely; Case 4.3.1: Morse-Morse, Case 4.3.2: EAM-Morse and Case 4.3.3: EAM-LJ. For all the cases, the C-C (tool atoms) interactions were modelled by Tersoff potential and the simulations were carried out with the variation of the depth of cut from 0.01nm to 4 nm.

4.3.2. The Effect of Interatomic Potentials on the Evaluation of the Minimum Depth Cut in Nanomachining

Case 4.3.1:

The Morse potential was used for the Cu-Cu and the Cu-C interactions. The following parameters were used.

For Cu-Cu interactions: (Girifalco and Weizer1959, Pei et al 2006)

$$D = 0.3429eV, \alpha = 0.13588(nm)^{-1}, r_e = 0.2866nm$$

For Cu-C interactions: (Hwang et al 2004)

$$D = 0.087\text{eV}, \alpha = 0.17(\text{nm})^{-1}, r_e = 0.22\text{nm}$$

Case 4.3.2:

The EAM potential was used for the Cu-Cu interactions and the Morse potential was used for the Cu-C interactions.

The potential parameters used for the Cu-Cu interactions were read from the file - Cu_u3.eam in LAMMPS. The file contains the following, namely; the lattice constant of copper (3.615 Angstroms), the spacing in density (5.01E-4) and the spacing in distance (1.00E-2). Also, it contains three arrays of tabulated values of the embedding function, $G_i(\rho_{h,i})$ -500 values; effective charge function, Z_{ij} ,- 500 values, from which the pair potential interaction is calculated (the relationship between the effective charge and the pair potential is given by the equation $V_{ij}(r_{ij}) = \frac{Z^2(r_{ij})}{r_{ij}}$ and the density function, $\rho_{h,i}$ - 500 values (A total of 1500 tabulated values). The cut-off distance was 4.95 Angstroms.

For Cu-C interactions: (Hwang et al 2004)

$$D = 0.087\text{eV}, \alpha = 0.17(\text{nm})^{-1}, r_e = 0.22\text{nm}$$

Case 4.3.3:

The EAM potential was used for the Cu-Cu interactions and the LJ potential was used for the Cu-C interactions.

The parameters used for the EAM potential are the same as in case 4.3.2.

The parameters used for the Cu-C interfaces are below, with a cut-off distance of 2.5 Angstroms;

$$\varepsilon = 0.4096\text{eV}, \sigma = 2.338 \text{ Angstroms}$$

For the C-C interactions, the Tersoff potential parameters used are in the following Table 4.

The other simulation parameters used are given in Table 3.2

Simulation Results and Discussions

The simulation results for the three cases, for the variation of the depth of cut (0.01 – 4nm) are shown in Table C.1. Also, the comparison of the cutting forces, the potential and total energies and

the temperature distribution are shown in Tables C.2, C.3 and C.4 respectively. The summary of the results and comments are given in Tables 4.6 and 4.7. It can be observed that the choice of interatomic potentials for the atomic interactions affects the evaluation of the minimum depth cut in nanomachining. The MD simulation results show that from the depth cut of 0.01 to 0.15nm, rubbing phenomena are observed for all the 3 cases; where no atoms are moved from their original positions after the tool cuts through them. But, sometimes some atoms at the edge of the surface are knocked off. For Case A, ploughing initiates at the depth of cut of 0.25nm with a pile-up of a layer of atoms; for Case B, ploughing starts at the depth of cut of 0.20nm and for Case C, ploughing starts from 0.30nm. It has been suggested that from theory, chip formation/cutting starts when the tangential cutting force component, F_x is greater than the normal cutting force component, F_z . This is clearly visible in Case C, where chip formation starts at the depth of cut of 1.5nm. For Cases B and C, these are also seen, but they are not readily clear when compared to the shapes of the chip.

In Figure 4.15, the variation of the tangential cutting force component, F_x with depth of cut for the three cases are shown. The F_x is smallest for Case 4.3.3 – EAM-LJ pair, then for Case 4.3.2 – EAM-Morse and largest for Case 4.3.1 – Morse-Morse. Similarly, the variation of the normal cutting force component, F_z with depth of cut for all the three cases are shown in Figure 4.16. The magnitude of F_z is smallest for Case 4.3.3 – EAM-LJ pair, then for Case 4.3.2 – EAM-Morse and largest for Case 4.3.1 – Morse-Morse. Figure 4.17 shows the variation of the lateral cutting force component, F_y with depth of cut for completion. Theoretically, these should be zero, but due to atomic vibrations there are some fluctuations. Figures 4.18 to 4.21 show the variation of the potential and the total energies with depth of cut for the three cases. The potential and total energies are lowest for Case 4.3.2. However the variation of the kinetic energy with depth of cut for the three cases show similar results in Figure 4.22.

Using a different approach of using the force ratio (F_x/F_z) to predict the phenomena of rubbing, ploughing and cutting (Table 4.8): for the Morse-Morse pair, there is a transition at the depth of cut of 0.1nm; for the EAM-Morse pair, there is a transition at the depth of cut of 0.2; and for the EAM-LJ pair, there is a transition at the depth of cut of 1.5nm. For the Morse-Morse pair the transition may be from rubbing to ploughing and this may also be the case for the EAM-Morse pair. The transition for the EAM-LJ pair may be from ploughing to cutting. These observations may need some experimental validations to confirm. The particularly high values of the force ratio for Morse-Morse: depth of cut-0.15nm; EAM-Morse: depth of cuts-0.3nm and 0.45nm may be due to high friction or problems of size effects. Also, there are exceptional high values for EAM-LJ: depth of

cuts-0.01nm and 0.03nm, which may be due to high frictions are the way the pair of potentials model the interface for very low depth of cut.

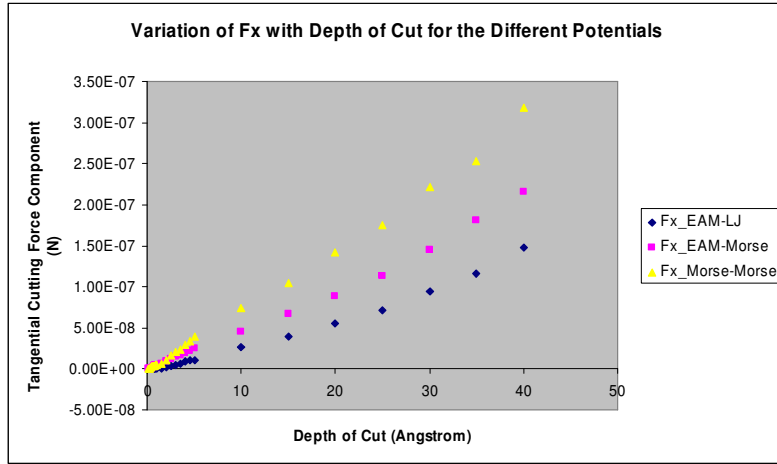


Figure 4.16: Variation of the Tangential Cutting Force with Depth of Cut for the Potential Pairs

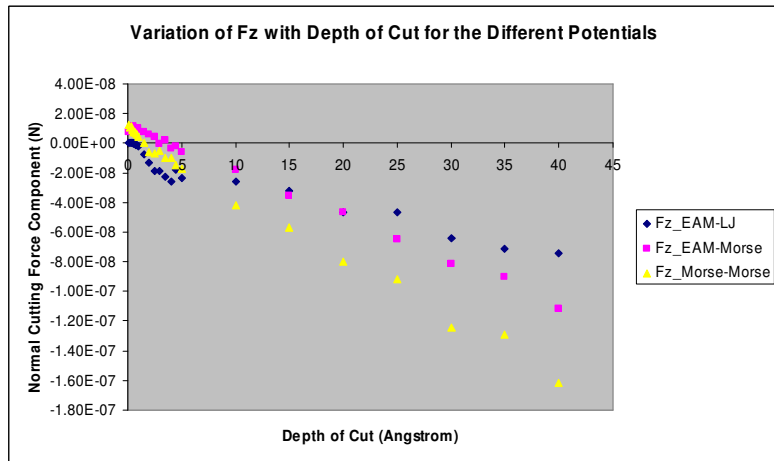


Figure 4.17: Variation of the Normal Cutting Force with Depth of Cut for the Potential Pairs

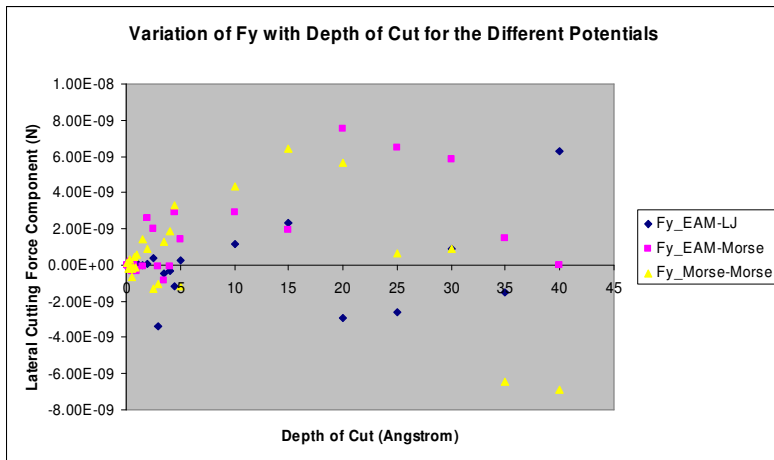


Figure 4.18: Variation of the Lateral Cutting Force with Depth of Cut for the Potential Pairs

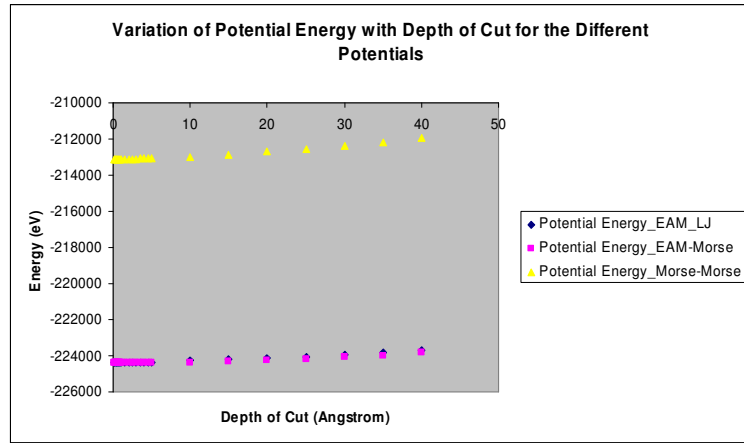


Figure 4.19: Variation of the Potential Energy with Depth of Cut for the Potential Pairs

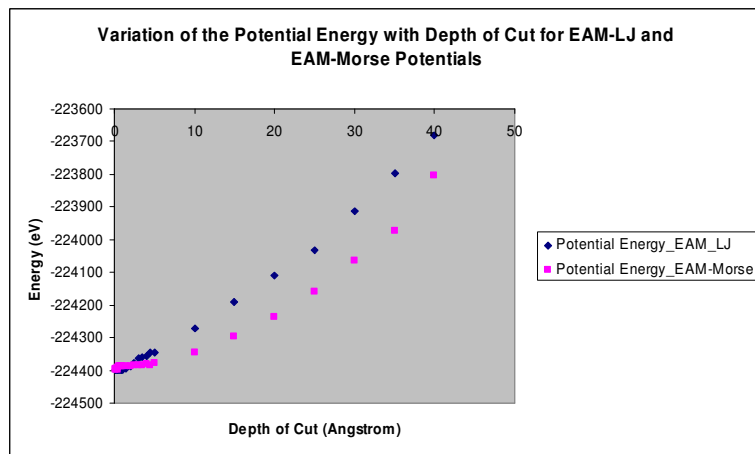


Figure 4.20: Variation of the Potential Energy with Depth of Cut for the EAM-LJ and EAM-Morse Potential Pairs

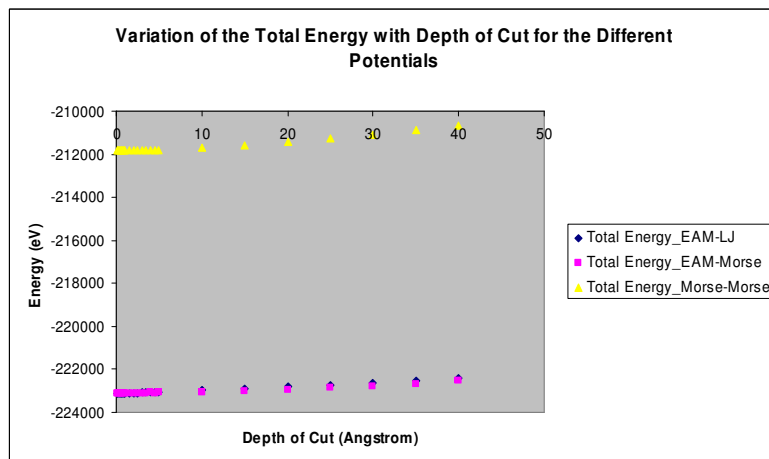


Figure 4.21: Variation of the Total Energy with Depth of Cut for the Potential Pairs

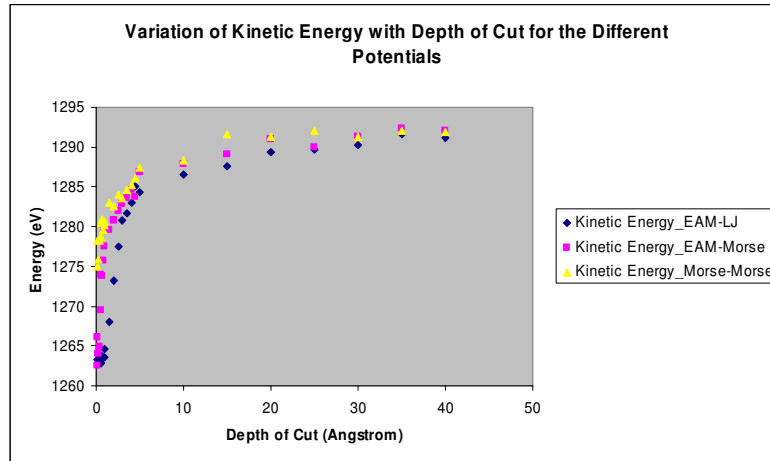


Figure 4.22: Variation of the Kinetic Energy with Depth of Cut for the Potential Pairs

Table 4.6: Summary on Minimum Depth Cut

Depth of Cut (nm)	Build-up/Pile-up Phenomena	Build-up/Pile-up Phenomena	Build-up/Pile-up Phenomena
	Morse-Morse (Case 4.3.1)	EAM-Morse (Case 4.3.2)	EAM-LJ (Case 4.3.3)
0.00	None	None	None
0.01	None	None	None
0.02	None	None	None
0.03	None	None	None
0.04	None	None	None
0.05	None	None	None
0.06	None	None	None
0.07	None	None	None
0.08	None	None	None
0.09	None	None	None
0.10	None	None	None
0.15	None	None	None
0.20	None	No pile-up atoms, but side atoms	None
0.25	One layer of atoms	One to two layers of atoms	None
0.30	Up to two layers of atoms	Two layers of atoms	One layer of atoms
0.35	Two layers of atoms (More)	Two layers of atoms (More)	One layer of atoms
0.40	Three layers of atoms	Three layers of atoms	Three layers of atoms
0.45	Three layers of atoms	Four layers of atoms	Two layers of atoms
0.50	Four layers of atoms	Four layers of atoms	Two layers of atoms
1.00	Six layers of atoms	Seven layers of atoms	Six layers of atoms
1.50	Eight layers of atoms	Eight layers of atoms	Ten layers of atoms
2.00	Ten layers of atoms	Twelve layers of atoms	Thirteen layers of atoms
2.50	Ten layers of atoms	Thirteen layers of	Sixteen layers of atoms

		atoms	
3.00	Eleven layers of atoms	Fifteen layers of atoms	Eighteen layers of atoms
3.50	Fourteen layers of atoms	Seventeen layers of atoms	Twenty six layers of atoms
4.00	Sixteen layers of atoms	Seventeen layers of atoms	Twenty Three layers of atoms

**Table 4.7: Comments on the Minimum Depth Cut Simulation
(By Observation of the Chip Formation)**

Depth of Cut (nm)	Comments on the onset of Ploughing and Cutting	Comments on the onset of Ploughing and Cutting	Comments on the onset of Ploughing and Cutting
	<i>Morse-Morse (Case 4.3.1)</i>	<i>EAM-Morse (Case 4.3.2)</i>	<i>EAM-LJ (Case 4.3.3)</i>
0.00	Rubbing/Elastic deformation	Rubbing/Elastic deformation	Rubbing/Elastic deformation
0.01	Rubbing/Elastic deformation	Rubbing/Elastic deformation	Rubbing/Elastic deformation
0.02	Rubbing/Elastic deformation	Rubbing/Elastic deformation	Rubbing/Elastic deformation
0.03	Rubbing/Elastic deformation	Rubbing/Elastic deformation	Rubbing/Elastic deformation
0.04	Rubbing/Elastic deformation	Rubbing/Elastic deformation	Rubbing/Elastic deformation
0.05	Rubbing/Elastic deformation	Rubbing/Elastic deformation	Rubbing/Elastic deformation
0.06	Rubbing/Elastic deformation	Rubbing/Elastic deformation	Rubbing/Elastic deformation
0.07	Rubbing/Elastic deformation	Rubbing/Elastic deformation	Rubbing/Elastic deformation
0.08	Rubbing/Elastic deformation	Rubbing/Elastic deformation	Rubbing/Elastic deformation
0.09	Rubbing/Elastic deformation	Rubbing/Elastic deformation	Rubbing/Elastic deformation
0.10	Rubbing/Elastic deformation	Rubbing/Elastic deformation	Rubbing/Elastic deformation
0.15	Rubbing/Elastic deformation	Rubbing/Elastic deformation	Rubbing/Elastic deformation
0.20	Rubbing/Elastic deformation	Ploughing starts	Rubbing/Elastic deformation
0.25	Ploughing starts	Ploughing	Rubbing/Elastic deformation
0.30	Ploughing	Ploughing	Ploughing starts
0.35	Ploughing	Ploughing	Ploughing
0.40	Ploughing	Ploughing	Ploughing
0.45	Ploughing	Ploughing	Ploughing

0.50	Ploughing	Ploughing	Ploughing
1.00	Ploughing	Ploughing	Ploughing
1.50	Not sure	Not sure	Chip formation/Cutting starts
2.00	Not sure	Not sure	Cutting
2.50	Not sure	Not sure	Cutting
3.00	Not sure	Not sure	Cutting
3.50	Not sure	Not sure	Cutting
4.00	Not sure	Not sure	Cutting

Table 4.8: Force Ratio (F_x/F_z) Tangential Force Component/Normal Force Component for the Different Potentials

Depth of Cut (nm)	Morse-Morse (Case 4.3.1)	EAM-Morse (Case 4.3.2)	EAM-LJ (Case 4.3.3)
0.01	0.04829	0.007444	<i>1.073072</i>
0.02	0.095067	0.046829	0.824648
0.03	0.105248	0.017279	<i>1.950004</i>
0.04	0.245986	0.021446	0.020337
0.05	0.378409	0.06574	0.077502
0.06	0.423499	0.131955	0.025004
0.07	0.443842	0.232347	0.032497
0.08	0.605915	0.354004	0.054916
0.09	0.791126	0.538339	0.062184
0.10	1.027395	0.467178	0.086716
0.15	56.41053	0.844059	0.106155
0.20	1.682874	1.7182	0.123895
0.25	2.371085	2.76516	0.164905
0.30	3.847903	38.84269	0.259996
0.35	2.306841	9.556566	0.289789
0.40	2.867722	5.249375	0.347683
0.45	2.279018	10.35213	0.576208
0.50	2.21402	4.273372	0.465918
1.00	1.751497	2.561116	0.996866
1.50	1.842891	1.90825	1.200217
2.00	1.773755	1.904111	1.183491
2.50	1.900488	1.759073	1.551487
3.00	1.773196	1.766835	1.464213
3.50	1.960791	2.010869	1.630837
4.00	1.969789	1.927434	1.98491

4.3.3 Prediction of the Onset of Plasticity

Similarly, if the focus is on the prediction of the onset of plasticity; ploughing starts from 0.1-0.3nm. For Case 4.3.1, ploughing initiates at the depth of cut of 0.25nm with a pile-up of a layer of atoms; for Case 4.3.2, ploughing starts at the depth of cu of 0.20nm and for Case 4.3.3, ploughing starts from 0.30nm. In Figure 4.16, the variation of the tangential cutting force component, F_x with depth of cut for the three cases are shown. The F_x is smallest for Case 4.3.3 – EAM-LJ pair, then for Case 4.3.2 – EAM-Morse and largest for Case 4.3.1 – Morse-Morse.

Using the force ratio (F_x/F_z) to predict the phenomena of the incipient of plastic deformation, (Table 3): for the Morse-Morse pair, there is a transition at the depth of cut of 0.1nm; for the EAM-Morse pair, there is a transition at the depth of cut of 0.2nm; and for the EAM-LJ pair, there is a transition at the depth of cut of 1.5nm. For the Morse-Morse and EAM-Morse pairs, the transition may be from rubbing to ploughing, whereas it may be from ploughing to cutting for the EAM-LJ pair. The high value for the Case 1 (depth of cut of 0.15nm) may be due to friction or problem of size effects.

4.3.4 Conclusion

From the MD simulation results, the phenomena of rubbing, ploughing and cutting are observed. Ploughing starts from 0.1~0.3nm and the formation of chips starts to occur from the depth of cut thickness of 1.5nm. So it can be suggested that the extreme accuracy attainable or MDC for copper atoms workpiece, machined with extremely sharp diamond tool is around 1.5nm to 3nm. This is around the value of 1nm suggested by Ikawa et al [1], but the tool edge radius may affect the evaluation of this value. Also, it can be suggested that the onset of plasticity for copper atoms workpiece, machined with extremely sharp diamond tool is around 0.1nm to 0.3nm. The observation of the elastic-plastic transition is predicted differently by using using pile-up and material removal information; and the force ratio (F_x/F_z) information. These observations may need some time to be confirmed by experiments as current observations are not down to these length scales. The particularly high values of the force ratio for Morse-Morse: depth of cut-0.15nm; EAM-Morse: depth of cuts-0.3nm and 0.45nm may be due to high friction or problems of size effects.

4.4. The Effect of Tool Geometry on Rubbing and Ploughing in Nanomachining

4.4.1 Introduction

The selection of effective and optimal machining parameters is a major challenge for the manufacturing industries. The tool-work interactions may be affected by many process parameters including depth of cut, cutting speed, feed rate, cutting tool geometry et cetera. Proper selection of these parameters is critical in material removal processes. The effect of different geometric end shapes was investigated on the phenomena of rubbing and ploughing in nanomachining. The shapes used were flat, pointed, spherical and trapezoidal.

In the investigation, the workpiece consists of 16000 copper atoms with FCC lattice. It includes 3 types of atoms namely; boundary atoms, thermostat atoms and Newtonian atoms. The boundary atoms are kept fixed to reduce edge effects. The thermostat atoms conduct the heat generated during the cutting process out of the workpiece and the Newtonian atoms obey the Newton's equation of motion. The cutting tools consist of carbon atoms with diamond lattice structure and have varying number of atoms because of the different shapes. The flat end tool consists of 1824 atoms, the pointed end tool consists of 1936 atoms, the spherical end tool consists of 1839 atoms and the trapezoidal end tool consists of 1924 atoms. The different cutting tools were modelled as deformable, non-rigid bodies.

The atomic interactions in the simulation are the following, namely;

Cu-Cu : interactions between copper atoms

Cu-C : interactions between copper atoms and diamond atoms

C-C : interactions between the diamond atoms

The EAM potential was used for the Cu-Cu interactions and the LJ potential was used for the Cu-C interactions. All the C-C (tool atoms) interactions were modelled by using the Tersoff potential.

The parameters used for the EAM potential are the same as in section 4.3.

The parameters used for the Cu-C interfaces are below, with a cut-off distance of 2.5 Angstroms;

$$\varepsilon = 0.4096eV, \sigma = 2.338 \text{ Angstroms}$$

For the C-C interactions, the Tersoff potential parameters used are in the following Table 2.7 and other parameters are given in Table 3.5.

Different Tool Geometries

The tools shapes investigated in this study are shown in Figures 1-4, namely; the tools with spherical, flat, trapezoidal and pointed ends.

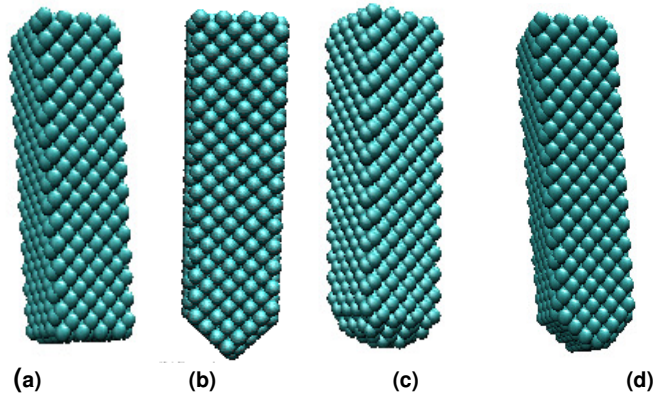


Figure 4.23: Different tool geometries; (a) Tool with flat end (b) Tool with pointed end, (c) Tool with spherical end, (d) Tool with trapezoidal end

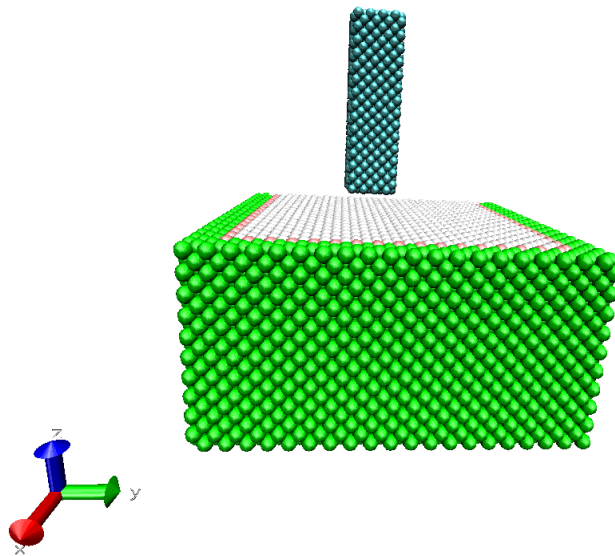


Figure 4.24: Tool with Flat End

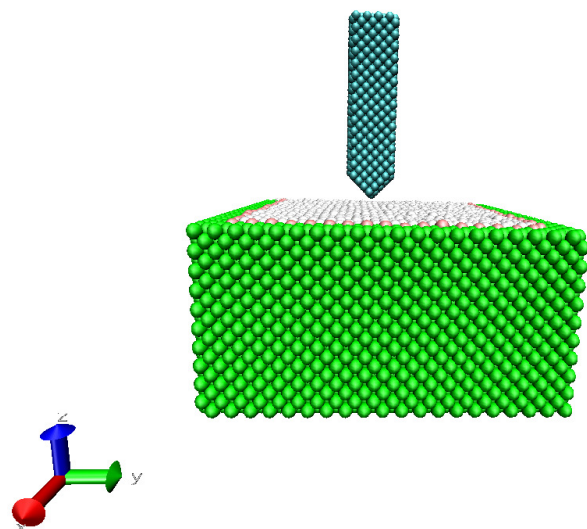


Figure 4.25: Tool with Pointed End

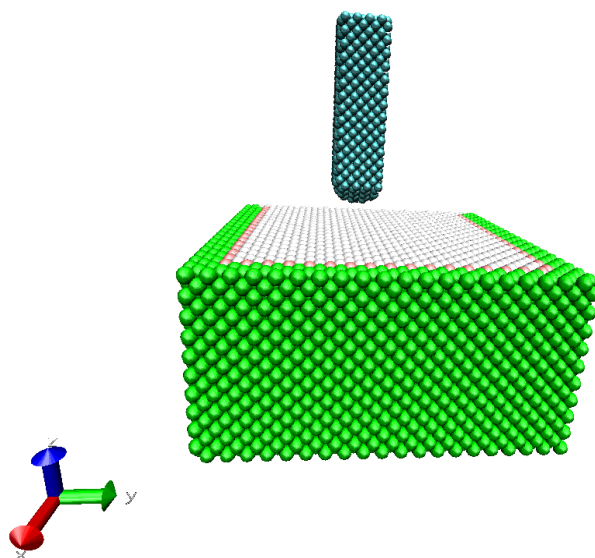


Figure 4.26: Tool with Spherical End

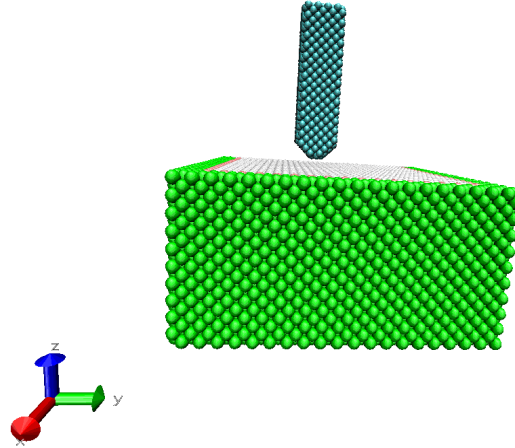


Figure 4.27: Tool with Trapezoidal End

The Morse potential was used and the other parameters used for the simulation are the following:

For Cu-Cu interactions: (Girifalco and Weizer1959, Pei et al 2006)

$$D = 0.3429\text{eV}, \alpha = 0.13588(\text{nm})^{-1}, r_e = 0.2866\text{nm}$$

For Cu-C interactions: (Hwang et al 2004)

$$D = 0.087\text{eV}, \alpha = 0.17(\text{nm})^{-1}, r_e = 0.22\text{nm}$$

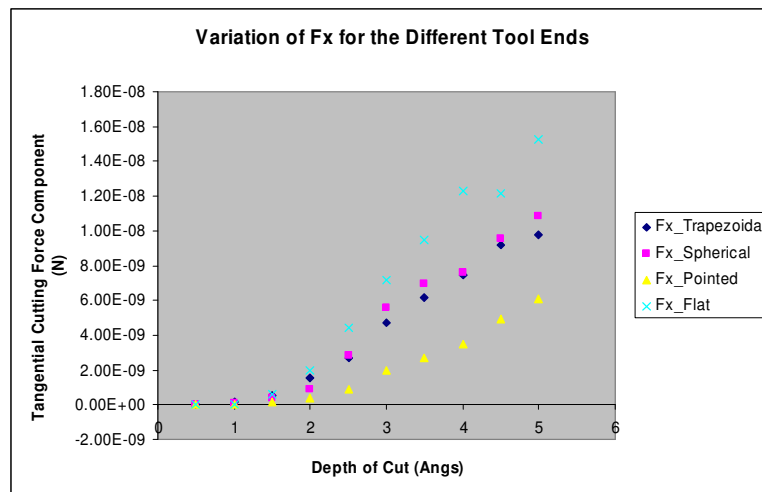


Figure 4.28: Variation of the Tangential Cutting Force with Depth of Cut for the Different Tool Ends

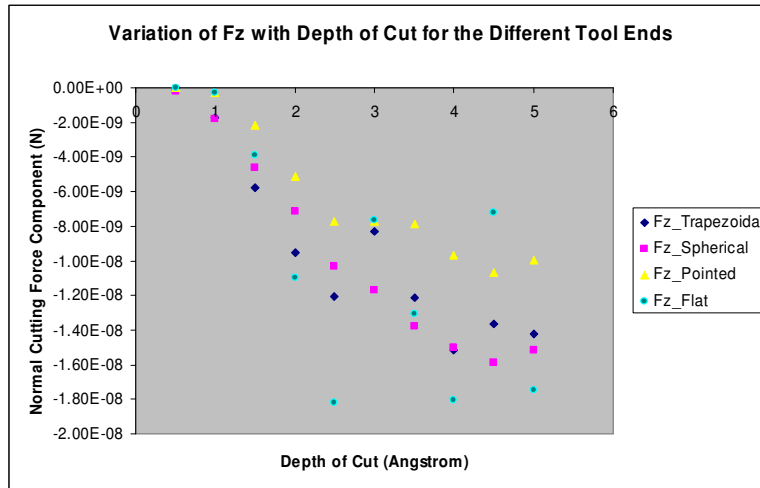


Figure 4.29: Variation of the Normal Cutting Force with Depth of Cut for the Different Tool Ends

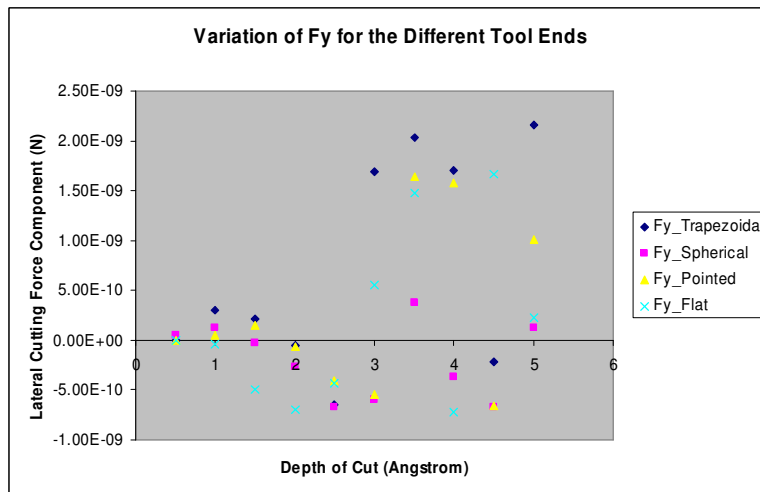


Figure 4.30: Variation of the Lateral Cutting Force with Depth of Cut for the Different Tool Ends

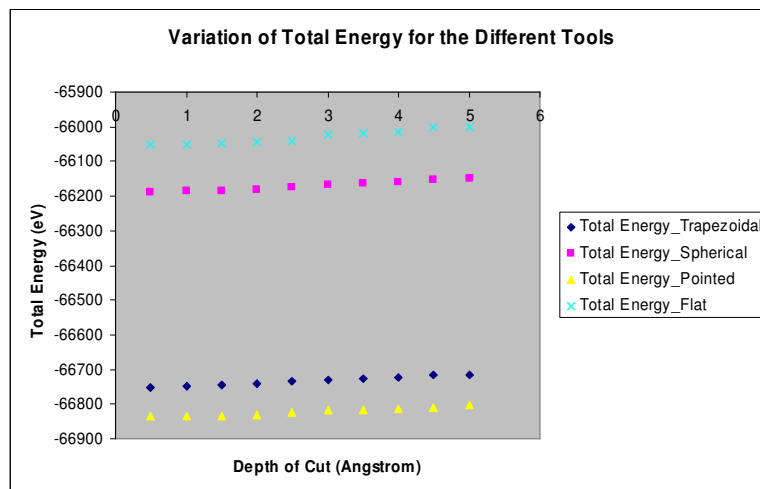


Figure 4.31: Variation of the Total Energy with Depth of Cut for the Different Tool Ends

Table 4.9: Summary on Various Tool Geometries (Observed Phenomena)

Depth of Cut (nm)	Flat Tool End	Pointed Tool End	Spherical Tool End	Trapezoidal Tool End
0.05	Rubbing	Rubbing	Rubbing	Rubbing
0.1	Rubbing	Rubbing	Rubbing	Rubbing
0.15	Rubbing	Rubbing	Rubbing	Rubbing
0.2	Rubbing	Rubbing	Rubbing	Rubbing
0.25	Rubbing	Rubbing	Rubbing	Rubbing
0.3	Ploughing with three layers of atoms	A slight initiation of ploughing with a number of side atoms	Ploughing with one layer of atoms	Ploughing with one layer of atoms
0.35	Ploughing with three layers of atoms	Ploughing with some few atoms	Ploughing with two layer of atoms	Ploughing with one layer of atoms
0.4	Ploughing with three layers of atoms	Ploughing with some few atoms	Ploughing with two layer of atoms	Ploughing with two layer of atoms
0.45	Ploughing with Five layers of atoms	Ploughing with some more side atoms	Ploughing with two layers of atoms	Ploughing with three layers of atoms
0.5	Ploughing with Four layers of atoms	Ploughing with two layers of atoms	Ploughing with three layers of atoms	Ploughing with three layers of atoms

Table 4.10: Force Ratio (F_x/F_z) Tangential Force Component/Normal Force Component for the Different Tool Ends

Depth of Cut (nm)	Flat Tool End	Pointed Tool End	Spherical Tool End	Trapezoidal Tool End
0.05	1.177343	0.291661	0.002823	0.471519
0.10	0.06136	0.031104	0.04312	0.078221
0.15	0.154636	0.068924	0.083595	0.095937
0.20	0.181458	0.077188	0.126165	0.165729
0.25	0.243493	0.117652	0.274466	0.22554
0.30	0.941763	0.251311	0.47619	0.569788
0.35	0.724397	0.340392	0.502437	0.508031
0.40	0.682284	0.357095	0.504867	0.490259
0.45	1.691561	0.463065	0.600268	0.671788
0.50	0.875725	0.612254	0.716174	0.69086

Discussion

The simulation results for the four different tool ends, for the variation of the depth of cut (0.05 – 0.5nm) are shown in Table C.5. Also, the comparison of the cutting forces, the potential and total energies and the temperature distribution for the various tool ends are shown in Tables C.6, C.7 and C.8 respectively. The summary of the results on rubbing and ploughing are presented in Table 4.9. Rubbing phenomena are observed in all the four geometries up to the depth of cut of 0.25nm (diameter of a copper atom is 2.5 Angstroms). Also, for all the tools, ploughing initiates at the depth of cut of 0.3nm, but the tool with the flat end geometry shows a faster initiation of ploughing with three layers of atoms, because it has the largest surface area to engage more atoms. The force ratio for the different tool ends are shown in Table 4.10. It can be observed that all the ratio values are under 1 (except for the flat tool end for the depth of cut of 0.05 and 0.45nm), which indicates that the material removal mechanism phenomena are rubbing and ploughing. The exceptions for the flat tool end might be due to spikes in the frictional force.

Figure 4.28 shows the variation of the tangential cutting force component, F_x with depth of cut for all the tools. It can be observed that the tool with the pointed end has the lowest cutting force and it is highest for flat end. The tools in increasing order of sharpness are the following, namely; the tool with the flat end (least sharp), the tool with the spherical end, the tool with the trapezoidal end and the tool with the pointed end (sharpest). The tools show the initiation of ploughing in that order. The tool with the flat end geometry shows a fast initiation of ploughing, because it has the largest surface area to engage more atoms. Figure 4.29 shows similar results for the normal cutting force component, F_z . Figure 4.30 shows the variation of the lateral cutting force component, F_y with depth of cut for all the tools and Figure 4.31 shows the variation of the total energy with depth of cut for all the tools. The total energy is lowest for the tool with the pointed end and highest for the tool with the flat end. This is similar to the results shown in Figure 4.28.

4.4.2 Conclusion

All the tools clearly show the phenomena of rubbing and ploughing in the depth of cut range of 0.05 to 0.5 nm. The tool with the pointed end has the lowest average cutting force and the tool with the flat end has the highest average cutting force. The total number of the various tool atoms may also have affected the results (See section 4.4.2). It is important to note that in nanomachining, the tool with the sharpest end may not necessarily cause the greatest material removal. This indicate that there may be a limit to sharpness of the tool, beyond which it would not necessarily contribute to

increased material removal. The different tool ends may be suitable for different metal machining applications.

4.5 The Effect of the Variation of Velocity in Nanomachining

4.5.1 Introduction

The MD simulation of the effect of the variation of velocity on nanomachining was investigated. The velocity range considered was from 80m/s to 260m/s in steps of 20.

Table 1 shows the simulation conditions applied in this research. The workpiece consists of 16000 copper atoms with perfect FCC lattice. It includes 3 kinds of atoms namely; boundary atoms, thermostat atoms and Newtonian atoms. The boundary atoms are kept fixed to reduce edge effects. The thermostat atoms conduct the heat generated during the cutting process out of the workpiece and the Newtonian atoms obey the Newton's equation of motion. The cutting tool consists of 1936 carbon atoms with perfect diamond lattice structure. The cutting tool is pointed shaped and it is modelled as a rigid body.

The atomic interactions in the simulation are the following, namely;
Cu-Cu : interactions between copper atoms
Cu-C : interactions between copper atoms and diamond atoms
C-C : interactions between the diamond atoms

Two potential pairs were used for the Cu-Cu and the Cu-C interactions namely; EAM-Morse and EAM-LJ and then the tool was treated as rigid and then deformable. In all, four cases were considered. For the C-C (tool atoms) interactions, the deformable cases were modelled by Tersoff potential.

Case 4.5.1:

The EAM potential was used for the Cu-Cu interactions and the Morse potential was used for the Cu-C interactions and the tool was treated as rigid.

The potential parameters used for the Cu-Cu interactions were read from the file - Cu_u3.eam in LAMMPS. The file contains the following, namely; the lattice constant of copper (3.615 Angstroms), the spacing in density (5.01E-4) and the spacing in distance (1.00E-2). Also, it contains three arrays of tabulated values of the embedding function, $G_i(\rho_{h,i})$ -500 values; effective

charge function, Z_{ij} , - 500 values, from which the pair potential interaction is calculated (the relationship between the effective charge and the pair potential is given by the equation

$$V_{ij}(r_{ij}) = \frac{Z_{ij}^2}{r_{ij}}$$

and the density function, $\rho_{h,i}$ - 500 values (A total of 1500 tabulated values). The

cut-off distance was 4.95 Angstroms.

For Cu-C interactions: (Hwang et al 2004)

$$D = 0.087eV, \alpha = 0.17(nm)^{-1}, r_e = 0.22nm$$

Case 4.5.2:

The EAM potential was used for the Cu-Cu interactions and the Morse potential was used for the Cu-C interactions, but the tool was treated as deformable/non-rigid. The parameters used are same as in case 4.5.1.

Case 4.5.3:

The EAM potential was used for the Cu-Cu interactions and the LJ potential was used for the Cu-C interactions and the tool was treated as rigid. The parameters used for the EAM potential are the same as in case 1. The LJ parameters used for the Cu-C interfaces are below, with a cut-off distance of 2.5 Angstroms;

$$\epsilon = 0.4096eV, \sigma = 2.338 Angstroms$$

Case 4.5.4:

The EAM potential was used for the Cu-Cu interactions and the LJ potential was used for the Cu-C interactions and the tool was treated as deformable/non-rigid. The parameters used are same as in case 4.5.3. For cases 4.5.2 and 4.5.4, where the tool was considered as deformable, the C-C interactions were modelled by the Tersoff potential parameters in the Table 2.7.

The cutting speed range is 80-260m/s and the depth of cut is 2.0nm. Table 4.11 shows the various timesteps required to advance the cutting distance of 7.2nm.

Table 4.11: The Various Timesteps for the Different Velocity for a Distance of 7.2nm

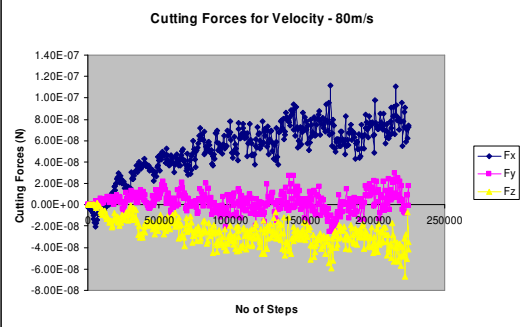
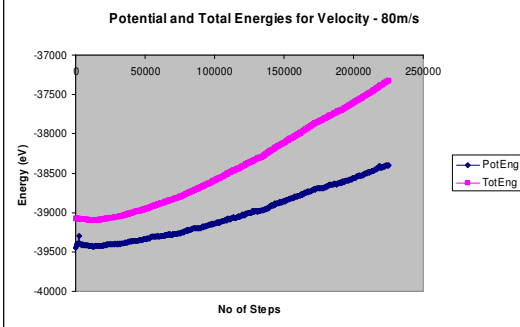
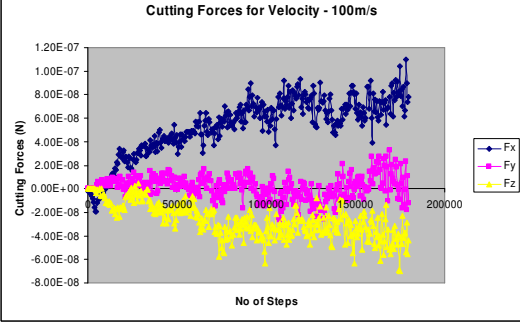
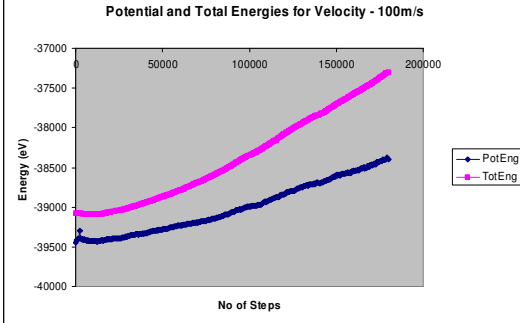
Velocity (m/s)	No of Steps	Time(s)
40	600000	1.80E-10
60	400000	1.20E-10
80	300000	9.00E-11
100	240000	7.20E-11
120	200000	6.00E-11
140	171000	5.14E-11
160	150000	4.50E-11
180	133000	4.00E-11
200	120000	3.60E-11
220	109000	3.27E-11

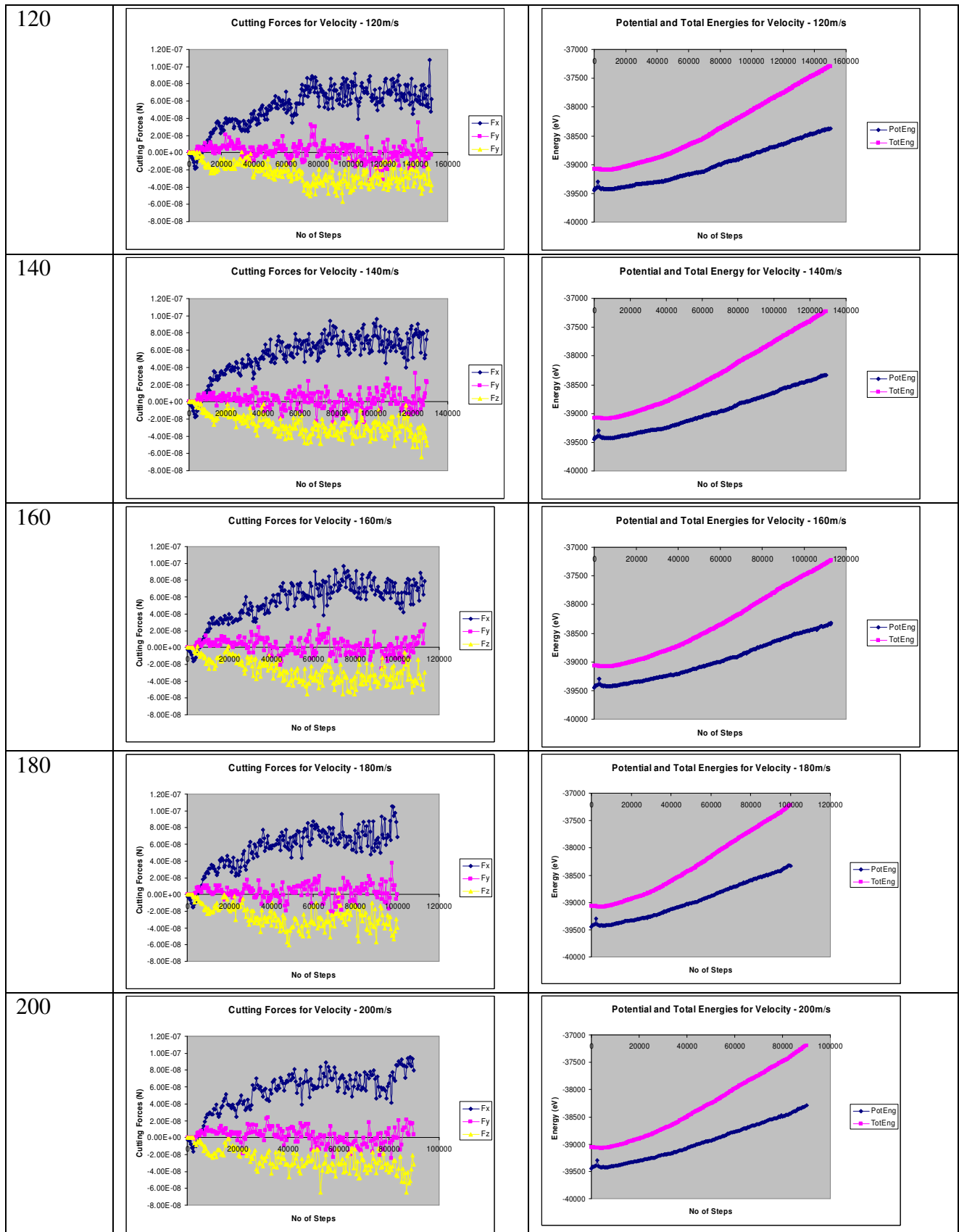
4.5.2 Modelling with EAM-Morse Potentials and Rigid Tool (Case 4.5.1)

Discussion

Results for the cutting forces and the energies for Case 4.5.1 are shown in Table 4.12. Also, Figure 4.32 shows the velocity variation with temperature. It can be observed that as velocity increases, the temperature variation increases and it is fairly linear as shown in Figure 4.34. Furthermore, the tangential cutting force component, F_x shows linear variation with the velocity (Figure 4.33), where as the normal forces do not show linear variation with the velocity (Figure 4.33b).

Table 4.12: Comparison of the Cutting Forces and the Energies for Velocities (80-260m/s)

Velocity (m/s)	Cutting Forces	Potential and Total Energies
80		
100		



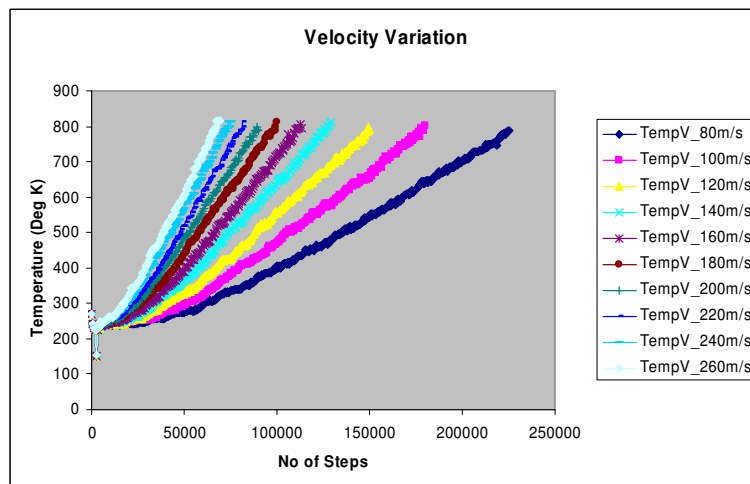
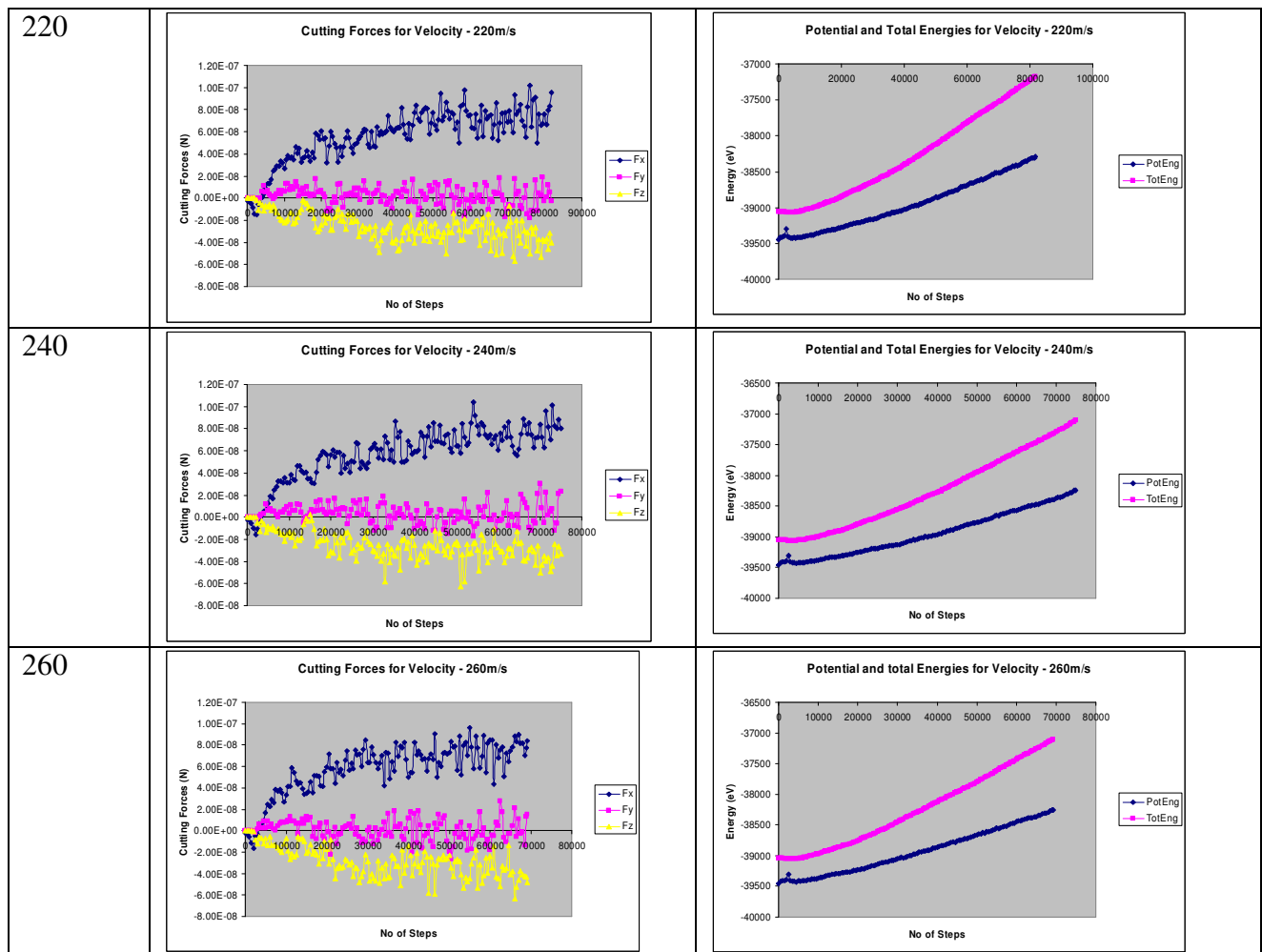


Figure 4.32: Velocity Variation with Temperature for EAM-Morse Potentials and Rigid Tool

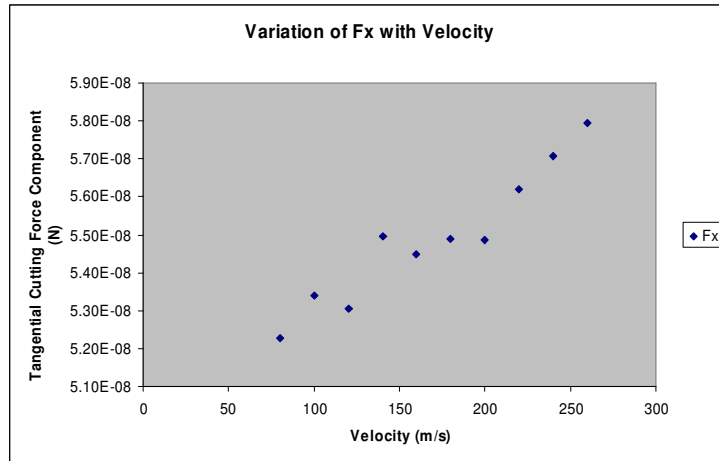


Figure 4.33: Variation of Tangential Cutting Force Component with Velocity for EAM-Morse Potentials and Rigid Tool

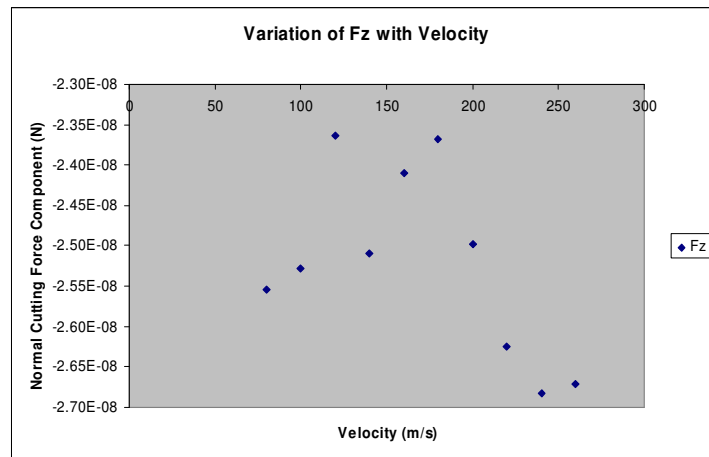


Figure 4.33b: Variation of Normal Cutting Force Component with Velocity for EAM-Morse Potentials and Rigid Tool

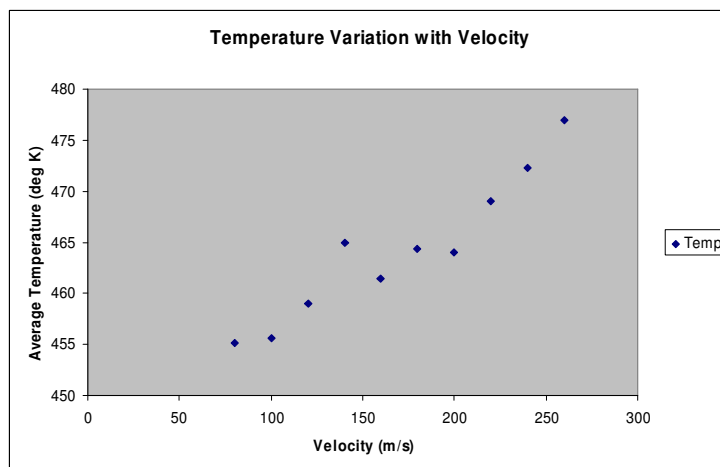
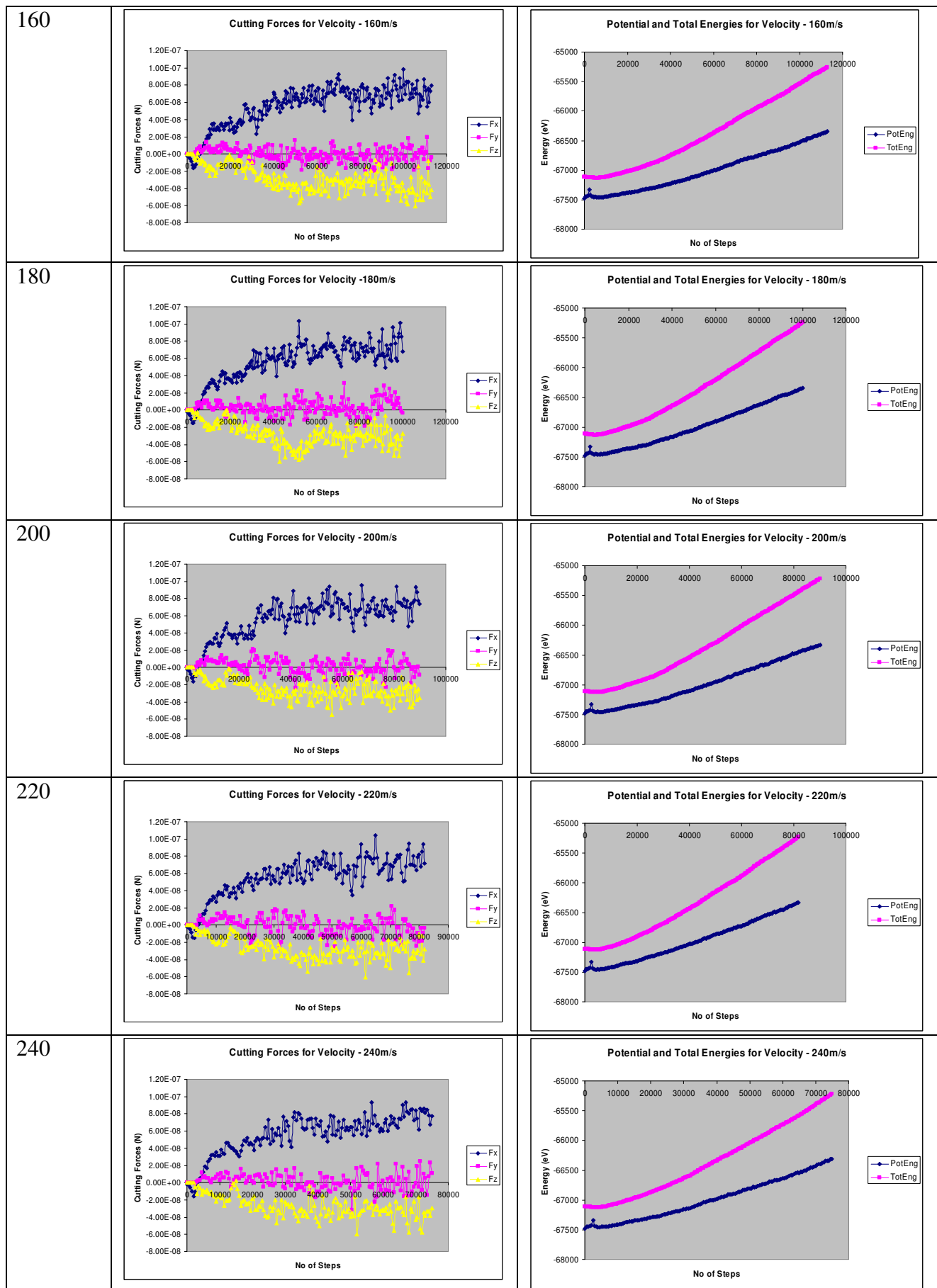


Figure 4.34: Variation of Temperature with Velocity for EAM-Morse Potentials and Rigid Tool

4.5.3 Modelling with EAM-Morse Potentials and Non-Rigid Tool (Case 4.5.2)

Table 4.13: Comparison of the Cutting Forces and the Energies for Velocities (80-260m/s)

Velocity (m/s)	Cutting Forces	Potential and Total Energies
80		
100		
120		
140		



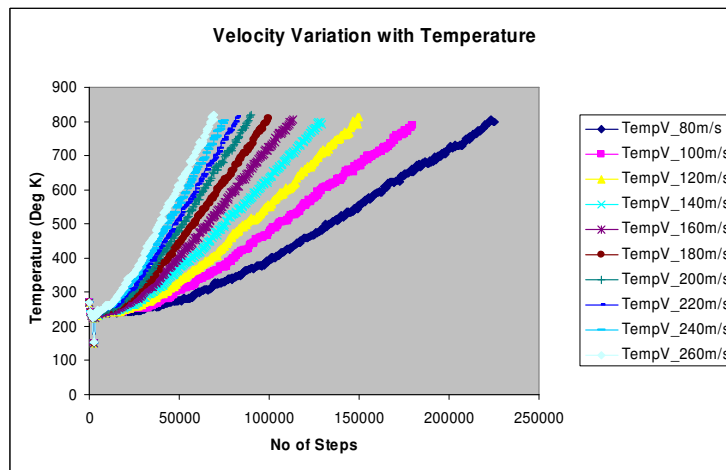
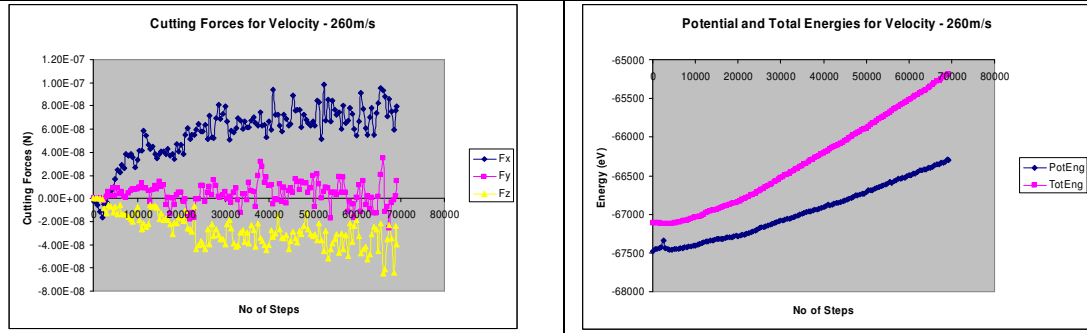


Figure 4.35: Velocity Variation with Temperature for EAM-Morse Potentials and Non-Rigid Tool

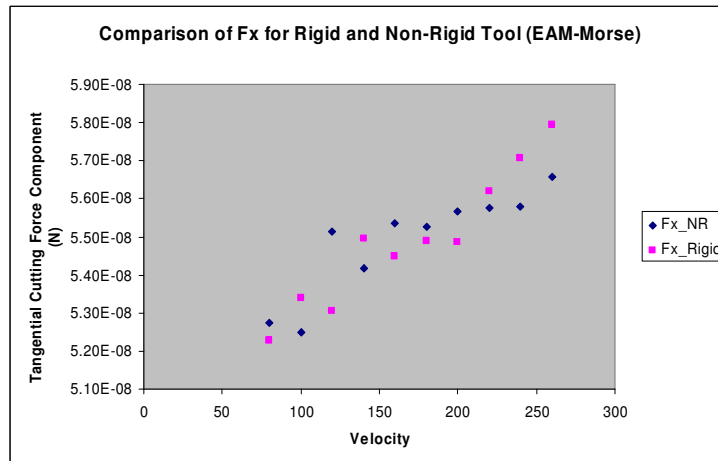


Figure 4.36: Comparison of Variation of Tangential Cutting Force Component with Velocity for EAM-Morse Potentials (Rigid Tool and Non-Rigid Tool)

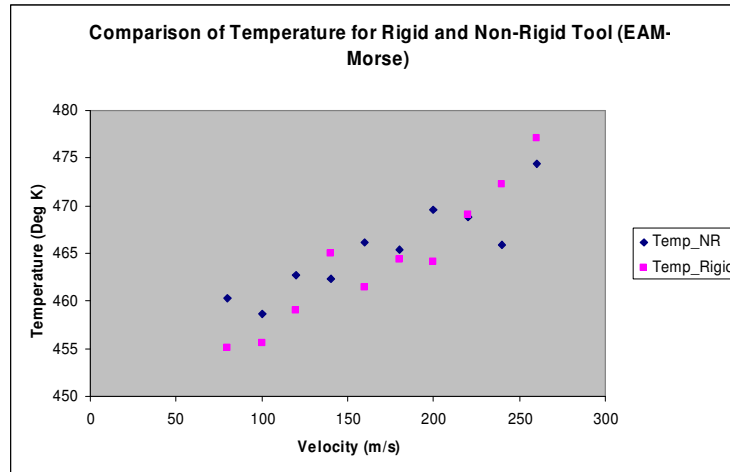


Figure 4.37: Comparison of Variation of Temperature with Velocity for EAM-Morse Potentials (Rigid Tool and Non-Rigid Tool)

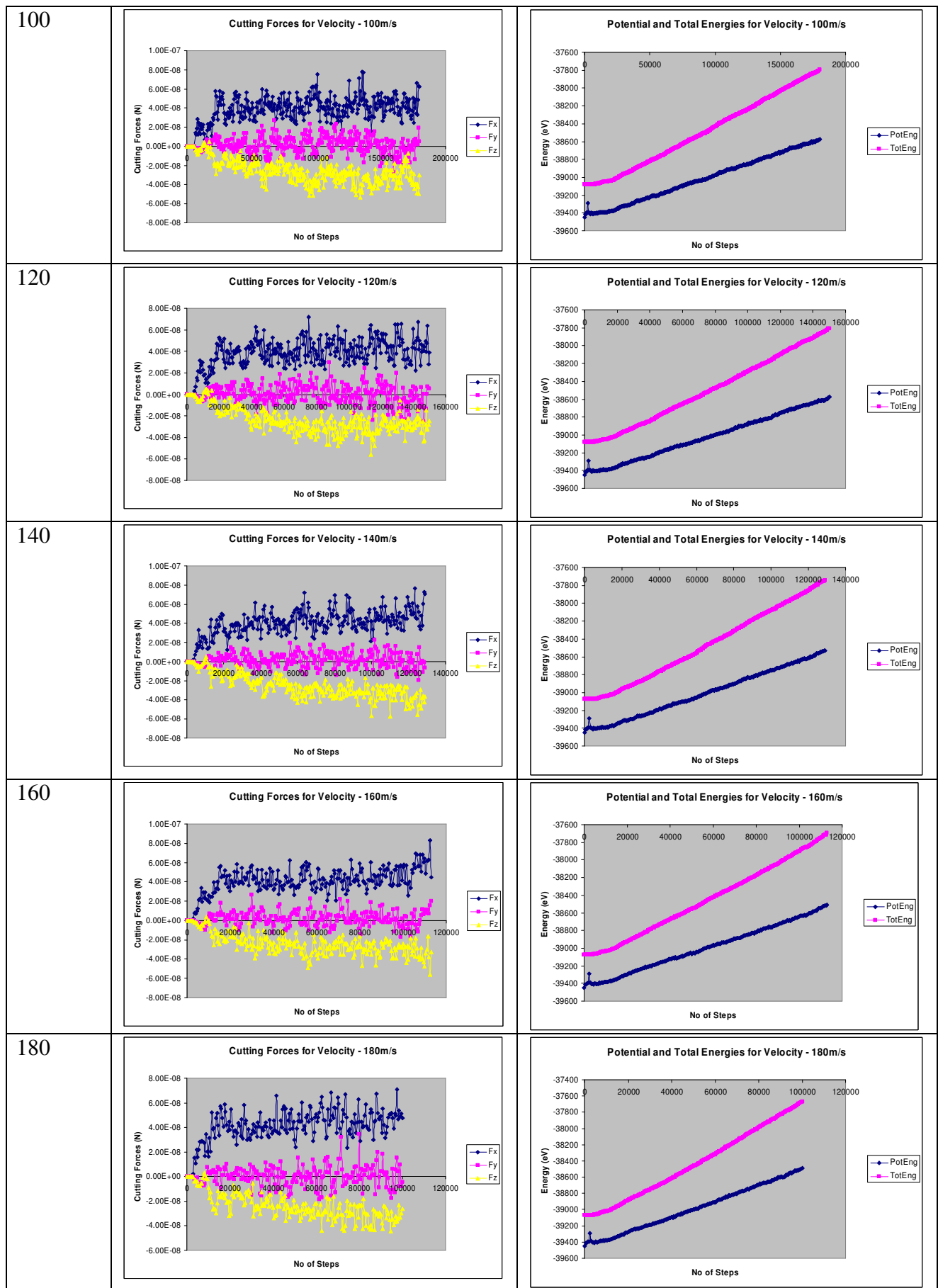
Discussion

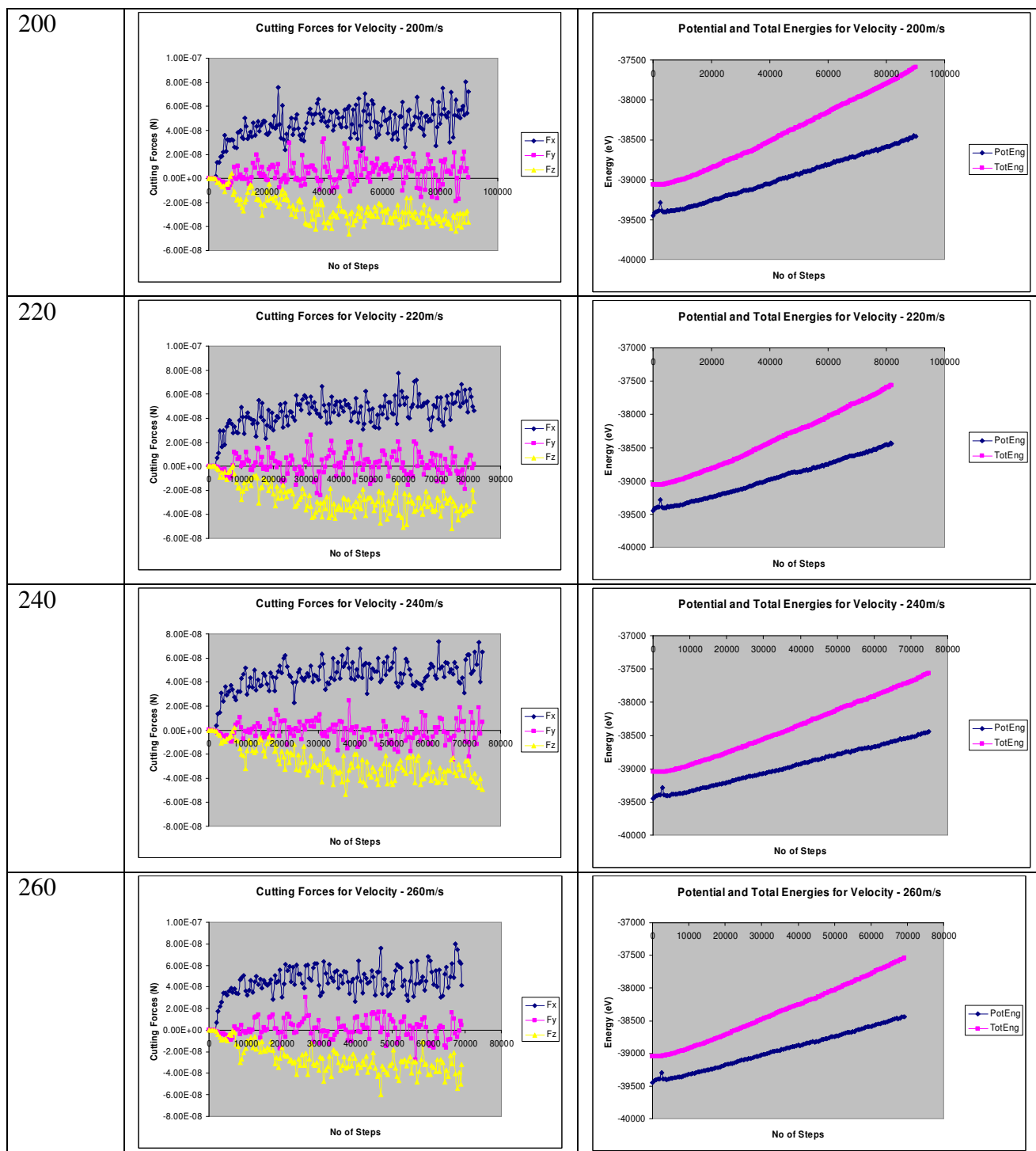
Results for the cutting forces and the energies for Case 4.5.2 are shown in Table 4.13. Figure 4.35 shows the velocity variation with temperature. It can be observed that as velocity increases, the temperature variation also increases. Figures 4.36 and 4.37 show the comparisons of Case 4.5.1 and Case 4.5.2. Figure 4.36 compares the variation of the tangential cutting force component with velocity and Figure 4.37 compares the variation of the temperature with velocity. There seems to be no much difference between the use of rigid and non-rigid tool for the EAM-Morse potential pair.

4.5.4 Modelling with EAM-LJ Potentials and Rigid Tool (Case 4.5.3)

Table 4.14: Comparison of the Cutting Forces and the Energies for Velocities (80-260m/s)

Velocity (m/s)	Cutting Forces	Potential and Total Energies
80		

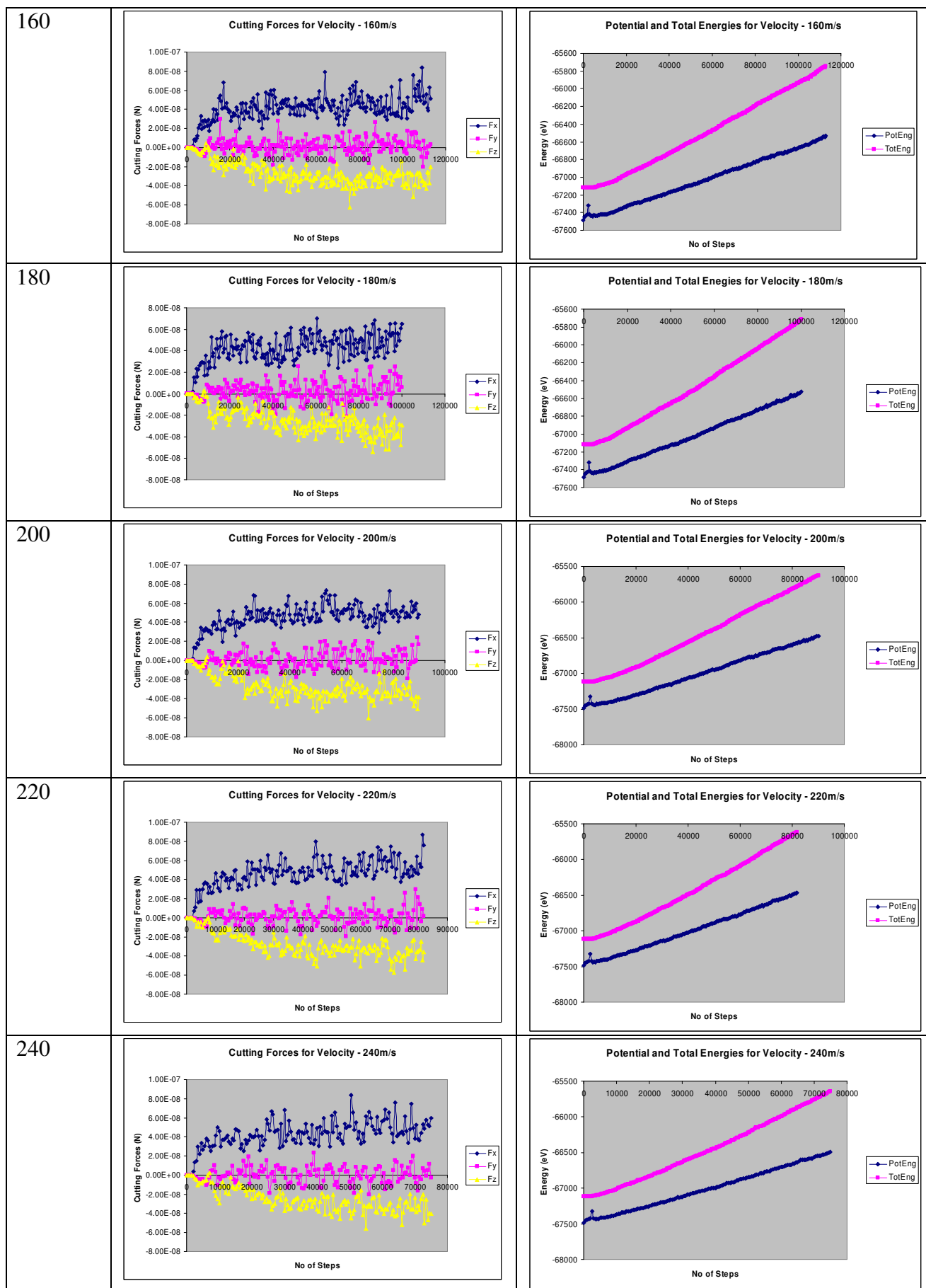




4.5.5 Modelling with EAM-LJ Potentials and Non-Rigid Tool (Case 4.5.4)

Table 4.15: Comparison of the Cutting Forces and the Energies for Velocities (80-260m/s)

Velocity (m/s)	Cutting Forces	Potential and Total Energies
80		
100		
120		
140		



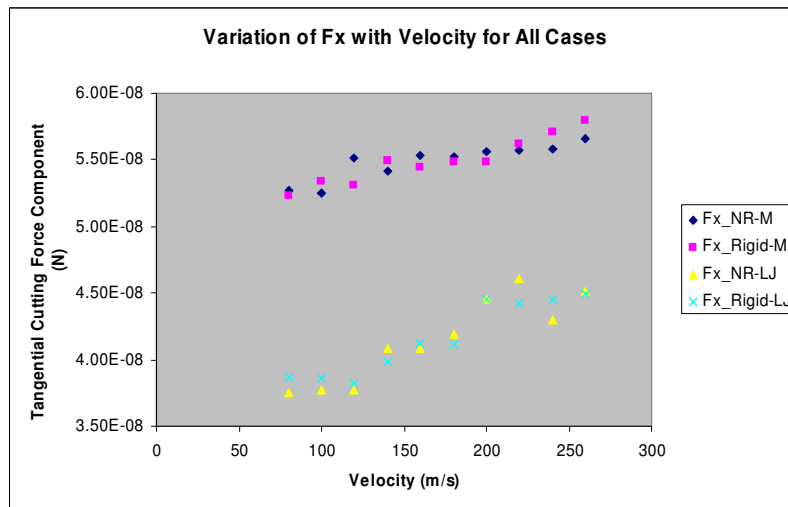
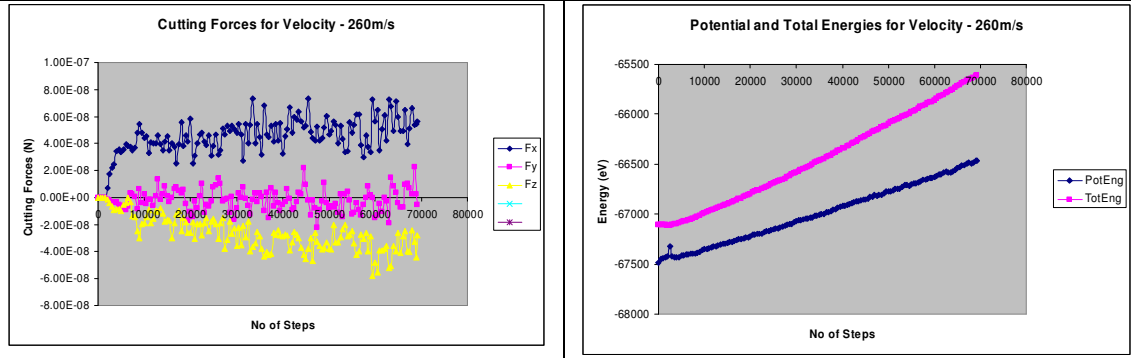


Figure 4.38: Comparison of Variation Tangential Cutting Force Component with Velocity for All Potentials (Rigid Tool and Non-Rigid Tool)

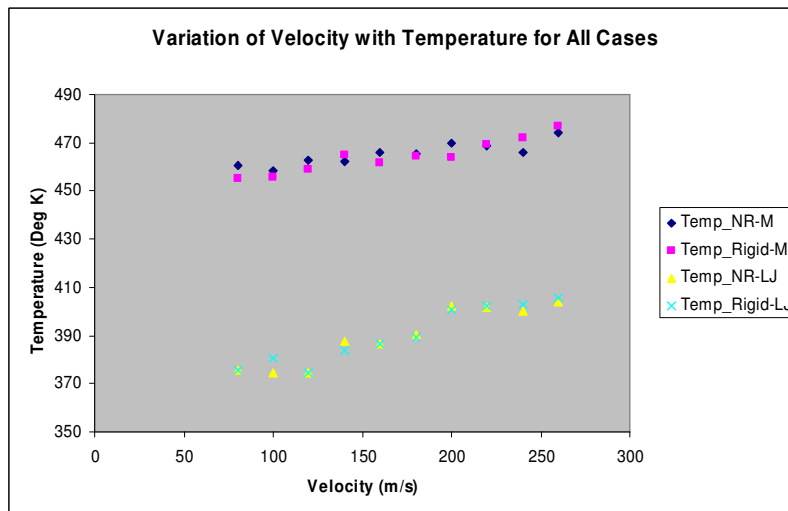


Figure 4.39: Comparison of Variation of Velocity with Temperature for All Potentials (Rigid Tool and Non-Rigid Tool)

Discussion

Results for the cutting forces and the energies for Cases 4.5.3 and 4.5.4 are shown in Tables 4.14 and 4.15 respectively. Figures 4.38 and 4.39 show the comparison of all the cases. It can be observed that the tangential cutting force component, F_x and the temperature variation are lower for Cases 4.5.3 and 4.5.4 (the EAM-LJ potential pair) as was observed previously in section 4.2.

To extend the investigation to a wider range of lower velocities, further simulations were carried out down to 1m/s (with EAM-LJ potential pair). The variation of the cutting force components for the whole range of velocities are shown in Figure 4.40. It can be observed that the tangential and the normal cutting force components relatively increase with increase in velocity.

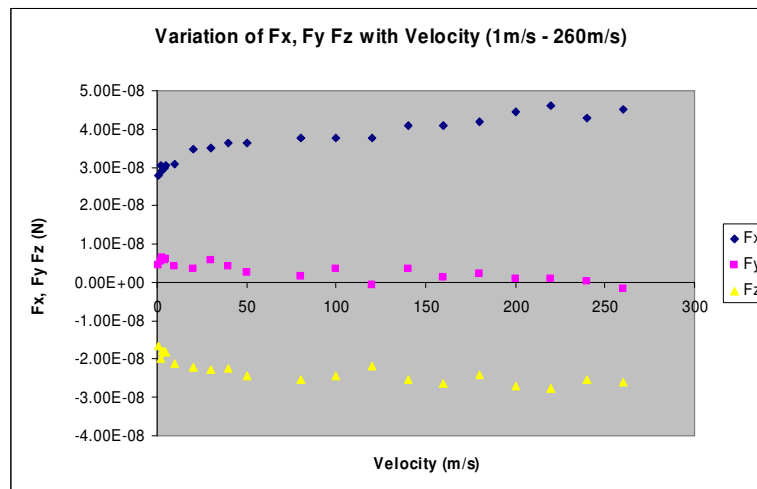


Figure 4.40: Variation of the Cutting Forces with Velocity (1m/s-260m/s)

4.5.6. Conclusion

It can be concluded that the interatomic potential readily affect the velocity variation simulation in nanomachining, whereas the use of rigid and non-rigid tools doesn't show appreciable difference.

Chapter 5. Multiple-Pass Nanometric Machining Simulation Results

5.1 Introduction

The existing MD simulation studies on nanometric cutting have been limited to single pass of tool movement. In practice, most machining processes involve the use of multiple passes to create new surface. To address this issue, a 3-pass cutting was employed to simulate the surface creation in single point diamond turning.

Table 3.5 shows the simulation conditions applied in this study, with depth of cut – 2.0nm, Rake angle – 0 degree, feed – 1.5nm and run of 150000 steps. The configuration of the simulation has a total of 54232 atoms. The workpiece consists of 43240 copper atoms with perfect FCC lattice. It includes 3 kinds of atoms namely; boundary atoms, thermostat atoms and Newtonian atoms. The boundary atoms are kept fixed to reduce edge effects. The thermostat atoms conduct the heat generated during the cutting process out of the workpiece and the Newtonian atoms obey the Newton's equation of motion. The cutting tool consists of 10992 carbon atoms with diamond lattice structure. The cutting tool has a trapezoidal end as illustrated in Figure 5.1.

The atomic interactions in the simulation are the following, namely;

Cu-Cu : interactions between copper atoms

Cu-C : interactions between copper atoms and diamond atoms

C-C : interactions between the diamond atoms

For the simulations, 6 different cases were considered, which are shown below;

Case 5.1: The Cu-Cu interactions were modelled by Morse, the Cu-C interactions were modelled by Morse potential and the tool was assumed to be rigid.

Case 5.2: The Cu-Cu interactions were modelled by Morse, the Cu-C interactions were modelled by Morse potential and the tool was assumed to be non-rigid.

Case 5.3: The Cu-Cu interactions were modelled by EAM, the Cu-C interactions were modelled by Morse potential and the tool was assumed to be rigid.

Case 5.4: The Cu-Cu interactions were modelled by EAM, the Cu-C interactions were modelled by Morse potential and the tool was assumed to be non-rigid.

Case 5.5: The Cu-Cu interactions were modelled by EAM, the Cu-C interactions were modelled by LJ potential and the tool was assumed to be rigid.

Case 5.6: The Cu-Cu interactions were modelled by EAM, the Cu-C interactions were modelled by LJ potential and the tool was assumed to be non-rigid (Tersoff Potential was used).

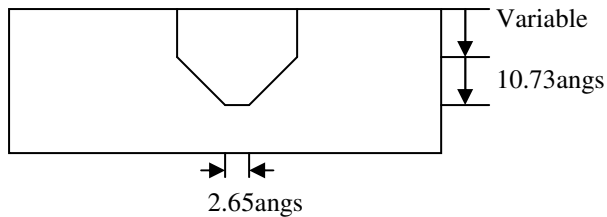
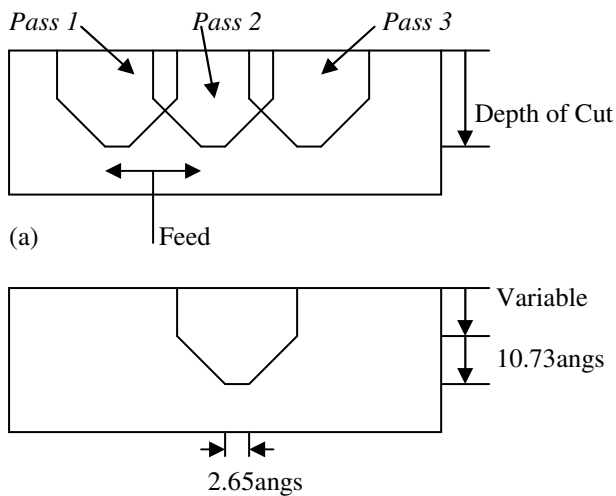


Figure 5.1a: Cross Section of the Machined Grooves with Passes 1-3 (direction of cut is perpendicular to the paper face) 1b: Tool Tip Dimensions

5.2 The Effect of Interatomic Potentials

Table 5.1: Comparison of the Material Removal for the Different Interatomic Potentials and the Tool (Rigid and Deformable) *Pass 1*

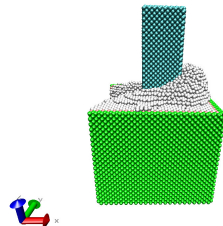
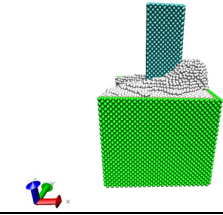
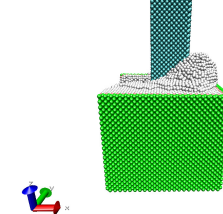
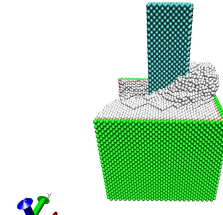
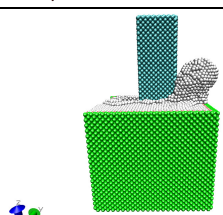
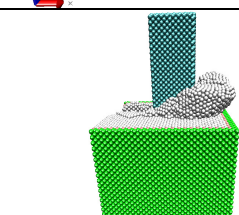
Interatomic Potentials	Tool (Rigid or Deformable)	Simulation (Material Removal)
Cu-Cu Interaction: Morse Cu-C Interaction: Morse	Rigid	
Cu-Cu Interaction: Morse Cu-C Interaction: Morse	Deformable	
Cu-Cu Interaction: EAM Cu-C Interaction: Morse	Rigid	
Cu-Cu Interaction: EAM Cu-C Interaction: Morse	Deformable	
Cu-Cu Interaction: EAM Cu-C Interaction: LJ	Rigid	
Cu-Cu Interaction: EAM Cu-C Interaction: LJ	Deformable	

Table 5.2: Comparison of the Cutting Forces and Energies for the Different Interatomic Potentials and the Tool (Rigid and Deformable) *Pass 1*

Simulation Cases	Cutting Forces	Potential and Total Energies
Case 5.1	<p>Cutting Forces for Morse-Morse Potentials (Rigid Tool) - Pass 1</p>	<p>Potential and Total Energies for Morse-Morse Potentials (Rigid Tool) - Pass 1</p>
Case 5.2	<p>Cutting Forces for Morse-Morse Potentials (Non Rigid Tool) - Pass 1</p>	<p>Potential and Total Energies for Morse-Morse Potentials (Non Rigid Tool) - Pass 1</p>
Case 5.3	<p>Cutting Forces for EAM-Morse Potentials (Rigid Tool) - Pass 1</p>	<p>Potential and Total Energies for EAM-Morse Potentials (Rigid Tool) - Pass 1</p>
Case 5.4	<p>Cutting Forces for EAM-Morse Potentials (Non Rigid Tool) - Pass 1</p>	<p>Potential and Total Energies for EAM-Morse Potentials (Non Rigid Tool) - Pass 1</p>

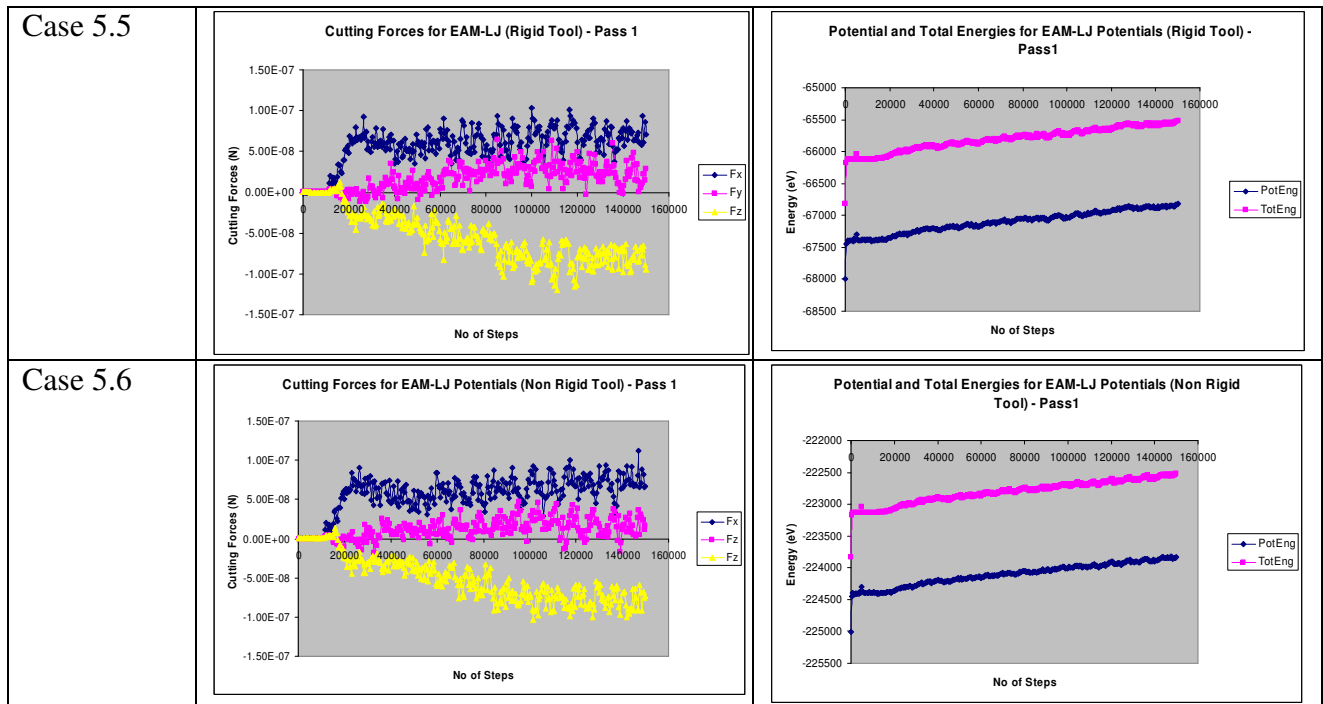


Table 5.3: Comparison of the Material Removal for the Different Interatomic Potentials and the Tool (Rigid and Deformable) *Pass 2*

Interatomic Potentials	Tool (Rigid or Deformable)	Simulation (Material Removal)
Cu-Cu Interaction: Morse Cu-C Interaction: Morse	Rigid	
Cu-Cu Interaction: Morse Cu-C Interaction: Morse	Deformable	
Cu-Cu Interaction: EAM Cu-C Interaction: Morse	Rigid	

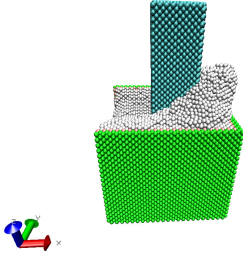
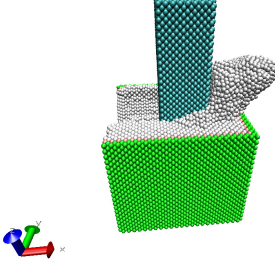
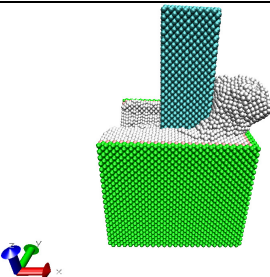
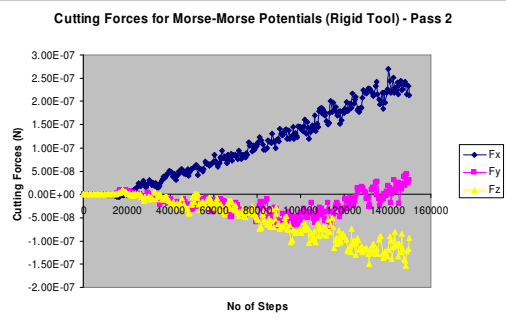
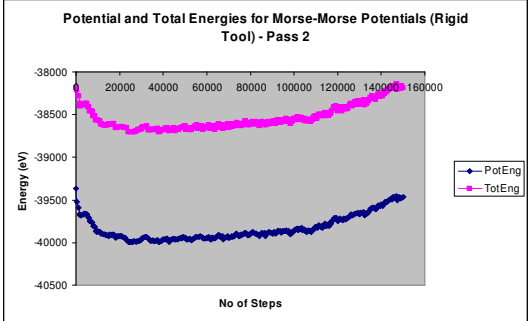
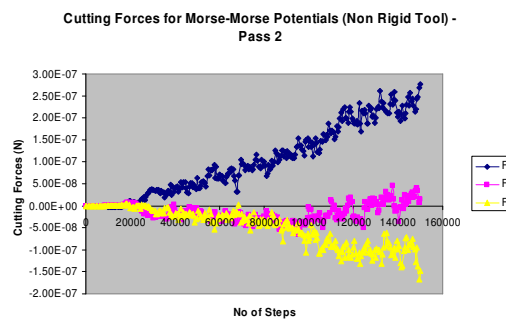
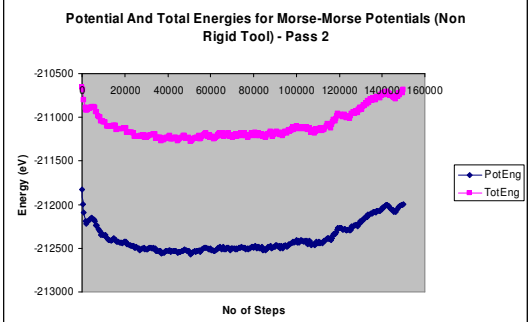
Cu-Cu Interaction: EAM Cu-C Interaction: Morse	Deformable	
Cu-Cu Interaction: EAM Cu-C Interaction: LJ	Rigid	
Cu-Cu Interaction: EAM Cu-C Interaction: LJ	Deformable	

Table 5.4: Comparison of the Cutting Forces and Energies for the Different Interatomic Potentials and the Tool (Rigid and Deformable) *Pass 2*

Simulation Cases	Cutting Forces	Potential and Total Energies
Case 5.1		
Case 5.2		

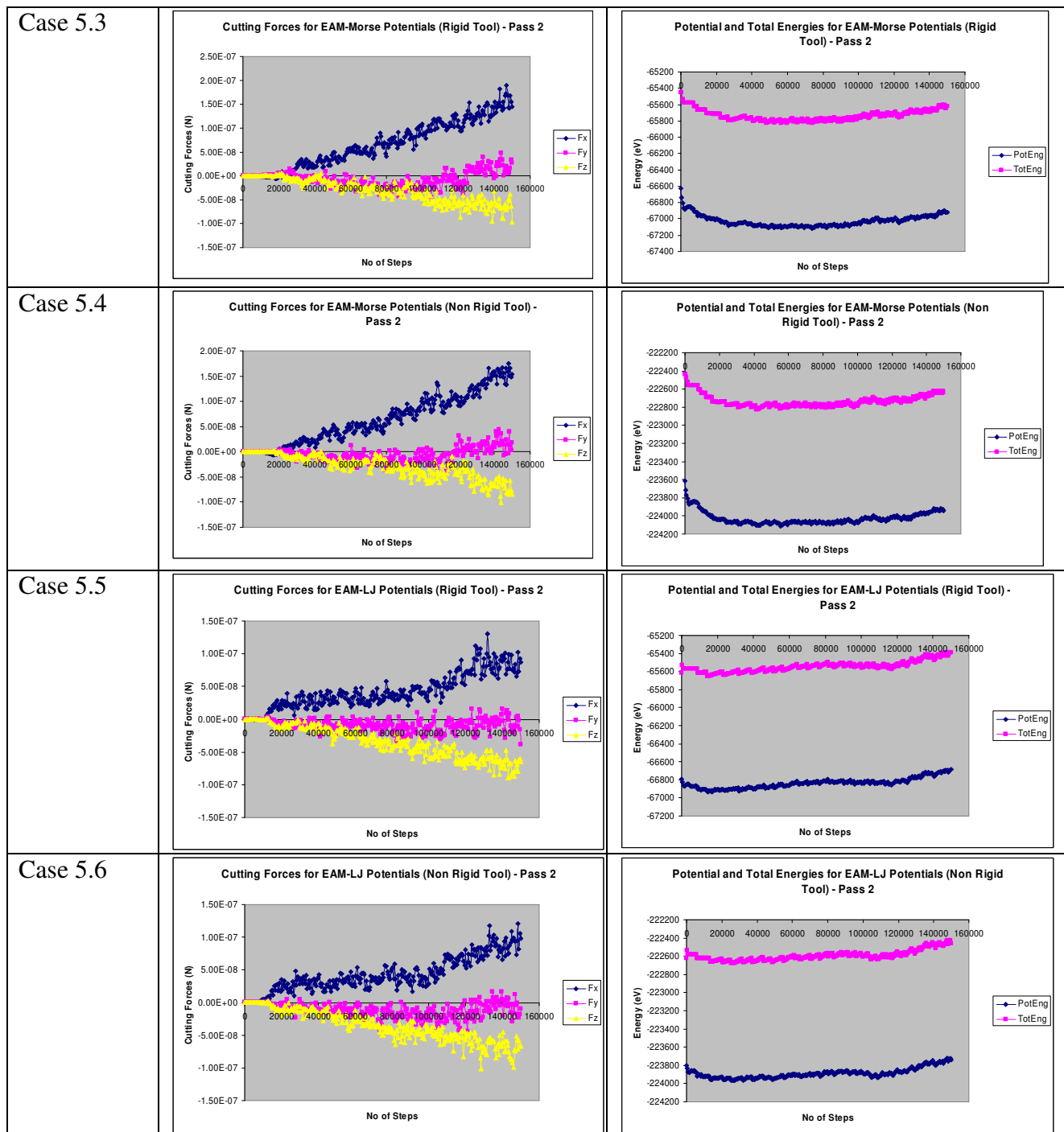


Table 5.5: Comparison of the Material Removal for the Different Interatomic Potentials and the Tool (Rigid and Deformable) *Pass 3*

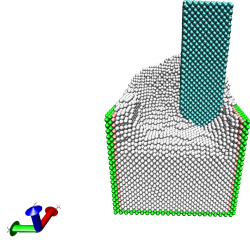
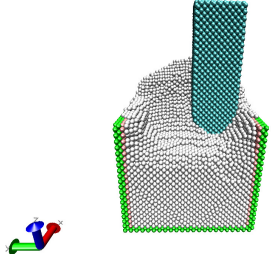
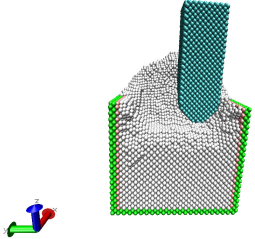
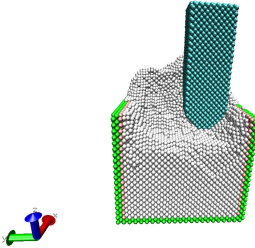
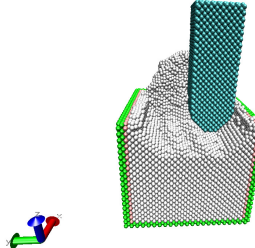
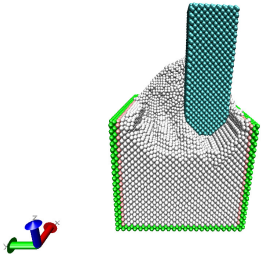
Interatomic Potentials	Tool (Rigid or Deformable)	Simulation (Material Removal)
Cu-Cu Interaction: Morse Cu-C Interaction: Morse	Rigid	
Cu-Cu Interaction: Morse Cu-C Interaction: Morse	Deformable	
Cu-Cu Interaction: EAM Cu-C Interaction: Morse	Rigid	
Cu-Cu Interaction: EAM Cu-C Interaction: Morse	Deformable	
Cu-Cu Interaction: EAM Cu-C Interaction: LJ	Rigid	
Cu-Cu Interaction: EAM Cu-C Interaction: LJ	Deformable	

Table 5.6: Comparison of the Cutting Forces and Energies for the Different Interatomic Potentials and the Tool (Rigid and Deformable) *Pass 3*

Simulation Cases	Cutting Forces	Potential and Total Energies
Case 5.1		
Case 5.2		
Case 5.3		
Case 5.4		
Case 5.5		

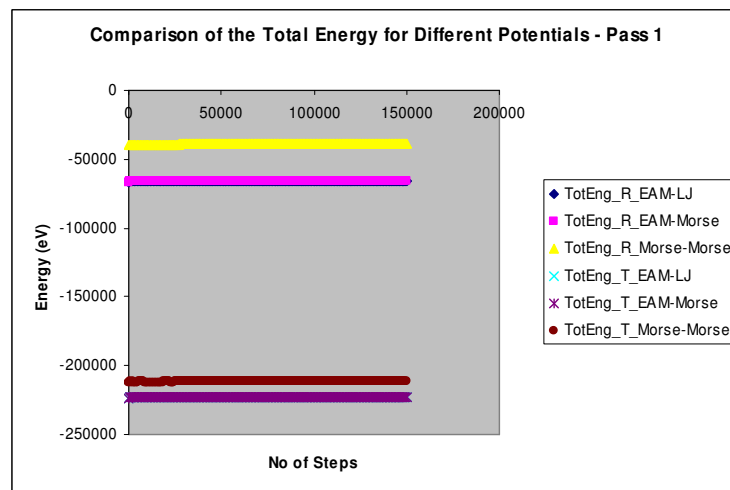
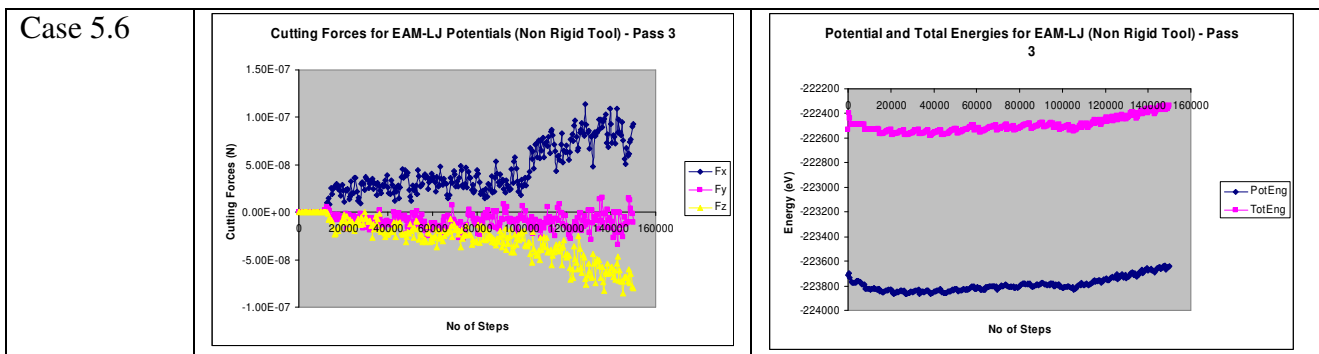


Figure 5.2: Comparison of the Total Energy for the Different Potential Pairs (Rigid and Non Rigid Tool)

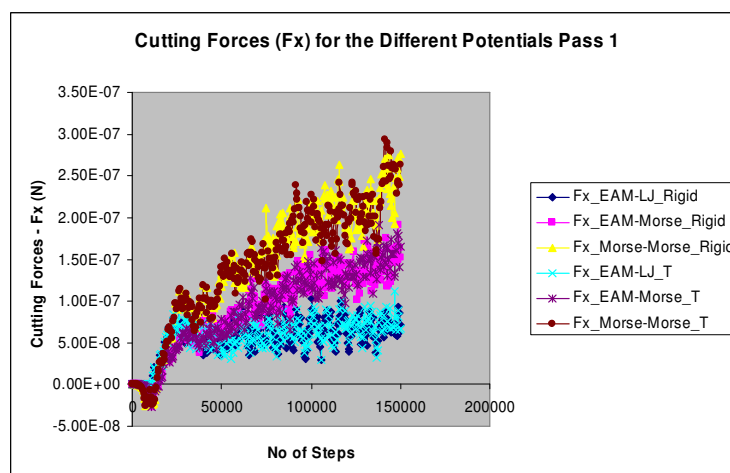


Figure 5.3: Tangential Cutting Force Components for the Different Potentials – Pass 1

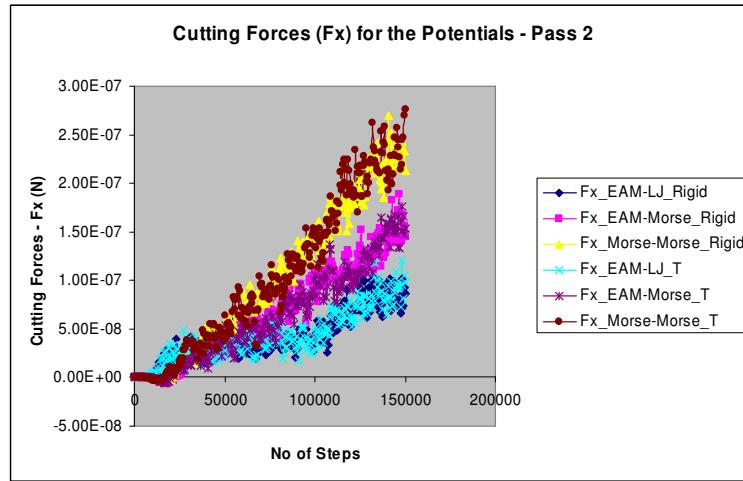


Figure 5.4: Tangential Cutting Force Components for the Different Potentials – Pass 2

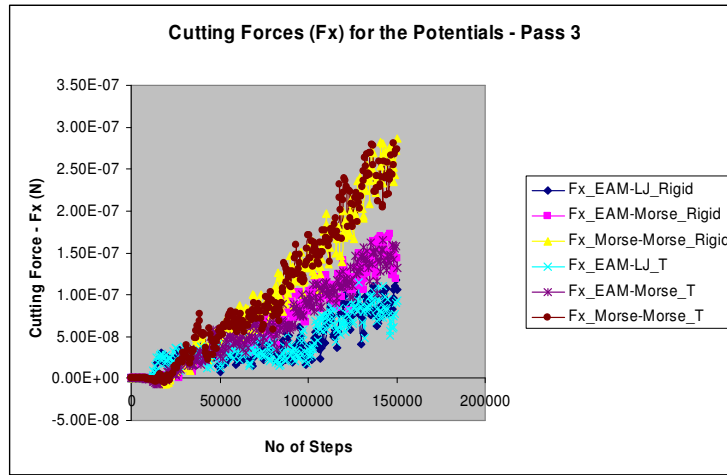


Figure 5.5: Tangential Cutting Force Components for the Different Potentials – Pass 3

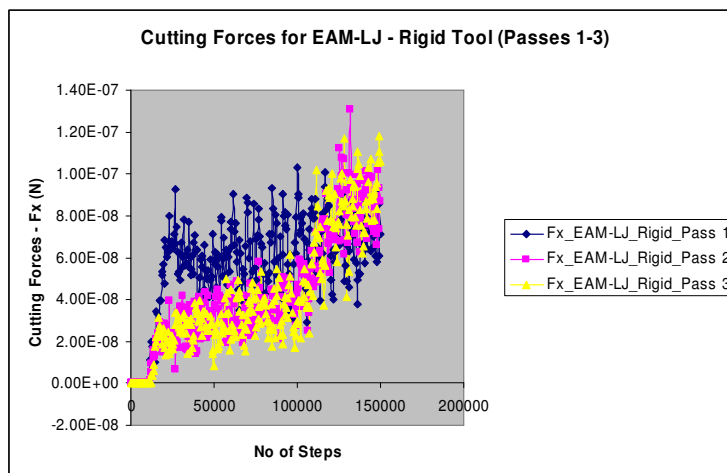


Figure 5.6: Tangential Cutting Force Components for the EAM-LJ Potentials (Rigid Tool) Passes 1-3

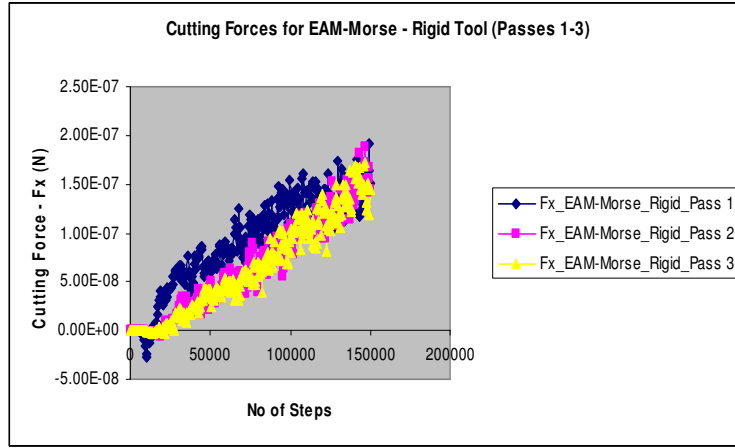


Figure 5.7: Tangential Cutting Force Components for the EAM-Morse Potentials (Rigid Tool) – Passes 1-3

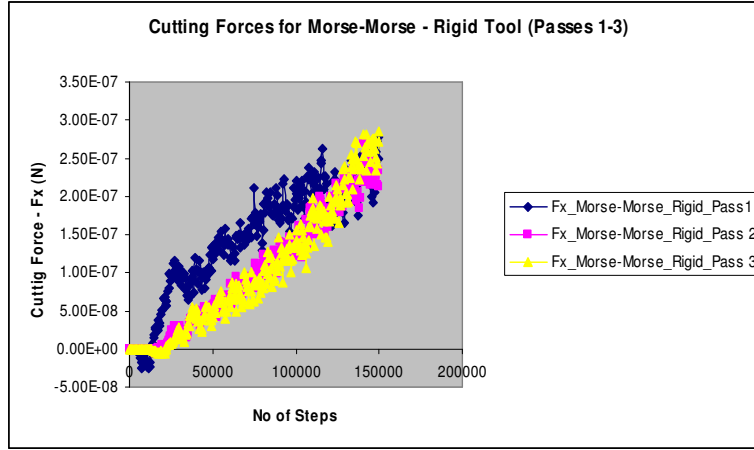


Figure 5.8: Tangential Cutting Force Components for the Morse-Morse Potentials (Rigid Tool) – Passes 1-3

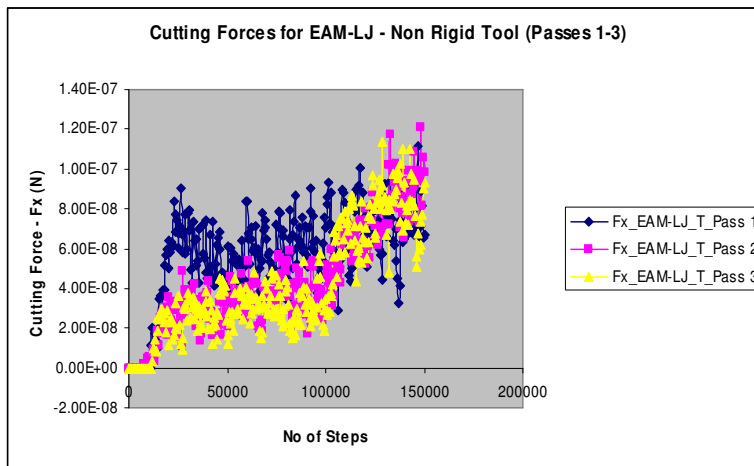


Figure 5.9: Tangential Cutting Force Components for the EAM-LJ Potentials (Non Rigid Tool) – Passes 1-3

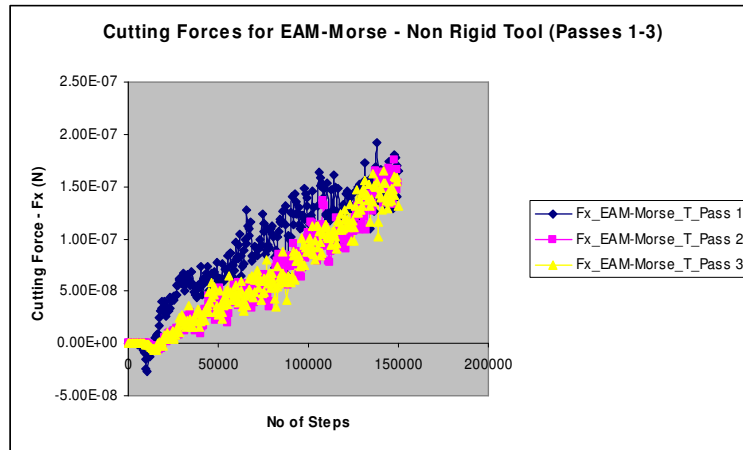


Figure 5.10: Tangential Cutting Force Components for the EAM-Morse Potentials (Non Rigid Tool) – Passes 1-3

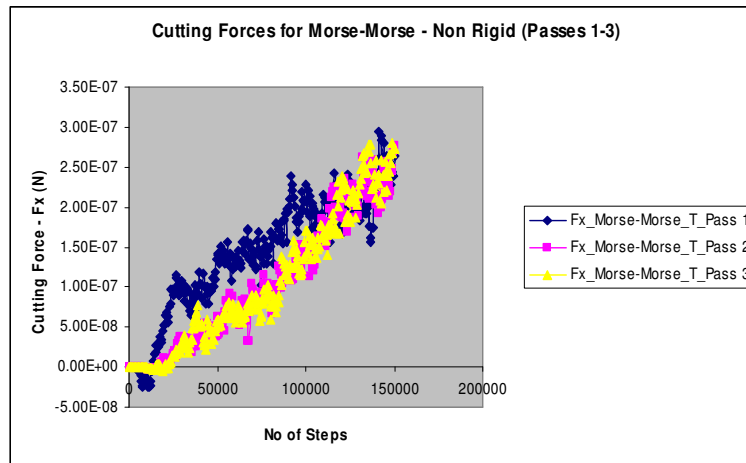


Figure 5.11: Tangential Cutting Force Components for the Morse-Morse Potentials (Non Rigid Tool) – Passes 1-3

Table 5.7: Comparison for the Different Potential Pairs: Total Energy (eV)

Potentials	Cases	Total Energy (eV) Pass 1	Total Energy (eV) Pass 2	Total Energy (eV) Pass 3
EAM-Morse(Non-Rigid Tool)	Case	-222940	-222735	-222661
EAM-LJ (Non-Rigid Tool)	Case	-222816	-222595	-222497
Morse-Morse (Non-Rigid Tool)	Case	-211396	-211095	-210935
EAM-Morse (Rigid Tool)	Case	-65928.9	-65735.5	-65657.7
EAM-LJ (Rigid Tool)	Case	-65814.2	-65545.4	-65438.2
Morse-Morse (Rigid Tool)	Case	-38889	-38540.4	-38427.3

Discussion

Table 5.1 shows the comparison of the material removal for the different interatomic potentials and the tool (both rigid and deformable) for pass 1. The comparison of the cutting forces and the energies are shown in table 5.2. Similar results for passes 2 and 3 are shown in Tables 5.3, 5.4, 5.5 and 5.6 respectively. Tables C.9 and C.10 also show the comparison of the cutting forces and the temperature variation for all the cases respectively.

The comparison of the total energy for the different potentials and for both rigid and non rigid tool is shown in Figure 5.2. With reference to Table 5.7, the EAM-Morse (Non-Rigid Tool) has the lowest total energy for each of the passes and Morse-Morse has the highest. Table 5.9 is in ascending order of total energy. Figures 5.3 - 5.5 show the tangential cutting forces for the different potentials for passes 1-3. It can be observed that the cutting forces are lowest for the EAM-LJ potential pairs both for the rigid and the non rigid tools. The Morse-Morse potential pairs have the highest cutting forces. Also, it can be observed that the tool rigidity doesn't have significant effect on the cutting forces. Figures 5.6 – 5.11 show the comparison of the tangential force component for the different potentials for passes 1-3. It can be seen that the cutting forces for pass 1 is always slightly higher than for passes 2 and 3.

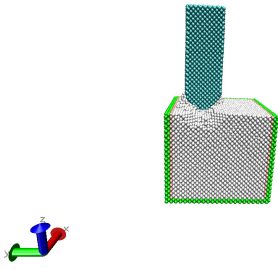
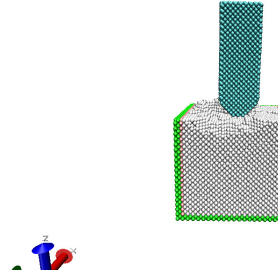
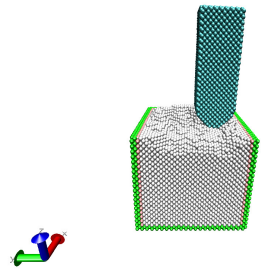
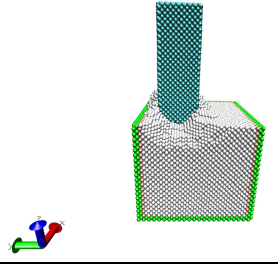
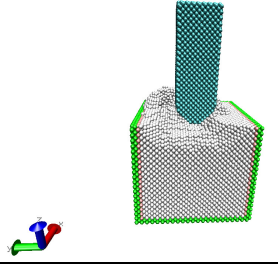
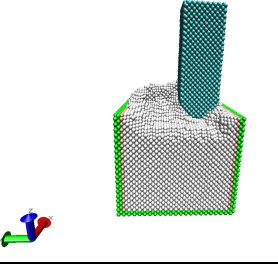
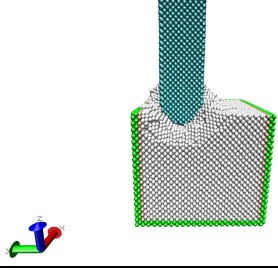
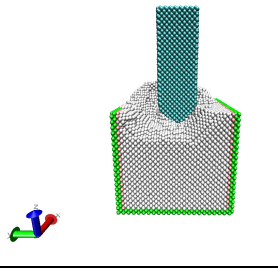
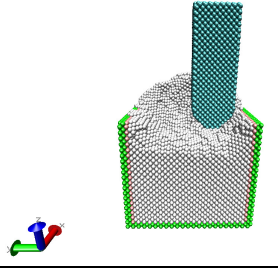
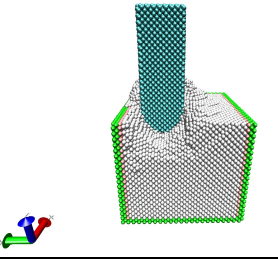
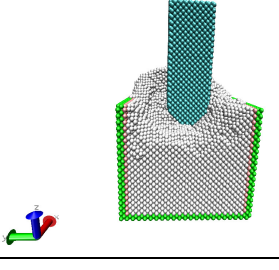
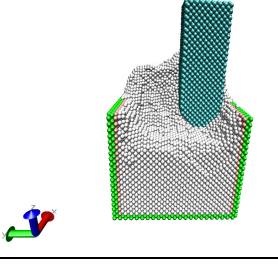
5.2.1 Conclusion

It can be seen that the tangential cutting force components are considerably affected by the interatomic potential pair used, but they are not greatly affected by whether the tool is rigid or deformable. The total energy of the system on the other hand is much lower when the tool is non rigid than when it is rigid. The choice of the use the interatomic potentials can be based on the ones with lowest cutting forces and the total energies.

5.3 The Effect of Depth of Cut

The depths of cut used in the study are 0.5nm, 1.0nm, 1.5nm, 2nm, 2.5nm and 3 nm.

Table 5.8: Comparison of the Material Removal for the Three Passes for Depth of Cut (0.5-3nm)

Depth of Cut (nm)	Pass 1	Pass 2	Pass 3
0.5			
1			
1.5			
2			

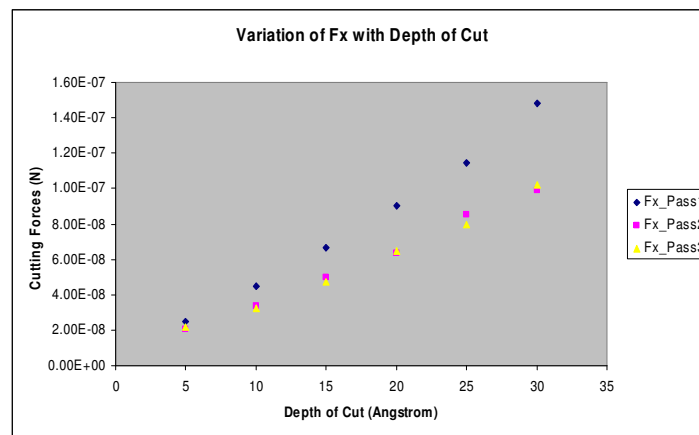
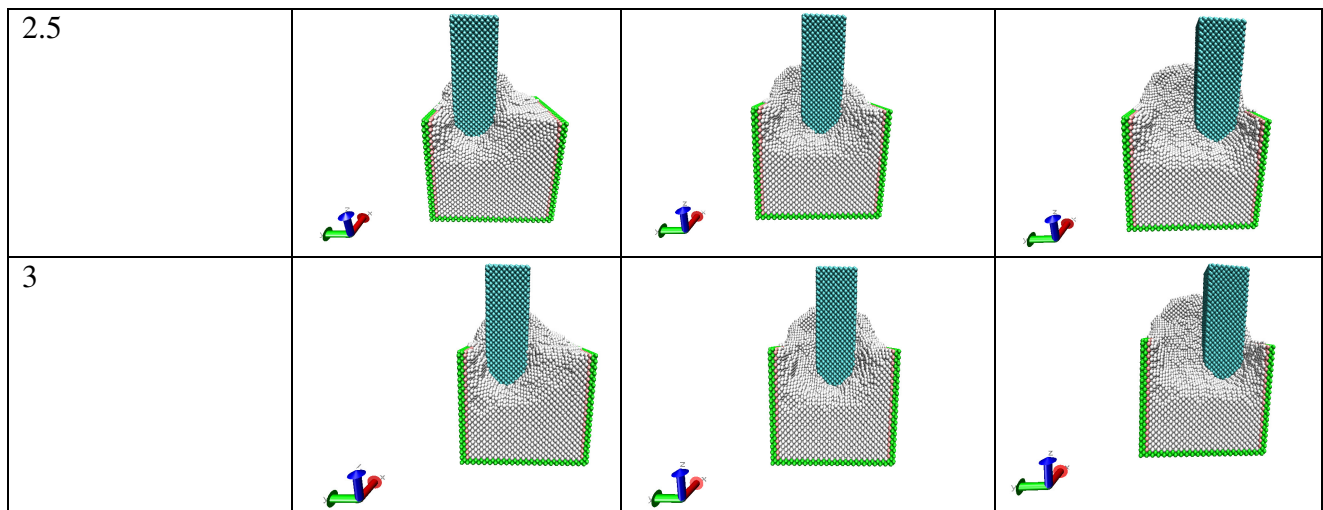


Figure 5.12: Variation of F_x with Depth of Cut

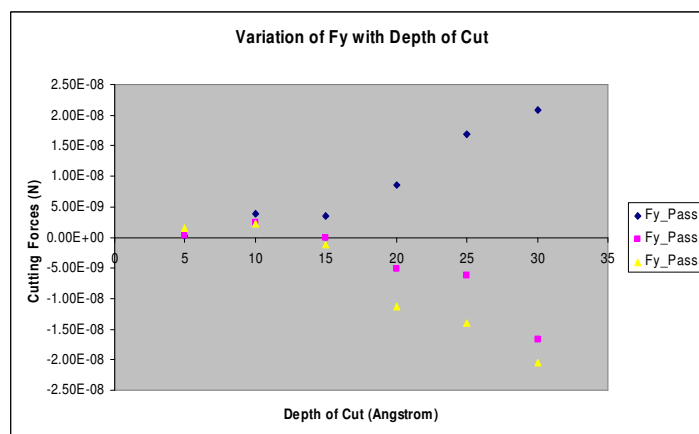


Figure 5.13: Variation of F_y with Depth of Cut

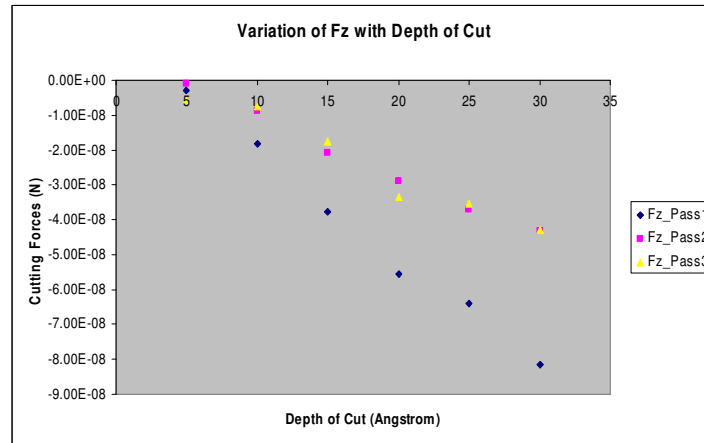


Figure 5.14: Variation of F_z with Depth of Cut

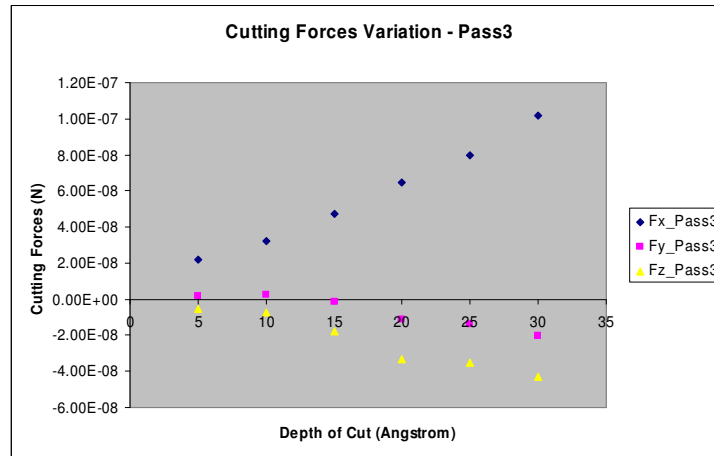


Figure 5.15: Variation of F_x , F_y and F_z in Pass 3 with Depth of Cut

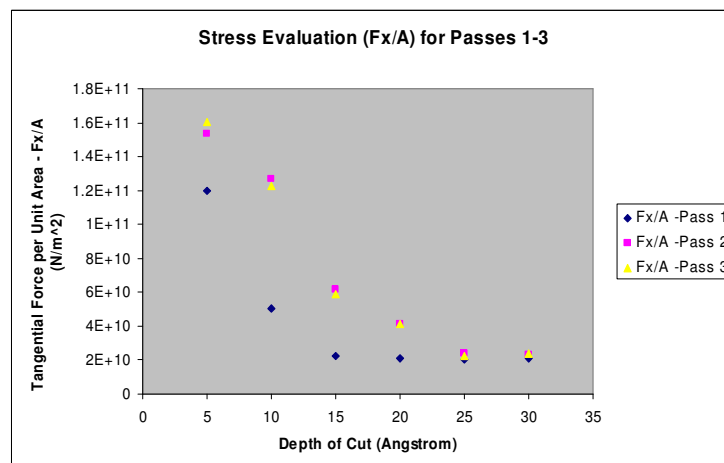


Figure 5.16: Stress Variation with Depth of Cut for Passes 1-3

Discussion

Table 5.8 shows the comparison of the material removal for the three passes for the depth of cut (0.5-3nm). From the table, it can be observed that the amount of atoms removed increases as the depth of cut increases, which is logical, because as the depth increases, there is more volume of material atoms to be removed. The associated cutting forces are shown in Table C.11. The average tangential and the normal cutting force components decrease with the consecutive passes. Figure 5.9 shows the variation of F_x with depth of cut. It can be seen that for the different passes, F_x increases with increase in depth of cut and F_x is larger in pass 1 than in passes 2 and 3. F_y increases in pass 1 and decreases in pass 2 and 3; with increase in the depth of cut. The variation is quite small as shown in Figure 5.13, as F_y is supposed to be zero theoretically. F_z , as shown in Figure 5.14, is similar also to F_x . It increases in magnitude with increase in depth of cut. Figure 5.15 shows the variation of the cutting forces in pass 3 with depth of cut. Figure 5.16 shows the stress variation with depth of cut for the three passes. It can be observed that as the depth of cut increases, the stress values decrease and it is higher for passes 2 and 3. The stress values are in the range from 160GPa to 20GPa. The values remain constant at around 20 GPa for all passes for higher depth of cut – from 2.5nm. This is due to the tool geometry, which becomes similar for higher depths of cut. The highest stress values are for depth of cut of 0.5nm during passes 2 and 3. It shows that the cutting resistance of the copper material is highest at very small depth cuts.

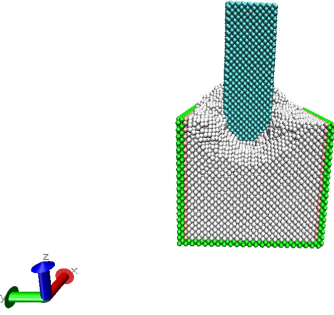
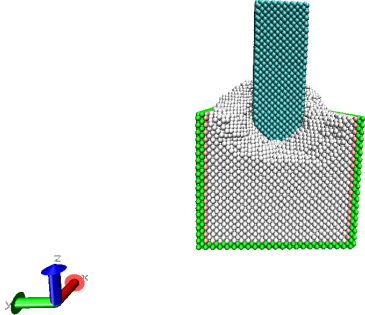
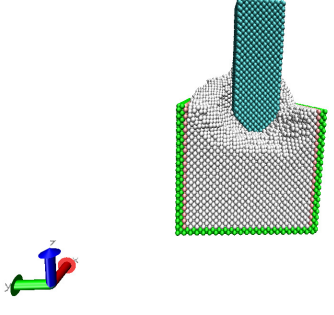
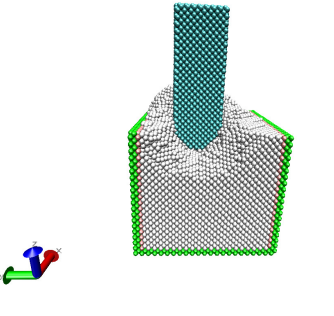
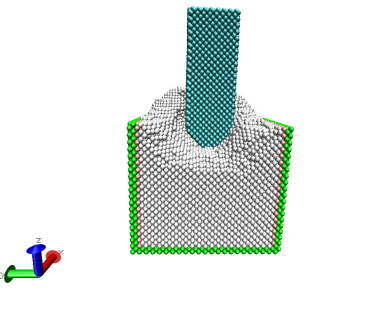
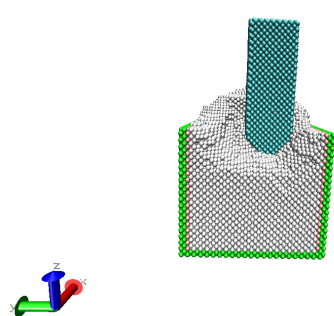
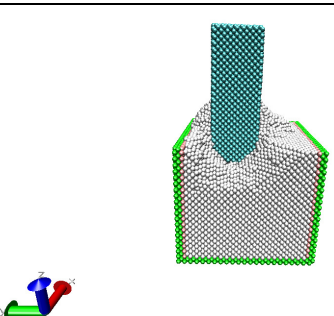
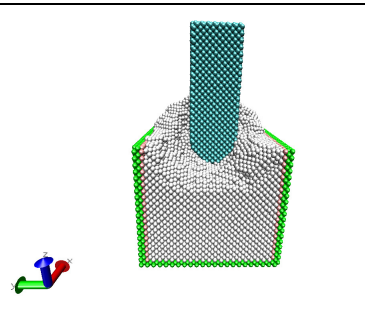
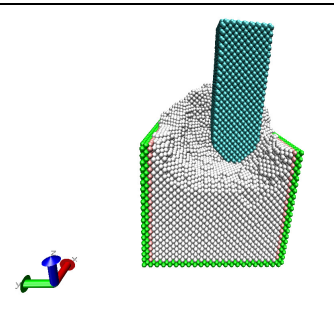
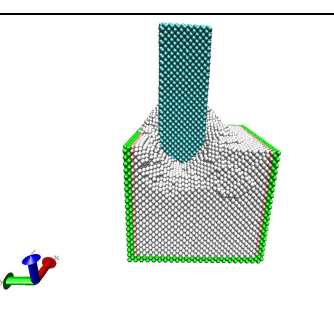
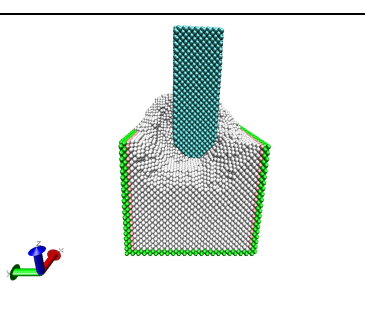
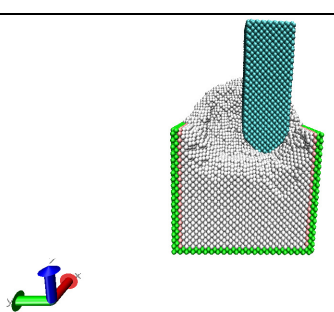
5.3.1. Conclusion

It can be concluded that the magnitude of the tangential and the normal components of the cutting forces increase with increase in the depth of cut. The ratios of the tangential to normal force components decrease as depth of cut increases, but remain fairly constant for each of the passes after the depth of cut of 1.5nm, with values in the range of 1.1-2.3. Stress values decrease with increase in the depth of cut and remain constant for high depth of cut (> 2.5nm). This is due to the shape of the tool; as the depth of cut increases, the shape of the tool above the end has the same cross sectional area.

5.4 The Effect of Feed Rate

For the feed rate; the following were used namely; 0.5nm, 0.75nm, 1.0nm, 1.25nm and 1.5nm.

Table 5.9: Simulations for Different Feeds (0.5 – 1.5nm)

Feed (nm)	Pass 1	Pass 2	Pass 3
0.5			
0.75			
1.0			
1.25			

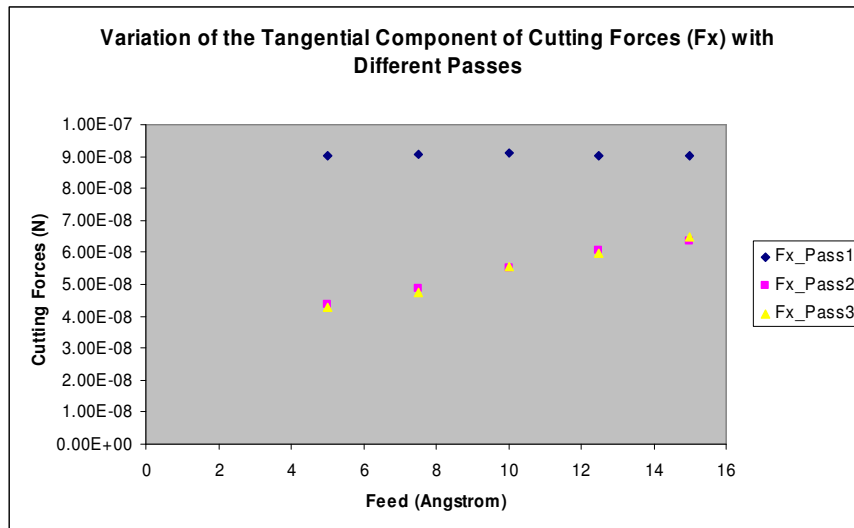
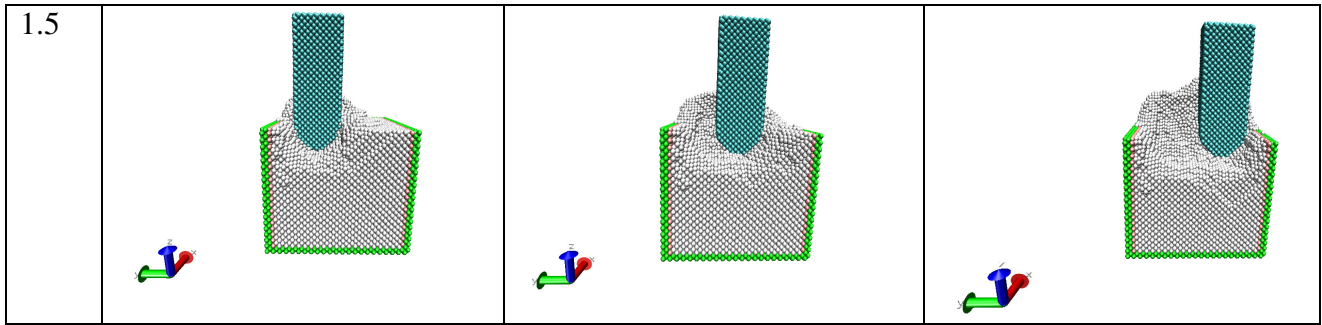


Figure 5.17: Variation of F_x with Passes 1-3

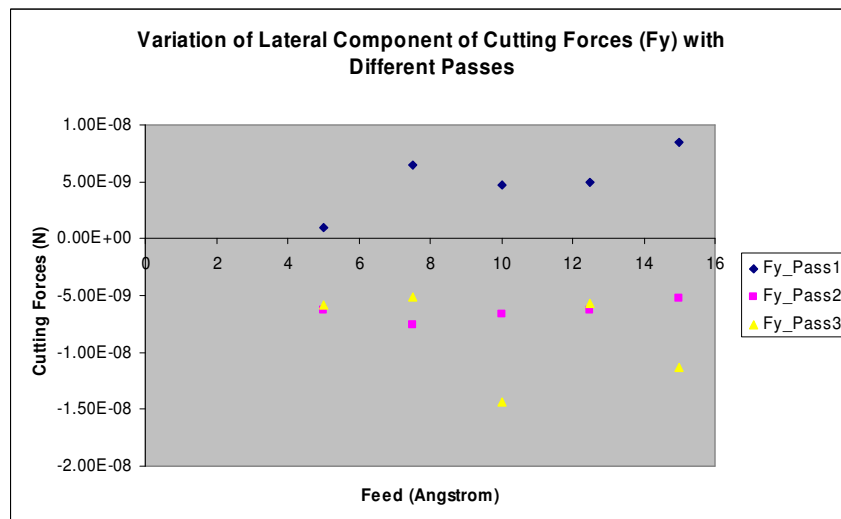


Figure 5.18: Variation of F_y with Passes 1-3

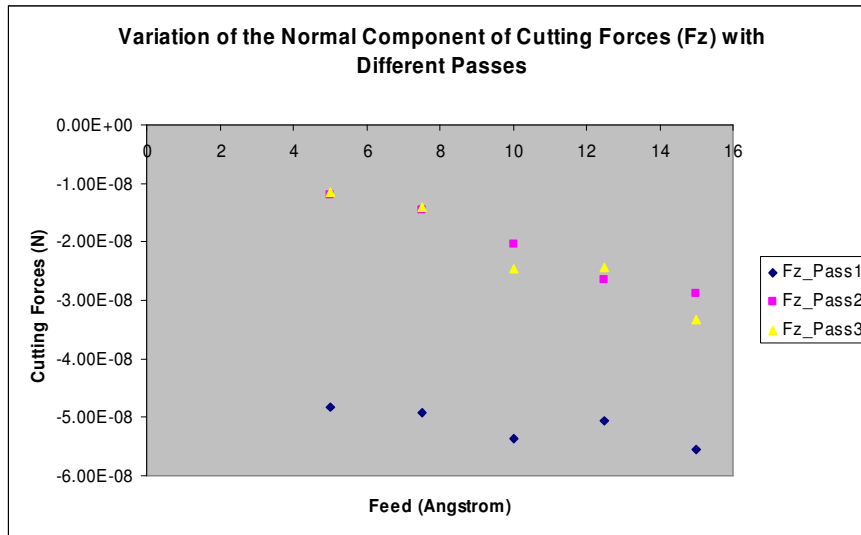


Figure 5.19: Variation of F_z with Passes 1-3

Discussion

Table 5.9 shows the comparison of the material removal for the three passes for feed of (0.5-1.5nm). The associated cutting forces are shown in Table C.12. The tangential and the normal components of the cutting forces decrease for the consecutive passes. Figures 5.17-5.19 show the variation of the cutting forces with feed rate for passes 1-3. It can be seen that F_x and F_z increases with the increase in the feed rate. This is because as the feed rate increases, the amount of material to be removed increases and so this increase in resistance will increase the F_x and F_z . For F_y , it fluctuates around zero.

5.4.1 Conclusion

The average tangential and normal components of the cutting forces increase with increase in the feed rate. Also, the amount of material removal increases with increase in the feed.

5.5 The Effect of Rake Angle

The rake angles used in the study are -5° , -10° and -15°

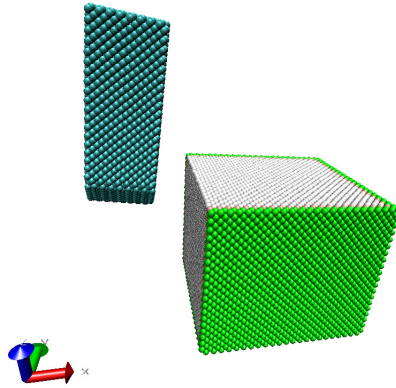


Figure 5.20: Rake Angle Negative 5 (-5°)

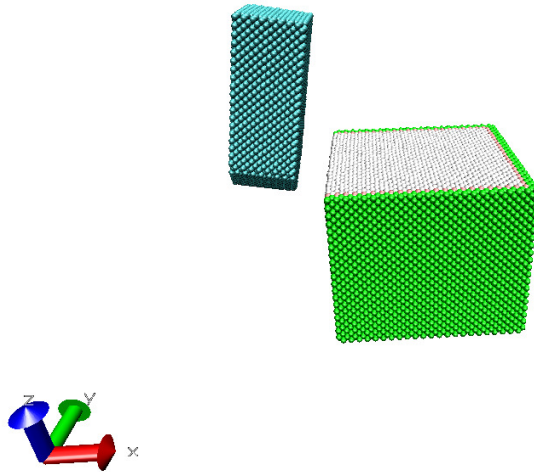


Figure 5.21: Rake Angle Negative 10 (-10°)

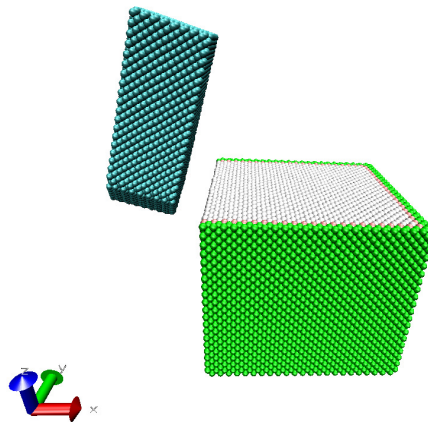
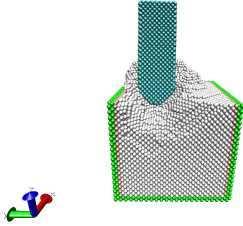
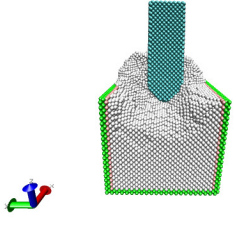
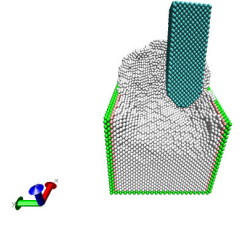
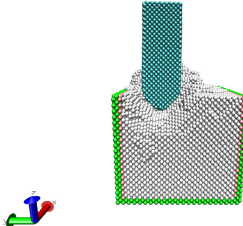
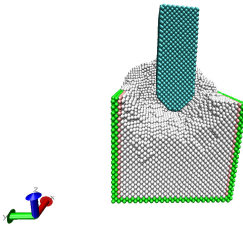
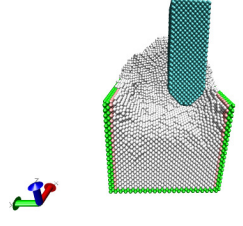
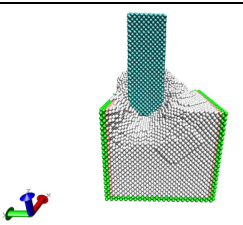
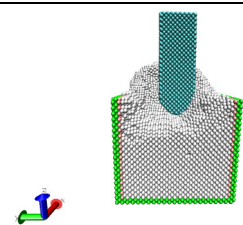
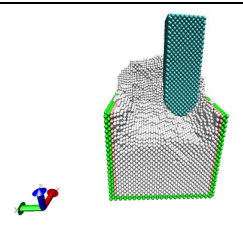


Figure 5.22: Rake Angle Negative 15 (-15°)

Table 5.10: Simulations for Different Rake Angles (-15°, -10°, and -5°)

Rake Angle (degrees)	Pass 1	Pass 2	Pass 3
-15			
-10			
-5			

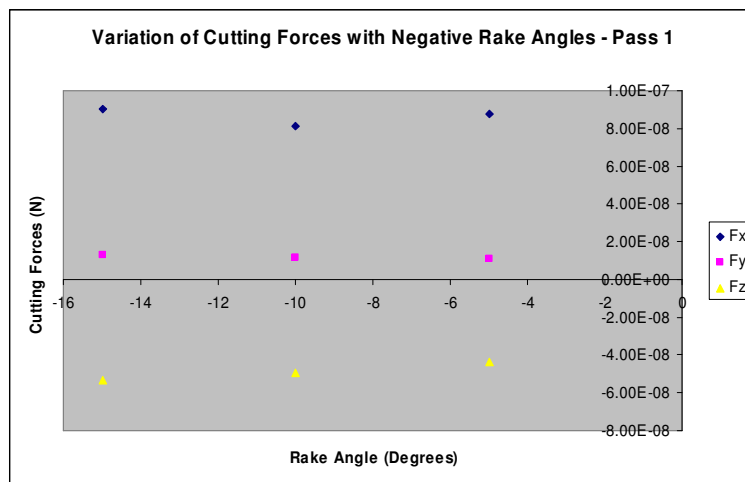


Figure 5.23: Variation of Cutting Forces with Rake Angles – Pass 1

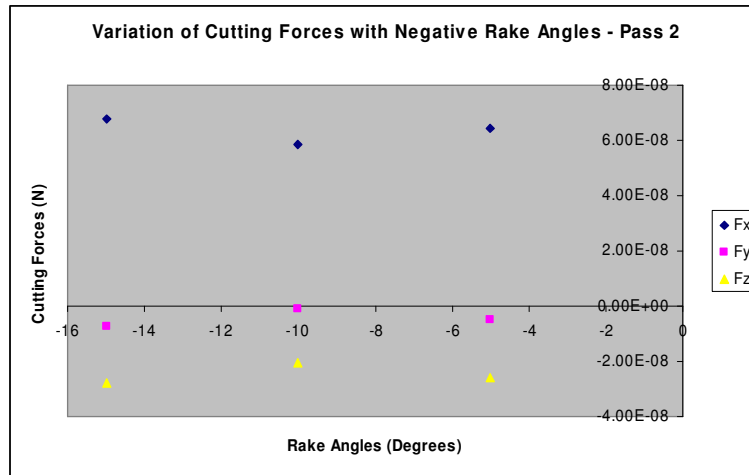


Figure 5.24: Variation of Cutting Forces with Rake Angles – Pass 2

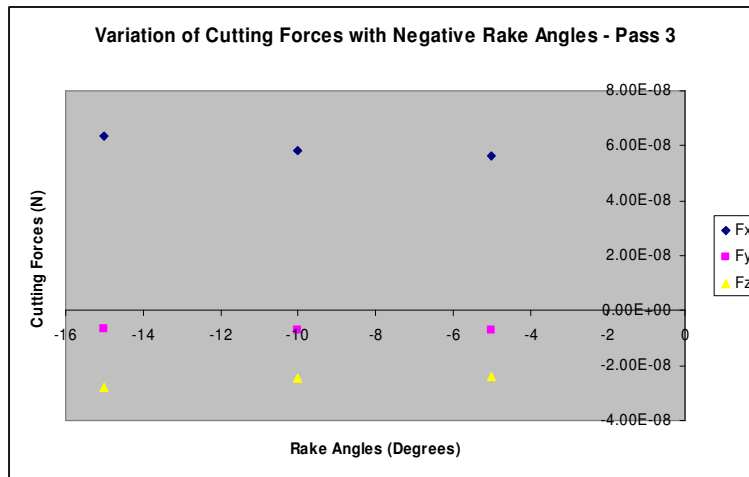


Figure 5.25: Variation of Cutting Forces with Rake Angles – Pass 3

Discussion

Figures 5.20-5.22 show the initial configuration for the rake angle of negative 5° , negative 10° and negative 15° . Table 5.10 shows the comparison of the material removal for the three passes for the different rake angles and Table C.13 shows the associated cutting forces. As can be observed in Figure 5.23, the variation of the cutting forces components F_x , F_y and F_z appear to increase with increase in the negative rake angles (-5° to -15°) for pass 1. Similar features are observed for passes 2 and 3 (Figures 5.24 and 5.25).

5.5.1 Conclusion

The cutting force component doesn't show considerable change as the rake angle increases from negative 5° to negative 15° , which is not in agreement with macroscale machining results.

Chapter 6. Atomic Surface Roughness Evaluation

6.1 Introduction

As highlighted in section 2.1.5, the atomic surface roughness is very significant in assessing the quality of performance nano surfaces. The theoretical value for the atomic roughness of copper (rms) is given as 0.032nm (Namba et al 2000).

In this study multi-pass nanometric atomistic simulations were carried and the results provide the platform from which the atomic surface roughness is evaluated.

6.2 The Algorithm for the Evaluation of Atomic Surface Roughness

The following are steps to take to evaluate the surface roughness from the simulation results;

- Read the input file of the simulated results
- Extract the surface atoms that contribute to the surface roughness evaluation

To extract the surface atoms:

- Carry out coordination analysis to determine the number of nearest neighbours of each atom
 - Then the area of interest on the surface, for the evaluation of the surface roughness is selected
- Obtain the (x,y,z) data of the surface atoms
 - Transform the (x,y,z) data to a grid data
 - The grid data is then fed into a suitable surface analysis software to obtain the surface roughness

6.3 The Implementation and Comparison of Surface Roughness for the Multiple Pass Simulations

The above algorithm was implemented by using the following:

The OVITO visualization software was used to extract the surface atoms. Then the (x,y,z) data of the surface atoms was transformed into a grid data by using the Matlab. The grid data was used as input to Surfstand, a 3D surface roughness standard software developed at the Centre for Precision Technologies, for the evaluation of the surface roughness.

The results of the multipass simulations carried out in Chapter 5 were used. The results for the EAM-LJ and the EAM-Morse potential pairs were used. The depth of cut range (0.5-3.0nm) and the velocity range (40-220m/s) were used. The results are shown in Tables 6.1 – 6.4. Figures 6.1 and 6.2 show the near perfect surface of the workpiece and the surface atoms contributing to the surface roughness. The Sa value was indeterminate, as this may be close to zero.

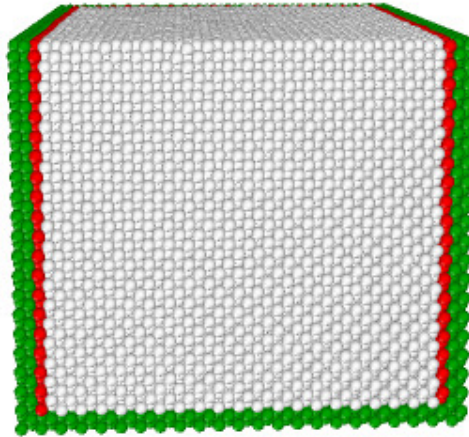


Figure 6.1: The Near Perfect Surface of the Workpiece

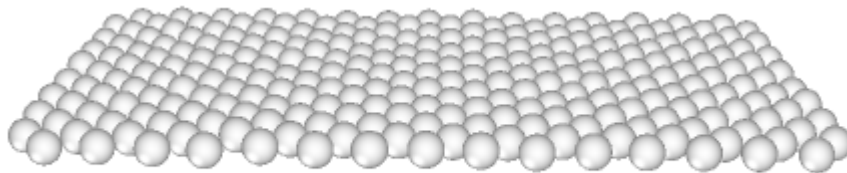
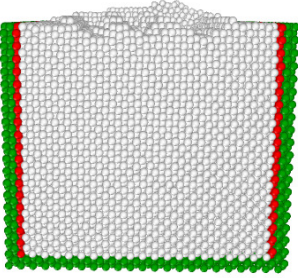
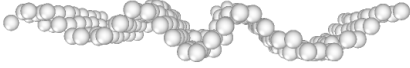
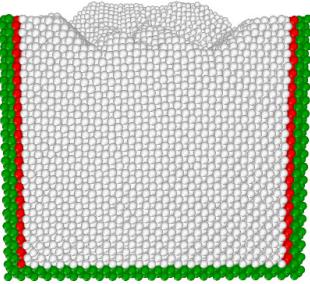
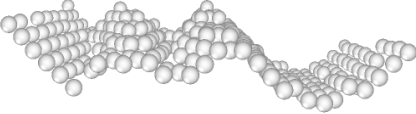
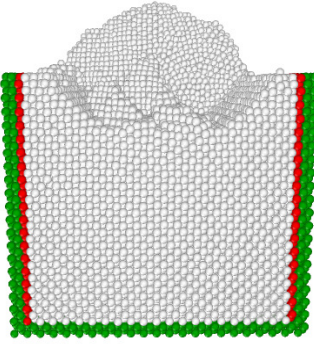
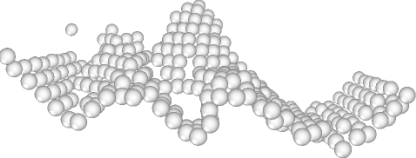
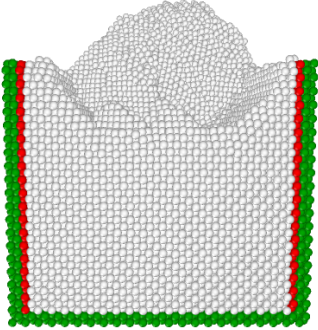
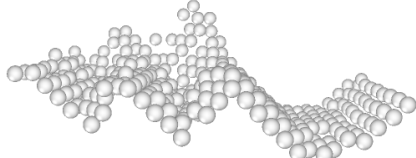
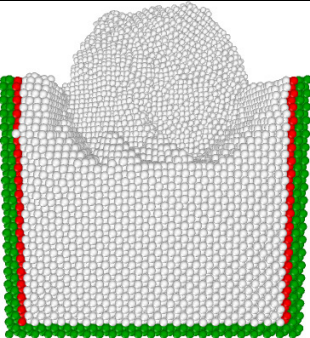
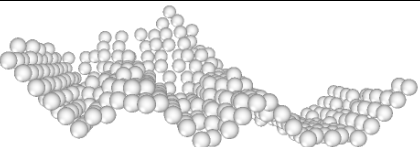
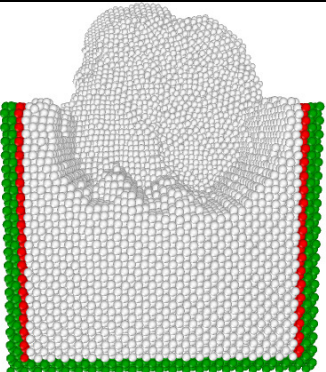
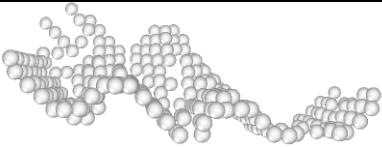


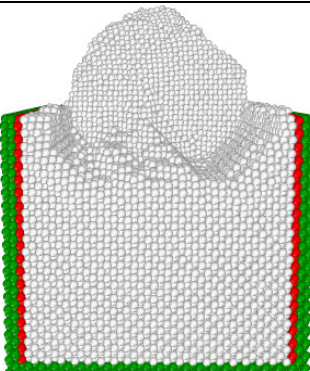
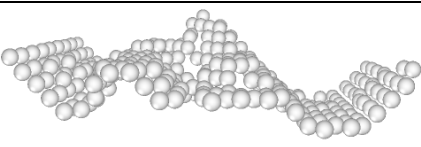
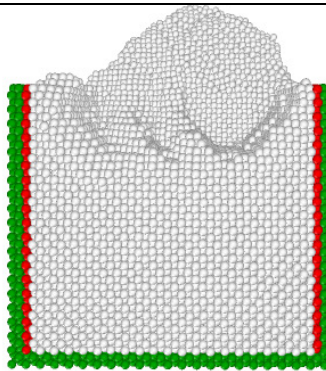
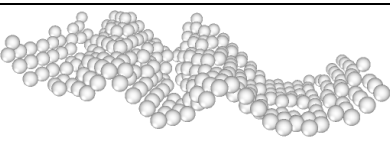
Figure 6.2: The Surface Atoms Contributing to the Surface Roughness

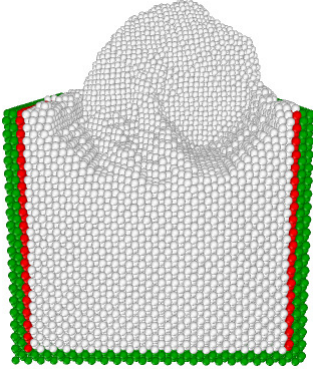
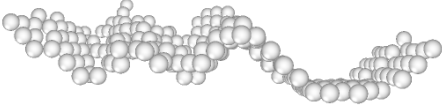
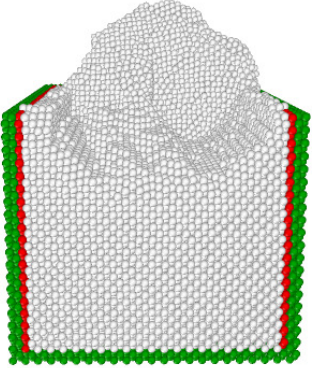
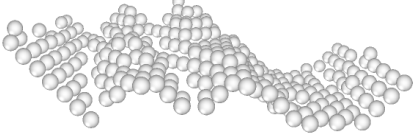
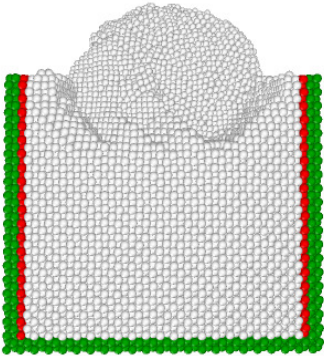
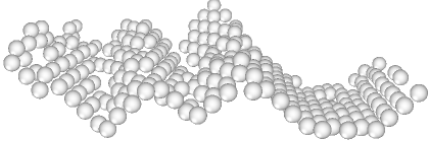
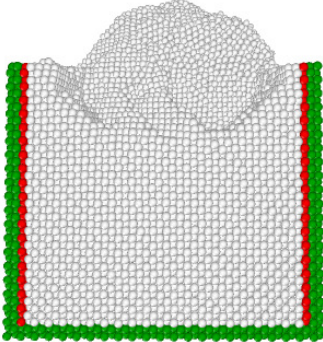
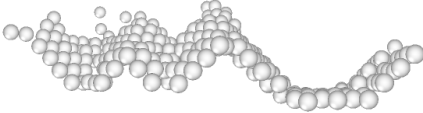
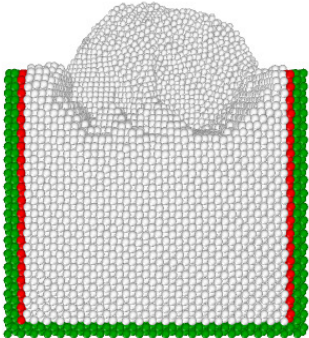
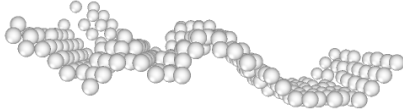
Table 6.1: Surface Roughness Results for the EAM-LJ Potentials for Depth of Cut (0.5-3.0nm)

Depth of Cut (nm)	Simulation Results	Surface Atoms Contributing to Sa	Sa (m)
0.5			1.89E-10
1.0			2.73E-10
1.5			3.45E-10
2.0			2.76E-10

2.5			2.51E-10
3.0			3.23E-10

**Table 6.2: Surface Roughness Results for the EAM-LJ Potentials for Velocity (40-220m/s)
(Depth of Cut – 2.0nm)**

Velocity (m/s)	Simulation Results	Surface Atoms Contributing to Sa	Sa (m)
40			2.60E-10
60			2.94E-10

80			2.68E-10
100			3.00E-10
120			2.70E-10
140			3.22E-10
160			2.65E-10

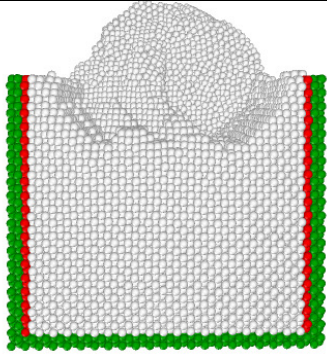
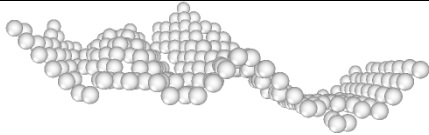
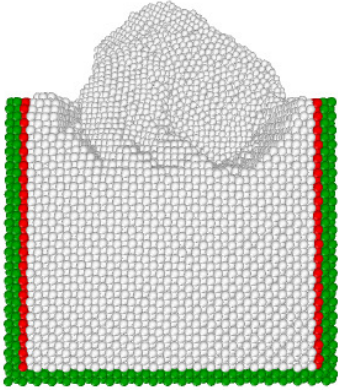
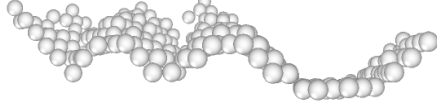
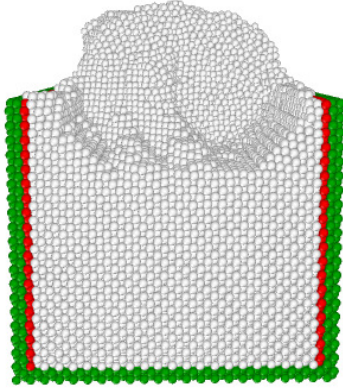
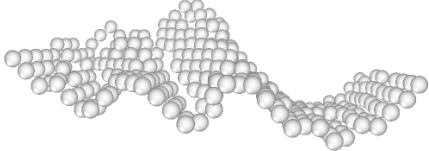
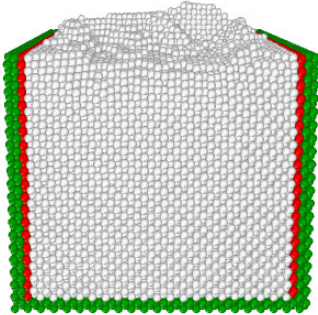
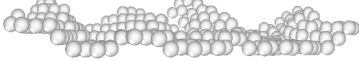
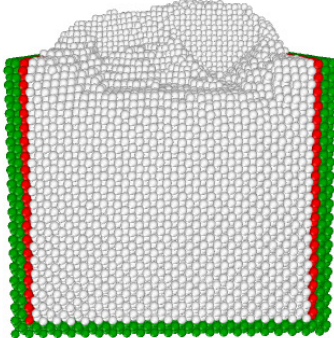
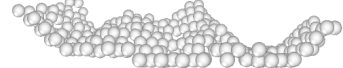
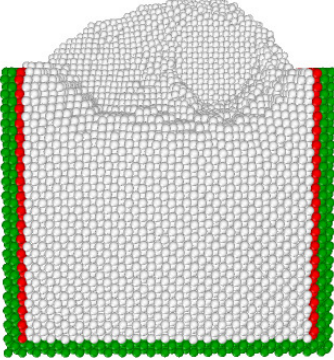
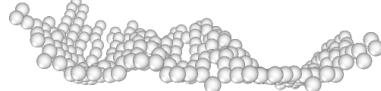
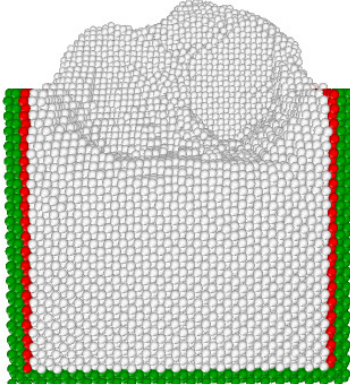
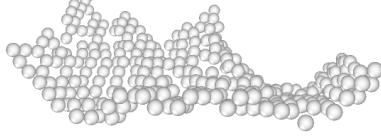
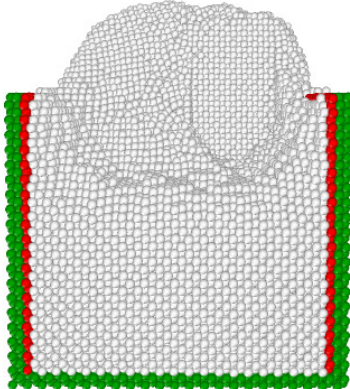
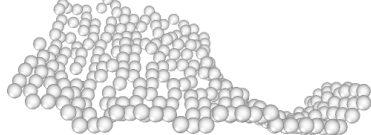
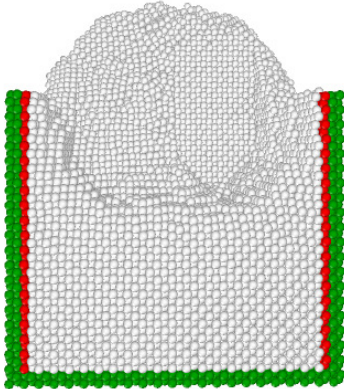
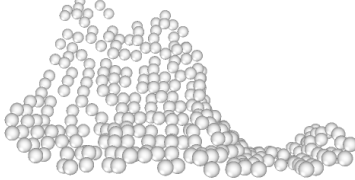
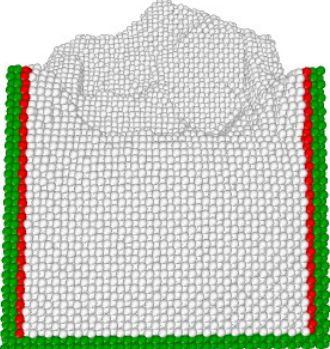
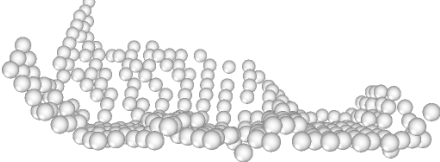
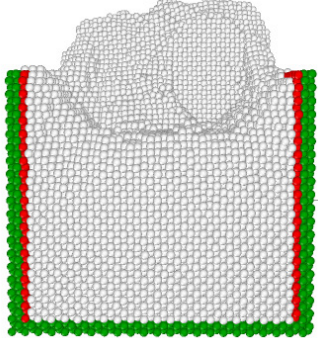
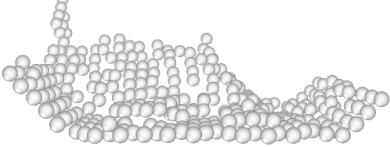
180			3.16E-10
200			2.93E-10
220			3.44E-10

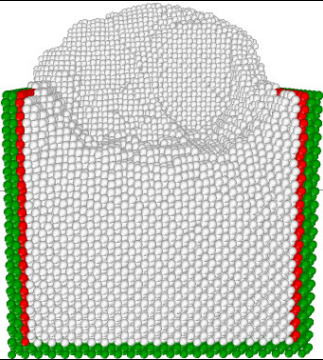
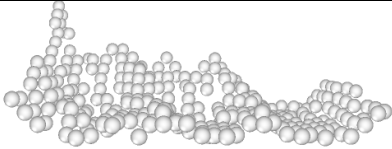
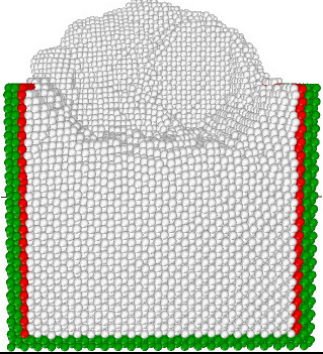
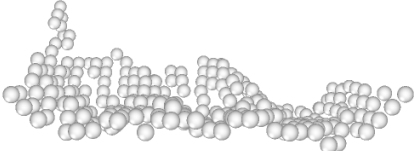
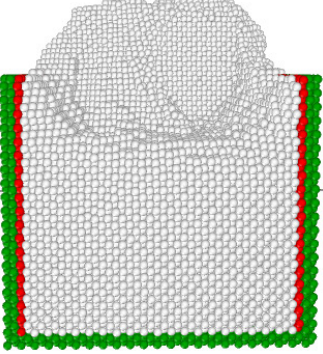
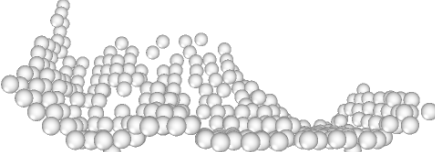
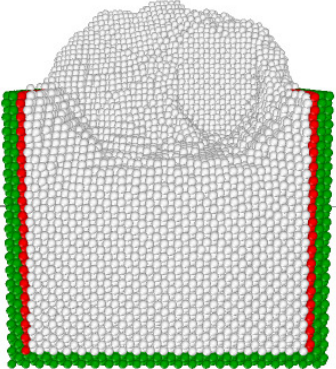
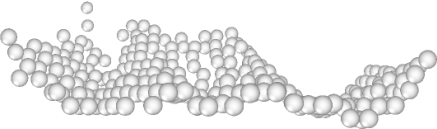
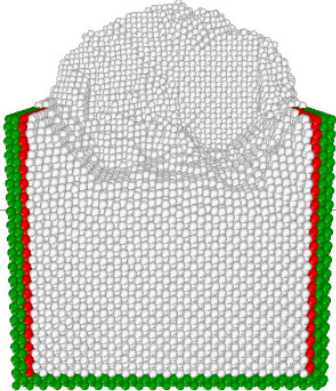
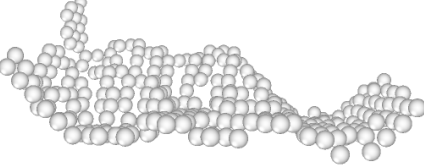
Table 6.3: Surface Roughness Results for the EAM-Morse Potentials for Depth of Cut (0.5-3.0nm)

Depth of Cut (nm)	Simulation Results	Surface Atoms Contributing to Sa	Sa (m)
0.5			1.67E-10
1.0			2.64E-10
1.5			2.83E-10
2.0			3.49E-10

2.5			5.26E-10
3.0			5.59E-10

**Table 6.4: Surface Roughness Results for the EAM-Morse Potentials for Velocity (40-220m/s)
(Depth of Cut – 2.0nm)**

Velocity (m/s)	Simulation Results	Surface Atoms Contributing to Sa	Sa (m)
40			2.25E-10
60			2.90E-10

80			2.28E-10
100			2.20E-10
120			3.06E-10
140			2.67E-10
160			3.04E-10

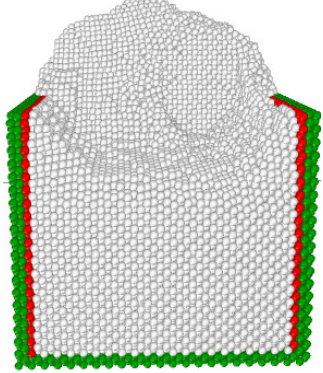
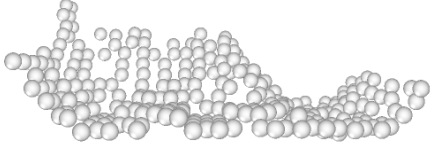
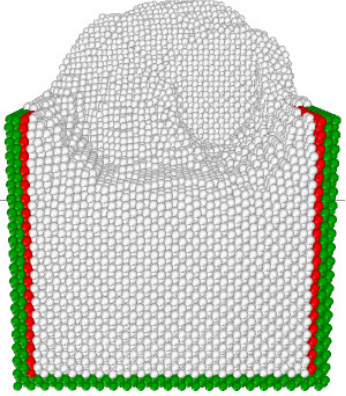
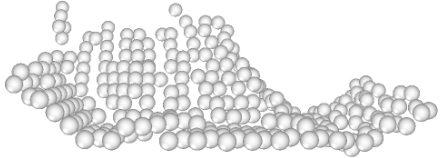
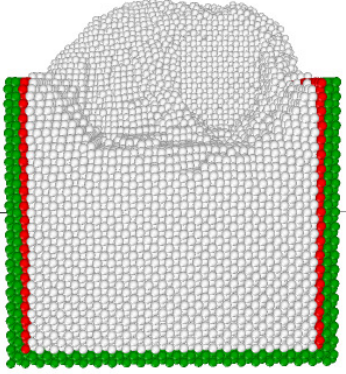
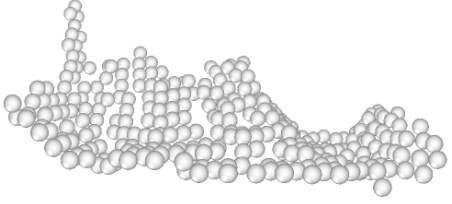
180			2.76E-10
200			3.35E-10
220			3.08E-10

Table 6.5: Surface Roughness Results for the EAM-LJ and EAM-Morse Potential Pairs for Depth of Cut – (0.5-3.0nm)

Depth of Cut (nm)	Sa (EAM-LJ Potentials) (m)	Sa (EAM-Morse) (m)
0.5	1.89E-10	1.67E-10
1.0	2.73E-10	2.64E-10
1.5	3.45E-10	2.83E-10
2.0	2.76E-10	3.49E-10
2.5	2.51E-10	5.26E-10
3.0	3.23E-10	5.59E-10

The variation of the surface roughness, Sa with the depth of cut for the EAM-LJ and the EAM-Morse potentials are shown in Figures 6.3 and 6.4

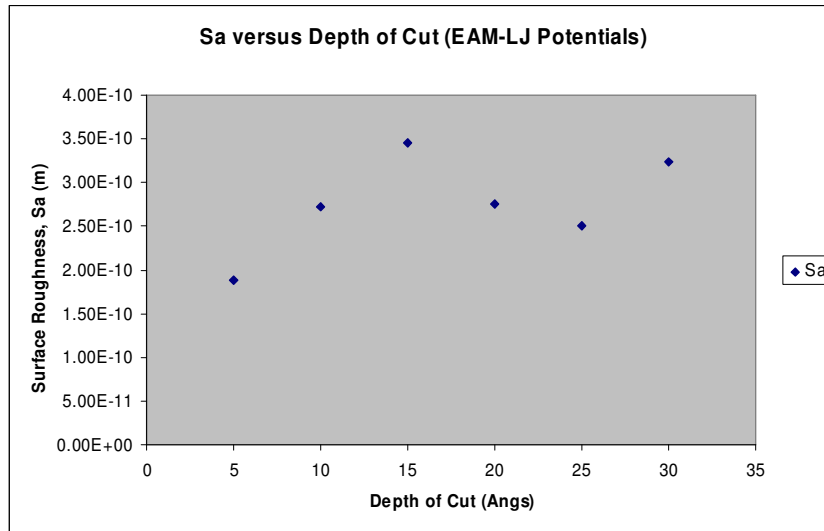


Figure 6.3: Variation of Sa with Depth of Cut for the EAM-LJ Potentials

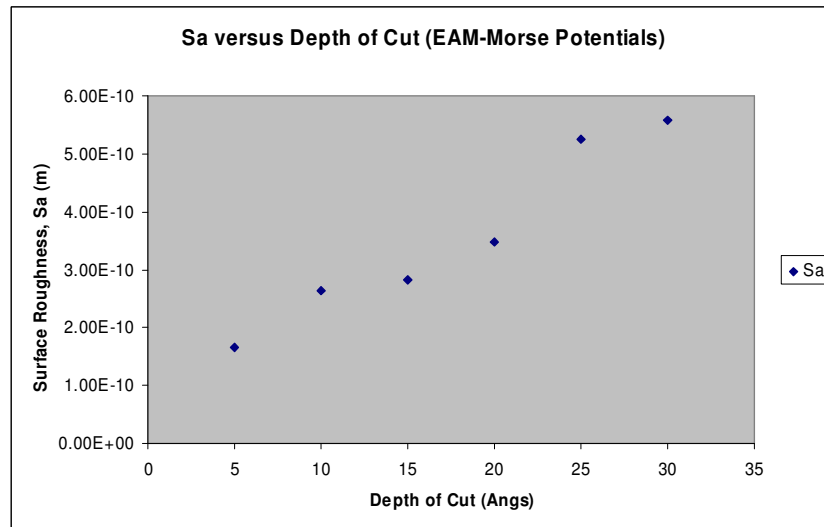


Figure 6.4: Variation of Sa with Depth of Cut for the EAM-Morse Potentials

Table 6.6: Surface Roughness Results for the EAM-LJ and EAM-Morse Potential Pairs for Velocity – (40-220m/s)

Velocity (m/s)	Sa (EAM-LJ Potentials) (m)	Sa (EAM-Morse) (m)
40	2.60 E-10	2.25E-10
60	2.94 E-10	2.90E-10
80	2.68 E-10	2.28E-10
100	3.00 E-10	2.20E-10
120	2.70 E-10	3.06E-10
140	3.22 E-10	2.67E-10
160	2.65 E-10	3.04E-10
180	3.16 E-10	2.76E-10
200	2.93 E-10	3.35E-10
220	3.44 E-10	3.08E-10

The variation of the surface roughness, Sa with velocity for the EAM-LJ and the EAM-Morse potentials are shown in Figures 6.5 and 6.6.

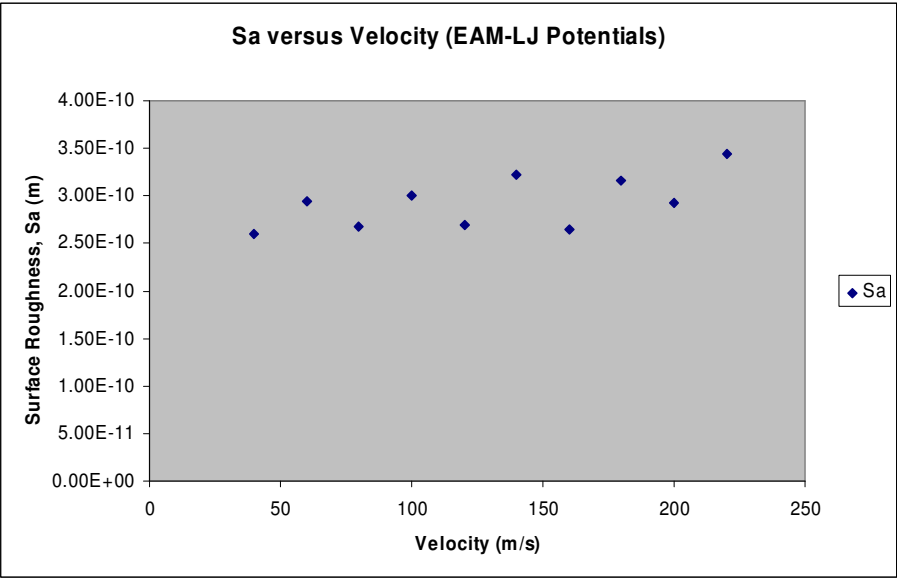


Figure 6.5: Variation of Sa with Velocity for the EAM-LJ Potentials

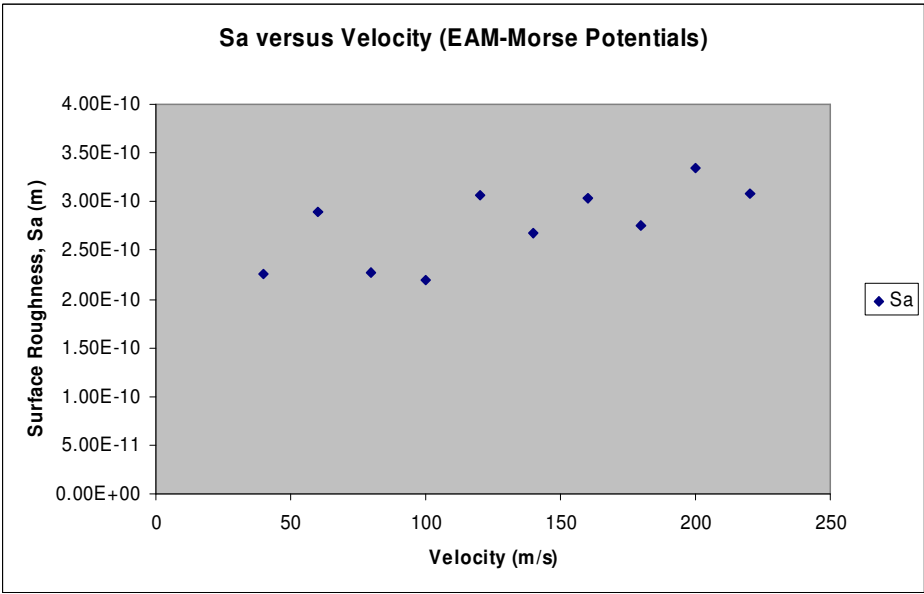


Figure 6.6: Variation of Sa with Velocity for the EAM-LJ Potentials

6.4. Discussions and Concluding Remarks

Figure 6.3 shows the variation of S_a with depth of cut for the EAM-LJ potentials. The S_a is lowest for the depth of cut of 0.5nm, it increases to 1.5nm and then decreases to 2.5nm, before increasing to 3. Figure 6.4 shows the variation of S_a with depth of cut for the EAM-Morse potentials. The S_a is lowest for depth of cut of 0.5nm and it increases linearly to 3.0nm. Figures 6.5 and 6.6 show the variation of S_a with velocity. The S_a seems to be increasing and decreasing as the velocity increases. On the macroscale, the S_a should decrease as the velocity increases. On the nanoscale, the parameters are very sensitive to small variations. This variation may either be size effects of the simulation model or some other factors. As it can be observed from Figures 6.1-6.4 that the choice of interatomic potentials affect the prediction of the surface roughness of nanomachining using the MD simulation. The S_a increase and decreases for a certain range as velocity increases.

Chapter 7. Experimental Set-up and Procedure

7.1 Introduction

The MD method has been used to simulate nanometric machining of monocrystalline diamond tool on monocrystalline copper workpiece. The objective of this chapter is to attempt to observe the mechanisms of material removal on the nanometre scale and to validate the simulation results.

The following illustrates the attempt and the difficulty of validating nanomachining simulation results. The aim of the experiment was to observe the phenomena of rubbing, ploughing and cutting/chip formation.

7.2 Sample Preparation

Copper specimen were obtained from the laboratory, They were then cut into smaller pieces of roughly 15 x 10 mm. Circular moulds were made using a metallographic sample moulding machine, with the copper inserted in them. The resulting workpiece specimens were later hand polished to mirror finish, using the following 2-stage procedural steps below:

Stage 1

The copper specimen were hand grinded using abrasive grits of 320, 800, and 1200 micron on a grinding machine, in that order, for around 3-5 minutes each.

Stage 2

The copper specimen were then hand polished using 6, 1 and 0.5 micron abrasive cloth on a polishing machine for 2-3 minutes each.

These produced mirror finish surfaces.

Table 7.1: Process Breakdown

Stage	Abrasive Type	Process Time
Stage 1- Grinding	Abrasive Grit: 320 800 1200 2500	3-5 Minutes
Stage 2- Polishing	Abrasive Cloth: 6 1 0.5	2-3 Minutes

The polishing steps can be summarized as below:

- Step 1: Polish the workpiece sample using 320 microns grit on a polishing/grinding table for 3-5mins
- Step 2: Then polish the workpiece sample using 800 microns grit on a polishing/grinding table for 3-5mins
- Step 3: Then polish the workpiece sample using 1200 microns grit on a polishing/grinding table for 3-5mins
- Step 4: Then polish the workpiece sample using 6 microns grit, using a 200mm polishing cloth on a polishing/grinding table for 3-5mins
- Step 5: Then polish the workpiece sample using 1 microns grit, using a 200mm polishing cloth on a polishing/grinding table for 3-5mins

7.3 Experimental and Measuring Equipment

The validation experiments were carried out on a Nanoform 250, shown below.



Figure 7.1: The Nanoform 250 Ultraprecision Machine

7.3.1 Experimental Set-up

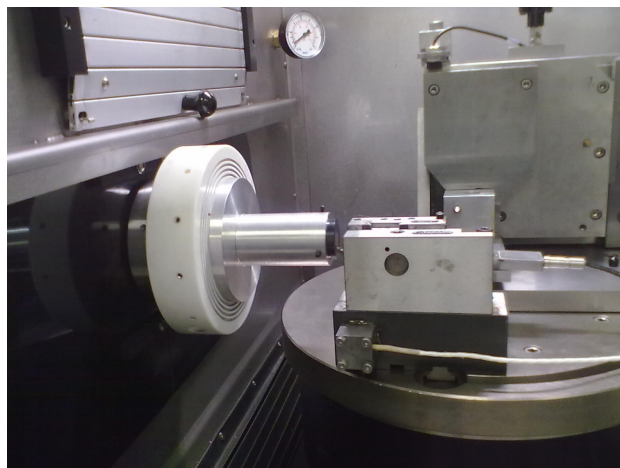


Figure 7.2: The Experimental Rig

7.3.2 Metrology Equipment

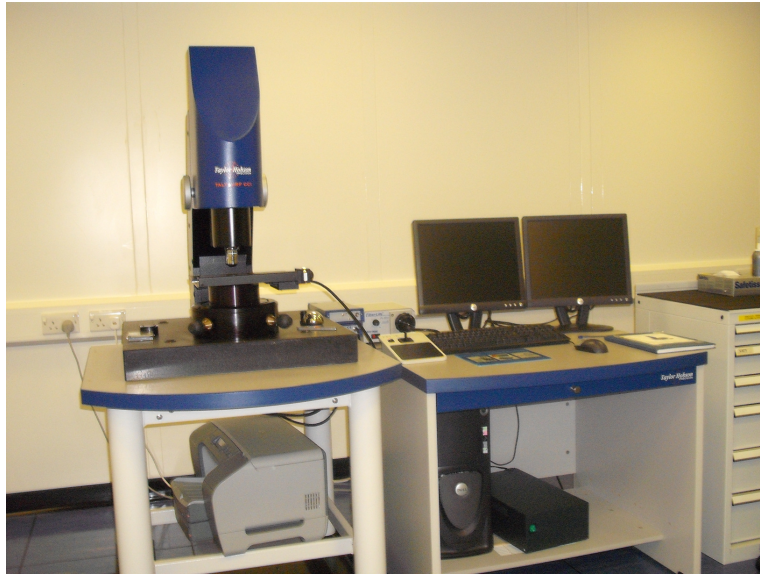


Figure 7.3: The CCI Interferometer



Figure 7.4: The AFM Machine

7.4 Experimental Procedure

The experiments were set-up on the Nanoform 250 diamond turning machine, by mounting the copper workpiece on the vertical spindle and the diamond tool on the horizontal spindle. The tool-workpiece contact was determined by running some preliminary passes and using Acoustic Emission (AE) sensors for the nano touch. The workpiece was fed in steps of 100nm and the diamond cutter was allowed to cut the copper specimen. The feed used was 15mm/min and the

spindle speed was varied from 2000rpm to 7000rpm in steps of 1000. For each of the spindle speed, three passes/scratches were made on the workpiece.

7.5 Analysis of the AE Signals

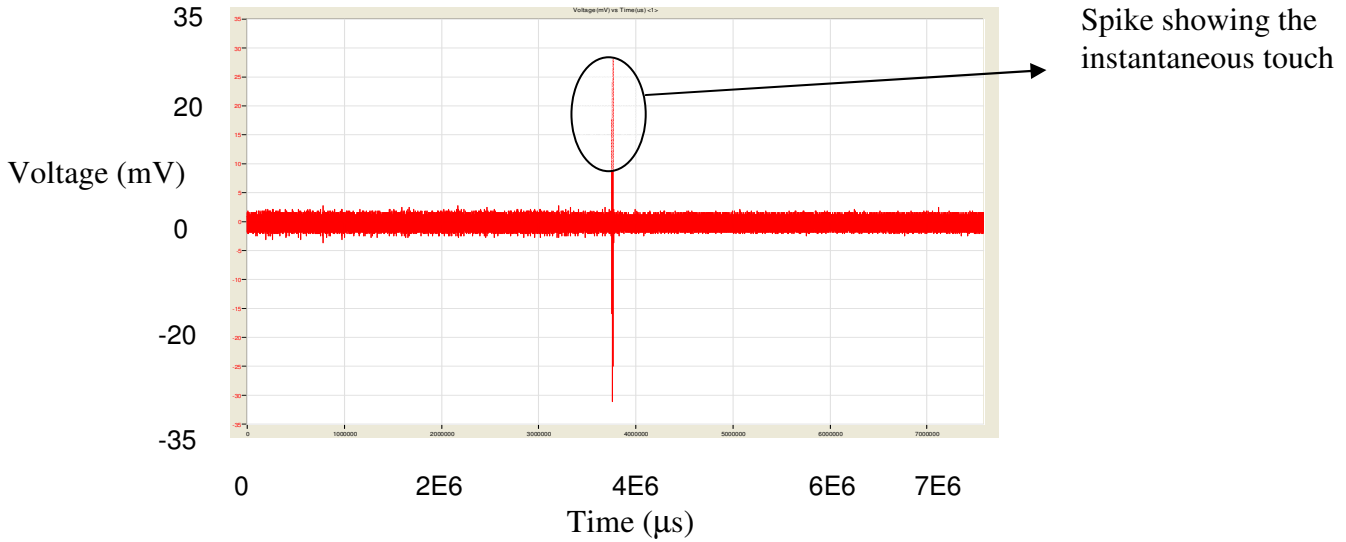


Figure 7.5: Raw AE Signal for RPM 7000 (Touch)

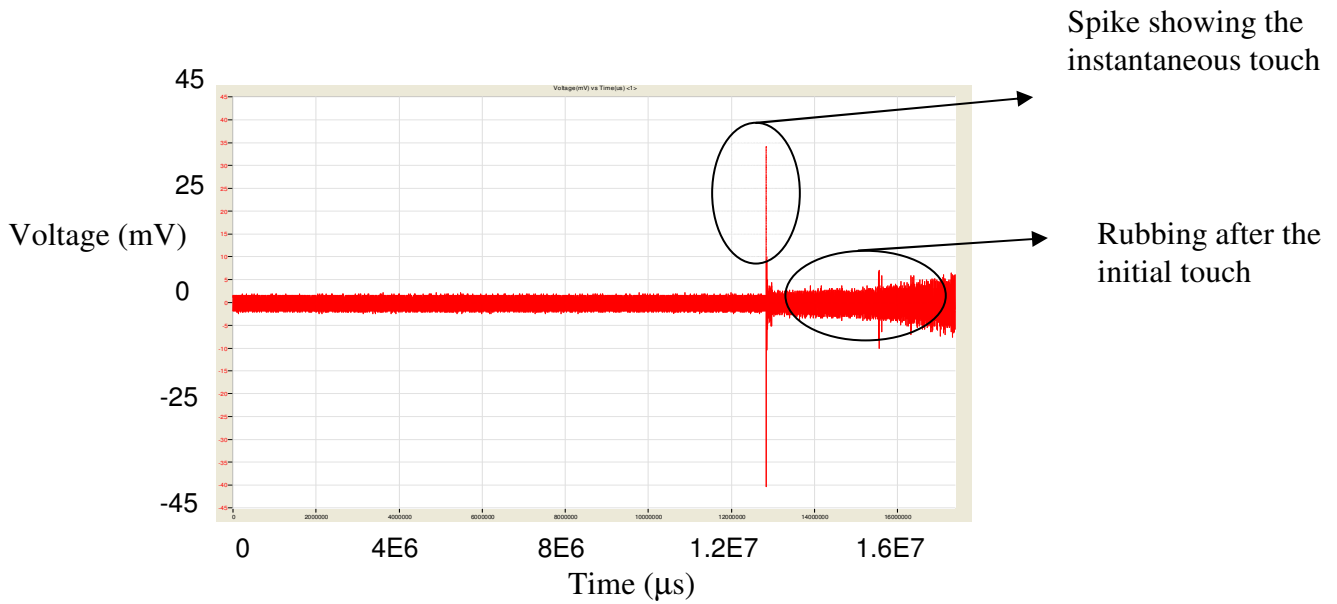


Figure 7.6: Raw AE Signal for RPM 7000 (Touch and rubbing)

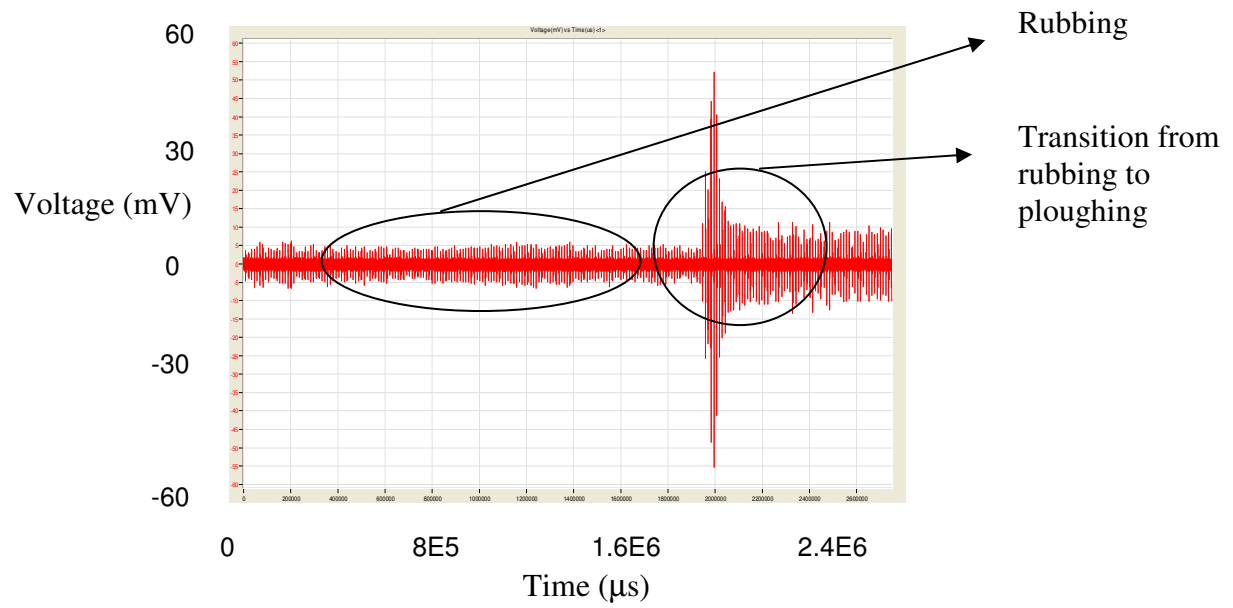


Figure 7.7: Raw AE Signal for RPM 5000 (Rubbing and Ploughing)

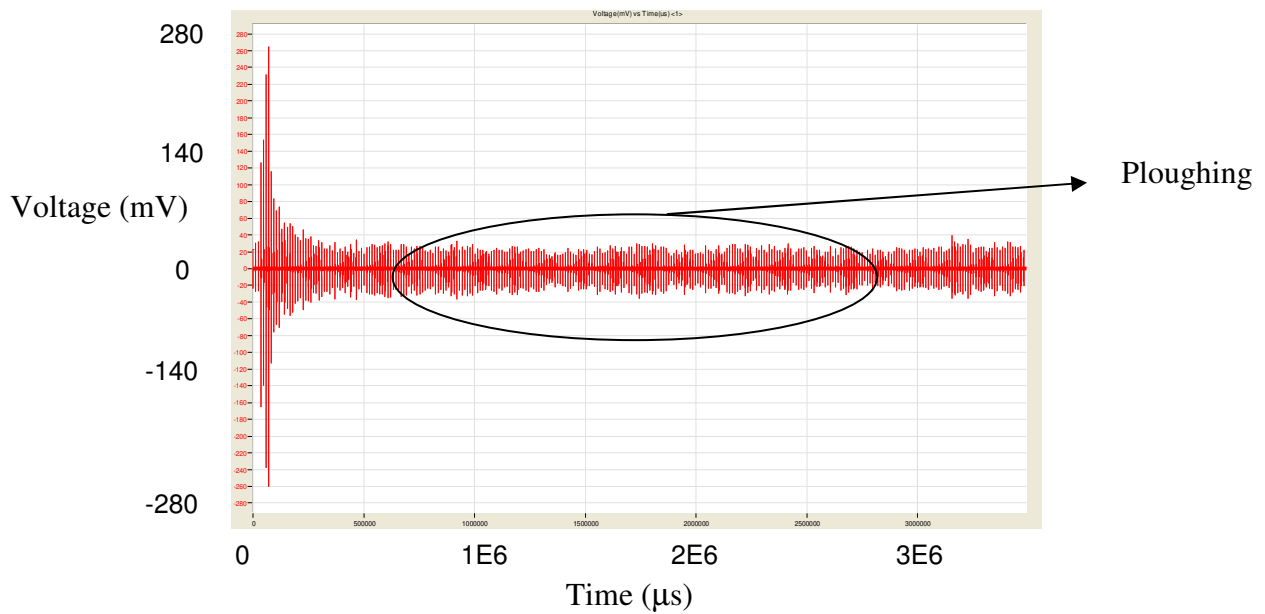


Figure 7.8: Raw AE Signal for RPM 5000 (Ploughing)

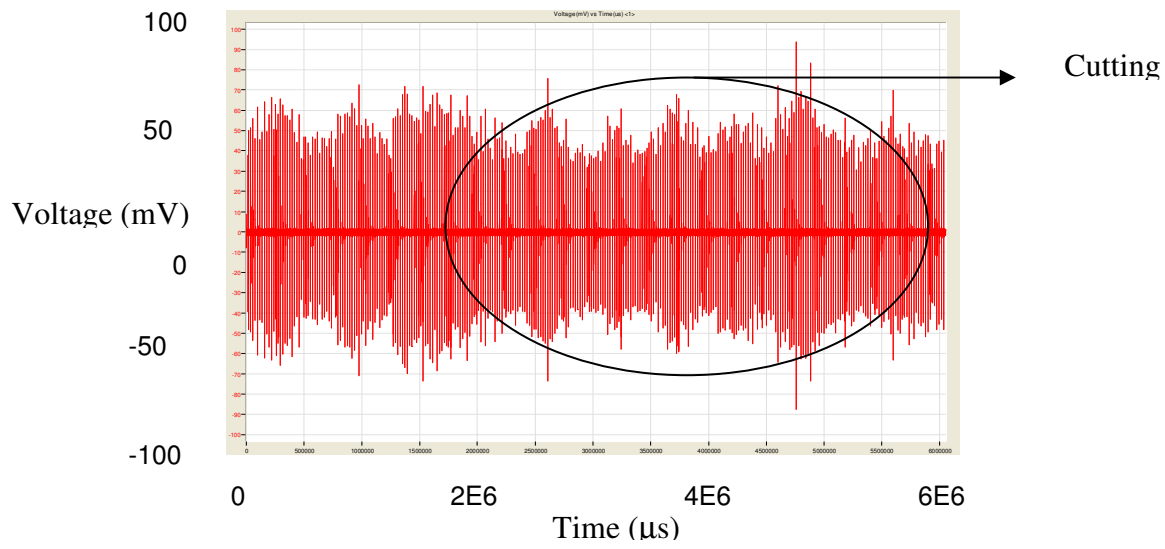


Figure 7.9: Raw AE Signal for RPM (Cutting)

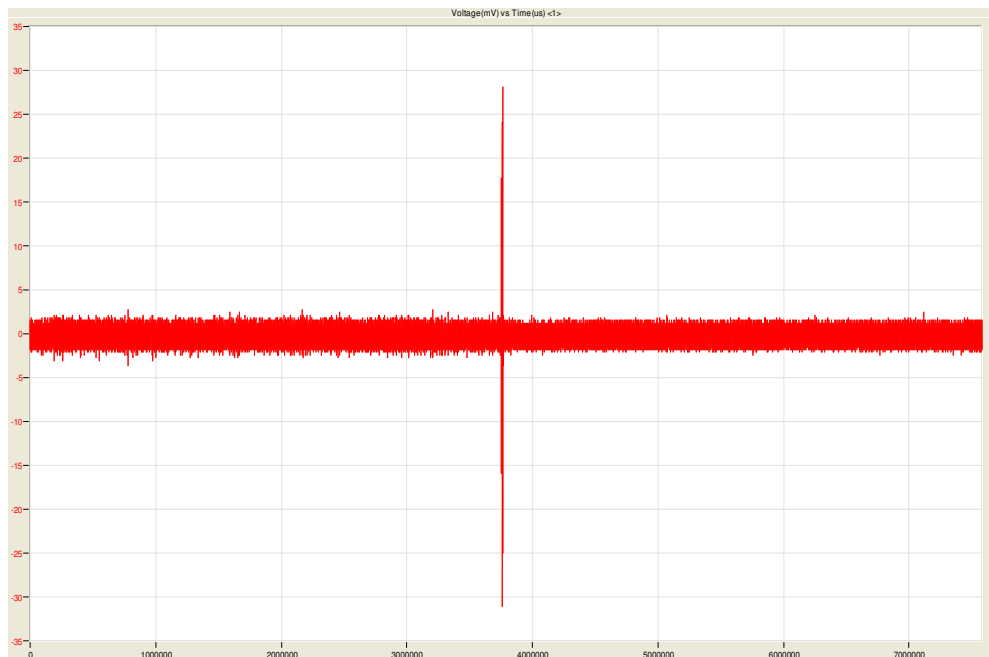


Figure 7.10: Raw AE Signal for RPM 7000 (Touch)

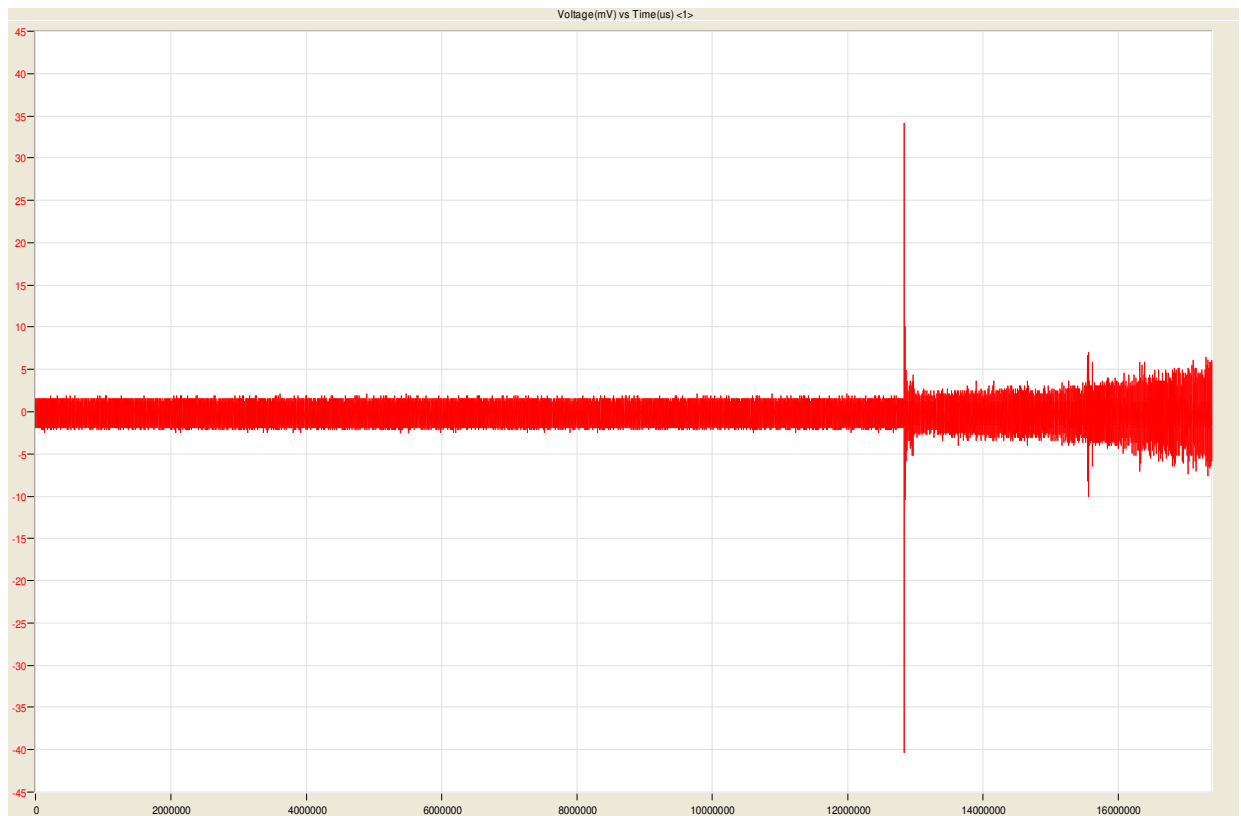


Figure 7.11: Raw AE Signal for RPM 7000 (Touch and rubbing)

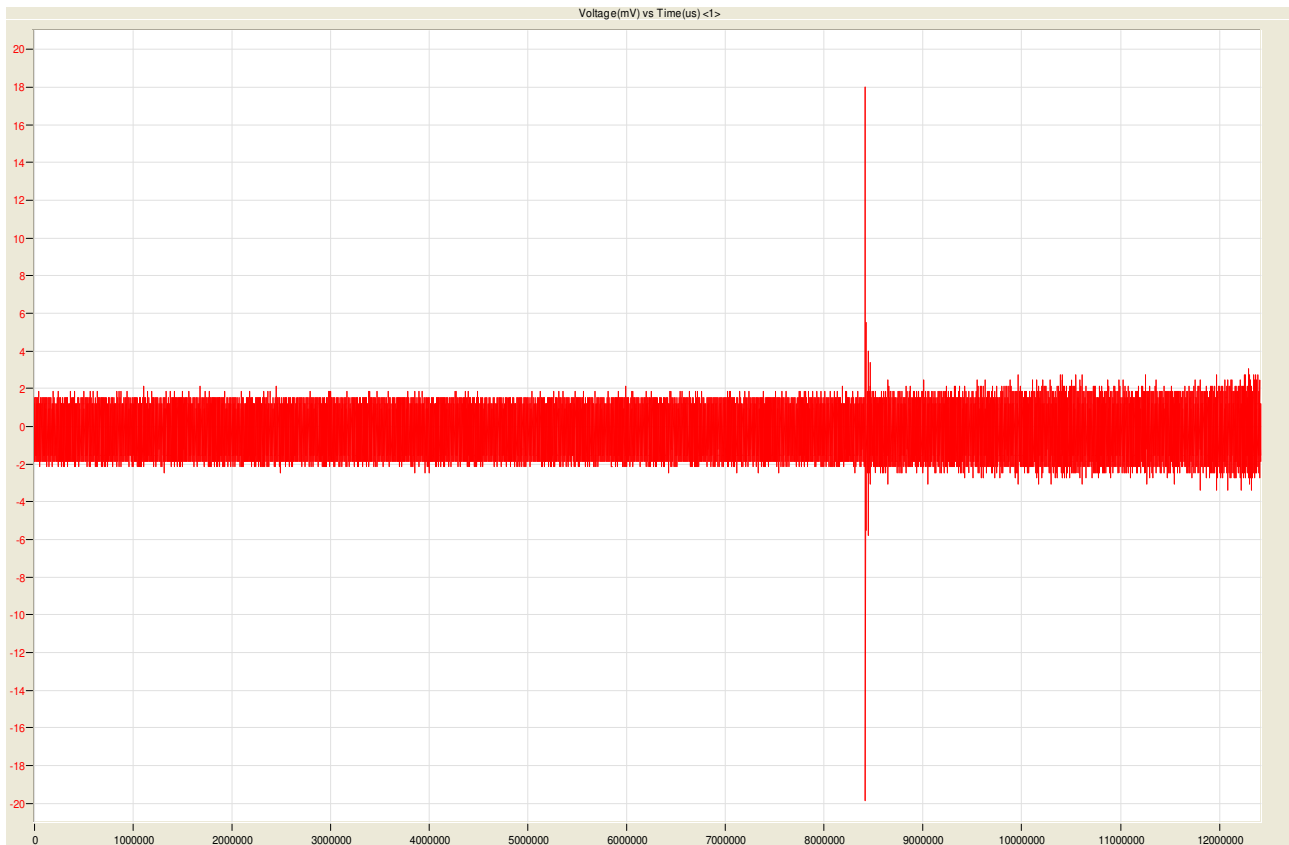


Figure 7.12: Raw AE Signal for RPM 7000 (Touch and rubbing)

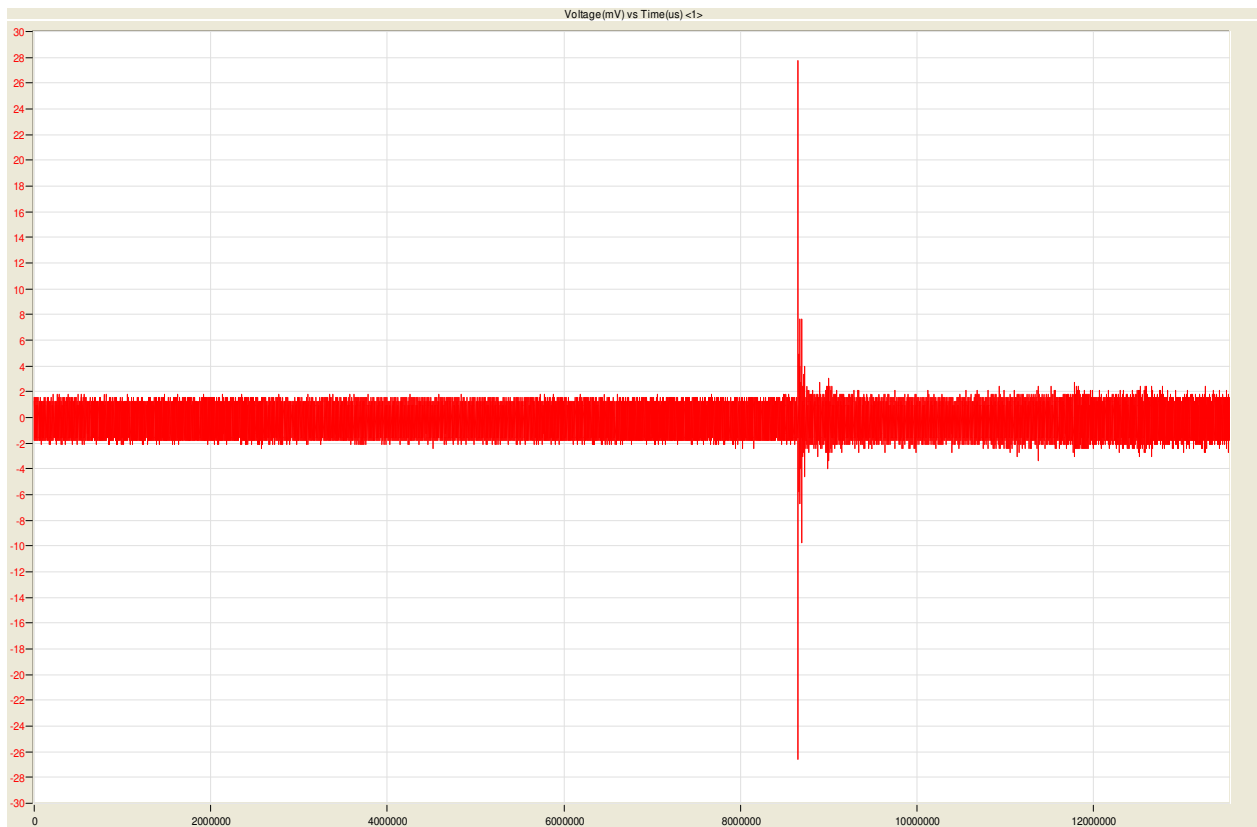


Figure 7.13: Raw AE Signal for RPM 6000 (Touch)

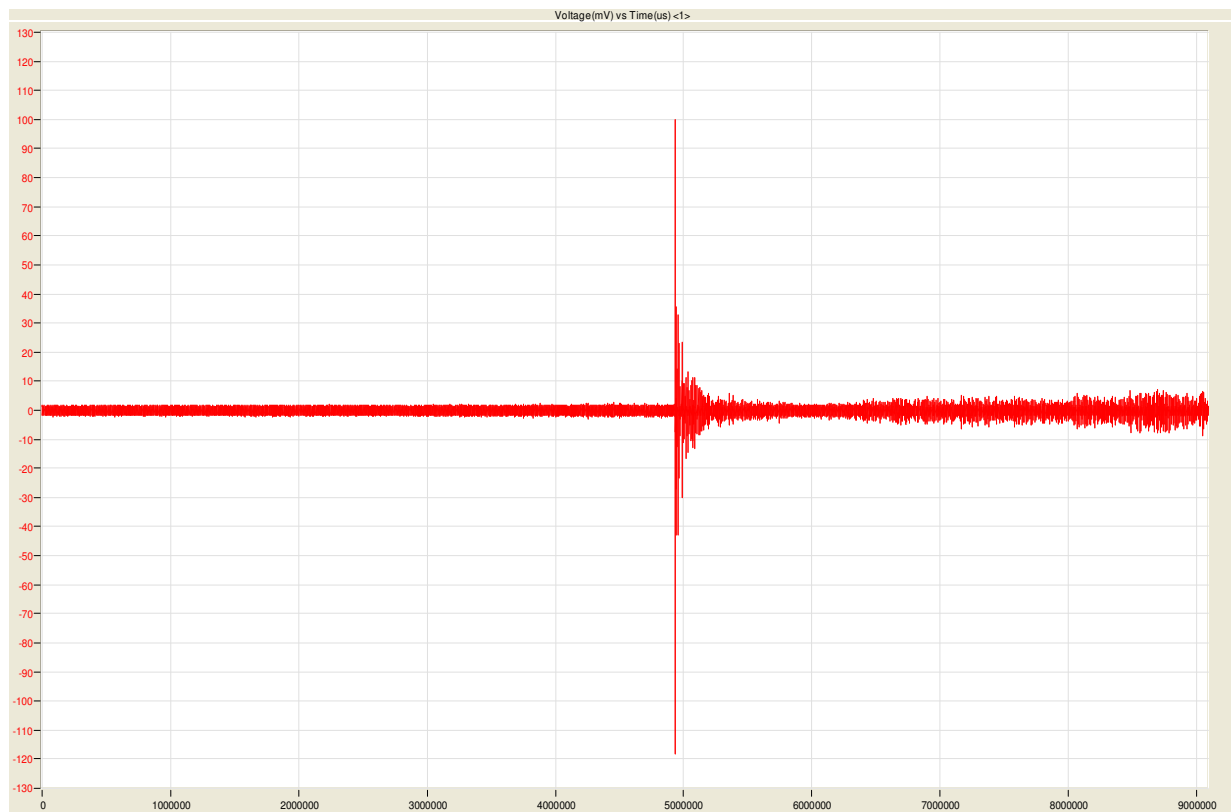


Figure 7.14: Raw AE Signal for RPM 6000 (Touch and Rubbing)

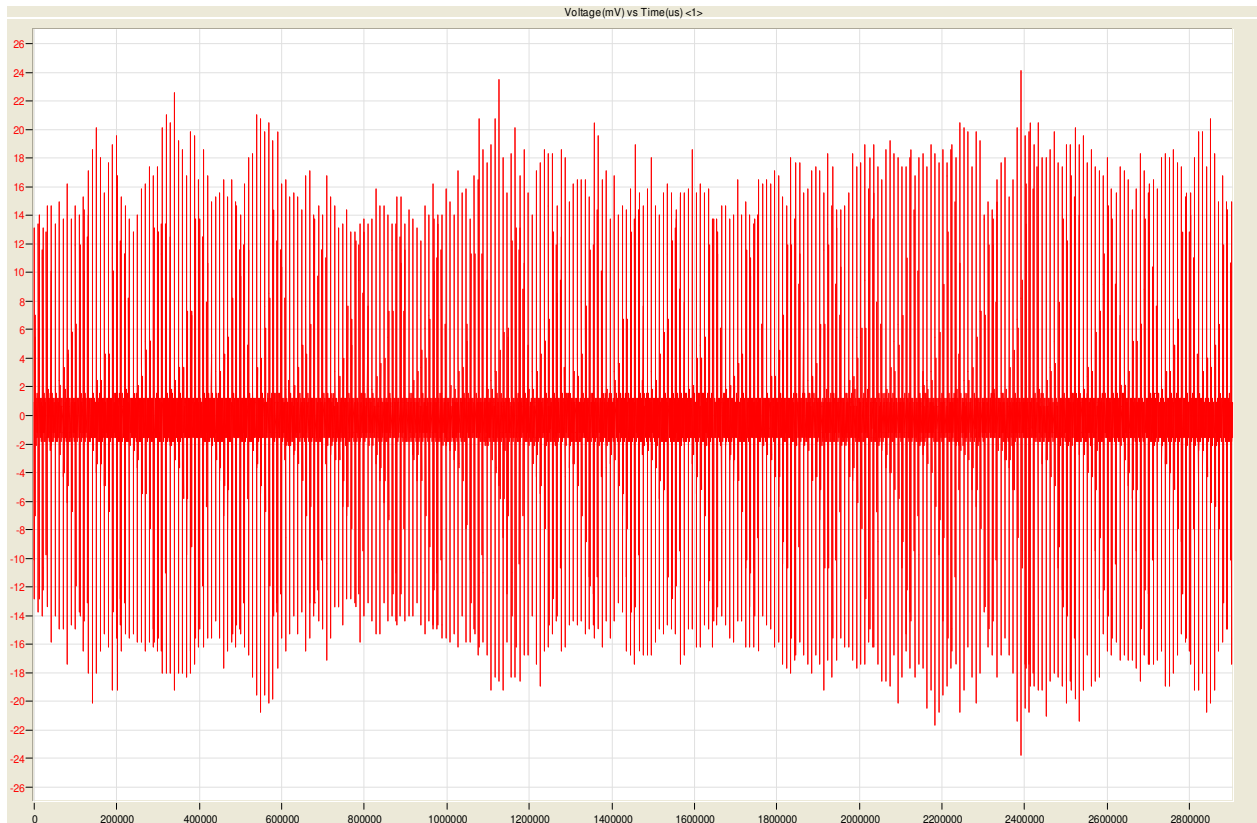


Figure 7.15: Raw AE Signal for RPM 6000 (Cutting)

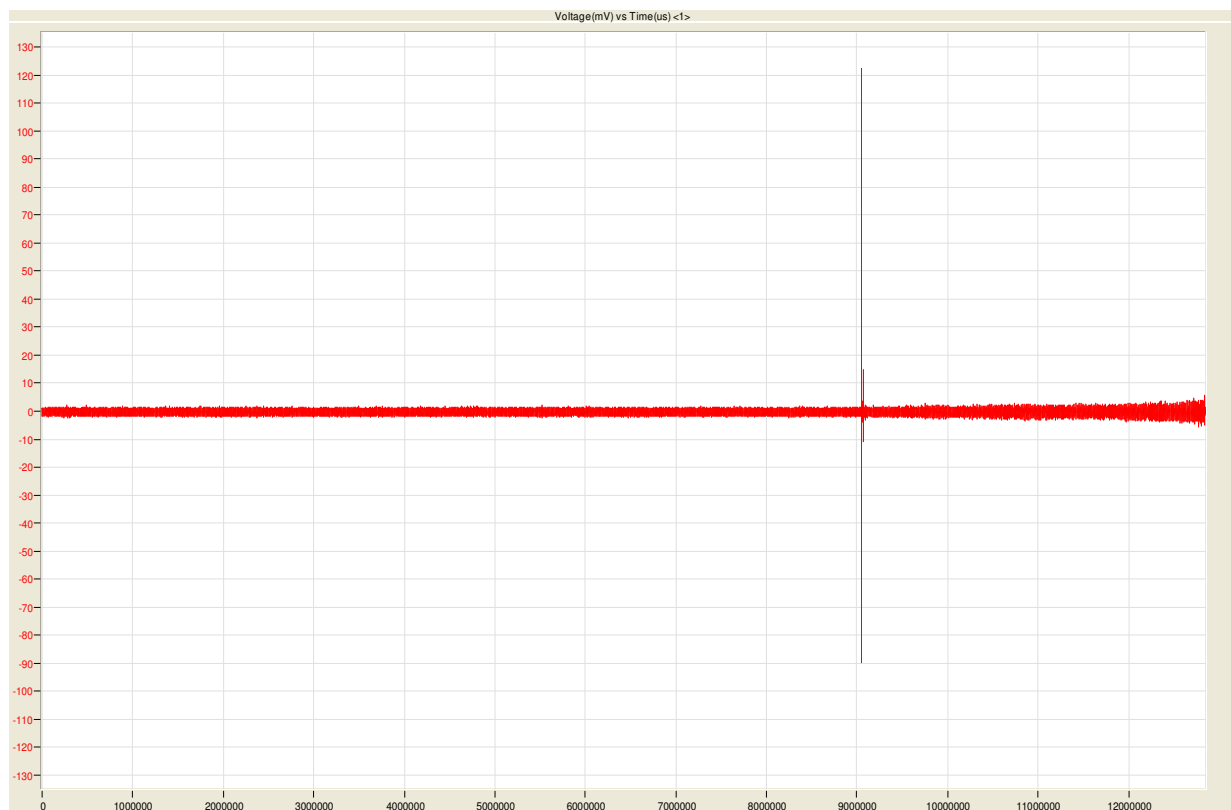


Figure 7.16: Raw AE Signal for RPM 5000 (Tough and some Rubbing)

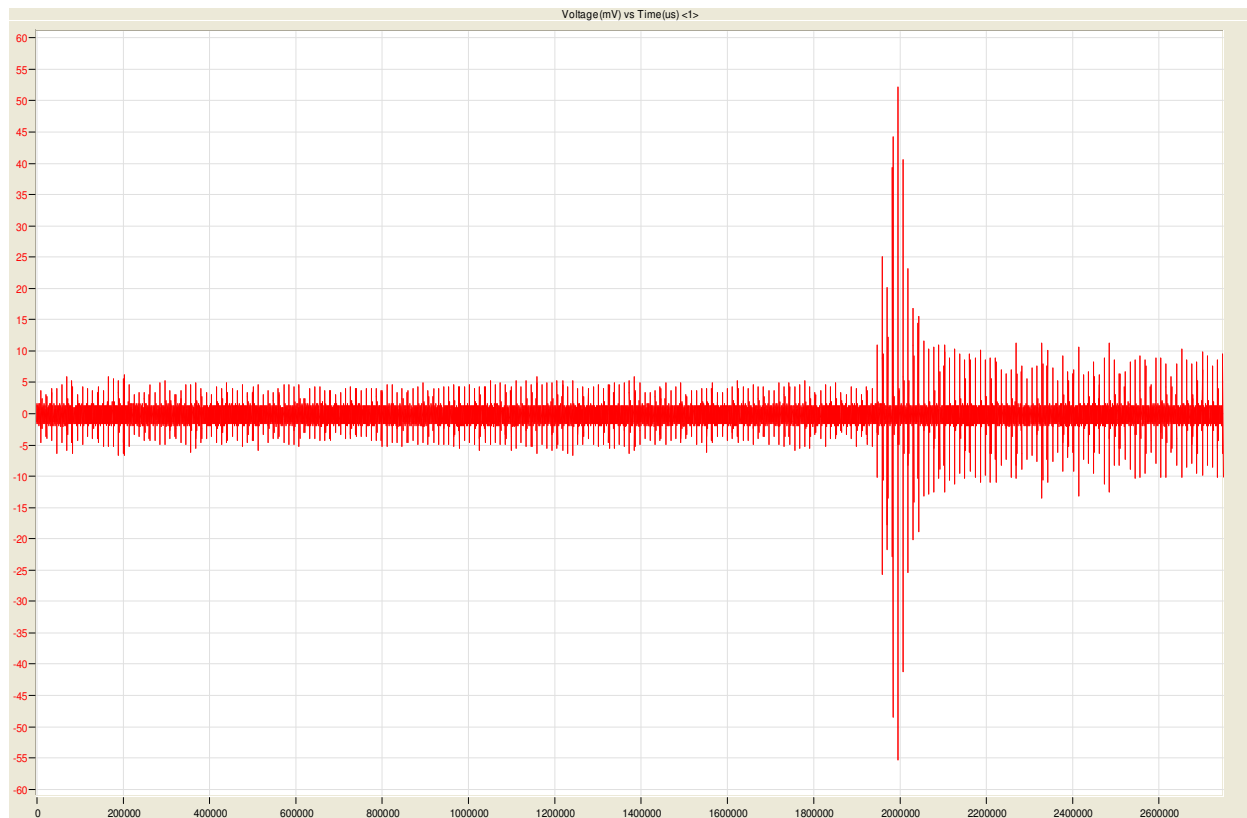


Figure 7.17: Raw AE Signal for RPM 5000 (Rubbing and Ploughing)

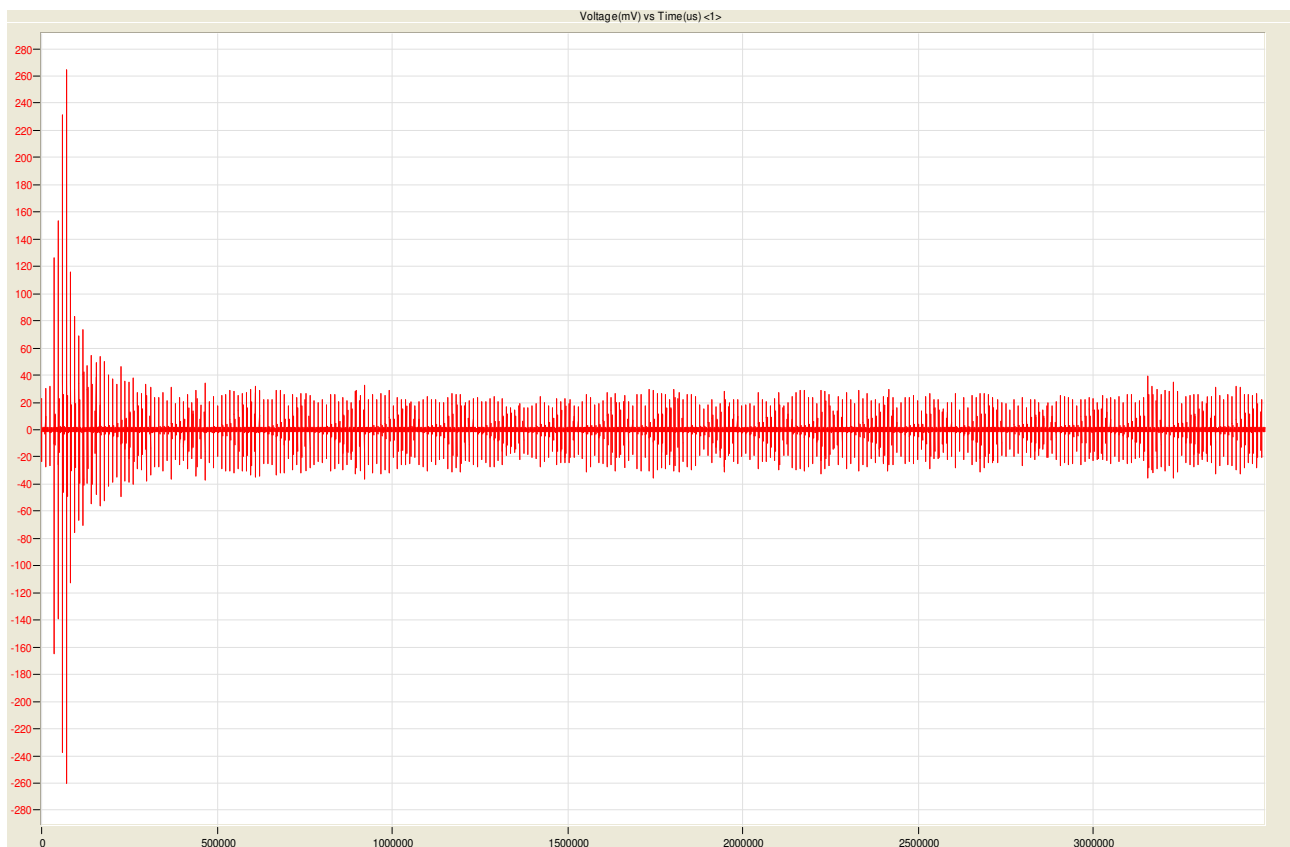


Figure 7.18: Raw AE Signal for RPM 5000 (Ploughing)

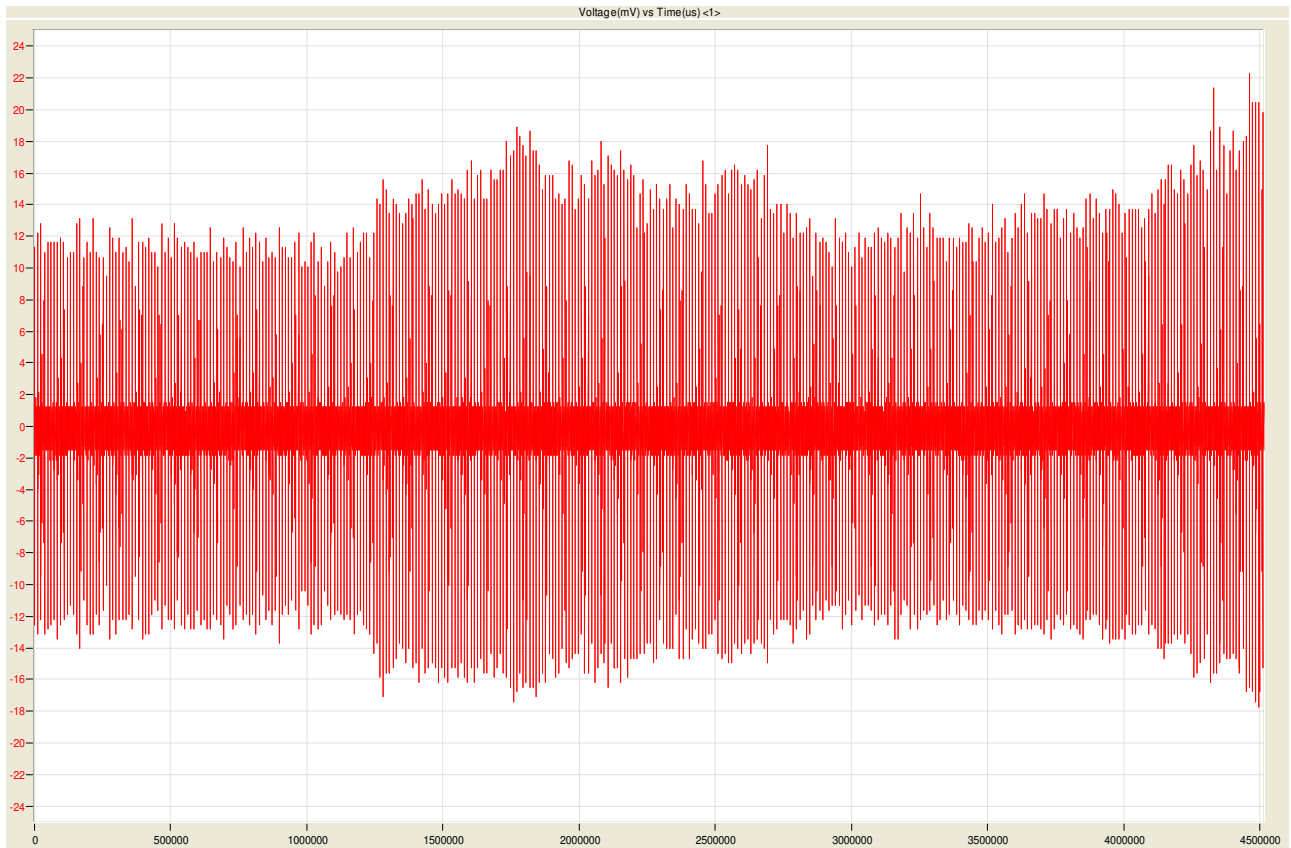


Figure 7.19: Raw AE Signal for RPM 5000 (Cutting)

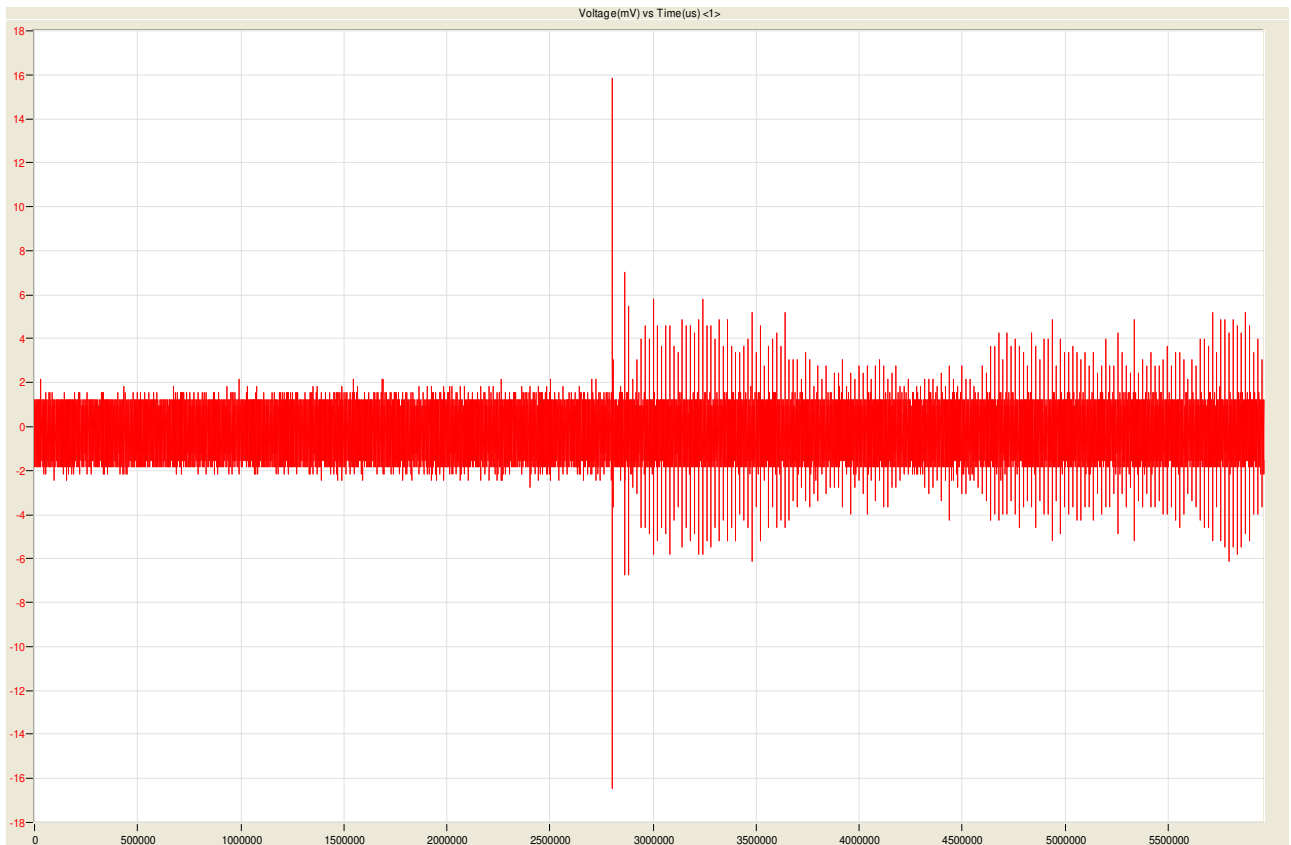


Figure 7.20: Raw AE Signal for RPM 4000 (Touch and Rubbing)

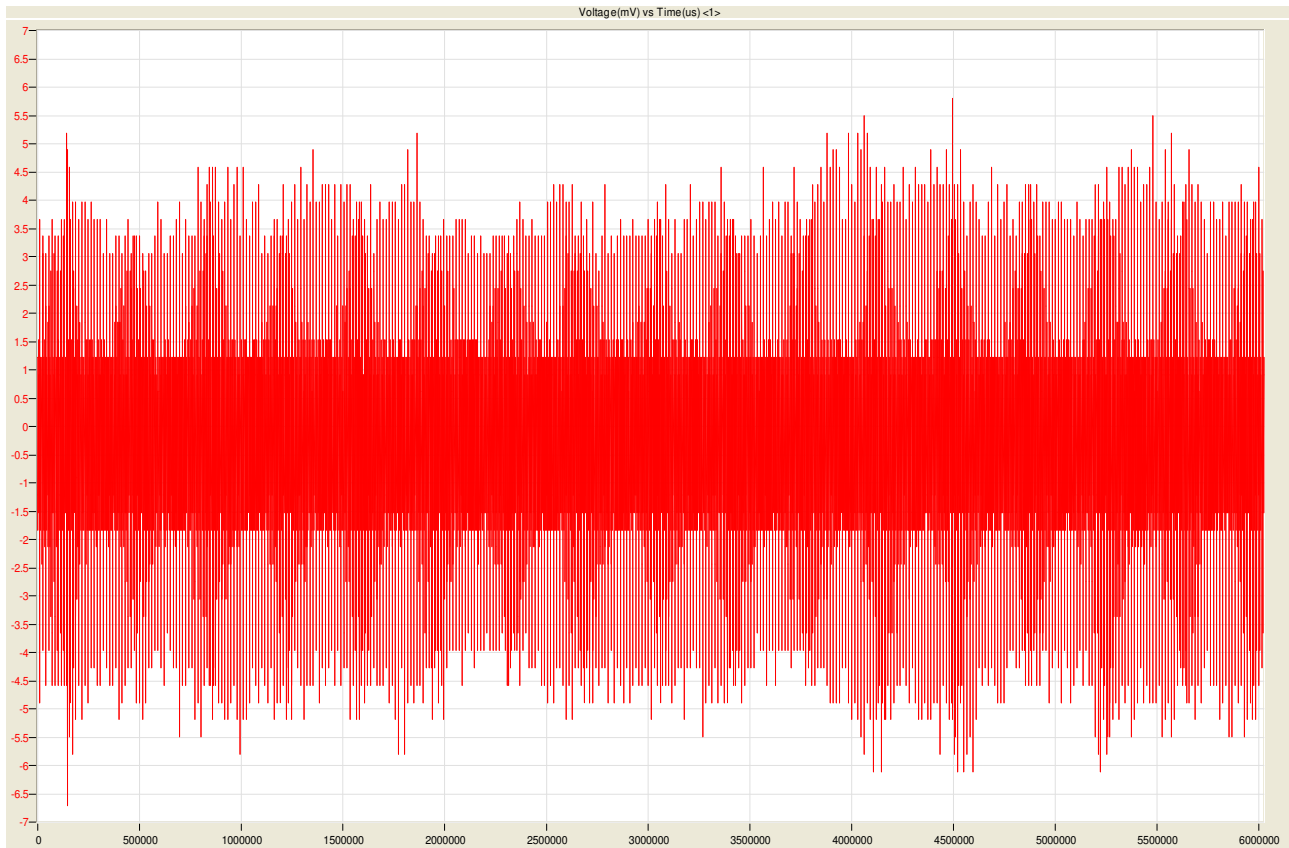


Figure 7.21: Raw AE Signal for RPM 4000 (Cutting)

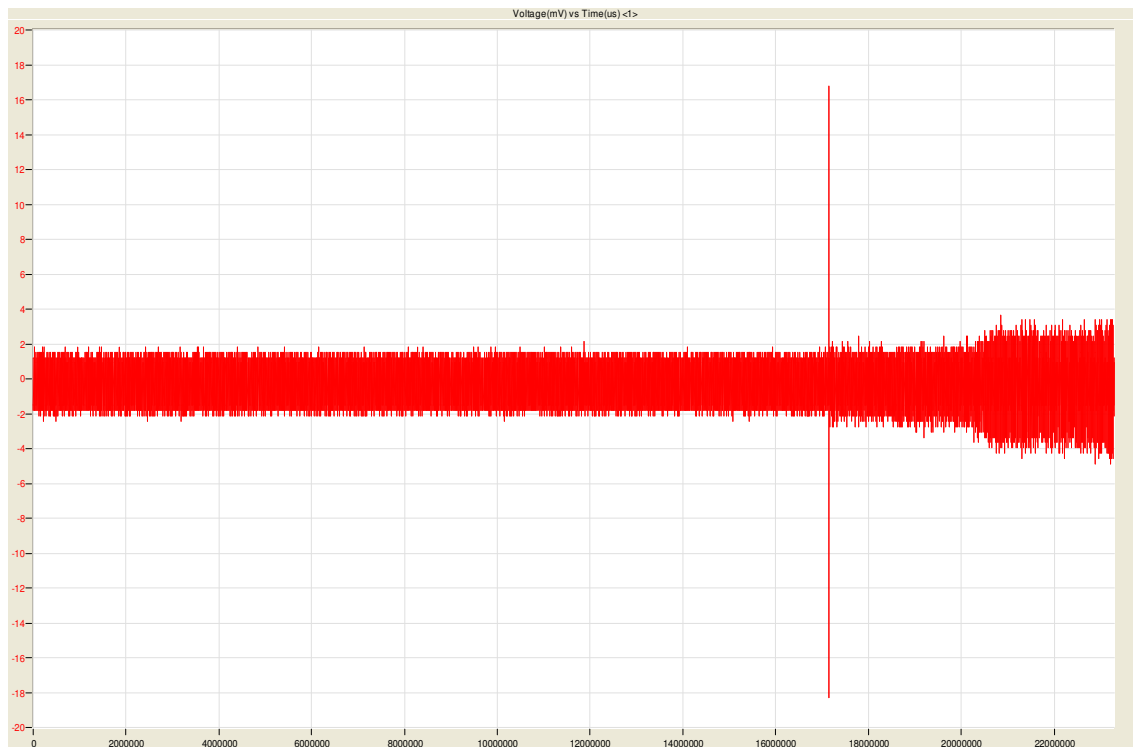


Figure 7.22: Raw AE Signal for RPM 3000 (Touch and Rubbing)

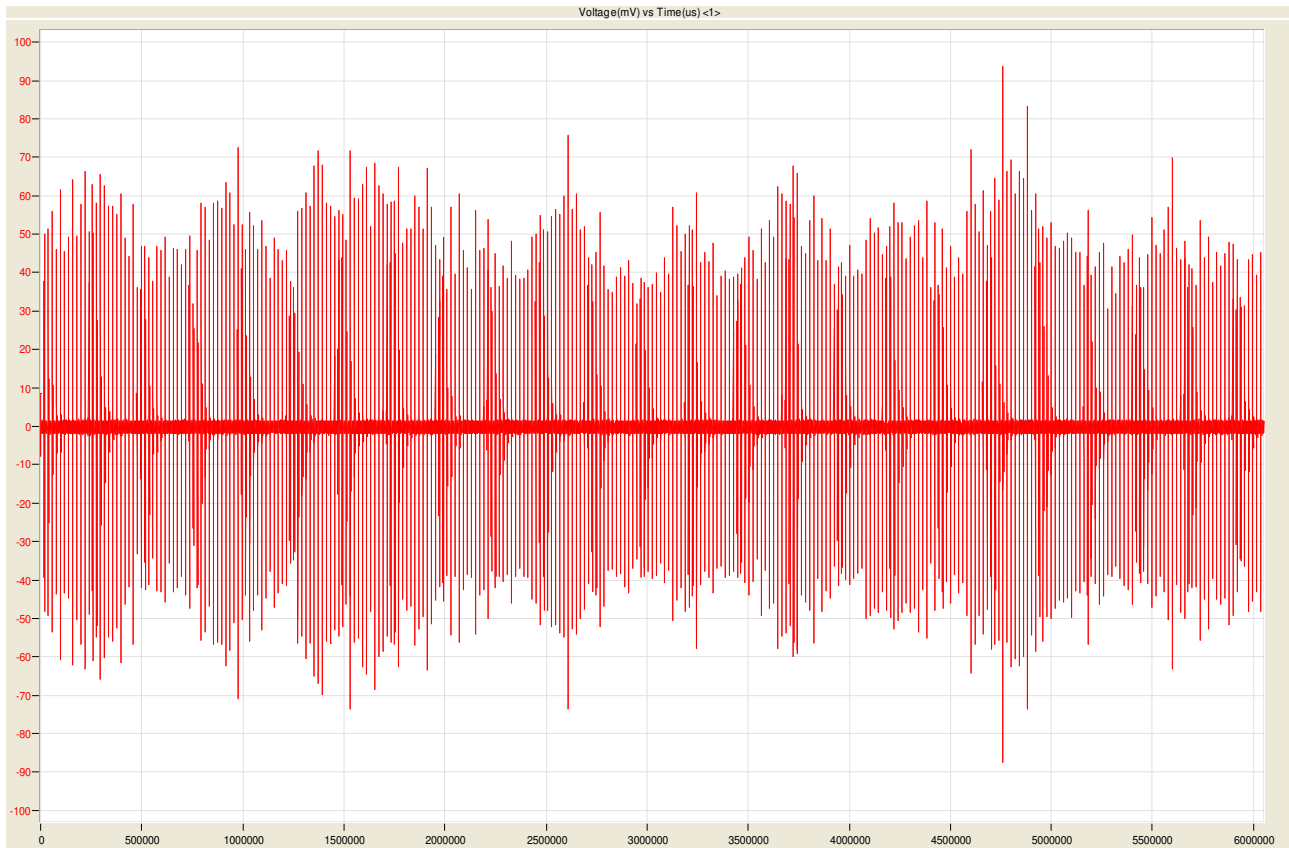


Figure 7.23: Raw AE Signal for RPM 3000 (Cutting)

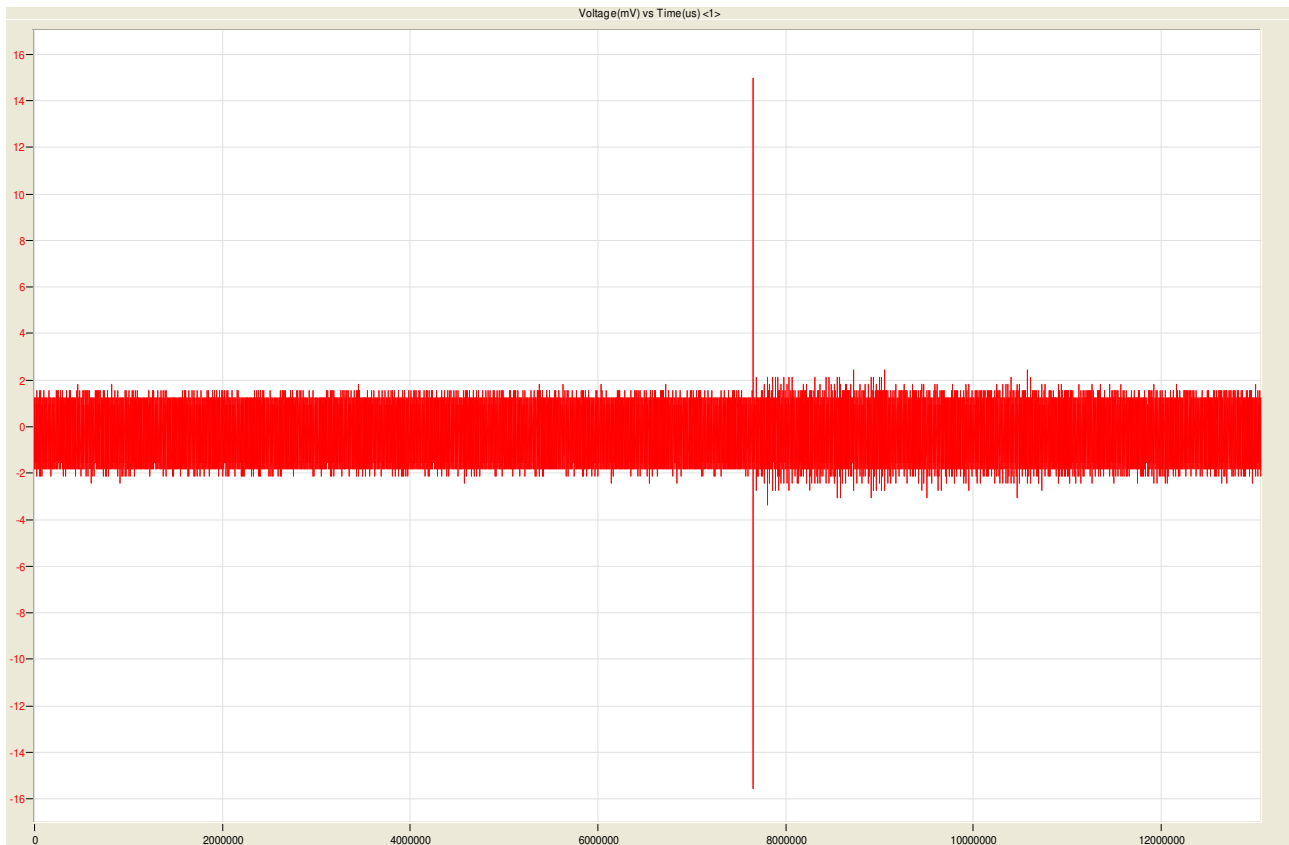


Figure 7.24: Raw AE Signal for RPM 2000 (Touch and Slight Rubbing)

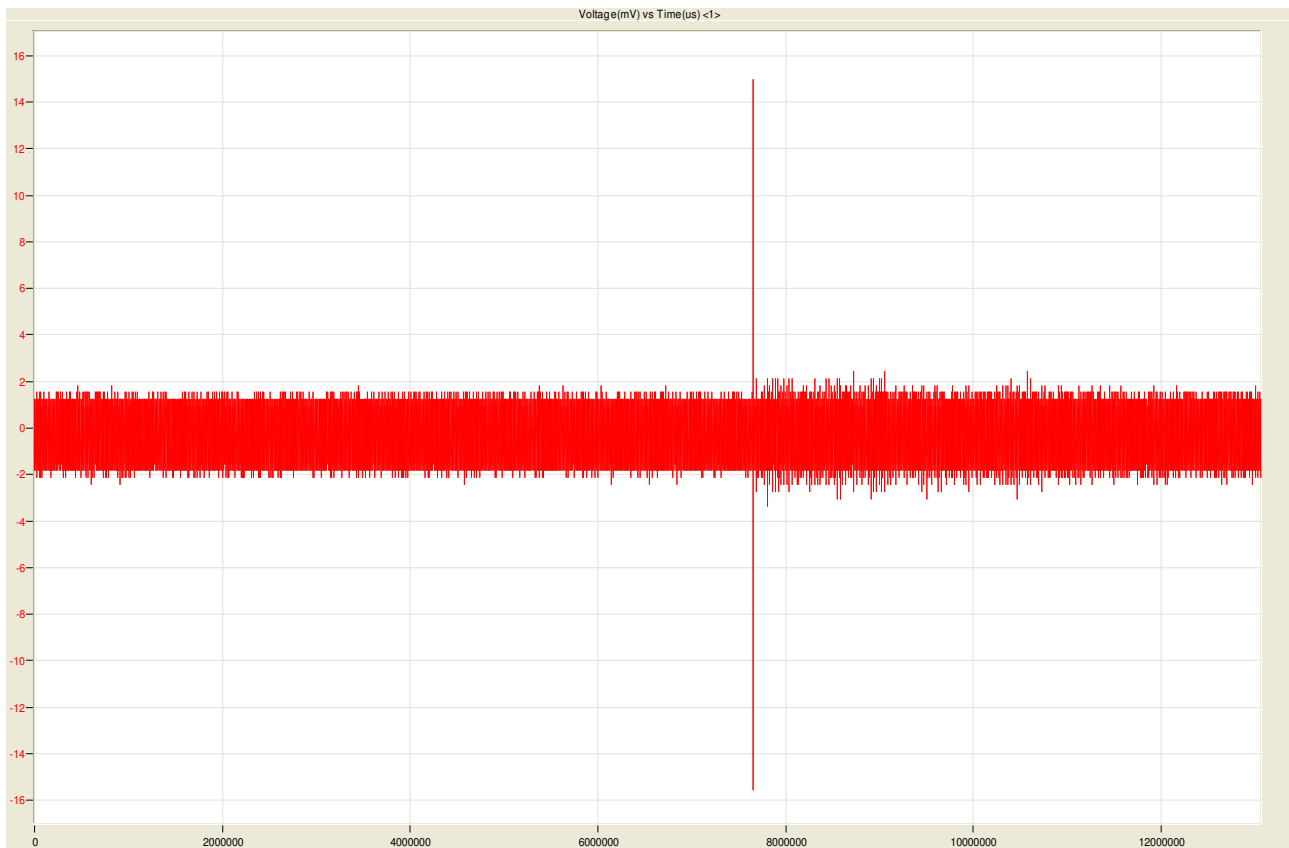


Figure 7.25: Raw AE Signal for RPM 2000

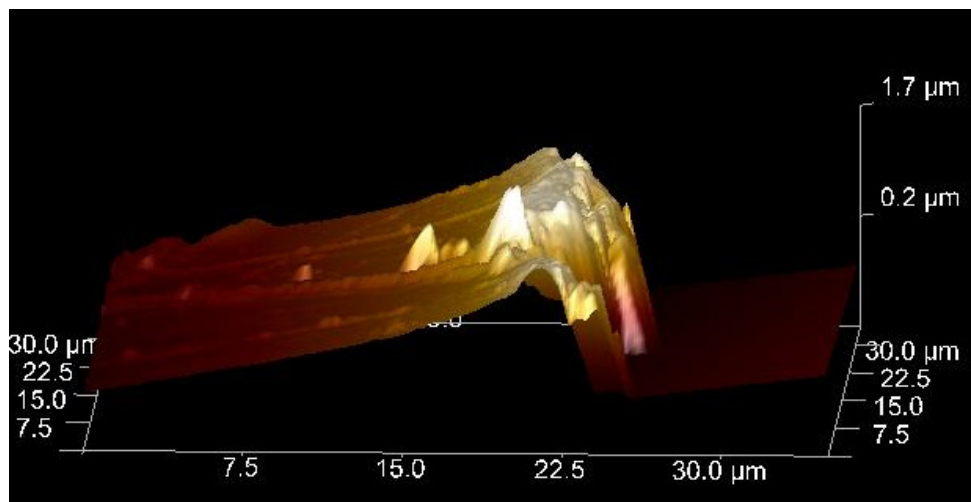


Figure 7.26: AFM Image of the Side of the Scratch

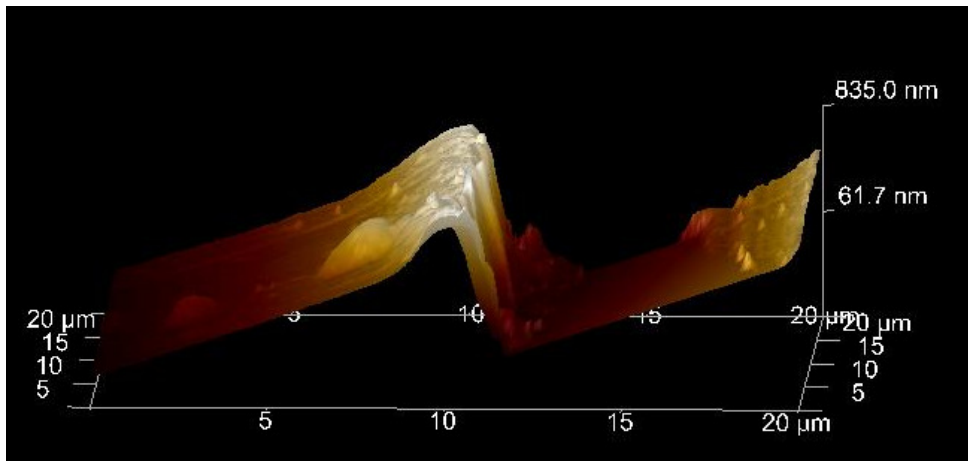


Figure 7.27: AFM Image of the Side of the Scratch for RPM 3000

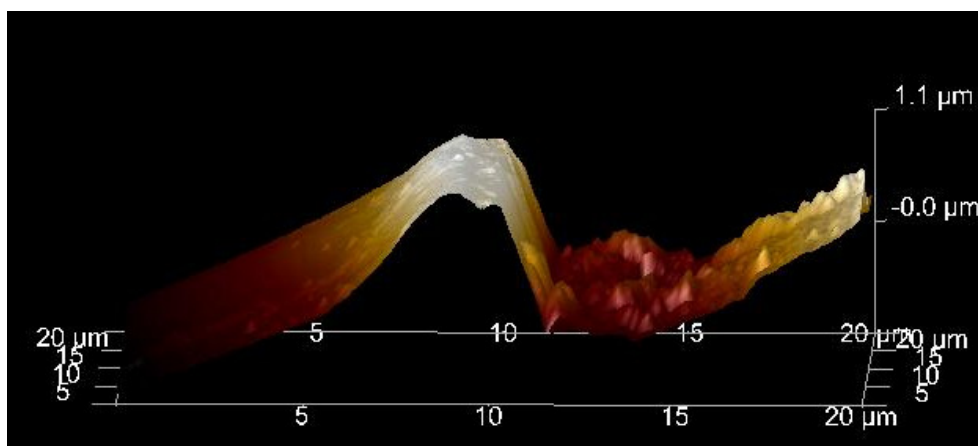


Figure 7.28: AFM Image of the Scratch for RPM 4000

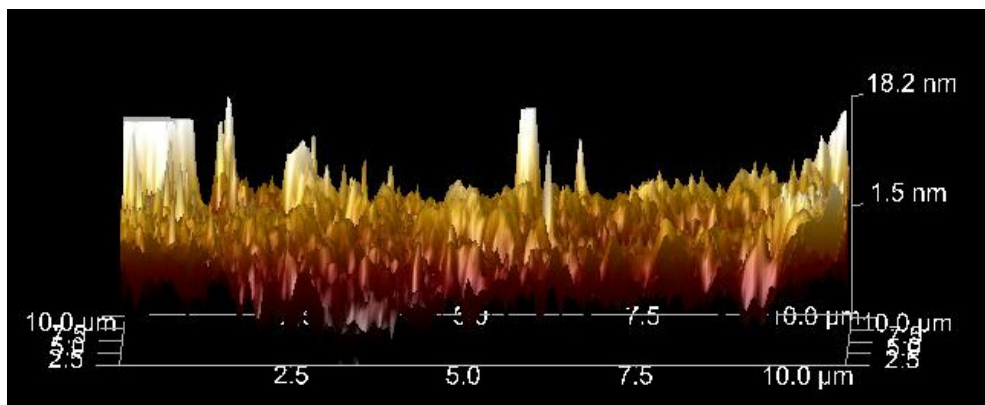


Figure 7.29: AFM Image of the cut (inside) Scratch for RPM 3000

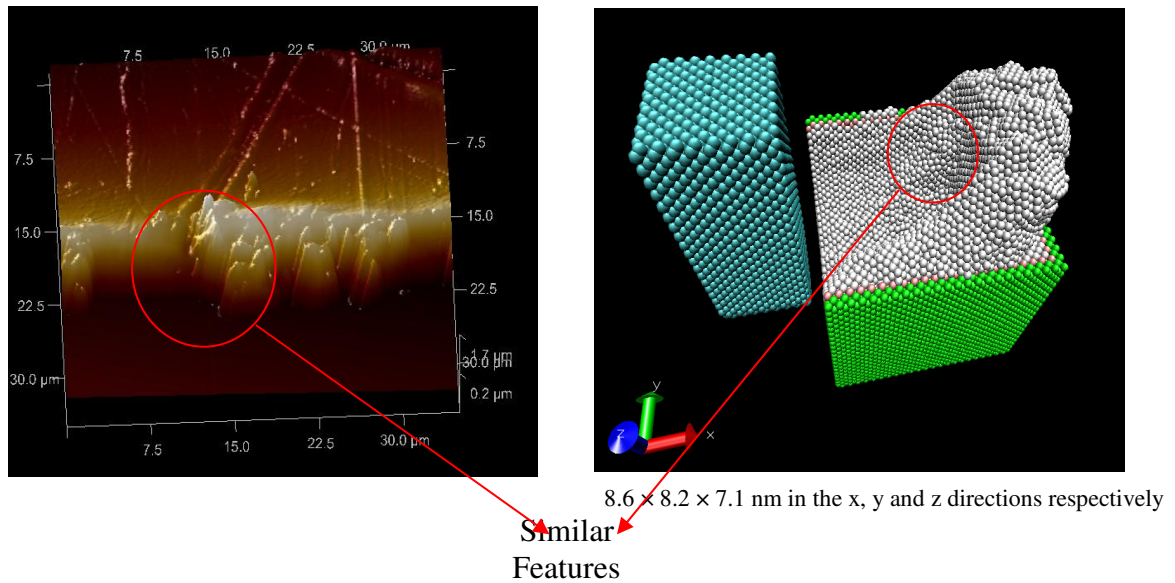


Figure 7.30: Comparison of Features in an AFM Image and Simulations

7.6 Discussion and Concluding Remarks

Figures 7.5 – 7-25 show an attempt to use the AE signals to characterize the material removal mechanisms of rubbing, ploughing and cutting in nanomachining. Certain features are seen during the touch of the tool on the workpiece as detected by the AE sensor. Also, some features seem to show the transition between the removal mechanism phenomena. Figures 7.26 – 7.30 show the AFM images of some of the scratches made by the Nanoform machine. Some certain features may seem to compare with the EAM-Morse multipass simulations, but the scales are in different order of magnitudes. It is still very difficult to validate nanometric simulation results and obtain experimental data at the sub-nano length scale especially on machine tools. The force sensor used could not acquire force data down to the nanometre level. However, the result of this study compare favourably with works of other researchers, Pei et al 2006 and Komanduri et al 2010. Komanduri et al 2010 observed the ploughing material removal phenomenon in aluminium by AFM scratches on Aluminium (Figure 7.31).

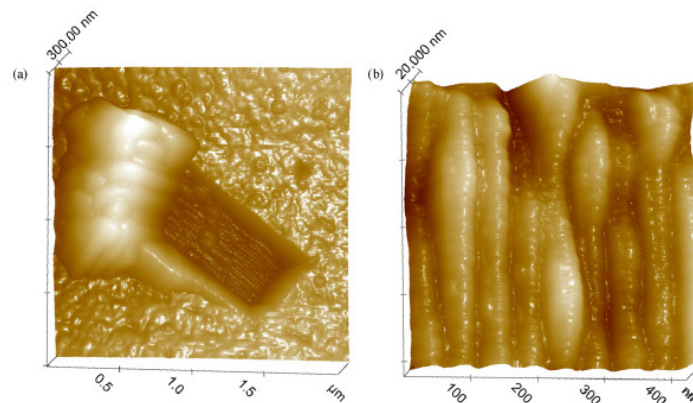


Figure 7.31: AFM Scratches on Aluminum (Komanduri et al 2010)

Chapter 8. Conclusions and Recommendations

A model of the tool-workpiece for nanometric machining has been developed and the mechanisms of material removal has been investigated by using the MD simulation method. Also, the effect of various machining parameters on the material removal has been studied and the following below are the contribution of this research to scientific knowledge.

8.1 Contribution to Knowledge

- The effects of the interatomic potentials on the nanometric machining of copper workpiece with a diamond tool have been shown.
- The MD simulation method have been used to estimate and evaluate the minimum depth of cut in nanomachining.
- The MD simulation method have been used to predict the onset of plasticity in nanomachining.
- The multi-pass MD simulation which realistically models the machining process have been carried out and new results have been obtained.
- The atomic surface roughness of nanometric machining have been evaluated.

8.2 Conclusions

Also, the following are the conclusions from this research work.

- It has been identified that the EAM potential is the most appropriate of the 3 potentials commonly used for the modelling of nanomachining of copper with diamond tool. The choice of the best potential is based on the cutting forces and the potential energy. The EAM potential provides the best description of the metallic bonding in the workpiece, also, the cutting forces variation is smallest; the potential and total energies fluctuations are least for the depth of cut considered. Therefore, the EAM potential should be used, rather than LJ and Morse potentials for the modelling of copper and other fcc metals in MD simulations of nanomachining. However the use of the EAM-Morse potentials (that is, EAM for the Cu-Cu interactions and Morse for the Cu-C interactions) is better than using EAM only for the simulations.

- For pair potentials in the modelling of nanomachining of copper with diamond tool, the EAM-LJ potential pair has the lowest average tangential cutting force component and the lowest force ratio. The EAM-Morse pair on the other hand has the lowest energy value of all the cases. So, the two pairs; EAM-LJ and EAM-Morse are appropriate for the modelling.
- The material removal phenomena of rubbing, ploughing and cutting have been clearly observed from MD simulation results. Ploughing starts from 0.2~0.3nm and the formation of chips starts to occur from the depth of cut thickness of 1.5nm. So it can be suggested that the extreme accuracy attainable or MDC for copper atoms workpiece, machined with extremely sharp diamond tool is around 1.5nm to 3nm.
- On the MD simulation with different tool ends; all the tools clearly show the phenomena of rubbing and ploughing in the depth of cut range of 0.05 to 0.5 nm. The tool with the pointed end has the lowest average cutting force and the tool with the flat end has the highest average cutting force. It is important to note that in nanomachining the tool with the sharpest end may not necessarily cause the greatest material removal! The different tool ends may be suitable for different metal machining applications.
- It can be observed that the tangential and the normal cutting force components relatively increase with increase in velocity.
- It can be seen that the tangential cutting force components are considerably affected by the interatomic potential pair used, but they are not greatly affected by whether the tool is rigid or deformable. The total energy of the system on the other hand is much lower when the tool is non rigid than when it is rigid.

8.3. Recommendations for Further Work

To extend this research work, the following are suggestions:

- The size of the simulation models should be increased (to say million atoms) so as to overcome size effects. This would also verify the extent of the effect of the model size on the nanomachining MD simulation results.

- Multi-scale simulation approach should be used for the study already carried out in this study. Since the MD can only handle small length (nano metres) and time scales (femto-nano metres), the spatial and the temporal multi-scale approach would extend the simulation length and time scales respectively.
- On the experimental design, a sharper diamond tool should be used for the trials.
- On the other hand, the AFM with a diamond probe should be used for nanocutting as this has a much smaller edge (2—8nm)

References

- Alder B.J. and T.E. Wainwright (1959), '*Studies in Molecular Dynamics. I. General Method*', Journal of Chemical Physics, Vol. 31, pp. 459-466
- Allen M.P. and D.J. Tildesley (1988), *Computer Simulation of Liquids*, (Oxford University Press)
- Allen M.P. (2004), '*Introduction to Molecular Dynamics Simulations*', in Computational Soft Matter: From Synthetic Polymers to Proteins, Lecture Notes, Attig N., K. Binder, H. Grumuller and K. Kremer (eds), NIC Series, Vol. 23, pp. 1-28
- Baskes M.I. (1992), '*Modified Embedded-Atom Potentials for Cubic Materials and Impurities*', Physical Review B, Vol. 46, pp. 2727-2742
- Basuray P.K., Misra B.K. and Lal G.K. (1977), '*Transistion from Ploughing to Cutting During Machining with Blunt Tools*', Wear, Vol. 43, pp. 341-349
- Beeman D. (1976), '*Some Multistep Methods for use in Molecular Dynamics Calculations*', Journal of Computational Physics, Vol. 20, pp. 130-139
- Belak, J. and Stowers, I. F. (1990), '*A Molecular Dynamics Model of the Orthogonal Cutting Process*', Proceedings of the American Society of Precision Engineering, pp. 76-79.
- Belak, J. and Stowers, I. F. (1991), '*The Indentation and Scratching of a Metal Surface: A Molecular Dynamics Study*', Fundamentals of Friction: Macroscopic and Microscopic, Singer, Pollock E, Vol. 220 pp. 1-10
- Binnig G and H. Rohrer (1982), '*Scanning Tunnelling Microscopy*', Helv. Phys. Acta, Vol. 55, pp. 726-735
- Binnig G, C.F. Quate and C. Gerber (1986), '*Atomic Force Microscope*', Phys. Rev. Lett., Vol. 56, pp. 930-933
- Born M. and J.E. Mayer (1932), '*Zur Gittertheorie de Ionenkristalle*', Z. Physik, Vol. 75, pp. 1
- Brinksmeier E., J. C. Aurich, E. Govekar, C. Heinzl, H.-W. Hoffmeister, F. Klocke, J. Peters, R. Rentsch, D. J. Stephenson, E. Uhlmann, K. Weinert and M. Wittmann (2006), '*Advances in Modelling and Simulation of Grinding Processes*', Annals of the CIRP Vol. 55, No 2, pp. 667-696
- Brush S.G. (1970), '*Interatomic Forces and Gas Theory from Newton to Lennard-Jones*', Archive for Rational Mechanics and Analysis, Vol. 39, pp. 1-29
- Cai M., X. Li and M. Rahman (2007), '*Molecular Dynamics Modelling and Simulation of Nanoscale Ductile Cutting of Silicon*', International Journal of Computer Applications in Technology, Vol. 28, pp. 2-8
- Cai M.B., X.P. Li and M. Rahman (2007), '*Study of the Temperature and Stress in Nanoscale Ductile Mode Cutting of Silicon using Molecular Dynamics Simulation*', Journal of Materials Processing Technology, Vol. 192-193, pp. 607-612

- Chamati H., N. Papanicolau, Y. Mishin and D.A. Papaconstantopoulos (2006), '*Embedded-Atom Potential for Fe and its Application to Self-Diffusion on Fe(100)*', Surface Science. Vol. 600, pp. 1793-1803
- Chen X. and Rowe W. (1999), '*Modelling Surface Roughness Improvement in Grinding*', Proc. Inst. Mech. Engr, Vol. 213, Part B, pp. 93-96
- Chen X. (2009), '*Machining Dynamics in Grinding Processes*', in Machining Dynamics: Fundamentals and Practices, Springer, Ed. by Cheng K.
- Cheng K., X. Luo, R. Ward and R. Holt (2003), '*Modelling and Simulation of the Tool Wear in Nanometric Cutting*', Wear, Vol. 255, pp. 1427-1432
- Cheong W.C.D, L. Zhang and H. Tanaka (2001), '*Some Essentials of Simulating Nano-Surface Processes Using the Molecular Dynamics Method*', Key Engineering Materials, Vol. 196, pp. 31-42
- Cox H., R.L. Johnston and J.M. Murrel (1999), '*Empirical Potentials for Modelling Solids, Surfaces and Clusters*', Journal of Solid State Chemistry, Vol. 145, pp. 517-540
- Curl R.F, H.W. Kroto and R.E. Smalley (1985), "*C60 Buckminsterfullerene*", Nature, Vol. 318, pp.162
- Das S.K., D. Roy and S. Sengupta (1977), '*Volume Change in some Substitutional Alloys using Morse Potential Function*', J. Physics F: Meta Phys., Vol. 7, No.1, pp. 5-13
- Ducobu F., E. Filippi, E. Rivière-Lorphèvre (2009), '*Chip Formation and Minimum Chip Thickness in Micro-milling*', In Proceedings of the 12th CIRP Conference on Modeling of Machining Operations, pp. 339-346.
- Eigler D.M. and E.K. Schweizer (1990), "*Positioning Single Atoms with a Scanning Tunnelling Microscope*", Nature, Vol. 344, pp. 524-526
- El-Hofy H. (2007), Machining Processes: Conventional and Non-Conventional Processes, Taylor and Francis Group
- Ercolessi F. (1997), '*A Molecular Dynamics Primer*', Spring College in Computational Physics, ICTP, Trieste, June 1997. <http://www.fisica.uniud.it/~ercolessi/md/md/> (Accessed in 2008)
- Ercolessi F., E. Tosatti and M. Parrinello (1986), '*Au (100) Surface Reconstruction*', Physical Review Letters, Vol. 57, pp. 719-722
- Ercolessi F. and J.B. Adams (1994), '*Interatomic Potentials from First Principles Calculations: The Force-Matching Method*', Europhysics Letters, Vol. 26, No. 8, pp. 583-588
- Fang F.Z., Wu H., Liu X.D., Liu Y.C. and Ng S.T. (2003), '*Tool Geometry Study in Micromachining*', Journal of Micromechanics and Microengineering, Vol. 13, pp. 726-731
- Fang T. and C. Weng (2000), '*Three-Dimensional Molecular Dynamics Analysis of Processing using a Pin Tool on the Atomic Scale*', Nanotechnology, Vol. 11, pp. 148-153
- Feynman R. (1959), "*There's Plenty of Room at the Bottom*" Pasadena, American Physical Society

- Field M.J. (1999), *A Practical Introduction to the Simulation of Molecular Systems*, Cambridge University Press
- Finnis M. (2003), *Interatomic Forces in Condensed Matter*, Oxford University Press
- Finnis M.W. and J.E. Sinclair (1984), '*A Simple Empirical N-Body Potential for Transition Metals*', *Philosophical Magazine A*, Vol.50, Iss. 1, pp. 45 -50
- Foiles S.M. (1985), '*Application of the Embedded Atom Method to Liquid Transition Metals*', *Physical Review B*, Vol. 32 No 6, pp. 3409-3415
- Foiles S.M., M.I. Baskes and M.S. Daw (1986), '*Embedded-Atom-Method Functions for the FCC Metals Cu, Ag, Au, Ni, Pd, Pt, and their Alloys*', *Physical Review B*, Vol. 33, No 12, pp. 7983-7991
- Freedonia Group (2009), *World Machine Tools to 2009 : Demand and Sales Forecasts, Market Share, Market Size, Market Leaders*, <http://www.freedoniagroup.com>
- Frenkel D. and B. Smit (2001), *Understanding Molecular Simulations: From Algorithms to Applications (Computational Science)*, (Academic Press)
- Gates T.S, G.M. Odegard, S.J.V. Frankland, T.C. Clancy (2005), "*Computational Materials: Multi-scale Modelling and Simulation of Nanostructured Materials*", *Composite Science and Technology* Vol. 65, pp. 2416-2434
- Gear C.W. and K.W. Tu (1974), '*The Effect of Variable Mesh Size on the Stability of Multistep Methods*', *SIAM Journal of Numerical Analysis*, Vol. 11, No. 5, pp. 1025-1043
- Gear C.W. and D.S. Watanabe (1974), '*Stability and Convergence of Variable Order Multistep Methods*', *SIAM Journal of Numerical Analysis*, Vol. 11, No. 5 pp. 1044-1058
- Giese T. (2009), *The Abrasives Industry in Europe and North America*, Materials Technology Publication
- Girifalco L.A. and V.G. Weizer (1959), '*Application of the Morse Potential Function to Cubic Metals*', *Phys. Rev.*, Vol. 114, pp. 687-680
- Guo Y., Y. Liang, M. Chen, Q. Bai and L. Lu (2010), '*Molecular Dynamics Simulations of Thermal Effects in Nanometric Cutting Process*', *Science China Technological Sciences*, Vol. 53, No.3, pp. 870-874
- Haile J.M. (1997), *Molecular Dynamics Simulation: Elementary Methods*, (Wiley-Interscience)
- Han X.S., B. Lin, S.Y. Yu and S.X. Wang (2002), '*Investigation of Tool Geometry in Nanometric Cutting by Molecular Dynamics Simulation*', *Journal of Materials Processing Technology*, Vol. 129, pp. 105-108
- Hansen J. D. and J. R. McDonald (1976), *Theory of Simple Liquids*, (Academic Press, N.Y.)
- Hernandez E.R. (2008), '*Molecular Dynamics from Basic Techniques to Applications (A Molecular Dynamics Primer)*', *Frontiers in Contemporary Physics, AIP Conference Proceedings*, Vol. 1077, Iss.1, pp. 95-123

- Hohenberg P. and W. Kohn (1964), '*Inhomogeneous Electron Gas*', Physical Review, Vol. 136, pp. 864-871
- Huang Z.G., Z.N. Guo, X. Chen, Z.Q. Yu, T.M. Yu and W.B. Lee (2007), '*Microscopic Machining Mechanism of Polishing Based on Vibrations of Liquid*', Nanotechnology, Vol. 18, 105703 (11pp)
- Hwang H.J., O-K Kwon and J. W. Kang (2004), '*Copper Nanocluster Diffusion in Carbon Nanotube*', Solid St. Comm., Vol. 129, pp. 687-690
- Iijima S. (1991), '*Helical Microtubes of Graphitic Carbon*', Nature, Vol. 354, pp.56
- Ikawa N., S. Shimada, H. Tanaka and G. Ohmori (1991), '*An Atomistic Analysis of Nanometric Chip Removal as Affected by Tool-Work Interaction in Diamond Turning*', Annals of the CIRP, Vol. 40, Iss. 1, pp. 551-554
- Ikawa N., S. Shimada and H. Tanaka (1992), '*Minimum Thickness of Cut in Micromachining*', Nanotechnology, Vol. 3, pp. 6-9
- Inamura T., N. Takezawa and Y. Kumaki (1993), '*Mechanics and Energy Dissipation in Nanoscale Cutting*', Annals of the CIRP Vol. 42, No 1, pp. 79-82
- Inasaki I., H.K. Tonshoff and T.D. Howes (1993), '*Abrasive Machining in the Future*', Annals of the CIRP Vol. 42, No 2, pp. 723-732
- Jackson M.J. (2008), '*Micro and Nanomachining*', in Machining: Fundamentals and Recent Advances, J.P. Davin (Ed.)
- Kenny S.D., D. Mulliah, C.F. Sanz-Navarro and R. Smith (2005), '*Molecular Dynamics Simulations of Nanoindentation and Nanotribology*', Philosophical Transactions of the Royal Society A, Vol. 363, No. 1833, pp. 1949-1959
- Khukhryansky Y. P., E.A. Shunikov and V.V. Emelyanov (2004), '*Study of Cluster Forming at Growth of A3B5 Semiconductor Compounds from Liquid Phase*', Journal of Crystal Growth Vol. 269, pp. 292-297
- Komanduri R., Chandrasekaran N. and Raff L.M. (1998), '*Effect of Tool Geometry in Nanometric Cutting: A Molecular Dynamics Simulation Approach*', Wear, Vol. 219, pp. 84-97
- Komanduri R., N. Chandrasekaran and L.M. Raff (1999), '*Some Aspects of Machining with Negative-Rake Tools Simulating Grinding: A Molecular Dynamics Simulation Approach*', Philosophical Magazine Part B, Vol. 79, No. 7, pp. 955-968
- Komanduri R., and L.M. Raff (2001), '*A Review on the Molecular Dynamics Simulation of Machining at the Atomic Scale*', Proceedings of the Institution of Mechanical Engineers Vol. 215, Part B, pp. 1639-1672
- Komanduri R., S. Varghese and N. Chandrasekaran (2010), '*On Mechanism of Material Removal at the Nanoscale by Cutting*', Wear, Vol. 269, pp. 224-228

- Kragelsky I.V., Dobychin M.N., and Kombalov V.S. (1982), *Friction and Wear-Calculation Methods*, Pergamon Press, New York
- Kureshi I., (2010), 'Establishing a University Grid for HPC Application', Masters Thesis, University of Huddersfield
- LAMMPS Manual, <http://lammps.sandia.gov/doc/Manual.pdf> (Accessed in 2009)
- Leach A. (2001), *Molecular Modelling: Principles and Applications*, (Prentice Hall)
- Lee B, B.D.Wirth, J. Shim, J. Kwon, S.C. Kwon and J. Hong (2005), '*Modified Embedded-Atom Method Interatomic Potential for the Fe-Cu Alloy System and Cascade Simulations on Pure Fe and Fe-Cu Alloys*', *Physical Review B*. Vol. 71, pp. 184205 (1-15)
- Lennard-Jones J.E. (1924), '*On the Forces between Atoms and Ions*', *Proc. Royal Soc.*, Vol. 109, pp. 584-597
- Li J.H., X.D. Dai, S.H. Liang, K.P. Tai, Y. Kong and B.X. Lin (2008), '*Interatomic Potentials of the Binary Transition Metal Systems and Some Applications in Materials Physics*', *Physics Reports* Vol. 455, pp. 1-134
- Lin B., S.Y. Yu and S.X. Wang (2003), '*An Experimental Study on Molecular Dynamics Simulation in Nanometer Grinding*', *Journal of Materials Processing Technology*, Vol. 138, pp. 484-488
- Lin Z-C, Z-D. Chen and J-C. Huang (2007), '*Establishment of a Cutting Force Model of the Stress-Strain Distribution in Nanoscale Copper Material Orthogonal Cutting*', *International Journal of Advanced Manufacturing Technology*, Vol. 33, pp. 425-435
- Liu X., R.E. DeVor and S.G. Kapoor (2006), '*An Analytical Model for the Prediction of Minimum Chip Thickness*', *Micromachining, Transactions of the ASME, Journal of Manufacturing Science and Engineering*, Vol.128, pp. 474-481
- Luo X., K. Cheng, X. Guo and R. Holt (2003), '*An Investigation on the Mechanics of Nanometric Cutting and the Development of its Test-bed*', *International Journal of Production Research*, Vol.41 No.7, pp.1149-1165
- Luo X. (2004), '*High Precision Surfaces Generation: Modelling, Simulation and Machining Verification*', PhD Thesis, Leeds Metropolitan University
- Luo X. and K. Cheng (2004), '*Abrasive Nanometric Machining: Modelling, Simulation and its Application Promise*', *Key Engineering Materials*, Vols. 257-258, pp. 27-32
- Marx D. and J. Hutter (2000), '*Ab Initio Molecular Dynamics: Theory and Implementation*', in *Modern Methods and Algorithms of Quantum Chemistry*, J. Grotendorst (Ed.), John von Neumann Institute for Computing, Julich, NIC Series, Vol. 1, pp. 301-449
- Marinescu I.D., W.B. Rowe, B. Dimitrov and I. Inasaki (2004), *Tribology of Abrasive Machining Processes*, (William Andrew Publishing), pp. 239-262
- Medyanik S.N. (2007), *Atomistic Simulation Methods and Multiscale Modelling*, Accessed October 2011 <http://multiscale.emsl.pnl.gov/docs/atomistic.pdf>

- Medyanik S.N. and W.K. Liu (2008), Multiple Time Scale Method for Atomistic Simulations, *Computational Mechanics*, Vol. 42, pp. 569-577
- Merchant M. (1945a), '*Mechanics of the Metal Cutting Process I: Orthogonal Cutting and Type 2 Chip*', *Journal of Applied Physics*, Vol.16, No. 5, pp. 267-275
- Merchant M. (1945b), '*Mechanics of the Metal Cutting Process II: Plasticity Conditions in Orthogonal Cutting*', *Journal of Applied Physics*, Vol.16, No. 5, pp. 318-324
- Morse P.M. (1929), '*Diatomic Molecules according to Wave Mechanics II Vibrational Levels*', *Physical Review*, Vol. 34, pp. 57-64
- Murrell J.N. and R.E. Mottram (1990), '*Potential Energy Functions for Atomic Solids*', *Molecular Physics*, Vol. 69, pp. 571-588
- Namba Y., J. Yu, J.M. Bennett and K. Yamashita (2000), '*Modelling and Measurements of Atomic Surface Roughness*', *Applied Optics*, Vol. 39, No. 16, pp. 2705-2718
- Narulkar R., L.M. Raff and R. Komanduri (2004), '*Monte Carlo-Steepest Descent (MC-SD) Simulations of Nanometric Cutting*', *Proceedings of the Inst. of Mech. Eng. Part N: Journal of Nanoengineering and Nanosystems*, Vol. 218, pp. 7-16
- Noreyan A. and J.G. Amar (2008), '*Molecular Dynamics Simulations of Nanoscratching of 3C SiC*', *Wear*, Vol. 265, pp. 956-962
- Opoz T. T. (2012), '*Investigation of Material Removal Mechanism in Grinding: A Single Grit Approach*', PhD Thesis, University of Huddersfield
- Pei Q.X., C. Lu, F.Z. Fang and H. Wu (2006), '*Nanometric Cutting of Copper: A Molecular Dynamics Study*', *Comp. Mat. Sci.*, Vol. 37, pp. 434-441
- Plimpton S. J., (1995), '*Fast Parallel Algorithms for Short-Range Molecular Dynamics*', *J Comp Phys*, Vol. 117, pp. 1-19 and www.lammps.sandia.gov
- Potirniche G. P., M.F. Horstemeyer, G.J. Wagner and P.M. Gullett (2006), '*A Molecular Dynamics Study of Void Growth and Coalescence in Single Crystal Nickel*', *International Journal of Plasticity*, Vol. 22, pp. 257-278
- Promyoo R. H. El-Mounayri and X. Yang (2008), "*Molecular Dynamics Simulation of Nanometric Machining under Realistic Cutting Conditions*", 2008 ASME International Conference on Manufacturing Science and Engineering (MSEC2008), October 7-10, 2008, Evanston, IL.
- Rafii-Tabar and G.A. Mansoori (2003), '*Interatomic Potential Models for Nanostructures*', in *Encyclopedia of Nanoscience and Nanotechnology*, edited by H.S. Nalwa, American Scientific Publishers, Vol. X, pp. 1-17
- Rafii-Tabar H. and A.P. Sutton (1991), '*Long Range Finnis-Sinclair Potentials for FCC Metallic Alloys*', *Philosophical Magazine Letters*, Vol. 63, pp. 217-224

- Rahman A. (1964), '*Correlations in the Motions of Atoms in Liquid Argon*', Physical Review A Vol.136, pp. 405-411
- Rapaport D.C. (2004), *The Art of Molecular Dynamics Simulation*, (Cambridge University Press)
- Rentsch R. and I. Inasaki (1994), '*Molecular Dynamics Simulation for Abrasive Processes*', Annals of the CIRP Vol. 43, No 1, pp. 327-330
- Rentsch R. and I. Inasaki (2006), '*Effects of Fluids on the Surface Generation in Material Removal Processes*', Annals of the CIRP Vol. 55 No1, pp. 1-4
- Rentsch R. (2008), '*Nanoscale Cutting*', in Nano and Micromachining, edited by Davin .J.P. and M.J. Jackson, Wiley-ISTE, pp.1-24
- Ruszaj A., M. Zybura, R. Zurek and G. Skrabalak (2003), '*Some Aspects of the Electrochemical Machining Process Supported by Electrode Ultrasonic Vibrations Optimization*', Proceedings of the IMechE, Part B: Journal of Engineering Manufacture, Vol. 217, pp. 1365-1371
- Saito Y, N. Sasaki, H. Moriya, A. Kagatsume and S. Noro (2001), '*Parameter Optimization of Tersoff Interatomic Potentials Using Genetic Algorithms*', JSME International Series A, Vol. 44, No. 2, pp. 207-213
- Schlick T. (2002), *Molecular Modelling and Simulations: An Interdisciplinary Guide*, (Springer)
- Senthilkumar C., G. Ganesan and R. Karthikeyan (2011), '*Parametric Optimizations of Electrochemical Machining of Al/15 SiCp Composites using NSGA II*', Transactions of Nonferrous Metals Society of China, Vol. 21, Iss. 10, pp. 2294-2300
- Shimada S., N. Ikawa, G. Ohmori, H. Tanaka, and U. Uchikoshi (1992), '*Molecular Dynamics Analysis as Compared with Experimental Results of Micromachining*', Annals of the CIRP Vol. 41, No 1, pp. 117-120
- Shimada S., N. Ikawa, H. Tanaka, G. Ohmori and J. Uchikoshi (1993), '*Feasibility Study on Ultimate Accuracy in Microcutting using Molecular Dynamics Simulation*', Annals of the CIRP, Vol. 42, No.1, pp. 91-94
- Shimada S., H. Tanaka and N. Ikawa (1999), '*Atomistic Mechanism of Surface Generation in Micromachining of Monocrystalline Silicon*', Proceeding of the First International EUSPEN Conference, Vol. 1, Part1, pp. 230-233
- Shimizu J. H. Eda, M. Yoritsune and E. Ohmura (1998), '*Molecular Dynamics Simulations of Friction on the Atomic Scale*', Nanotechnology, Vol. 9, pp. 118-123
- Shimizu J., L. Zhou and H. Eda (2006), '*Molecular Dynamics Simulation of Vibration-Assisted Cutting: Influences of Vibration, Acceleration and Velocity*', Int. J. Nanomanufacturing, Vol. 1, No. 1, pp. 105-116
- Shimizu J., L. Zhou and H. Eda (2008), '*Molecular Dynamics Simulation of Effect of Grinding Wheel Stiffness on Nanogrinding Process*', Int. J. Abrasive Technology, Vol. 1, Nos. 3/4, pp. 316-326

Smith A.G. and G. Carter (1969), '*Computer Calculations of Binary Collision Scattering Angles using the Born-Mayer Potential for Interacting Argon and Gold Atoms*', J. Phys. B (Atom. Molec. Phys.), Ser. 2, Vol. 2, pp. 972-975

Smith R., D. Christopher and S. Kenny (2003), '*Defect Generation and Pileup of Atoms during Nanoindentation of Fe Single Crystals*', Physical Review B, Vol. 67, pp. 245405-10

Sokolowski A.P. (1955), Prazision in der Matallbearbeitung (Berlin:VEB Verlag Technik)

Son S.M., H.S. Lim and J.H. Ahn (2005), '*Effects of the Friction on the Minimum Cutting Thickness in Micro Cutting*', International Journal of Machine Tools and Manufacture, Vol.45, pp. 529-535

Stillinger F.H. and T.A. Weber (1985), '*Computer Simulation of Local Order in Condensed Phases of Silicon*', Physical Review B, Vol. 31, pp. 5262-5271

Stokes J. (2008), The Theory and Application of the High Velocity Oxy-Fuel (HVOF) Thermal Spray Process, Dublin City University, Ireland

Strenkowski J.S. and J.T. Carroll (1985), '*A Finite Element Model of Orthogonal Metal Cutting*', ASME Journal of Engineering for Industry, Vol. 107, pp. 349-354

Strenkowski J.S. and J.T. Carroll (1988), '*Finite Element Models of Orthogonal Cutting with Application to Single Point Diamond Turning*', International Journal of Mechanical Science, Vol. 30, pp. 899-920

Stukowski A. (2010), '*Visualization and Analysis of Atomic Simulation Data with OVITO – The Open Visualization Tool*', Modelling Simul. Mat. Scien. Eng., Vol. 18, 015012 (7pp)

Sutton A.P. and J. Chen (1990), '*Long-Range Finnis Sinclair Potentials*', Philosophical Magazine Letters, Vol. 61, Iss. 3, pp. 139-146

Taniguchi N. (1974), '*On the Basic Concept of 'Nanotechnology'*', Proc. Intl. Conf. Prod. Eng. Tokyo, Part II, Japan Society of Precision Engineering

Taniguchi N. (1983), '*Current Status in, and Future Trends of, Ultraprecision Machining and Ultrafine Materials Processing*', Annals of the CIRP, Vol. 32, No. 2, pp. 573-582

Tersoff J. (1988a), '*New Empirical Approach for the Structure and Energy of Covalent Systems*', Physical Review B, Vol. 37, No. 12, pp. 6991-7000

Tersoff J. (1988b), '*Empirical Interatomic Potential for Silicon with Improved Elastic Properties*', Physical Review B, Vol. 38, No. 14, pp. 9902-9905

Thijsee B. (2007), '*Molecular Dynamics in Materials Science*', IDEA Summer School Lecture Note

Van Gunsteren W. F. and H.J.C. Berendsen (1990), '*Computer Simulation of Molecular Dynamics: Methodology, Applications, and Perspectives in Chemistry*', Anew. Chem. Int. Ed. Engl., Vol. 29, pp. 992-1023

Verlet L. (1967), '*Computer Experiments on Classical Fluids I. Thermodynamics Properties of Lennard-Jones Molecules*', Physical Review D, Vol. 159, pp. 98-103

Visual Molecular Dynamics (VMD), <http://www.ks.uiuc.edu/Research/vmd/> (Accessed in 2010)

Volger M.P., R.E. DeVor and S.G. Kapoor (2004a), '*On the Modeling and Analysis of Machining Performance in Micro-Endmilling, Part I: Surface Generation*', Journal of Manufacturing Science and Engineering 126, pp 685-694

Volger M.P., R.E. DeVor and S.G. Kapoor (2004b), '*On the Modeling and Analysis of Machining Performance in Micro-Endmilling, Part II: Cutting Force Prediction*', Journal of Manufacturing Science and Engineering, Vol. 126, pp. 695-705

Wang C., T. Yu, W. Duan and L.Wang (1995), '*A First Principles Interatomic Potential and Application to the Grain Boundary in Ni*', Physics Letters A, Vol. 197, Iss.5-6, pp. 449-457

Weule H., Hüntrup V., and Trischler H. (2001), '*Micro-cutting of Steel to Meet New Requirements in Miniaturization*', Annals of the CIRP, Vol. 50, pp. 61-64

Ye Y., R. Biswas, J.R. Morris, A. Bastawros, and A. Chandra (2002), '*Simulation of Nanoscale Polishing of Copper with Molecular Dynamics*', Mat. Res. Soc. Symp. Proceedings Vol. 732E, pp. I4.8.1-6

Yu J. and Y. Namba (1998), '*Atomic Surface Roughness*', Applied Physics Letters, Vol. 73, pp. 3607-3609

Yuan Z.J., M. Zhou and S. Dong (1996), '*Effect of Diamond Tool Sharpness on Minimum Cutting Thickness and Cutting Surface Integrity in Ultraprecision Machining*', Journal of Materials Processing Technology, Vol. 62, pp. 327-330

Zhao K.J., C.Q. Chen, Y.P. Shen and T.J. Lu (2009), '*Molecular Dynamics Study on the Nano-void Growth in Face-centered Cubic Single Crystal Copper*', Computational Materials Science, Vol. 46, pp. 749-754

Appendixes

Appendix A: LAMMPS Input File Structure

```
# in.cu_C

units          metal
boundary       f f s
atom_style     atomic
pair_style     hybrid tersoff eam lj/cut 2.5

read_data      data.cu_C

pair_coeff      * * tersoff SiC.tersoff NULL C NULL NULL

pair_coeff     1 * eam Cu_u3.eam
pair_coeff     3 * eam Cu_u3.eam
pair_coeff     4 4 eam Cu_u3.eam

pair_coeff     1 2 lj/cut 0.4096 2.338
pair_coeff     2 3 lj/cut 0.4096 2.338
pair_coeff     2 4 lj/cut 0.4096 2.338

neighbor       3.0 bin
neigh_modify   delay 3
#neigh_modify  exclude type 1 1

group          newtonian type 1
group          tool type 2
group          thermostat type 3
group          boundary type 4
group          mobile subtract all boundary tool
#fix           1 tool rigid single
fix            1 thermostat rigid single

# initial velocities

compute        new mobile temp
velocity       mobile create 293 564329 temp new
velocity       tool set 1.5 0 0 sum yes units box
#fix           2 mobile nve
fix            2 all nve
#unfix         2
fix            3 mobile temp/rescale 1.0 293 293 10.0 1.0
fix_modify     3 temp new
fix            4 boundary setforce 0.0 0.0 0.0
fix            5 tool setforce 0.0 0.0 0.0
velocity       thermostat scale 293.0

thermo         500
thermo_style    custom step temp epair pe ke etotal vol press f_5[1] f_5[2]
f_5[3]
thermo_modify   temp new
thermo_modify   lost warn
compute_modify  new extra 4
dump           1 all atom 500 dump.cu_C
dump_modify    1 scale no
dump           2 all custom 1000 dump.forcecu_C.* id type x y z vx vy vz fx fy fz
timestep       0.0003
run            150000
```

Appendix B: A (Portable Batch System) PBS Job Script Template

```
#####
### Job Submission Script          ###
# Change items in section 1      #
# to suit your job needs        #
#####
# Section 1: User Parameters      #
#####
#
#!/bin/bash
#PBS -l nodes=2:ppn=4
#PBS -m abe
#PBS -M j.o.oluwajobi@hud.ac.uk
#PBS -N Sa_Tersoff_EAM_LJ_W15_D5
#PBS -q parastd
#PBS -j oe

#
#####
# Section 2: Environment Variables #
# State your executable path      #
# and anylicense info            #
# eg:                            #
# export LM_LICENSE_FILE=7241@mech1 #
#####

cd $HOME/Sa_Tersoff_EAM_LJ_W15_D5
NODES=`uniq $PBS_NODEFILE | wc -l`
CORES=`cat $PBS_NODEFILE | wc -l`
sort -r $PBS_NODEFILE | uniq > mpd.nodefile.$PBS_JOBID
PATH=/apps/libs/mpi/openmpi-1.4.1/bin:/apps/lammps/lammps-12Oct10/bin:$PATH
LD_LIBRARY_PATH=/apps/libs/mpi/openmpi-1.4.1/lib:$LD_LIBRARY_PATH
OPENMPI_HOME=/apps/libs/mpi/openmpi-1.4.1/
#####
# Section 3: Executing Commands   #
#####
mkdir /tmp/jide/
cp -R $HOME/Sa_Tersoff_EAM_LJ_W15_D5/* /tmp/jide/
cd /tmp/jide/

mpirun -machinefile mpd.nodefile.$PBS_JOBID -np $CORES --prefix
$OPENMPI_HOME -path $PATH lmp_bellatrix <in.cu_C

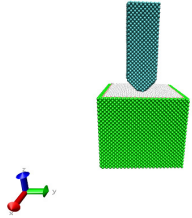
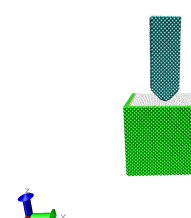
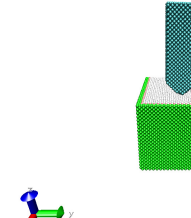
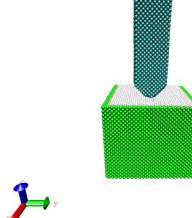
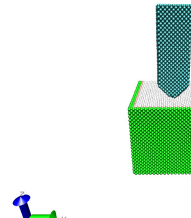
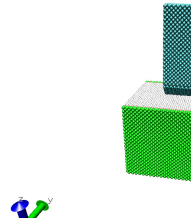
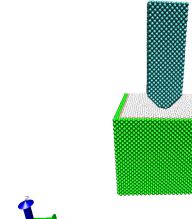
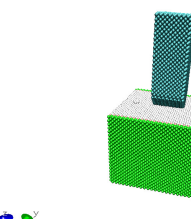
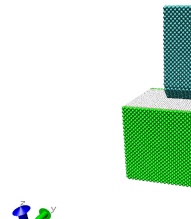
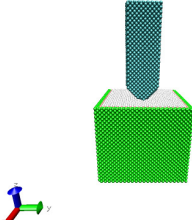
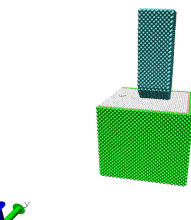
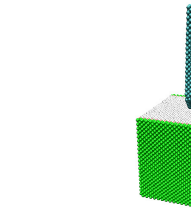
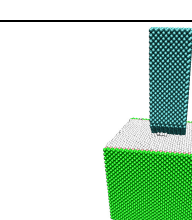
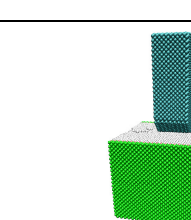
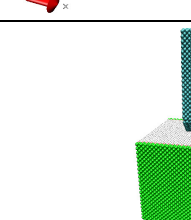
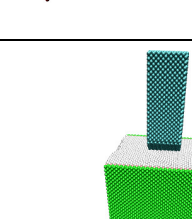
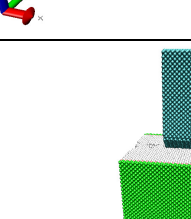
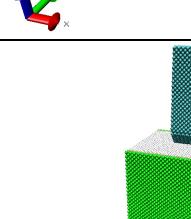
cp -R /tmp/jide/* $HOME/Sa_Tersoff_EAM_LJ_W15_D5/
cd $HOME/Sa_Tersoff_EAM_LJ_W15_D5
rm -Rf /tmp/jide/

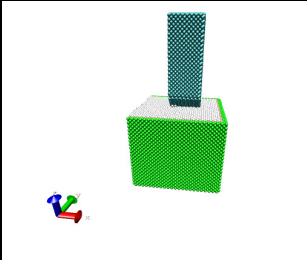
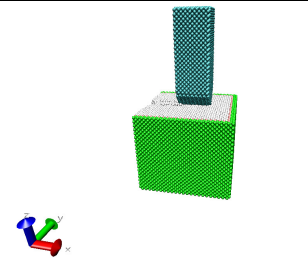
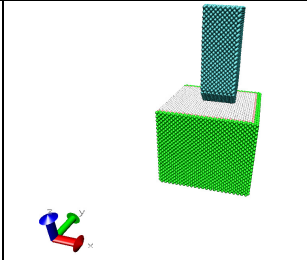
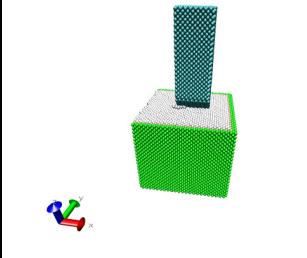
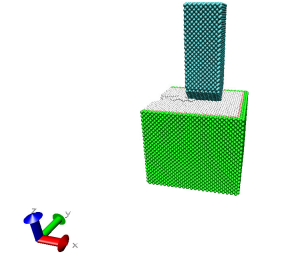
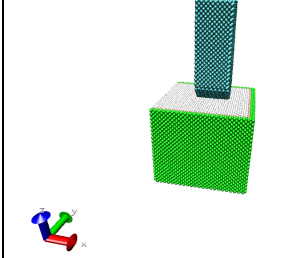
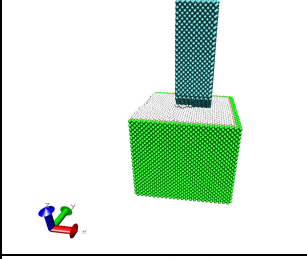
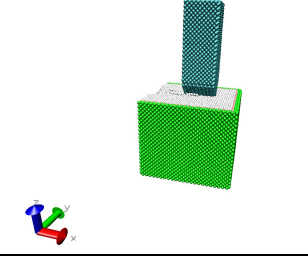
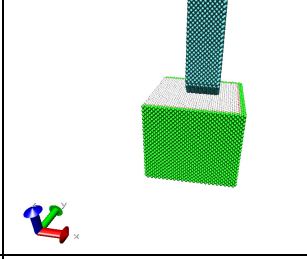
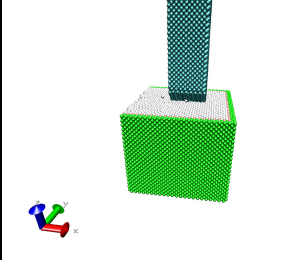
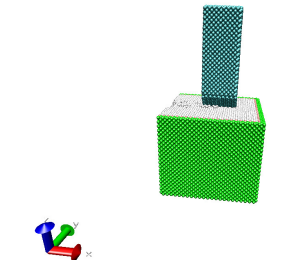
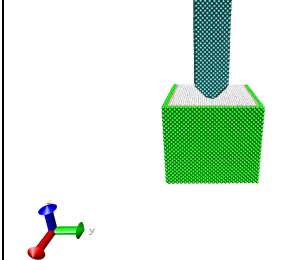
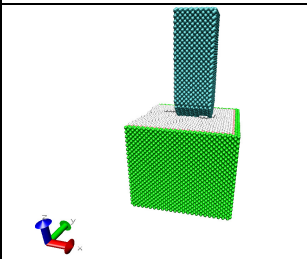
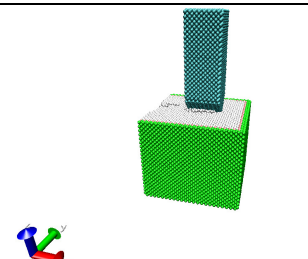
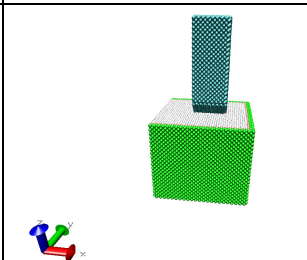
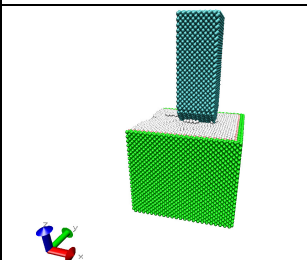
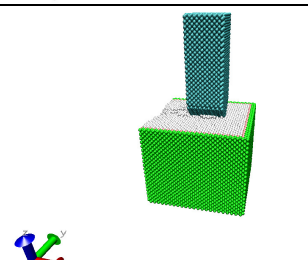
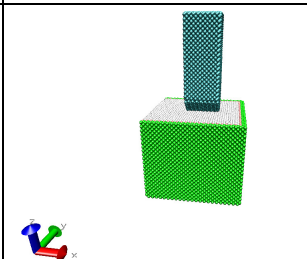
#####
# Section 4: Clean Temporary Files #
#####

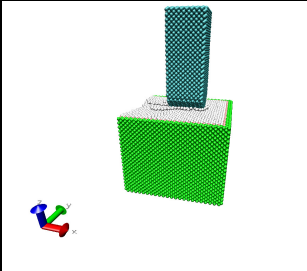
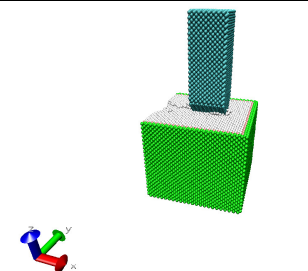
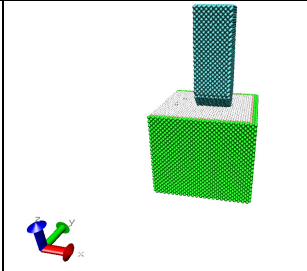
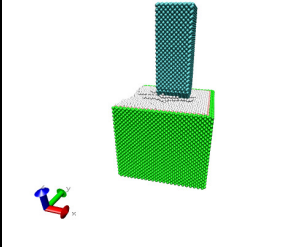
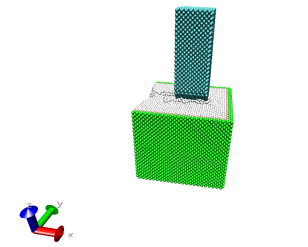
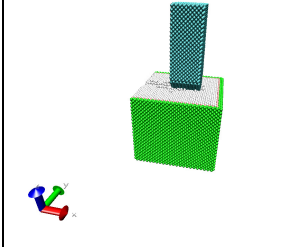
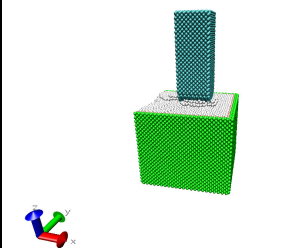
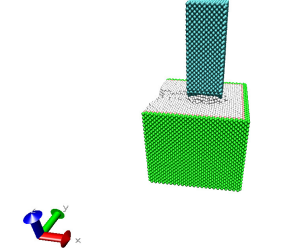
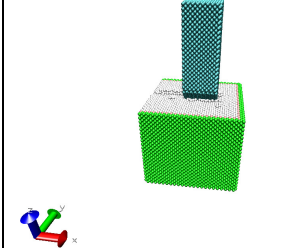
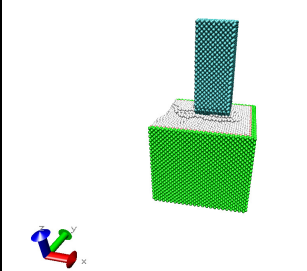
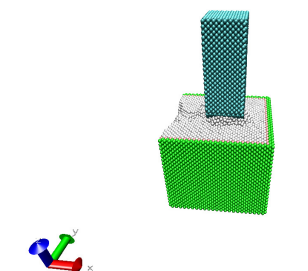
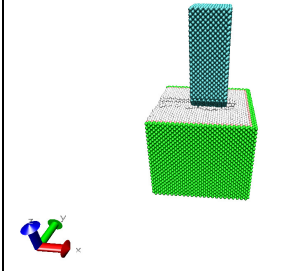
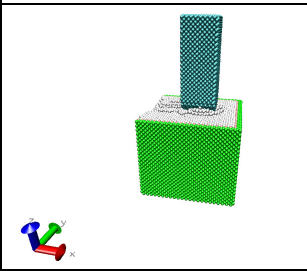
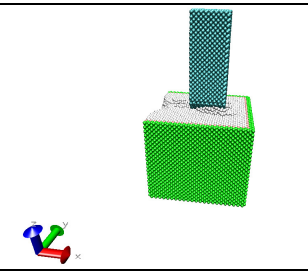
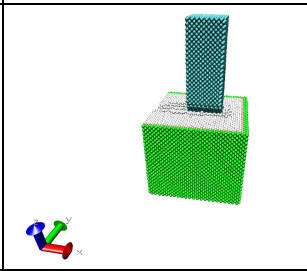
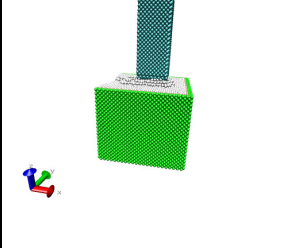
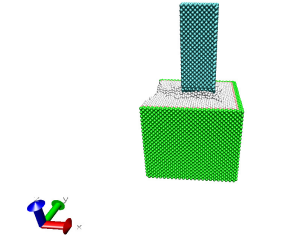
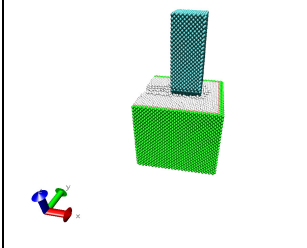
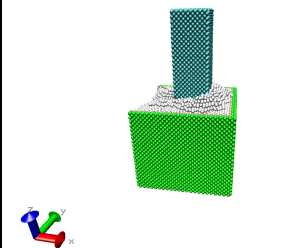
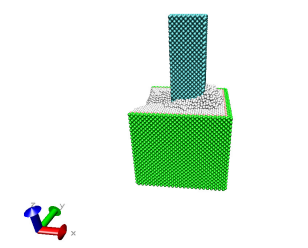
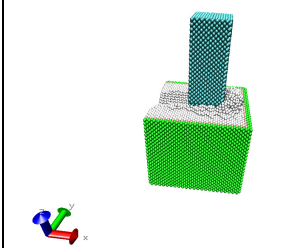
rm ./mpd.nodefile.$PBS_JOBID
```

Appendix C: More Simulation Results

Table C.1: Simulations with Variations of the Depth of Cut (0.01-4.0nm) for the Three Potential Combinations

Depth of Cut (nm)	Morse-Morse (Case 4.3.1)	EAM-Morse (Case 4.3.2)	EAM-LJ (Case 4.3.3)
0.01			
0.02			
0.03			
0.04			
0.05			
0.06			

0.07			
0.08			
0.09			
0.10			
0.15			
0.20			

0.25			
0.30			
0.35			
0.40			
0.45			
0.50			
1.00			

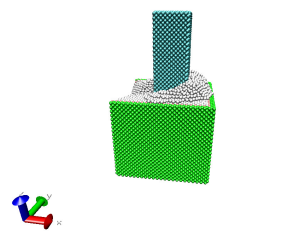
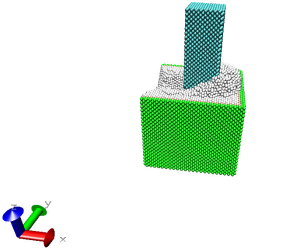
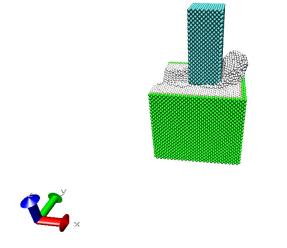
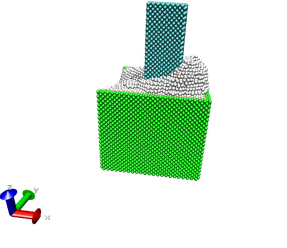
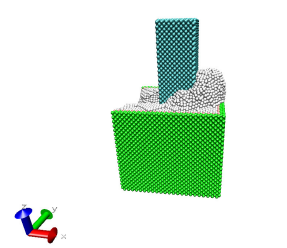
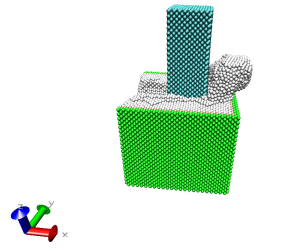
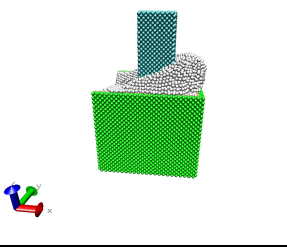
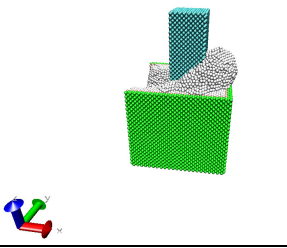
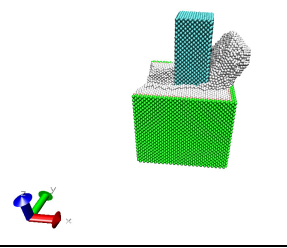
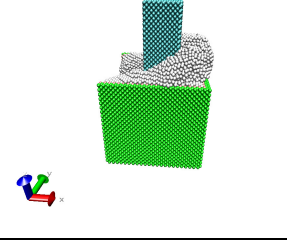
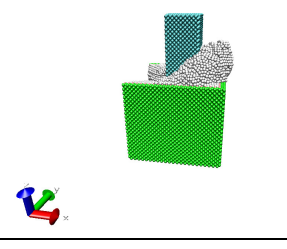
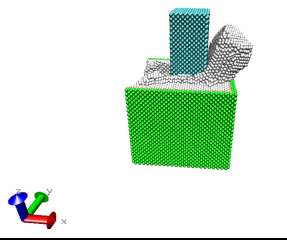
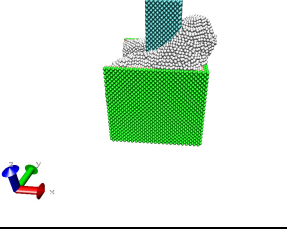
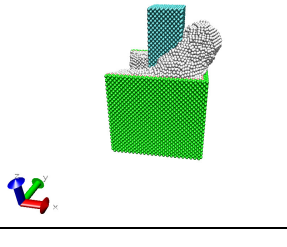
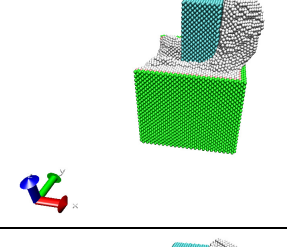
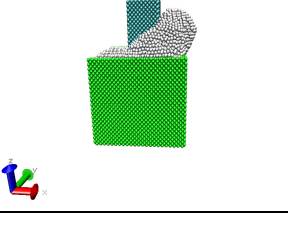
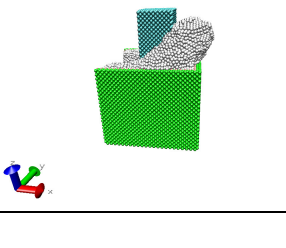
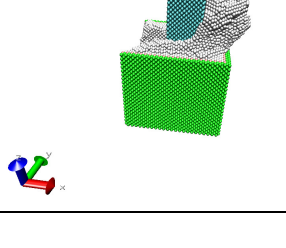
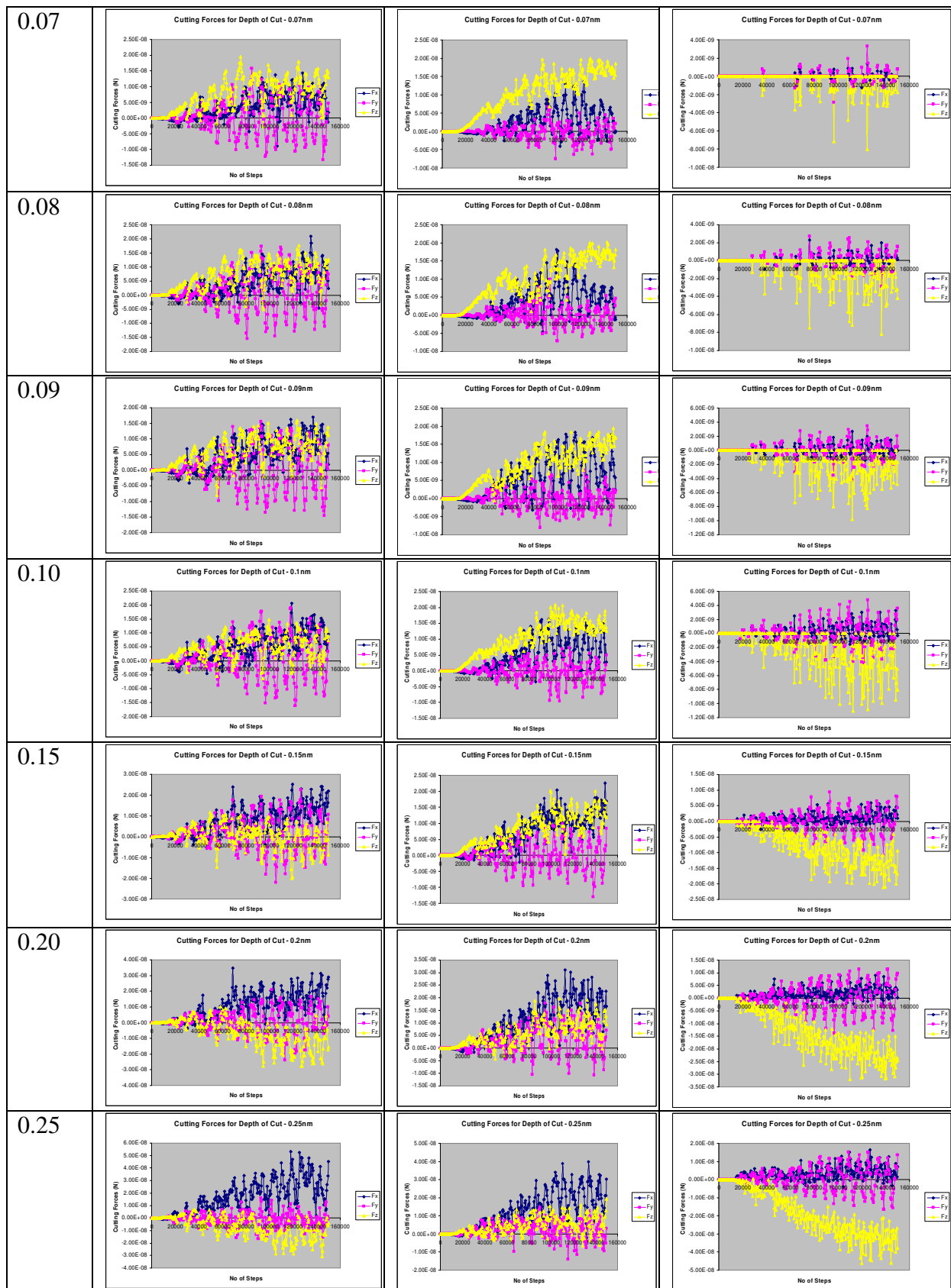
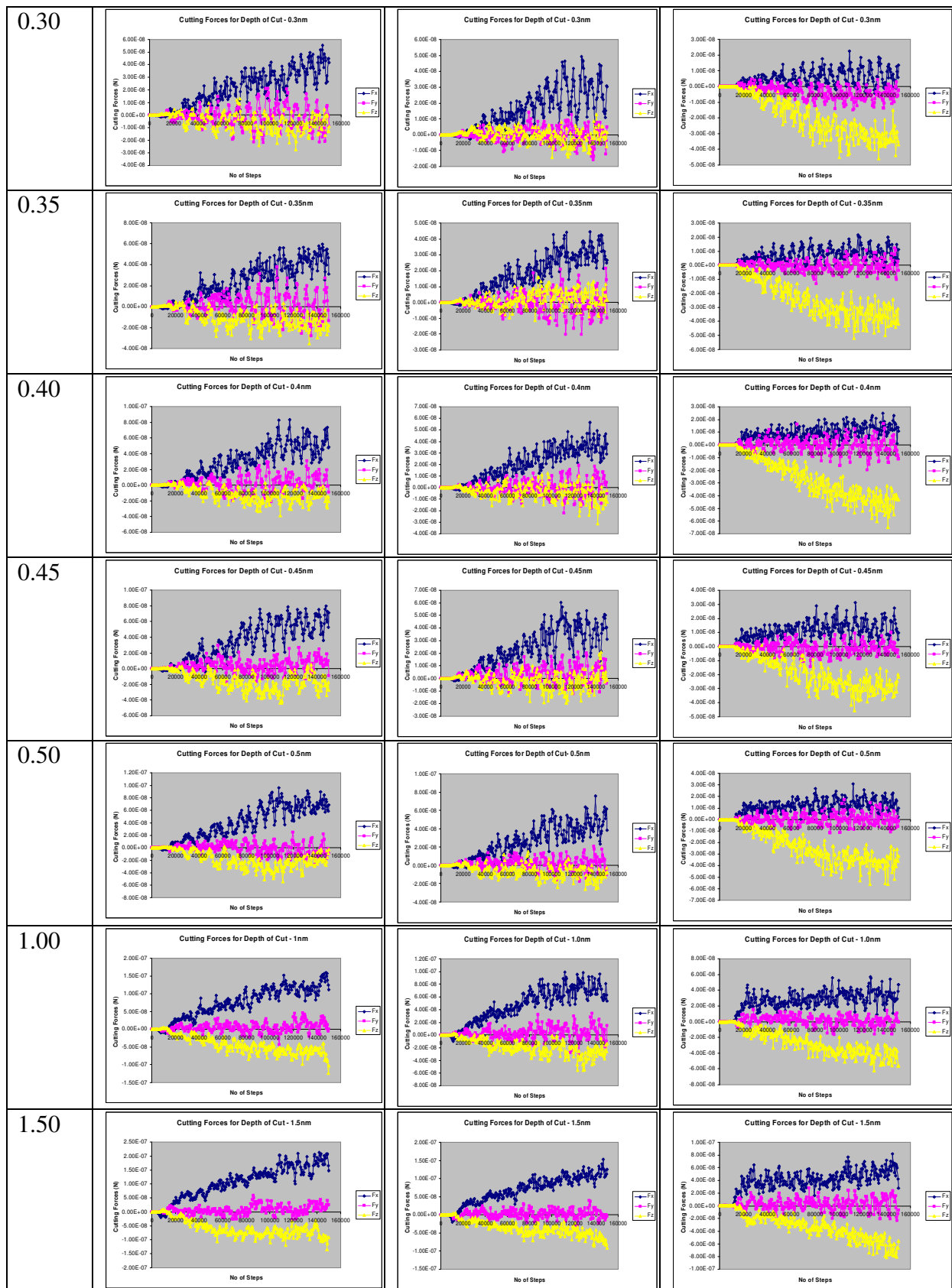
1.50			
2.00			
2.50			
3.00			
3.50			
4.00			

Table C.2: Comparisons of the Cutting Forces for the Simulations with Depth of Cut (0.01-4.0nm)

Depth of Cut (nm)	Morse-Morse (4.3.1)	EAM-Morse (4.3.2)	EAM-LJ (4.3.3)
0.01			
0.02			
0.03			
0.04			
0.05			
0.06			





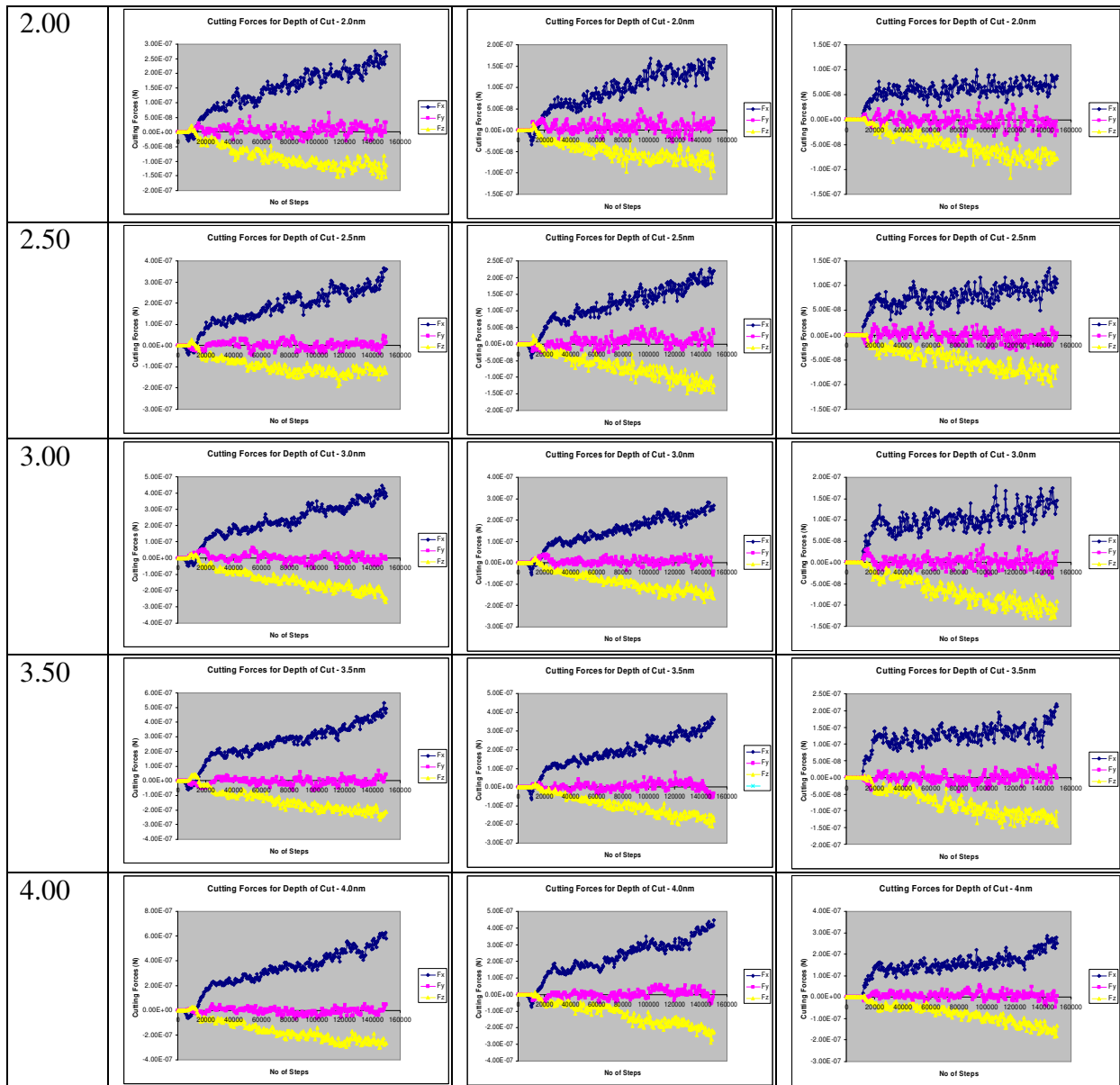
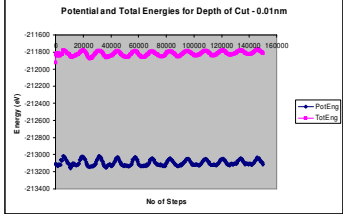
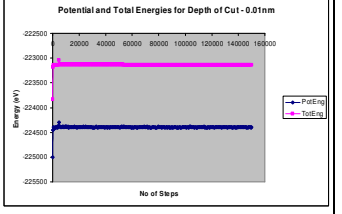
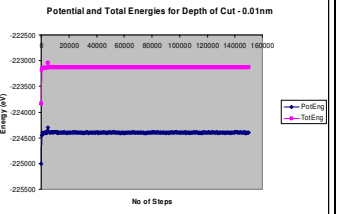
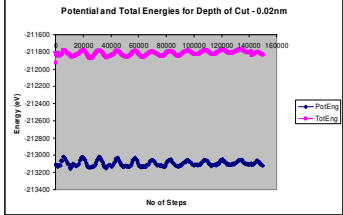
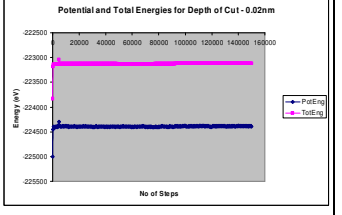
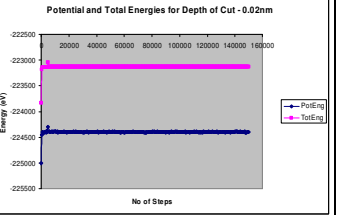
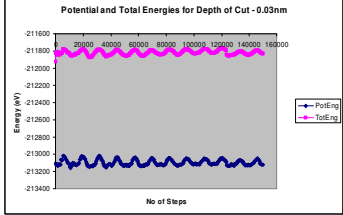
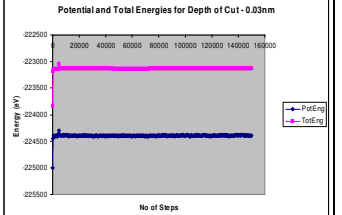
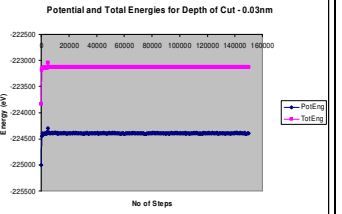
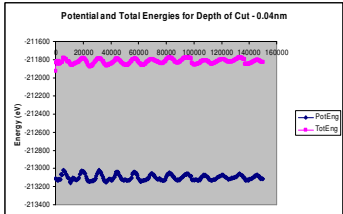
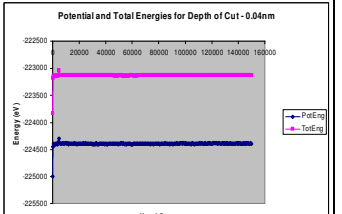
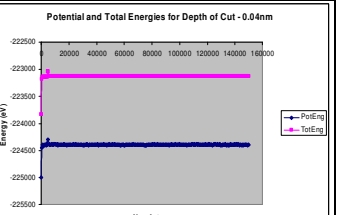
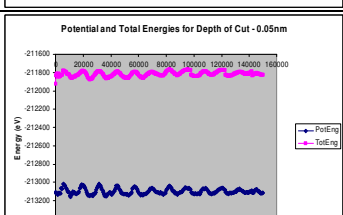
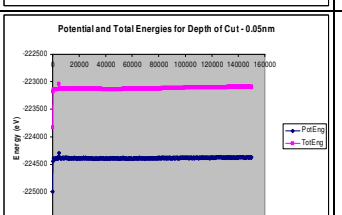
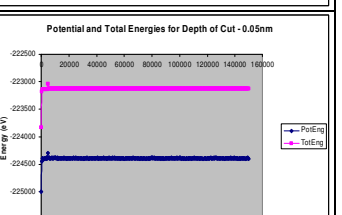
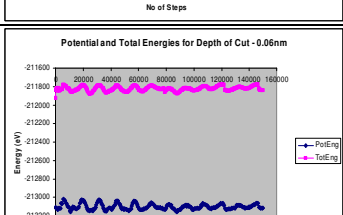
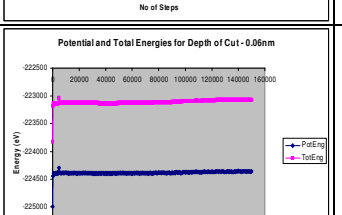
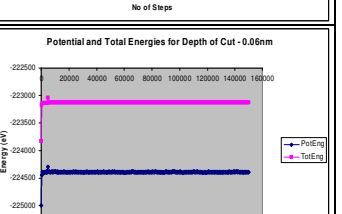
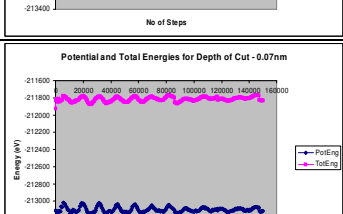
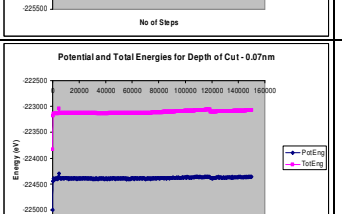
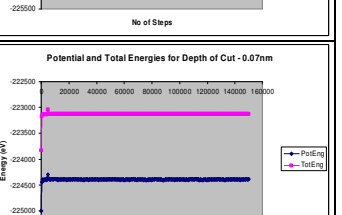
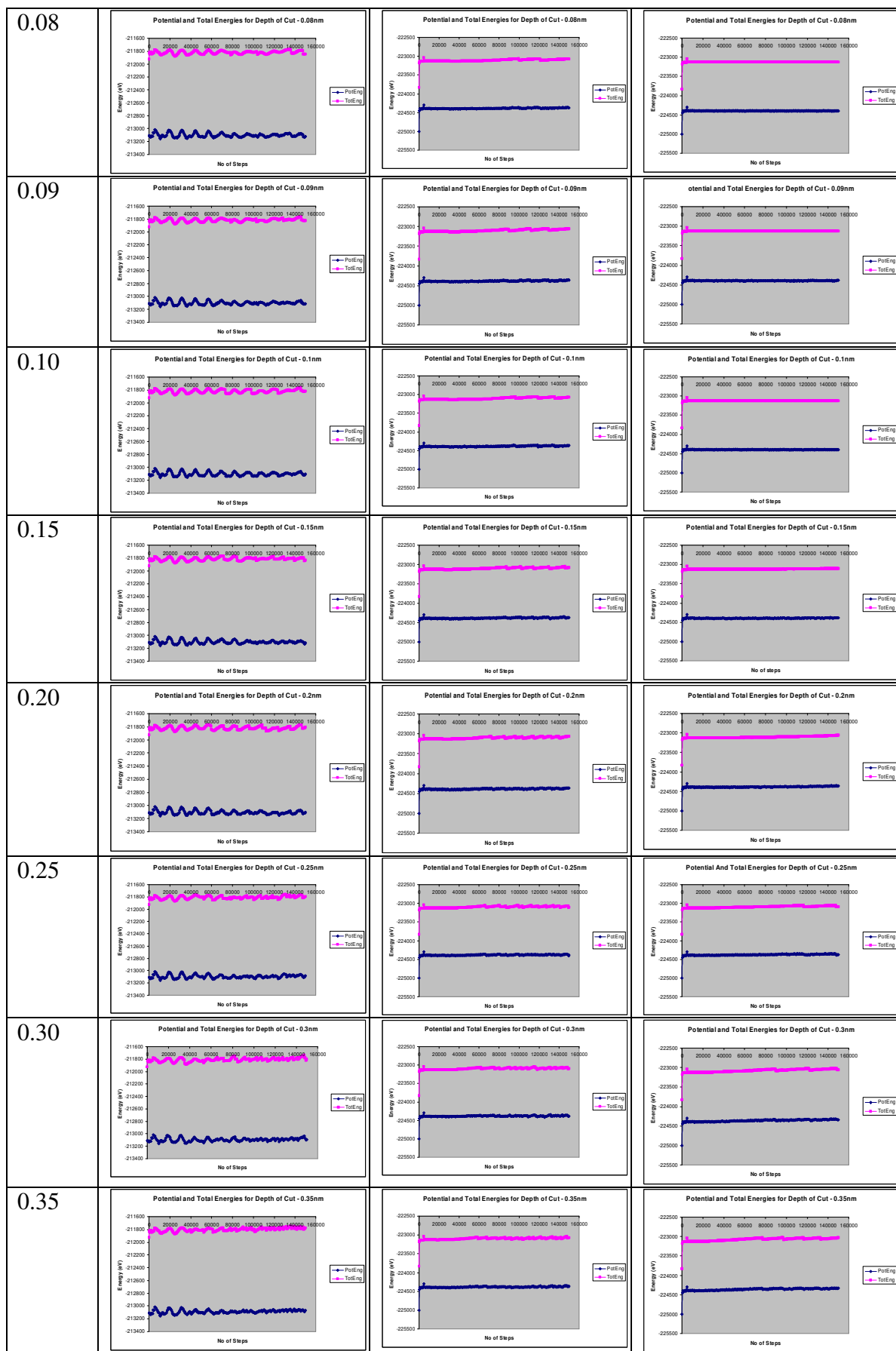
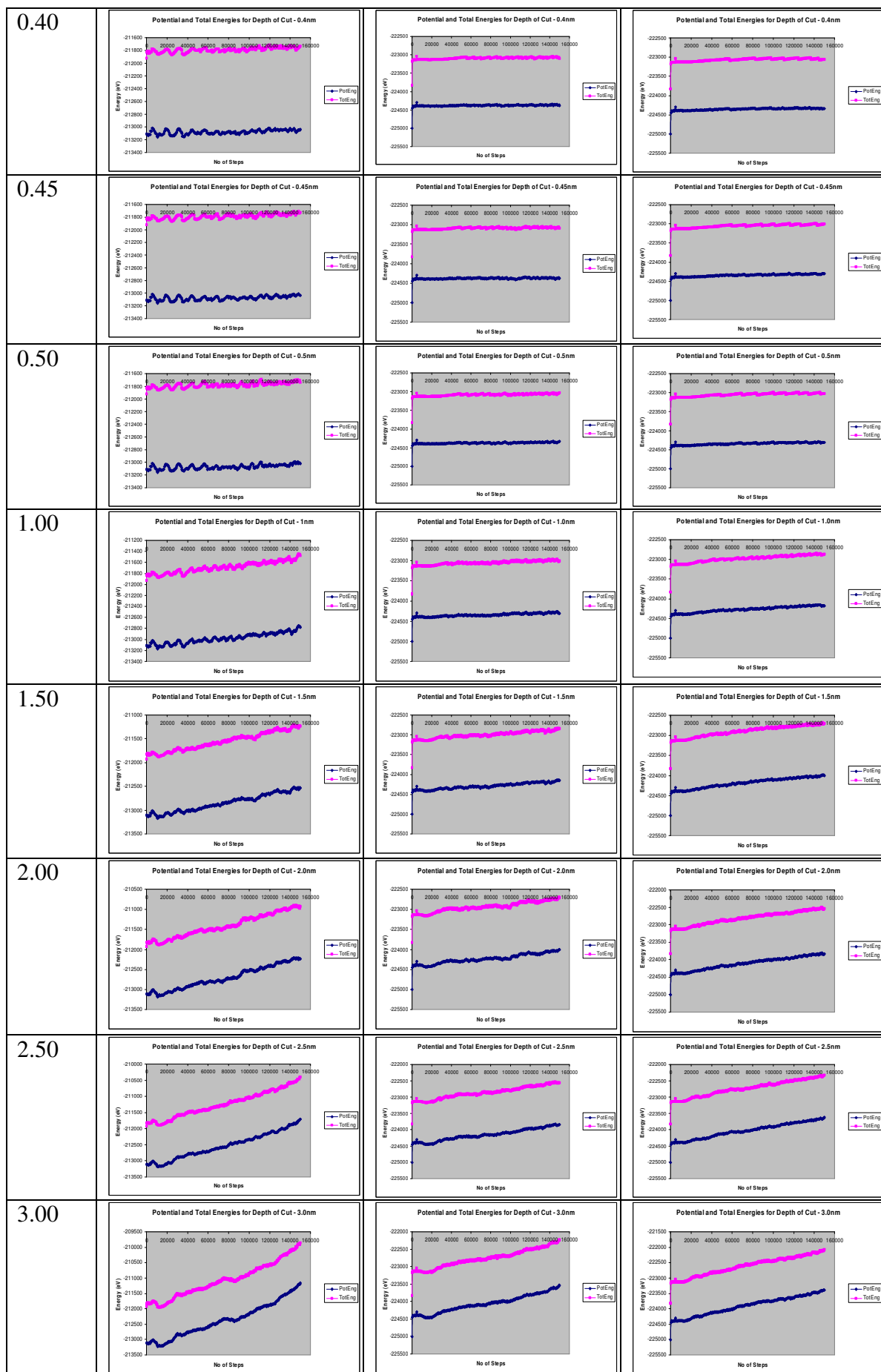


Table C.3: Comparisons of the Energies for the Simulations with Depth of Cut (0.01-4.0nm)

Depth of Cut (nm)	Morse-Morse (Case 4.3.1)	EAM-Morse (Case 4.3.2)	EAM-LJ (Case 4.3.3)
0.01			
0.02			
0.03			
0.04			
0.05			
0.06			
0.07			





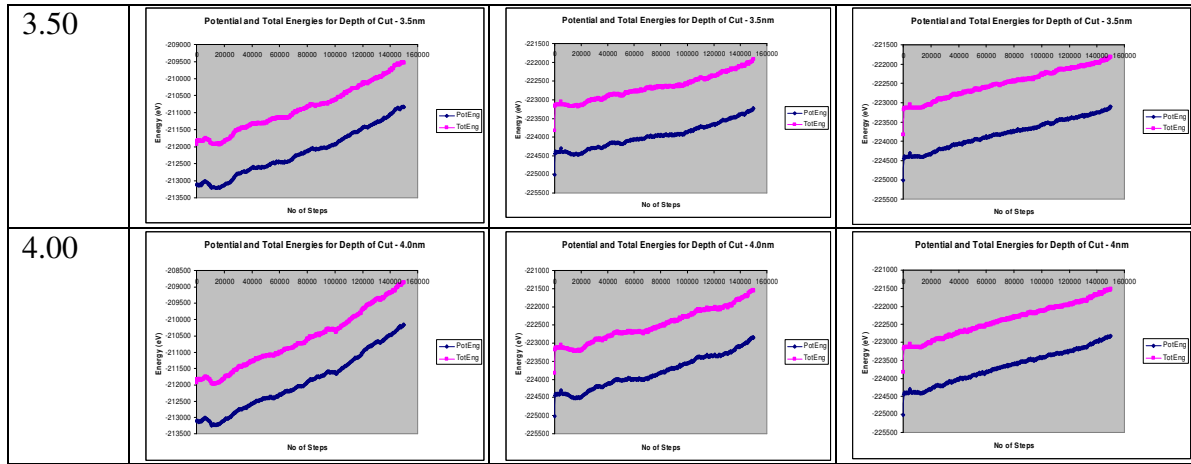
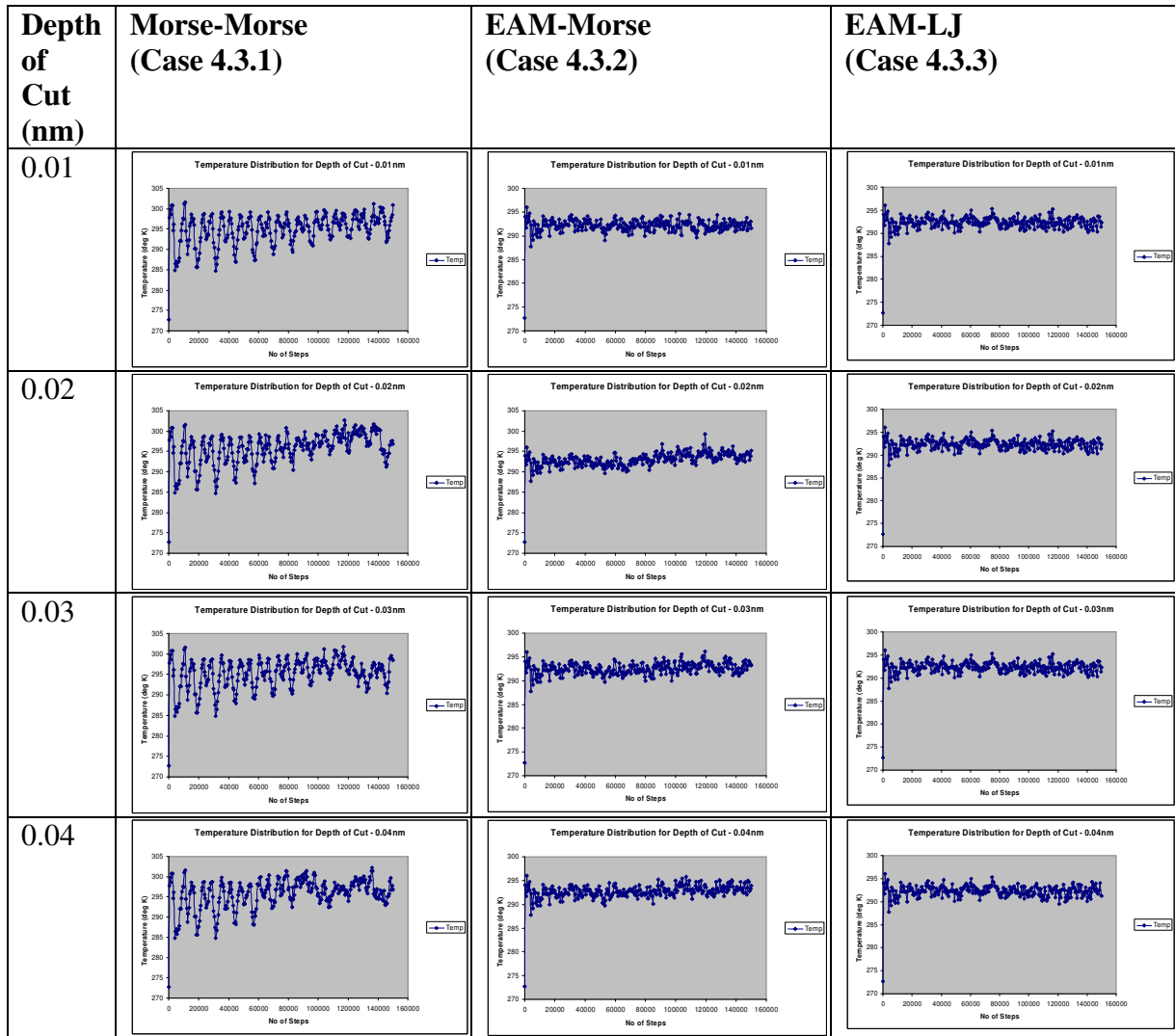
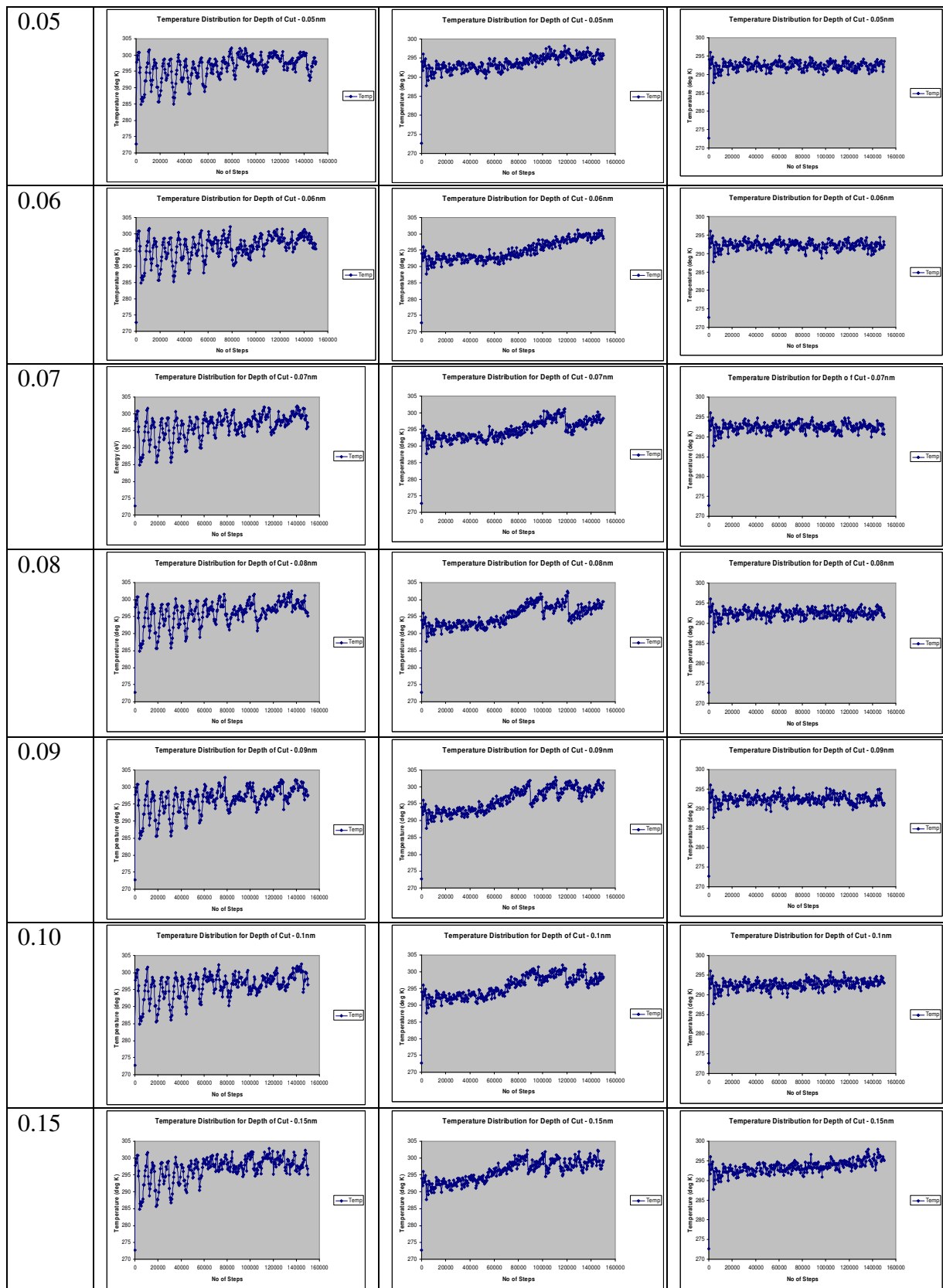
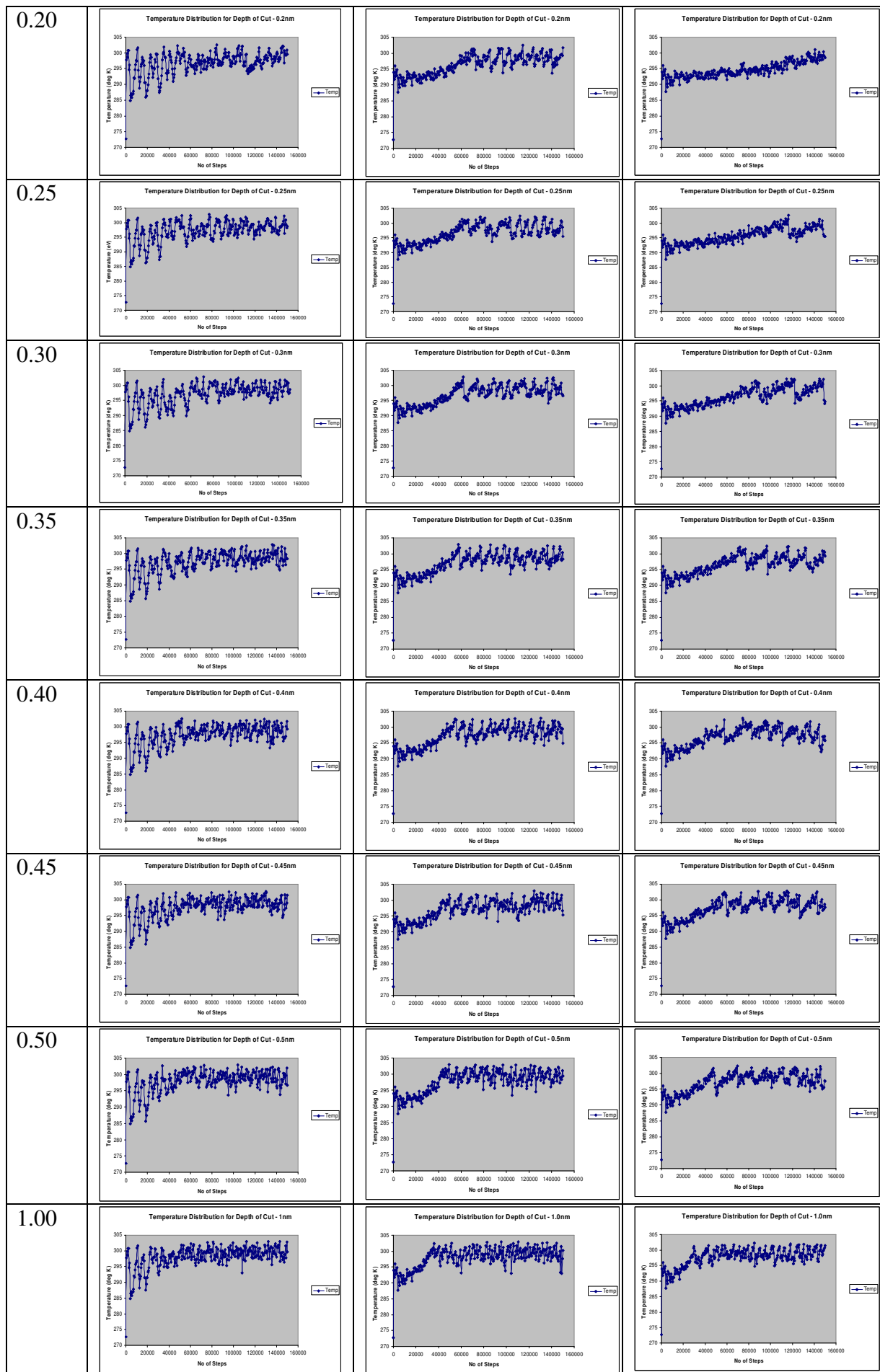


Table C.4: Comparisons of the Variation of Temperature for the Simulations with Depth of Cut (0.01-4.0nm)







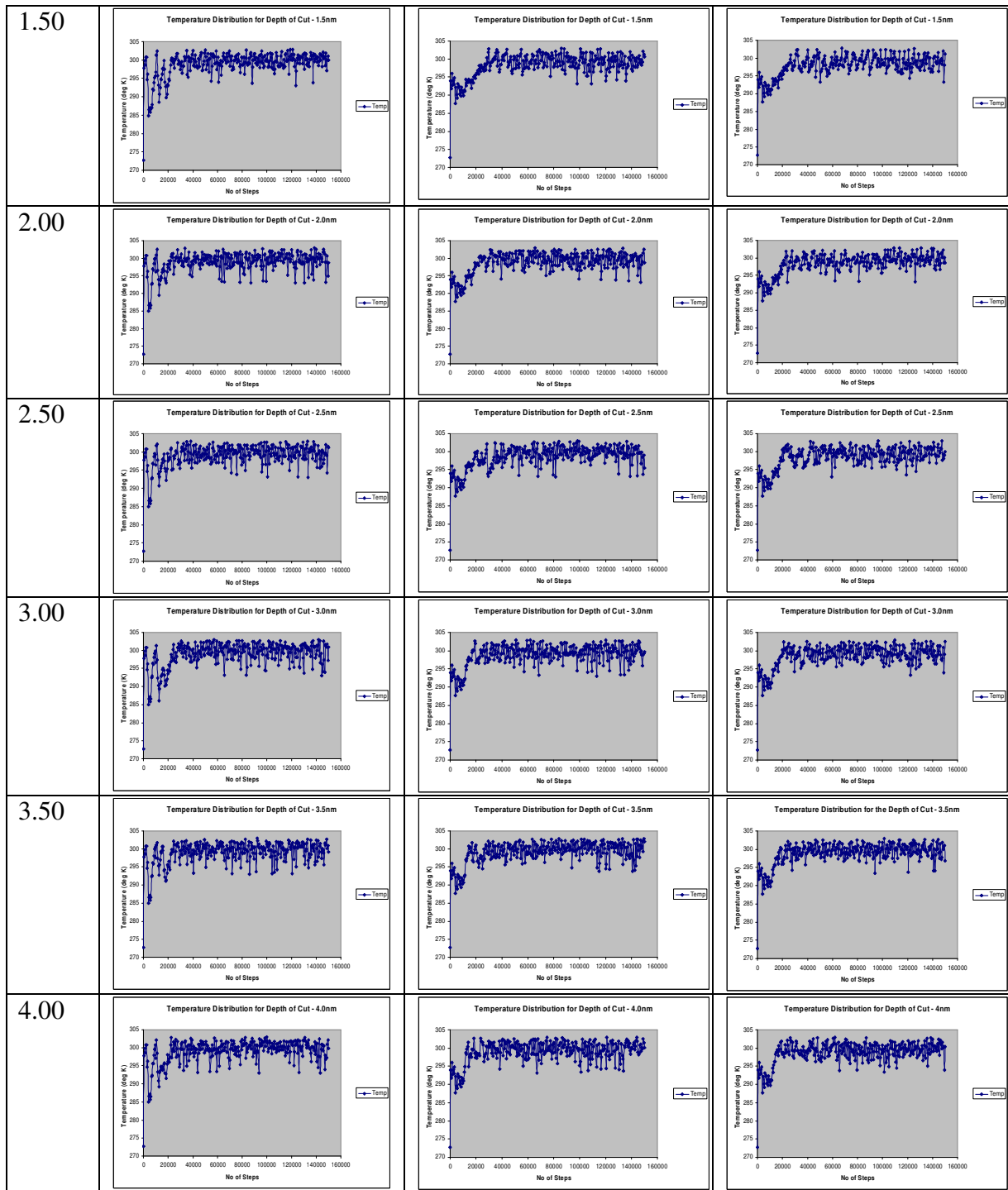
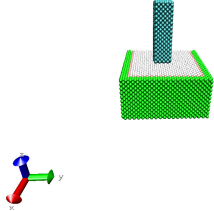
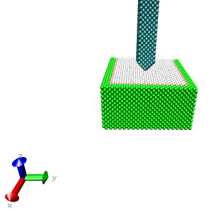
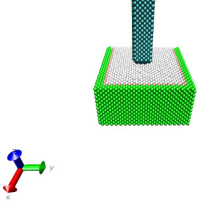
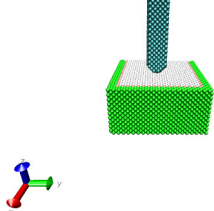
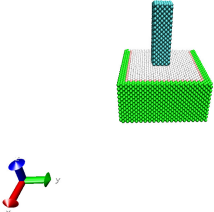
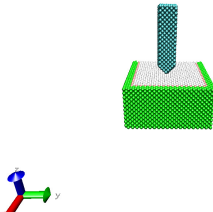
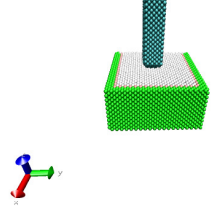
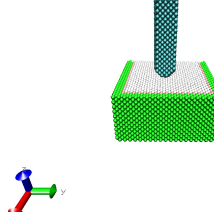
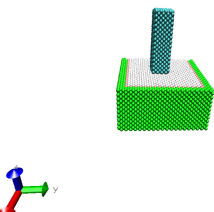
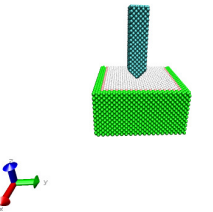
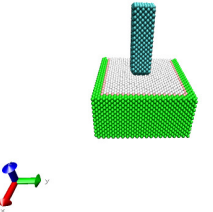
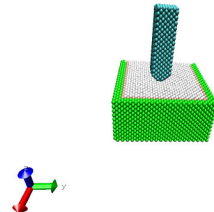
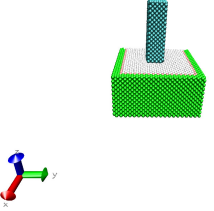
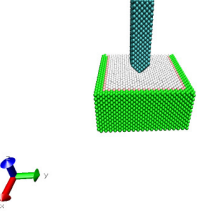
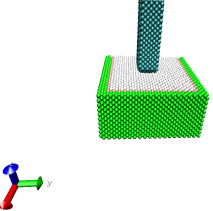
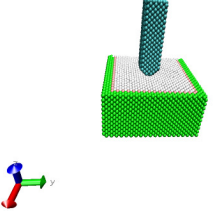
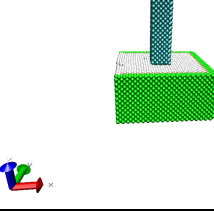
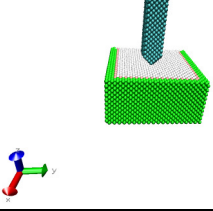
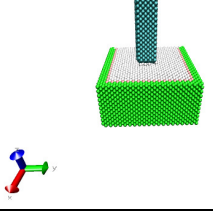
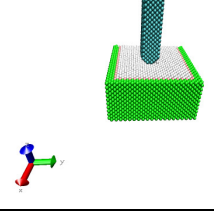
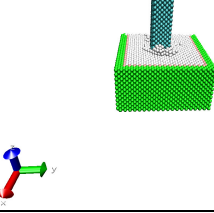
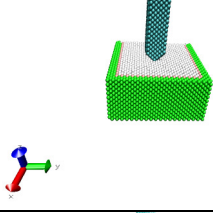
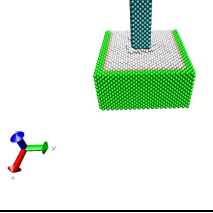
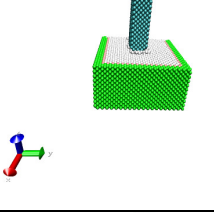
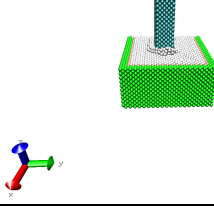
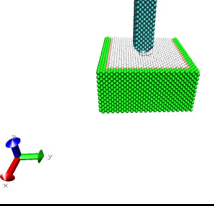
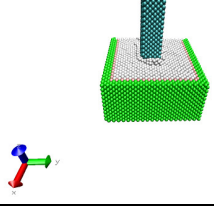
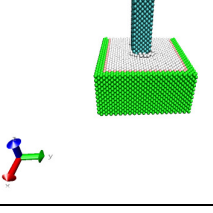


Table C. 5: Comparison of the Simulation for Different Tool Ends with Depth of Cut (0.05-0.5nm)

Depth of Cut (nm)	Flat Tool End	Pointed Tool End	Spherical Tool End	Trapezoidal Tool End
0.05				
0.1				
0.15				
0.2				
0.25				
0.3				
0.35				

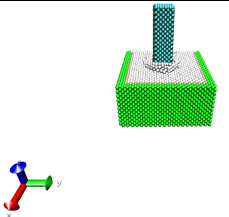
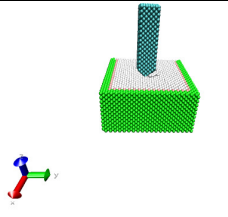
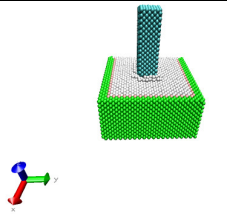
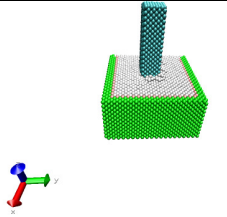
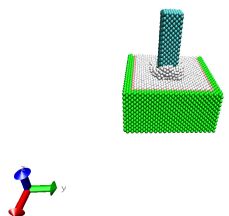
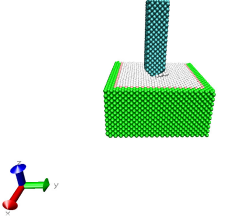
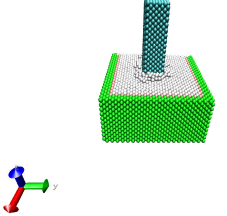
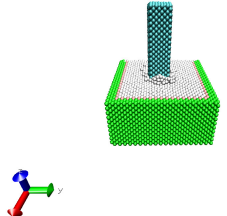
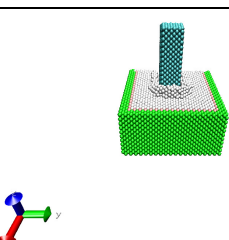
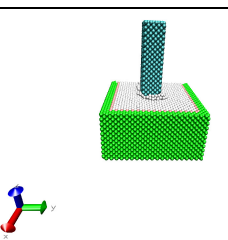
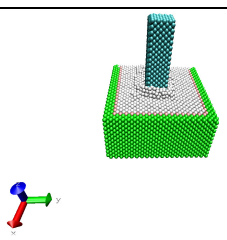
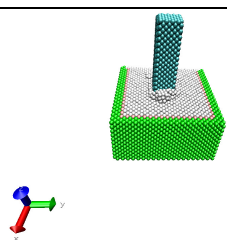
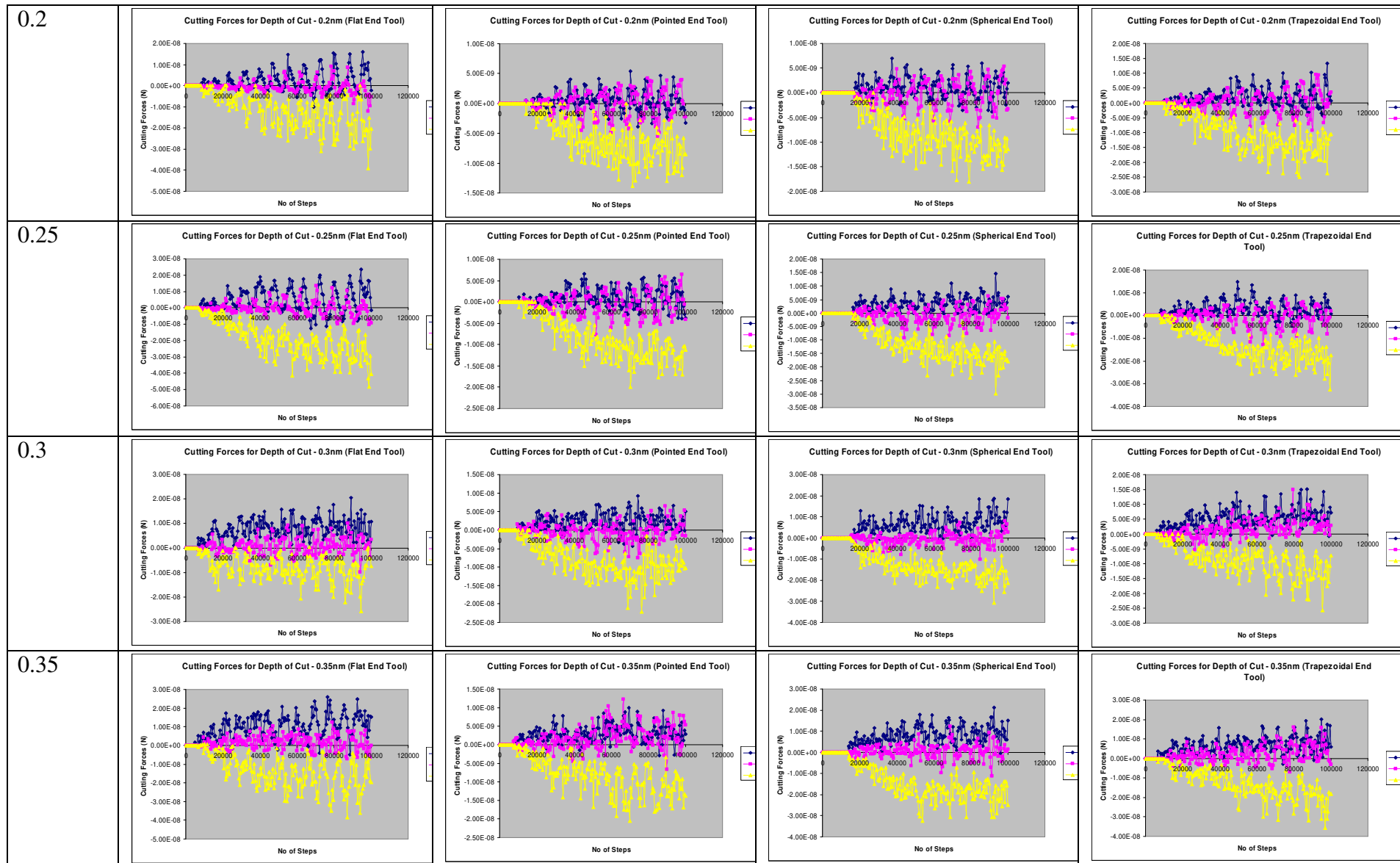
0.4				
0.45				
0.5				

Table C.6: Comparison of the Cutting Forces for the Different Tool Ends (Depth of Cut 0.05-0.5nm)

Depth of Cut (nm)	Flat Tool End	Pointed Tool End	Spherical Tool End	Trapezoidal Tool End
0.05	<p>Cutting Forces for Depth of Cut - 0.05nm (Flat End Tool)</p>	<p>Cutting Forces for Depth of Cut - 0.05nm (Pointed End Tool)</p>	<p>Cutting Forces for Depth of Cut - 0.05nm (Spherical End Tool)</p>	<p>Cutting Forces for Depth of Cut - 0.05nm (Trapezoidal End Tool)</p>
0.1	<p>Cutting Forces for Depth of Cut - 0.1nm (Flat End Tool)</p>	<p>Cutting Forces for Depth of Cut - 0.1nm (Pointed End Tool)</p>	<p>Cutting Forces for Depth of Cut - 0.1nm (Spherical End Tool)</p>	<p>Cutting Forces for Depth of Cut - 0.1nm (Trapezoidal End Tool)</p>
0.15	<p>Cutting Forces for Depth of Cut - 0.15nm (Flat End Tool)</p>	<p>Cutting Forces for Depth of Cut - 0.15nm (Pointed End Tool)</p>	<p>Cutting Forces for Depth of Cut - 0.15nm (Spherical End Tool)</p>	<p>Cutting Forces for Depth of Cut - 0.15nm (Trapezoidal End Tool)</p>



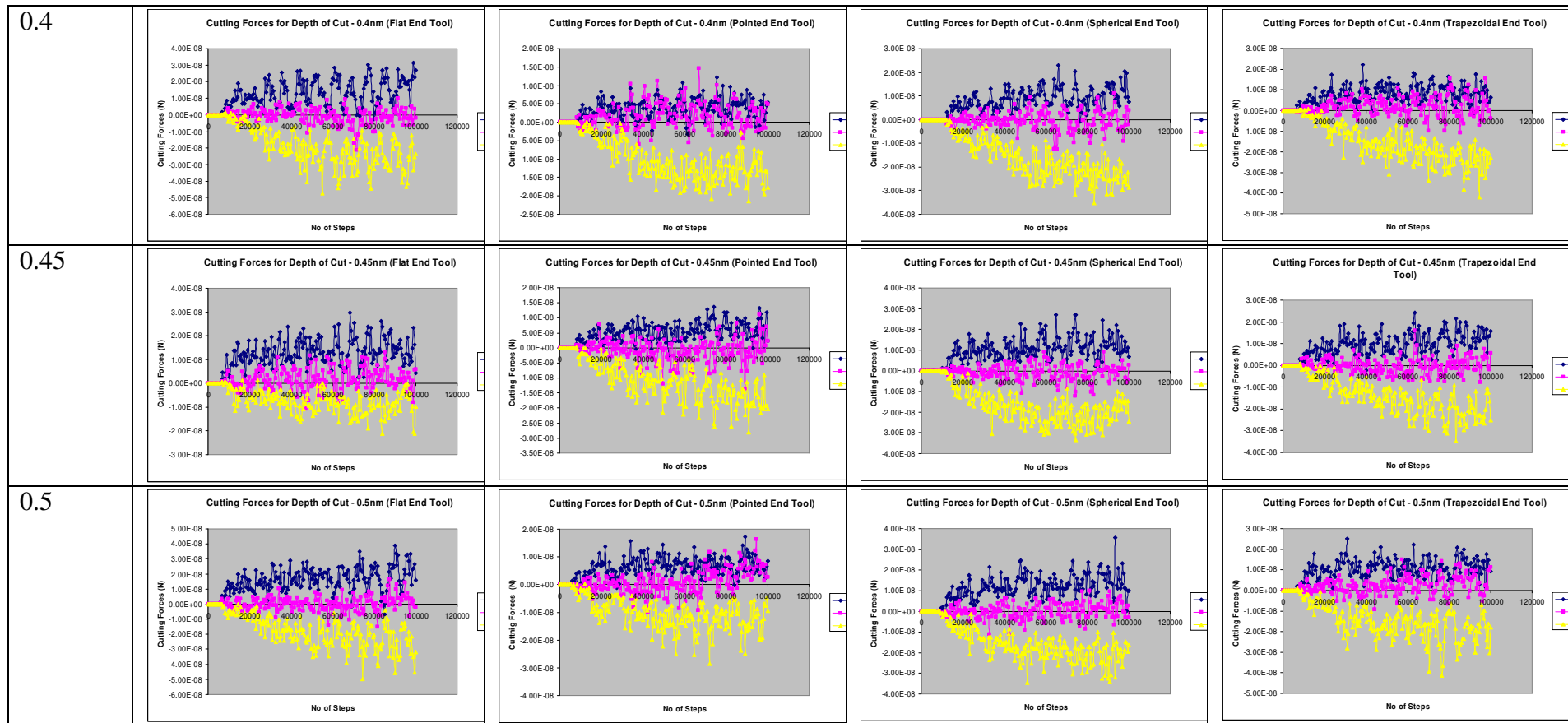
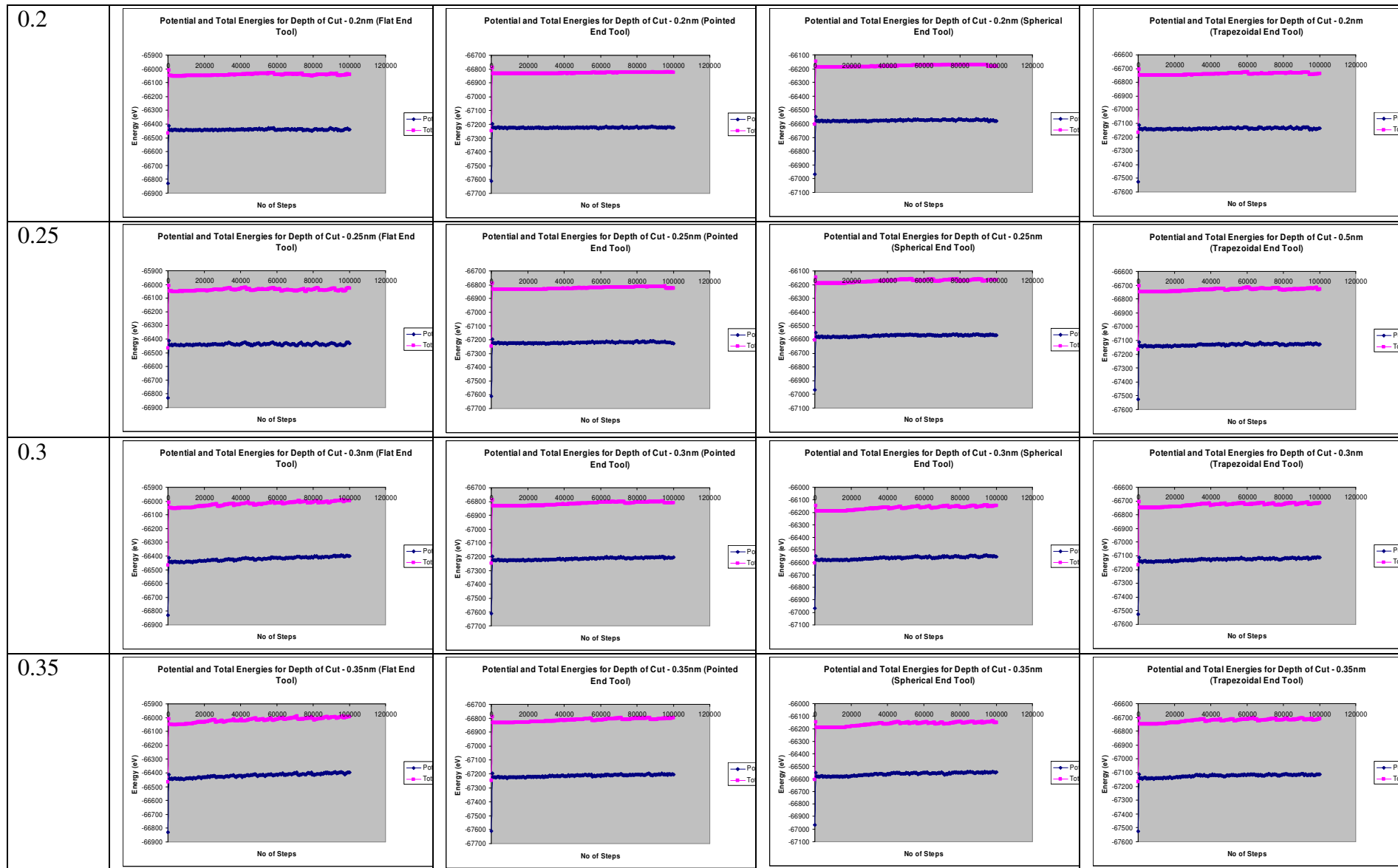


Table C.7: Comparison of the Energies for the Different Tool Ends (Depth of Cut 0.05-0.5nm)

Depth of Cut (nm)	Flat Tool End	Pointed Tool End	Spherical Tool End	Trapezoidal Tool End
0.05	<p>Potential and Total Energies for Depth of Cut - 0.05nm (Flat End Tool)</p>	<p>Potential and Total Energies for Depth of Cut - 0.05nm (Pointed End Tool)</p>	<p>Potential and Total Energies for Depth of Cut - 0.05nm (Spherical End Tool)</p>	<p>Potential and Total Energies for Depth of Cut - 0.05nm (Trapezoidal End Tool)</p>
0.1	<p>Potential and Total Energies for Depth of Cut - 0.1nm (Flat End Tool)</p>	<p>Potential and Total Energies for Depth of Cut - 0.1nm (Pointed End Tool)</p>	<p>Potential and Total Energies for Depth of Cut - 0.1nm (Spherical End Tool)</p>	<p>Potential and Total Energies for Depth of Cut - 0.1nm (Trapezoidal End Tool)</p>
0.15	<p>Potential and Total Energies for Depth of Cut - 0.15nm (Flat End Tool)</p>	<p>Potential and Total Energies for Depth of Cut - 0.15nm (Pointed End Tool)</p>	<p>Potential and Total Energies for Depth of Cut - 0.15nm (Spherical End Tool)</p>	<p>Potential and Total Energies for Depth of Cut - 0.15nm (Trapezoidal End Tool)</p>



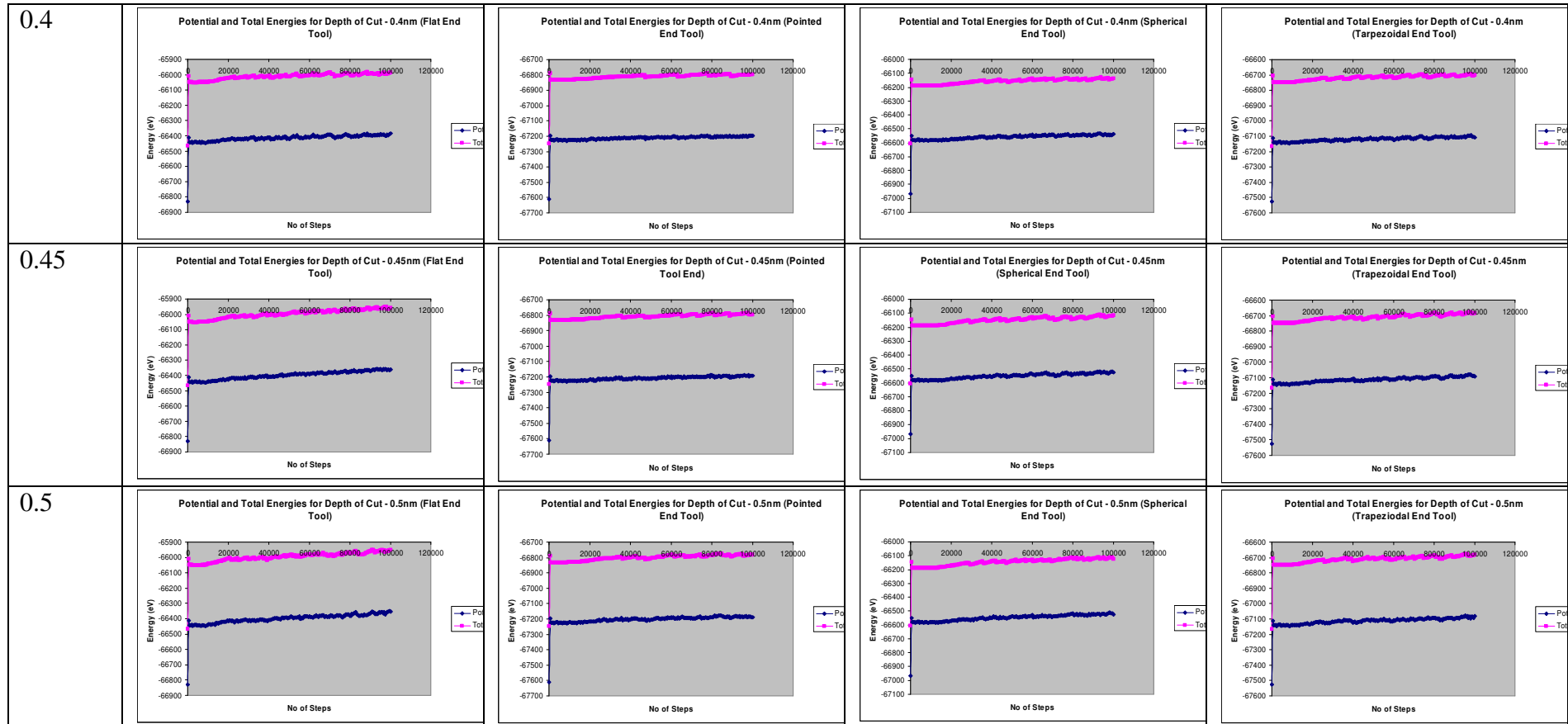
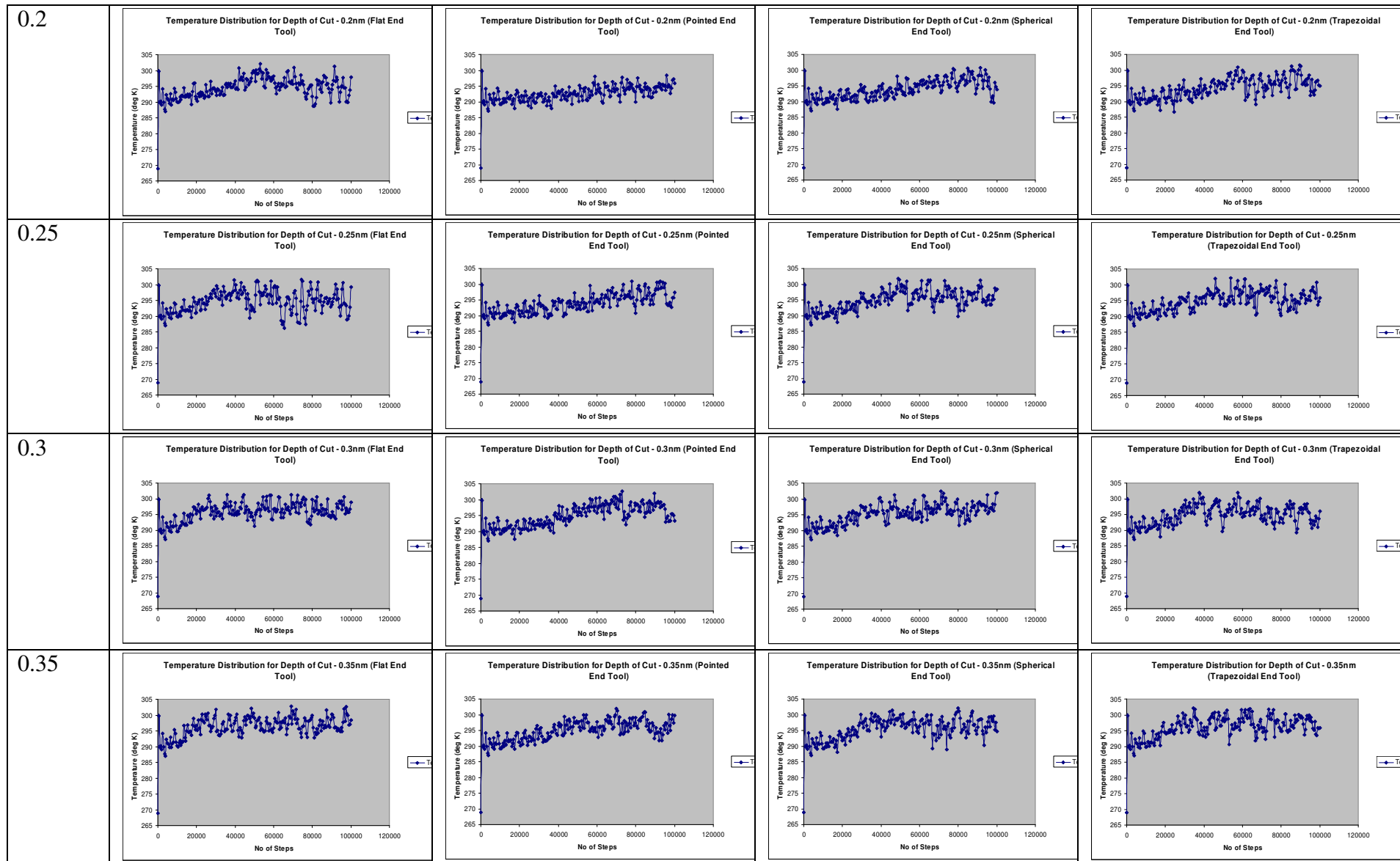


Table C.8: Comparison of the Temperature Variation for the Different Tool Ends (Depth of Cut 0.05-0.5nm)

Depth of Cut (nm)	Flat Tool End	Pointed Tool End	Spherical Tool End	Trapezoidal Tool End
0.05	<p>Temperature Distribution for Depth of Cut - 0.05nm (Flat End Tool)</p>	<p>Temperature Distribution for Depth of Cut - 0.05nm (Pointed End Tool)</p>	<p>Temperature Distribution for Depth of Cut - 0.05nm (Spherical End Tool)</p>	<p>Temperature Distribution for Depth of Cut - 0.05nm (Trapezoidal End Tool)</p>
0.1	<p>Temperature Distribution for Depth of Cut - 0.1nm (Flat End Tool)</p>	<p>Temperature Distribution for Depth of Cut - 0.1nm (Pointed End Tool)</p>	<p>Temperature Distribution for Depth of Cut - 0.1nm (Spherical End Tool)</p>	<p>Temperature Distribution for Depth of Cut - 0.1nm (Trapezoidal End Tool)</p>
0.15	<p>Temperature Distribution for Depth of Cut - 0.15nm (Flat End Tool)</p>	<p>Temperature Distribution for Depth of Cut - 0.15nm (Pointed End Tool)</p>	<p>Temperature Distribution for Depth of Cut - 0.15nm (Spherical End Tool)</p>	<p>Temperature Distribution for Depth of Cut - 0.15nm (Trapezoidal End Tool)</p>



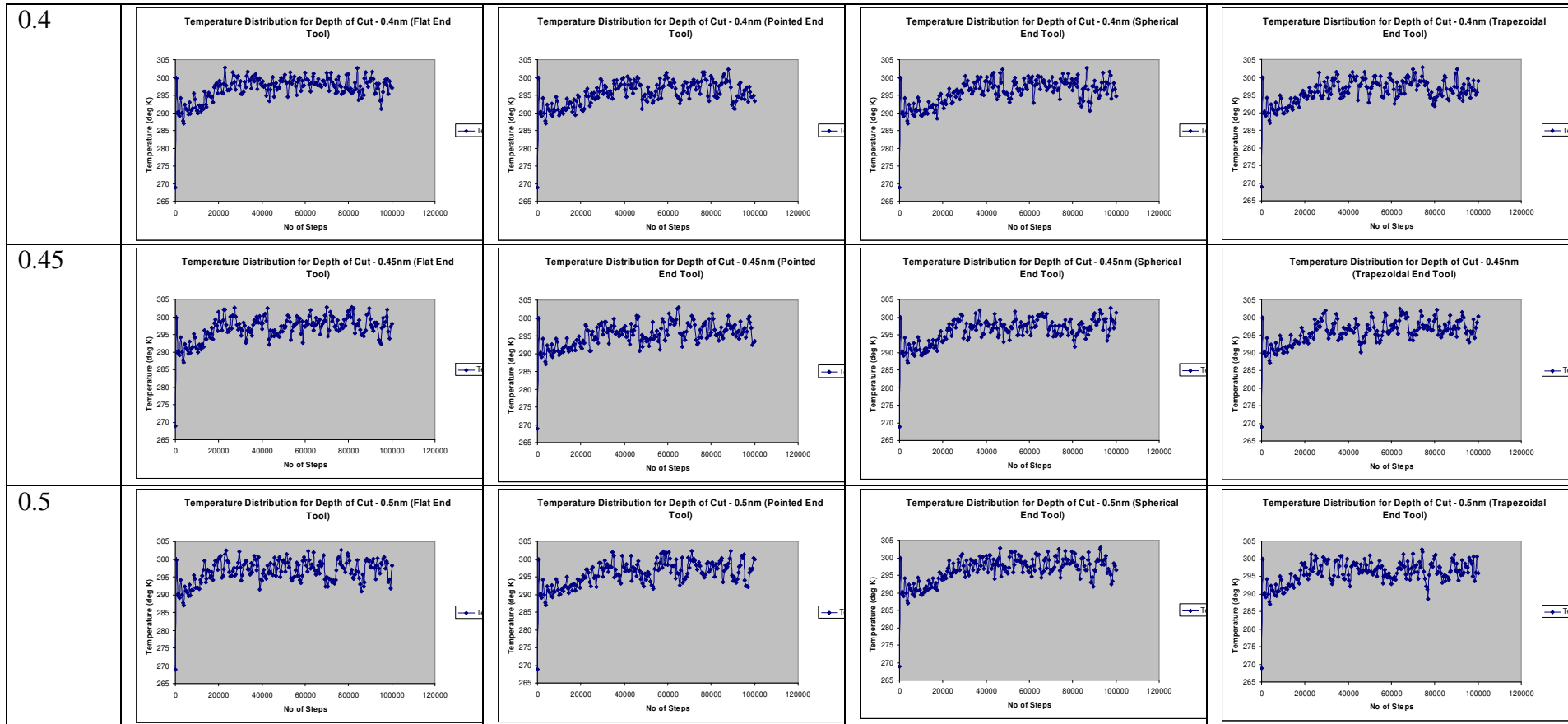


Table C.9: Cutting Forces for the Different Cases

Cases	Pass 1	Pass 2	Pass 3
Case 5.1			
Case 5.2			
Case 5.3			
Case 5.4			
Case 5.5			
Case 5.6			

Table C.10: Temperature Variation for the Different Cases

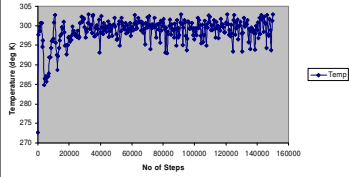
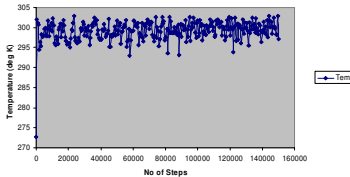
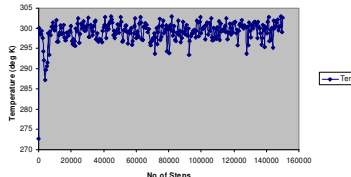
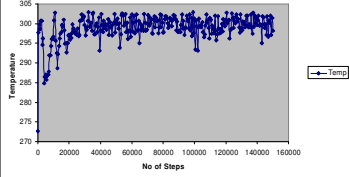
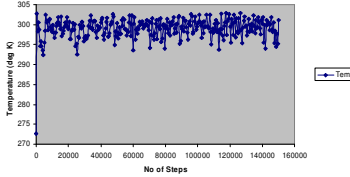
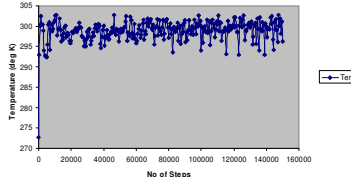
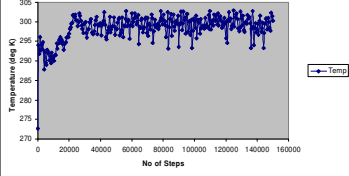
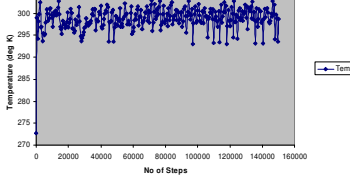
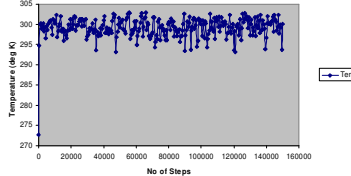
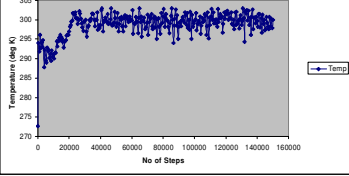
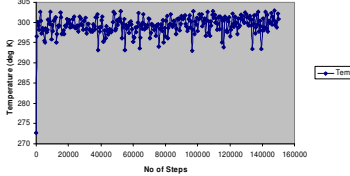
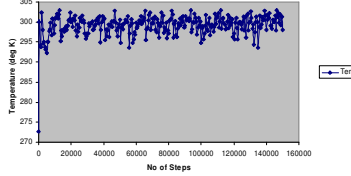
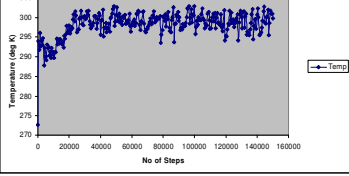
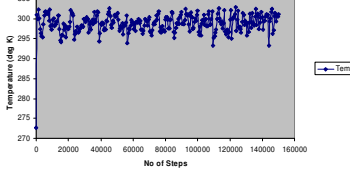
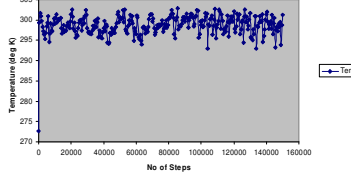
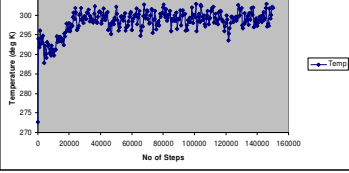
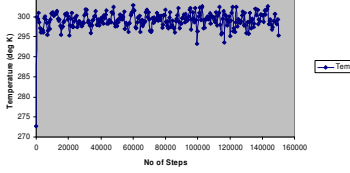
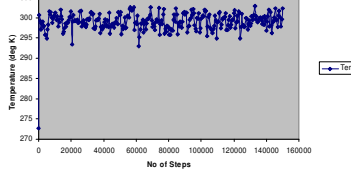
Cases	Pass 1	Pass 2	Pass 3
Case 5.1	<p>Temperature Distribution for Morse-Morse Potentials (Rigid Tool) - Pass 1</p> 	<p>Temperature Distribution for Morse-Morse Potentials (Rigid Tool) - Pass 2</p> 	<p>Temperature Distribution for Morse-Morse Potentials (Rigid Tool) - Pass 3</p> 
Case 5.2	<p>Temperature Distribution for Morse-Morse Potentials (Non Rigid Tool) - Pass 1</p> 	<p>Temperature Distribution for Morse-Morse Potentials (Non Rigid Tool) - Pass 2</p> 	<p>Temperature Distribution for Morse-Morse Potentials (Non Rigid Tool) - Pass 3</p> 
Case 5.3	<p>Temperature Distribution for EAM-Morse Potentials (Rigid Tool) - Pass 1</p> 	<p>Temperature Distribution for EAM-Morse Potentials (Rigid Tool) - Pass 2</p> 	<p>Temperature Distribution for EAM-Morse Potentials (Rigid Tool) - Pass 3</p> 
Case 5.4	<p>Temperature Distribution for EAM-Morse Potentials (Non Rigid Tool) - Pass 1</p> 	<p>Temperature Distribution for EAM-Morse Potentials (Non Rigid Tool) - Pass 2</p> 	<p>Temperature Distribution for EAM-Morse Potentials (Non Rigid Tool) - Pass 3</p> 
Case 5.5	<p>Temperature Distribution for EAM-LJ Potential (Rigid Tool) - Pass 1</p> 	<p>Temperature Distribution for EAM-LJ Potentials (Rigid Tool) - Pass 2</p> 	<p>Temperature Distribution for EAM-LJ Potentials (Rigid Tool) - Pass 3</p> 
Case 5.6	<p>Temperature Distribution for EAM-LJ Potentials (Non Rigid Tool) - Pass 1</p> 	<p>Temperature Distribution for EAM-LJ Potentials (Non Rigid Tool) - Pass 2</p> 	<p>Temperature Distribution for EAM-LJ Potentials (Non Rigid Tool) - Pass 3</p> 

Table C.11: Cutting Forces for Different Depths of Cut (0.5 – 3nm)

Depth of Cut (nm)	Pass 1	Pass 2	Pass 3
0.5			
1			
1.5			
2			
2.5			
3			

Table C.12: Cutting Forces Different Feeds (0.5 – 1.5nm)

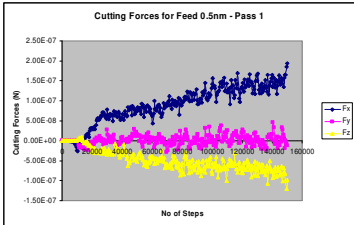
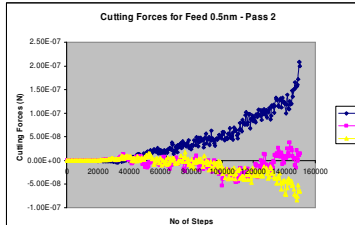
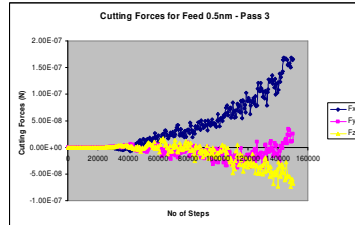

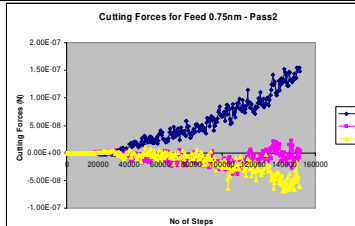
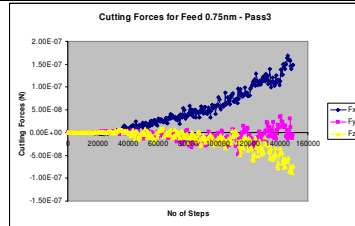
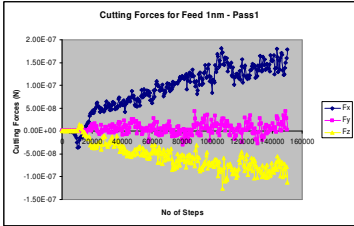
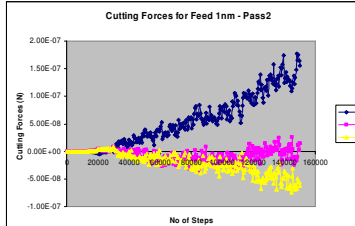
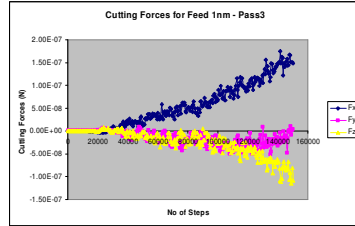


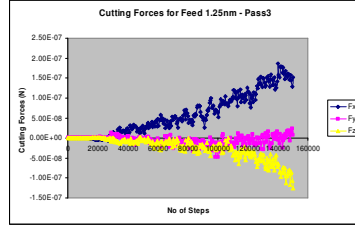

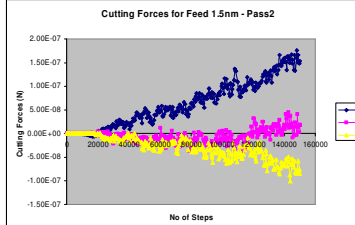

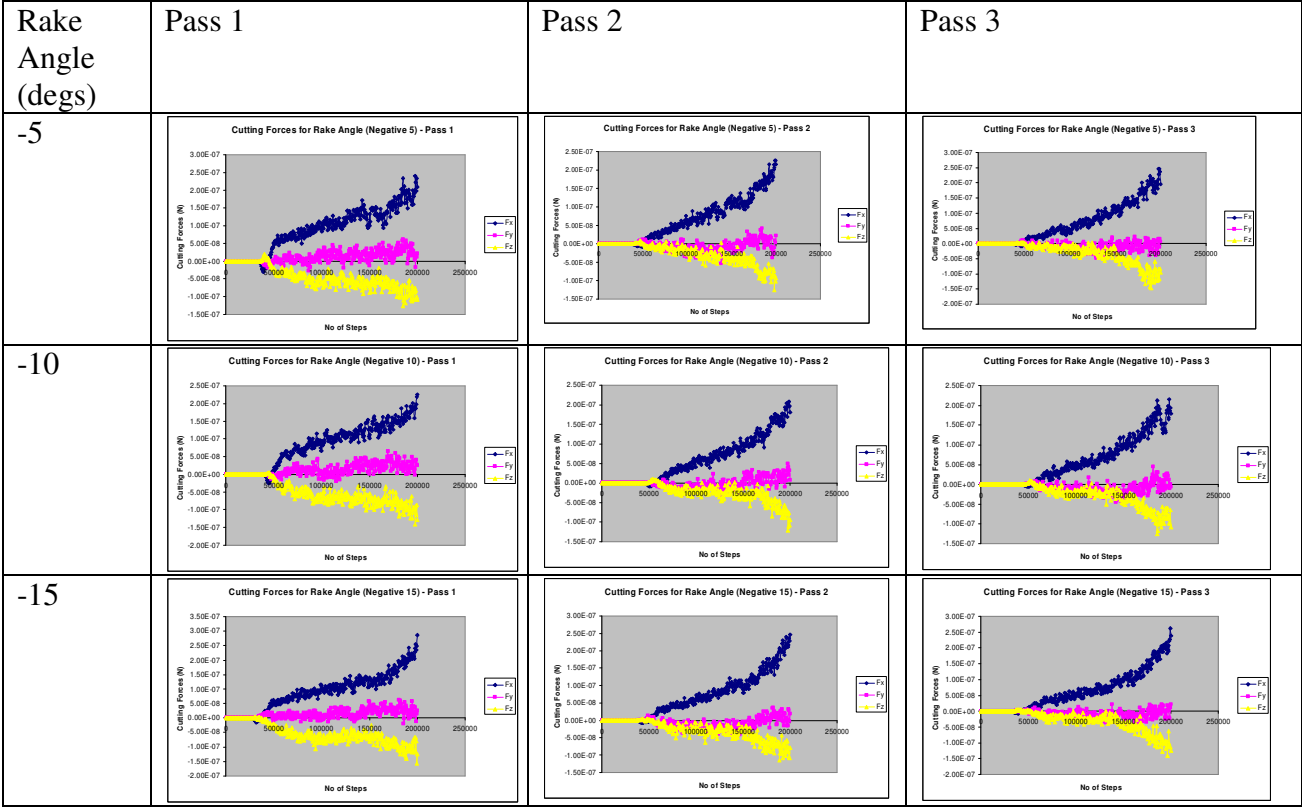
Feed (nm)	Pass 1	Pass 2	Pass 3
0.5			
0.75			
1.0			
1.25			
1.5			

Table C.13: Cutting Forces for Different Rake Angles (-5°, -10° and -15°)



Appendix D: Publications arising from this Research

Journal Articles

1. Oluwajobi A.O. and X. Chen (2010), 'The Fundamentals of Modelling Abrasive Machining Using Molecular Dynamics', *International Journal of Abrasive Technology*, Vol. 3, No 4, pp. 354-381
2. Oluwajobi A.O. and X.Chen (2011), 'The Effect of Interatomic Potentials on the Molecular Dynamics Simulation of Nanometric Machining', *International Journal of Automation and Computing*, Vol. 8, No. 3, pp. 326-332
3. Oluwajobi A.O. and X.Chen (2012), 'Multi-Pass Nanometric Machining Simulation using the Molecular Dynamics (MD)', *Key Engineering Materials*, Vol. 496, pp. 241-246
4. Chen X., T.T. Opoz and A. Oluwajobi (2012), 'Grinding Surface Creation using Finite Element Method and Molecular Dynamics', *Advanced Materials Research*, Vol. 500, pp. 314-319
5. Oluwajobi A.O. and X. Chen (2012), 'The Determination of the Minimum Depth Cut in Nanometric Machining using the Molecular Dynamics Simulation', *Advanced Materials Research*, Vol. 565, pp. 570-575
6. Oluwajobi A.O. and X. Chen (2013), 'The Effect of Interatomic Potentials on the Onset of Plasticity in the Molecular Dynamics (MD) Simulation of Nanometric Machining', *Key Engineering Materials*, Vols. 535-536, pp. 330-333
7. Oluwajobi A.O. and X. Chen (2012), 'The Effect of Machining Conditions on the Molecular Dynamics (MD) Simulation of Multi-Pass Nanometric Machining' (Submitted to *Computational Material Science*)
8. Oluwajobi A.O. and X. Chen, 'Choosing Appropriate Interatomic Potentials for Nanomachining Molecular Dynamics (MD) Simulations' (In Preparation)

Conference Proceedings Articles

1. Oluwajobi A.O. and X. Chen (2008), 'Modelling Abrasive Machining Techniques Using Molecular Dynamics', *Proceedings of Computing and Engineering Annual Researchers' Conference*, Huddersfield, pp.100-105
2. Oluwajobi A.O. and X. Chen (2009), 'Cellular Automata Modelling of Micro Abrasive Machining Modelling', *Proceedings of Computing and Engineering Annual Researchers' Conference*, Huddersfield, pp.159-164
3. Oluwajobi A.O. and X.Chen (2010), 'On Minimum Depth Cut in Nanomachining', In: *Advances in Manufacturing Technology: Durham University and Glasgow Caledonian University*, *Proceedings of the 8th International Conference on Manufacturing Research*, University of Durham, Durham, pp. 174-179
4. Oluwajobi A.O. and X.Chen (2010), 'The Effect of Interatomic Potentials on Nanometric Abrasive Machining', *Proceedings of the 16th International Conference on Automation & Computing*, University of Birmingham, Birmingham, pp. 130-135
5. Oluwajobi A.O. and X.Chen (2010), 'The Effect of Tool Geometry on Rubbing and Ploughing Phenomena in Nano Abrasive Machining', *Proceedings of Computing and Engineering Annual Researchers' Conference*, Huddersfield, pp. 160-165
6. Oluwajobi A.O. and X.Chen (2011), 'The Effect of Depth of Cut on the Molecular Dynamics (MD) Simulation of Multi-Pass Nanometric Machining', *Proceedings of the 17th*

- International Conference on Automation & Computing (IEEE Conference), University of Huddersfield, Huddersfield, pp. 40-45
7. Oluwajobi A.O. and X. Chen (2012), 'The Effect of The Variation of Tool End Geometry on Material Removal Mechanisms in Nanomachining', Proceedings of the 13th International Conference on Tools, University of Miskolc, Hungary, pp. 71-76
 8. Oluwajobi A.O. and X. Chen (2012), 'Acoustic Emission Detection Signals in the Experimental Validation of Nanometric Machining Simulations', Proceedings of the 13th International Conference on Tools, University of Miskolc, Hungary, pp. 395-400
 9. Oluwajobi A.O. and X. Chen (2012), 'The Effect of the Variation of Velocity on the Molecular Dynamics Simulation of Nanomachining', Proceedings of the 18th International Conference on Automation & Computing, Loughborough University, Leicestershire, UK, Sept. 2012, pp. 249-254